Results of the QUENCH-18 Bundle Experiment on Air Ingress and AgInCd absorber behavior

J. Stuckert, J. Kalilainen, T. Lind, U. Stegmaier, M. Steinbrück,

Y. Zhang

KIT
Karlsruher Institut für Technologie

Results of the QUENCH-18 Bundle Experiment on Air Ingress and AgInCd absorber behavior

J. Stuckert, J. Kalilainen*, T. Lind*, U. Stegmaier, M. Steinbrück, Y. Zhang**

Institut für Angewandte Materialien:

Angewandte Werkstoffphysik (IAM-AWP)

Programm Nukleare Sicherheitsforschung

*PSI, Switzerland

**XJTU, China

Abstract

The experiment QUENCH-18 on air ingress and aerosol release in an electrical heated test bundle with 24 rods and a length of about 2 m was successfully conducted at KIT on 27 September 2017. This test was performed in the frame of the EC supported ALISA program. It was proposed by XJTU Xi'an (China) and supported by PSI (Switzerland) and GRS (Germany). The primary aims were to examine the oxidation of M5$^{®}$ claddings in air/steam mixture following a limited pre-oxidation in steam, and to achieve a long period of oxygen and steam starvations to promote interaction with the nitrogen. QUENCH-18 was thus a companion test to the earlier air ingress experiments, QUENCH-10 and -16 (in contrast to QUENCH-18, these two bundle tests were performed without steam flow during the air ingress stage). Additionally, the QUENCH-18 experiment investigated the effects of the presence of two Ag-In-Cd control rods on early-stage bundle degradation (companion test to the QUENCH-13 experiment), and of two pressurized unheated rod simulators (60 bar, He). The low pressurized heater rods (2.3 bar, similar to the system pressure) were Kr-filled.

In a first transient, the bundle was heated from the peak cladding temperature $T_{pct} ≈ 900$ K in an atmosphere of flowing argon (3 g/s) and superheated steam (3.3 g/s) by electrical power increase to the peak cladding temperature of $T_{pct} ≈ 1400$ K. During this heat-up (with the heat-up rate 0.3 K/s), claddings of the two pressurized rods burst at a temperature of 1045 K. The attainment of $T_{pct} ≈ 1400$ K marked the start of the pre-oxidation stage to achieve a maximum cladding oxide layer thickness of about 80 μm. Then the power was reduced from 9 to 3.8 kW (simulation of decay heat) which effected a cooling of the bundle to $T_{pct} ≈ 1080$ K, as a preparation for the air ingress stage.

In the subsequent air ingress stage, the steam flow was reduced to 0.3 g/s, the argon flow was reduced to 1 g/s, and air was injected with the flow rate of 0.21 g/s. The change in flow conditions had the immediate effect of reducing the heat transfer so that the temperatures began to rise again. The first Ag-In-Cd aerosol release was registered at $T_{pct} = 1350$ K and was dominated by Cd bearing aerosols. Later in the transient, a significant release of Ag was observed along with continued Cd release, as well as a small amount of In. In contrast to the QUENCH-16 test (performed with the air ingress stage without steam flow), oxidation of bundle parts in air and steam caused release of higher chemical energy (power about 8 kW) and consequently acceleration of bundle heat-up. A strong temperature escalation started in the middle of the air ingress stage. Later a period of oxygen starvation occurred and was followed by almost complete steam consumption and partial consumption of the nitrogen, indicating the possibility of formation of zirconium nitrides. Following this the temperatures continued to increase and stabilized at melting temperature of Zr bearing materials until water injection. The total consumption of oxygen, steam and nitrogen was 100±3, 450±10 and 120±3 g, respectively. During the starvation period a noticeable production (about 25 mg/s, totally 45±1 g) of hydrogen was measured. Almost immediately after the start of reflood there was a temperature excursion in the mid to upper regions of the bundle, leading to maximum measured temperatures of about 2450 K with cladding melt release, relocation and oxidation. Reflood progressed rather slowly and final quench was achieved after about 800 s. A significant quantity of hydrogen was generated during the reflood (238±2 g). Nitrogen release (>54 g) due to re-oxidation of nitrides was also registered.

Zirconium nitrides and re-oxidized nitrides were found in the middle part of the bundle. In this bundle region, the claddings and cladding melt were strongly oxidized, the melt was collected mostly inside the grid spacer. Partially oxidized Zr-bearing melt was found down to elevation 160 mm; this elevation was the lowest with evidence of relocated pellet material. At the bundle bottom, only frozen metallic melt containing Zr, Ag, In and Cd was observed between several rods.

The data of the experiment are used for validation of severe accident code systems.

Contents

List of Tables

List of Figures

1   Introduction

The main goal of the QUENCH program at KIT is to investigate the core thermal response, the cladding oxidation with accompanying hydrogen release and the cooling efficacy of water injection under design basis (DBA) and beyond design basis (BDBA) accident conditions. The program was initiated in 1996 and is still on-going [1], [2], [3]. Nineteen high temperature bundle tests were performed so far (Table 1). Experiment QUENCH-18 on air ingress and aerosol release was conducted on 27 September 2017 in the framework of the EC supported ALISA program. It was proposed by XJTU Xi'an (China) and supported by PSI (Switzerland) and GRS (Germany). QUENCH-18 was the worldwide first bundle experiment on air ingress including a prototypic mixed air/steam atmosphere.

The primary aims of the experiment were to examine the oxidation of M5® claddings in air/steam mixture following a limited pre-oxidation in steam, and to achieve a long period of oxygen and steam starvations to promote interaction with the nitrogen. QUENCH-18 was thus a companion test to the earlier air ingress experiments, QUENCH-10 [4] and QUENCH-16 [5]. In contrast to QUENCH-18, these two bundle tests were performed without steam flow during the air ingress stage. Due to air ingress as a potential risk in low probable situations of severe accidents in nuclear power plants or accidents in spent fuel pools, also other research centers have performed bundle tests on air ingress with bundle geometries other than in the QUENCH facility [6]. In addition numerous separate-effect tests conducted at KIT and elsewhere have demonstrated the strong effect of nitrogen on the oxidation kinetics of Zr alloys [7]-[12].

Additionally, the QUENCH-18 experiment investigated the effects of the presence of two Ag-In-Cd control rods on early-stage bundle degradation (companion test to the QUENCH-13 experiment [13], [14]), and of two pressurized unheated rod simulators (60 bar, He).

2 Test facility

The main component of the QUENCH test facility is the test section with the test bundle (Figure 1…Figure 5). The facility can be operated in two modes: (a) a forced-convection mode and (b) a boil-off mode with the steam inlet line closed. QUENCH-18 was conducted in forced-convection mode, in which superheated steam from the steam generator and super-heater together with argon as a carrier gas for off-gas measurements enter the test bundle at the bottom. The system pressure in the test section is usually around 0.2 MPa absolute.

Additionally to the gas inlet (steam and argon as carrier gas), the test section has separate inlets at the bottom to inject synthetic air (80% N_2 + 20% O_2) during the air ingress stage and water for final reflood (bottom quenching). The steam, argon and all other gases injected or produced flow from the bundle outlet at the top through a water-cooled off-gas pipe to the condenser where the steam is separated from the non-condensable gases. The water cooling circuits for bundle head and off-gas pipe are temperature-controlled to guarantee that the steam/gas temperature is high enough so that condensation at the test section outlet and inside the off-gas pipe is avoided and measurement of steam by mass spectrometer, located at the end of the off-gas pipe, is possible.

The design characteristics of the bundle are given in Table 2. This table also presents the so-called effective number of fuel rod simulators (38 rods) to show the contribution of the shroud and corner rods to the total oxidizable surface; for comparison: this parameter for QUENCH-16 is 31 effective rods. The test bundle is made up of 22 approximately 2.5 m long fuel rod simulators (Figure 6, Figure 7) and 2 absorber rods (Figure 8, Figure 9). The fuel rod simulators are held in position by five AREVA grid spacers AH 32715 with a pitch of

12.6 mm. The rod cladding of the heated and unheated fuel rod simulators is M5® with 9.5 mm outside diameter and 0.570 mm wall thickness. Two fuel rod simulators are unheated and filled with He pressurized to 6.0 MPa (Figure 7). Twenty low-pressurized heater rods (0.23 MPa) were Kr-filled. Heating is electric by 5 mm diameter tungsten heaters of length 1024 mm installed in the rod center. The lower edge of the tungsten heaters corresponds to the bundle elevation of 0 mm. The tungsten heaters are surrounded by annular ZrO_2-TZP pellets of 10 mm height as simulator of UO_2 pellets (Table 3). At both ends of the tungsten heaters, molybdenum heaters and copper electrodes are connected. The copper electrodes are connected by gilded slide contacts to the cables leading to the DC electrical power supply. The electrical resistance of the bundle heating system, combined from W-, Mo-heaters and copper electrodes was measured at room temperature before and after the test (Table 4). The heating power is distributed between two groups of heated rods (10 + 10 heated rods).

There are eight corner rods installed in the bundle. Four of them, i.e. rods "A", "C", "E" and "G", are made of a Zircaloy-4 solid rod at the top and a Zircaloy-4 tube at the bottom and are used for thermocouple instrumentation. The other four rods (solid Zircaloy-4 rods of 6 mm diameter) are particularly designed to be withdrawn from the bundle during the test to check the amount of oxidation and hydrogen uptake at specific times during the experiment.

The test bundle is surrounded by a 3.05 mm thick shroud of Zirconium-702 (inner diameter 82.8 mm) with a 34 mm thick ZrO_2 fiber insulation (Table 5) extending from the bottom to the upper end of the heated zone and a double-walled cooling jacket of Inconel (inner tube) and stainless steel (outer tube) over the entire length. The annulus between shroud and cooling jacket is purged (after several cycles of evacuation) and then filled with stagnant argon at 0.22 MPa absolute. The absence of ZrO_2 insulation above the heated region and the water cooling of the bundle head are to avoid too high temperatures of the bundle in that upper bundle part.

3 Instrumentation and data acquisition

The bundle is instrumented with 37 high-temperature (W/Re) thermocouples (TC) in the upper hot region (bundle, shroud and corner rod thermocouples between elevations 650 and 1350 mm), 4 low-temperature (NiCr/Ni) thermocouples at elevations 1250 and 1350 mm (shroud), and 32 low-temperature (NiCr/Ni) thermocouples in the lower "cold" bundle region (bundle and shroud thermocouples between -250 and 550 mm) (Figure 10...Figure 13). The thermocouples are listed in Table 6 together with other measurement devices. Table 7 gives an overview of the positions of the bundle thermocouples. The dimensions of high temperature thermocouples, which were manufactured by KIT, are provided in Table 8, some properties of the TC insulator are given in Table 9. The thermocouples attached to the outer surface of the rod cladding at elevations between -250 and 1350 mm are designated "TFS" for all heated rods (21 thermocouples). At elevation 950 mm there are two centerline high-temperature thermocouples in the central rod (designation "TCC"), which are protected from oxidizing influence of steam and air. Four other protected high-temperature thermocouples are installed at elevations 550, 650, 750, and 850 mm inside the corner rods G, E, C and A and designated "TIT" (Figure 14). The shroud thermocouples (designation "TSH") are mounted at the outer surface between 250 and 1250 mm. Additionally, the test section incorporates pressure gauges, flow meters, and a water level detector.

The off-gas including Ar, He, Kr, H_2, O_2, N_2 and H_2O is analyzed by a quadrupole mass spectrometer Balzers "GAM300" whose sampling position is located at the off-gas pipe ≈2.66 m downstream the test section (Figure 15, Figure 16). The mass spectrometer allows indicating the failure of rod simulators by detection of He and Kr release.

Aerosol measurements were performed with two systems: 1) on-line device ELPI (electrical low pressure impactor) and 2) two particle collection devices BLPI (Berner low pressure impactor) (Figure 54). Additionally,

three polycarbonate filters (Nuclepore) were installed in parallel to BLPI and withdrawn successively during the air ingress stage.

4 Test performance and results of online measurements

The detailed sequence of the test events is described in Table 10. The test scenario is depicted in Figure 17. The data of the electric power input (current, voltage) from both DC generators are shown in Figure 18. The maximum current of about 1600 A (per generator) was measured in the relatively cold bundle at the beginning of the test. The maximum voltage of about 3.2 V was reached at the end of the pre-oxidation stage (oscillations during quench are noise at the generator switch-off). The change of electrical resistances of both heated rod groups are presented also in this Figure; the resistance values were calculated on the basis of measured currents and voltages. Whereas the lowest resistance of 0.45 mOhm was measured at the room temperature (Table 4), the highest resistance of about 3 mOhm was reached during the exothermic chemical heating in the quench stage.

Figure 19…Figure 35 show readings of thermocouples at bundle elevation -250…1350 mm. In a first transient, the bundle was heated by power increase to the peak cladding temperature of $T_{pct} \approx 1400$ K, reached at 4000 s (heat-up rate 0.3 K/s). During this heat-up, claddings of the two pressurized rods #9 and #15 burst at temperatures of ≈ 1035 and 1045 K, respectively (Figure 42). These burst temperature values are lower in comparison to the values observed during the bundle test QUENCH-L2 (T_{pct} = 1138 ± 34 K), which was performed with M5® claddings 10.75/0.725 mm and heat-up rate of 8 K/s, due to lower heat-up rate and thinner cladding wall [15], [16].

The attainment of Tpct ≈ 1400 K at the bundle elevation 950 mm marked the start of the pre-oxidation stage to achieve a maximum cladding oxide layer thickness of about 100 μm. The power was controlled via small variations between 8.8 to 9.4 kW, to maintain more or less constant temperatures. In line with pre-test planning calculations about 11.5 g of hydrogen were produced in this stage that lasted until 6310 s. At this point the power was reduced to 3.8 kW which effected a cooling of the bundle to $T_{pct} \approx 1080$ K, as a preparation for the air ingress stage. The cooling stage lasted about 1100 s, until 7400 s. The highest temperature was registered at the elevation 850 mm (axial temperature profile in Figure 39).

Towards the end of this stage, the corner rod D was extracted from the test bundle for determination of the degree of oxidation at various bundle elevations. Figure 60 shows results of eddy current measurements in comparison with metallographic data. Metallographic investigations of cross sections between 550 and 1150 mm showed formation of regular oxide layers without breakaway effect (Figure 61). The highest oxidation degree was reached at the hottest (during this test stage) bundle elevation of 950 mm with an oxide layer thickness of ≈80 μm, and ≈110 μm thickness of the α-Zr(O) layer.

In the subsequent air ingress stage, the steam flow was reduced to 0.3 g/s (7411 s), the argon flow was reduced to 1 g/s (7424 s), and air was injected at 7540 s with a flow rate of 0.21 g/s. The power was maintained at 3.8 kW. After some time measurements demonstrated a gradually increasing consumption of oxygen, starting at about 9000 s (Figure 48). The change in flow conditions had the immediate effect of reducing the heat transfer so that the temperatures began to rise again, especially at elevations below 900 mm (Figure 43). This temperature escalation was much more pronounced than during the air ingress stage in the QUENCH-16 bundle test performed without steam during the air ingress and had a total area of metallic zirconium only 8% less than that of QUENCH-18 (Figure 44). With the beginning of escalation, the absorber melt relocation to elevations -250…350 mm was registered by thermocouples installed at these elevations (Figure 45). No strong temperature escalation was observed at elevations below 100 mm (Figure 45) and above 900 mm (Figure 46). At the elevations 550…850 mm, the temperatures reached the melting

point of Zr alloy almost simultaneously and then remained constant until the quench initiation (Figure 43). Figure 40 depicts the axial temperature distribution at the beginning of bundle melting.

4.1   Aerosol release

The scheme of aerosol measurement devices is given in Figure 54. The detailed results, description as well the corresponding analysis are given in [17], [18]. The failure of absorber rods with helium release and first Ag-In-Cd aerosol release was registered at 10530 s with a corresponding temperature of T_{pct} = 1350 K (at 950 mm) and T_{550mm} = 1300 K (Figure 55). Effective diameter of sampled particles (ELPI and BLPI) was measured to be between 0.4 and 10 μm (the main part of released particles had a diameter of about 1 μm) (Figure 56). High aerosol concentration of several g/m^3 was measured until the quench initiation (Figure 57).

Based on the ICP-OES and SEM/EDX analysis, a rough estimation of absorber material releases during the whole test was performed (Table 11, Figure 58, Figure 59). The first aerosol release was dominated by Cd bearing aerosols. Later in the transient, a significant release of Ag was observed along with continued Cd release, as well as a small amount of In. A rough estimation of the release fraction of silver, indium and cadmium from the control rods can be made based on the average material concentrations obtained from the ICP analysis of the filter and BLPI samples. The estimated mass of released Ag, Cd and In, taking into account the estimated losses to the experimental facility, are shown in Table 12. Preliminary measurement of the deposit in the QUENCH facility revealed that approximately 100 mg of Cd had deposited at the bundle head on a surface of approximately 500 cm^2. The total release of aerosol in the QUENCH-18 test was substantially larger (6.6 g, 1.2 g and 9.0 g silver, indium and cadmium, respectively) than in the QUENCH-13 test (0.2 g, 1.5 g and 1.5 g silver, indium and cadmium, respectively [13]), even considering that in the QUENCH-18 test, two control rods were used in the bundle and in the QUENCH-13 only one. The two major differences between the aerosol concentrations in the two tests were that the concentration of indium was much lower, and the concentration of silver much higher in the QUENCH-18 as compared to the QUENCH-13 test.

4.2   Oxygen starvation, steam and nitrogen consumption.

A sharp increase of the steam consumption with simultaneous hydrogen release was registered at 10550 s (Figure 47). In contrast to the QUENCH-16 test (performed with 0.21 g/s air without steam flow in the air ingress stage), oxidation of bundle parts in steam caused additional release of chemical energy (power about *4 kW*, i.e. similar to electrical power of 3.8 kW during this air ingress stage) due to the exothermic oxidation by steam and consequently more intensive acceleration of bundle heat-up:

$$Zr + 2H_2O \rightarrow ZrO_2 + 2H_2 + \textbf{\textit{597 kJ/mol}} \textit{ (@1273 K)} \tag{1}$$
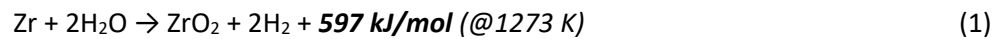
Additionally, consumption of oxygen and nitrogen are also exothermic processes with release of additional chemical energy of about 1.7+2.3 kW=4 kW (Figure 47):

$$Zr + O_2 \rightarrow ZrO_2 + \textbf{\textit{1096 kJ/mol}} \textit{ (@1273 K)} \tag{2}$$

$$2Zr + N_2 \rightarrow 2ZrN + \textbf{\textit{730 kJ/mol}} \textit{ (@1273 K)} \tag{3}$$

A strong temperature escalation started at about 10590 s at the bundle elevation of 550 mm and propagated to the upper and lower elevations between 150 and 850 mm. Due to the high temperatures at these elevations, most of the steam was absorbed here, and elevations above 950 mm had to be in steam starvation conditions with limited cladding oxidation. A period of oxygen starvation started at about 10700 s and was followed (about 300 s later) by almost complete steam consumption. Shortly before that time

(10640 s), partial consumption of the nitrogen was first observed, indicating local oxygen and steam starvation which promoted the onset of nitriding of claddings, shroud, corner rods and absorber guide tubes.

Following this, the temperatures continued to increase and *stabilized at melting temperature of Zr-bearing materials* at the bundle elevations 350…850 mm until water injection was initiated at 12330 s. Thus there was a period of 1630 s of strong steam and complete oxygen consumption and hence starvation in at least part of the bundle (Figure 48). Due to the relatively low heat input (≈3*4 kW=12 kW), as well as the high specific heat of fusion of zirconium (h_{fus}=185.7 kJ/kg) in comparison with its specific heat at the stage of temperature escalation (c≈0.27 kJ/kg/K), the escalation stopped when the melting point was reached. According to crucible experiments, a noticeable dissolution of zirconium oxide begins only from 2300 K [19]; therefore, the cladding melt appearing at ≈2000 K remains localized between the outer oxide layer and the pellet. This is also confirmed by the localization of the melt under the outer oxide layer in the previous QUENCH experiments, in which the melting temperature of the metal cladding was achieved [20], [21]. However, the cladding failures were registered by Kr release during the escalation and melting stage (Figure 49). The reason of this should be the crack development in the intensively growing oxide layer. The shroud failure with penetration of additional argon flow into the bundle was registered at the end of the temperature escalation (Figure 50). The probable penetration of gases to the outer metal shroud surface could additionally increase the chemical interactions between gas species and molten metal. The total consumption of oxygen, steam and nitrogen were 100±3, 450±10 and 120±3 g, respectively. During this starvation period a noticeable production (about 25 mg/s, totally *45±1 g*) of hydrogen was measured.

As temperatures approached the cladding melting point, a lower part of the second corner rod H (below elevation 550 mm) was withdrawn at t=11014 s. Figure 60 shows results of eddy current measurements in comparison with metallographic data. The upper part was shifted to cold lower positions and broke off during withdrawing. After the test, the segment 550…690 mm was also pulled out (Figure 66). Metallographic analysis of cross sections between 400 and 670 mm showed formation of α-Zr(O) and *ZrN* layers at the outer surface of the oxide layer at elevations above 500 mm (Figure 62…Figure 67). The nitrogen should have reacted with α-Zr(O) formed at the outer oxide surface during the oxygen and steam starvation [22].

4.3   Quench

The reflood was initiated simultaneously with turning off the air and steam flows, and switching the argon injection to the top of the bundle, followed by fast filling of the lower plenum of the test section with 4 kg of water, and continued by injecting 50 g/s of water. The electrical power remained at 3.8 kW during the reflood. Due to the established sufficient amount of evaporated water and the termination of steam starvation, almost immediately after the start of reflood there were a strong oxidation and temperature excursion in the mid to upper regions of the bundle (650 to 1350 mm), leading to maximum measured cladding temperatures T_{pct} = **2430 K** at 950 mm (Figure 51). Accordingly, the temperature of the gas passing through the bundle also underwent a jump: at the inlet to the off-gas pipe, the gas temperature rose in 100 s from 400 K to more than 1000 K (Figure 36).

A significant quantity of hydrogen was generated during the reflood (238 ± 2 g). Nitrogen release (> 54 g) due to re-oxidation of nitrides was also registered (Figure 53):

$$2ZrN + 4H_2O = 2ZrO_2 + 4H_2 + N_2 \tag{4}$$

According to this formula, during the nitride re-oxidation, 138.8 g of steam should have reacted and 15.4 g hydrogen should have been released. It means, the main part of hydrogen (238-15=223 g) was released due to oxidation of mostly molten Zr materials; the corresponding oxidation energy released is 33.3 MJ. A large part of the hydrogen and chemical energy escaped within 150 s; so, the estimated average chemical power during this period was 222 kW, which is significantly more than the electrical power to simulate decay (3.8 kW). Most likely, the process of explosive heating was accelerated due to the rapid dissolution of the

oxide layer of the cladding by the zirconium melt at temperatures >2400 K and the release of this melt from the cladding of the fuel elements [19]. The direct interaction of the melt with the steam leads to an even more accelerated heating of the bundle, since the rate of the steam-zirconium reaction with the melt is almost three times higher than its rate when interacting with metal claddings in the solid state [23].

Cooling was established at the middle bundle elevation (500 mm) about 70 s after the start of injection. However, a further increase in water level did not occur for almost 250 s. A possible reason for this was the failure of the shroud at elevations above 500 mm. Cooling was delayed further at upper elevations and reflood progressed rather slowly, due to 1) filling of space between the shroud and the cooling jacket with water and 2) the high temperatures, 3) intensive bundle melting and formation of partial blockages of the gas channel. Final quench was achieved after about 800 s. Due to failure of the shroud during the previous air ingress stage, the heat insulation was filled with water and steam, which was a reason for the enhanced heat transport to the cooling jacket and increase of temperatures at its inner wall from 650 up to 1500 K (Figure 37, Figure 52) and from 400 to 750 K at its outer wall (Figure 38).

5 Posttest investigations of bundle

5.1 Metallographic examination of corner rods

A maximum oxide layer thickness of 81 μm was determined for rod D at bundle elevation of 950 mm with direct metallographic measurements (Figure 61).

Metallographic investigations of corner rod H, withdrawn before reflood initiation, showed formation of porous nitrides ZrN at the outer surface of the oxide layer (Figure 62…Figure 67). The nitrides were formed at elevations above 500 mm under local or full oxygen starvation conditions. If the gas phase in the gas channel does not contain oxygen, the oxygen of the oxide layer is transported into the metal, especially from its outer surface. As a result, the formation of an α-Zr(O) layer at the oxide layer surface is observed [22]. The nitrogen reacted with α-Zr(O), resulting in the formation of zirconium nitride clusters. Due to the higher density of ZrN in comparison to that of α-Zr(O) (about 25% difference), the structure of the formed nitrides is very porous.

Concerning the cladding behavior after nitriding, the stresses induced during formation of nitrides lead to formation of cracks that go through the cladding and should be one of the reasons for cladding failure. Indeed, the first rod failures were detected about 70 s after beginning of nitrogen consumption and the corresponding formation of nitrides.

5.2 Visual and videoscope inspection

The overview of the bundle through the opening of the off-gas pipe connection showed very strong cladding oxidation at upper elevations with partial spalling of claddings (Figure 68, Figure 69). The thickness of outer oxide layers at elevation of 1350 mm reached 500 μm.

The videoscope inspection at the position of withdrawn corner rod D shows absorber melt relocation to the bundle bottom. According to thermocouple measurements, the first absorber melt relocation from elevations above 450 mm to lower elevations was registered at 10680…10700 s - shortly before failure of heated rods.

The facility was disassembled for post-test examinations. Due to extreme brittleness, the bundle broke into two parts at the elevation of about 1100 mm (Figure 70…71). It was practically not possible to separate the shroud and the ZrO_2 heat insulation between elevations 200 and 550 mm due to partial shroud melting. Frozen melt rivulets were recognized at oxidized cladding surfaces at elevations above 550 mm.

5.3 Metallographic examination of bundle cross sections

The two bundle parts were filled with epoxy resin, which was solidified after two weeks (Figure 73).

5.3.1 Elevations 1050…1480 mm

Up to the beginning of the flooding stage, temperatures in this zone with relatively low heat release from molybdenum heaters did not exceed 1570 K. After the initiation of the flooding, a sharp jump in temperatures by more than 1000 K occurred (Figure 32…Figure 35). Obviously, a relatively thin oxide layer formed here on the claddings at the stage of preoxidation then disappeared at the stage of oxygen starvation as a result of oxygen diffusion into the metal [22]. Consequently, during the flooding, a violent exothermic reaction occurred between zirconium and a large amount of steam, arising in the lower regions of the assembly due to the evaporation of the incoming water. The temperatures did not reach the melting point of molybdenum, but they were high enough for the intense sublimation of molybdenum oxidized in steam. In addition, some of the molybdenum heaters were liquefied as a result of eutectic interaction with zirconium (eutectic at 1823 K). As a consequence, the material of a significant part of the molybdenum rods was moved from this area of the bundle to its lower elevations.

The upper parts of rods #3 and #23 were slipped out from the bundle and separately investigated (Figure 74). Whereas practically only negligible cladding oxidation above the upper grid spacer (>1450 mm) was observed, a very strong oxidation below 1430 mm took place.

The separation of the bundle top (between 1090 and 1500 mm) into cross-sections (Figure 75) by diamond saw was performed according to Table 13. The metallographic investigation of claddings shows strong but not complete oxidation at elevations above 1350 mm and practically complete oxidation between 1100 and 1350 mm (Figure 76). At elevations below 1430 mm the metallic parts of the claddings were melted (Figure 77…Figure 82). During the melt relocation, the oxide layers and Mo heaters were partially dissolved. No Zr metallic melt was registered below 1350 mm - the melt was completely oxidized.

5.3.2 Elevations 65…950 mm

The separation of the bundle lower part into cross-sections by diamond saw was performed according to Table 14. These elevations are within the zone heated by tungsten heaters, and this is where most of the electrical energy was released. It was in this zone that temperatures escalated to the melting point of zirconium materials during the oxygen starvation stage. At the initial stage of escalation in this zone, the absorber rods failed and their eutectic melt moved to the bottom of this zone and even lower to the lower plenum of the bundle. Later, at the quench stage, zirconium melt, which had formed here during oxygen starvation, and also zirconium melt, formed at higher levels during flooding, moved through this zone. The melt was oxidized by steam and air during movement, its viscosity increased, as a result of which the downward movement speed decreased. The main part of the partially oxidized zirconium melt accumulated inside the spacer grid at the elevation 550-590 mm, but part of the melt also dropped to the elevation 160 mm (Figure 83).

5.3.3 Elevation 950 mm

In contrast to the lower elevations 250…850 mm, where the melting point of claddings of fuel simulators was reached already during oxygen starvation, the melting of the zirconium materials occurred at this elevation

firstly during reflood. The maximum temperature reached here during reflood was about **2430 K** and was measured inside unheated rods at 12450 s.

The bundle segment between angle positions 270°-0°-90°-135° is more damaged than other bundle parts (Figure 84). Even tungsten heaters in this segment were damaged by relocated melt. Obviously, there was a strong circumferential temperature gradient. This is also confirmed by the higher temperature peak measured by TFS 9/13 (about 2200 K at 12437 s) in comparison to the peak measured by TFS 15/23 (about 2100 K), see Figure 31.There is no metal cladding or shroud parts left her. Only completely oxidized parts of claddings and shroud as well as oxidized molten pools are observed. Several pellets were partially or completely dissolved by molten Zr (Figure 85). The bulk of frozen pools is very porous and the area of the pool cross section is strongly limited *without noticeable blockage* of the bundle cross section. Inside the oxidized zirconium melt, small inclusions of partially oxidized molybdenum are observed, transferred here in the molten state from the upper elevations.

A detailed study of cladding oxide scales and oxidized frozen melt shows the presence of porous clusters inside them, which should correspond to the locations of *nitrides* re-oxidized during reflood (Figure 86…Figure 88).

5.3.4   Elevation 750 mm

The melting point of Zr-bearing materials was reached during the oxygen starvation stage at 10850 s, after which the temperature remained constant until the beginning of reflood, i.e. the corresponding melting lasted 1480 s (Figure 29). The maximum temperature recorded at this elevation was 2190 K and was reached at 12400 s, i.e. 70 s after the reflood initiation.

Similar to 950 mm, the bundle segment 270°-0°-90°-135° had the highest temperatures and corresponding heated rods were strongly damaged (Figure 89). All parts of the unheated rod #9 were relocated downwards. Pellets of rods #19, #20, #2, #10 and #21 were strongly attacked by cladding melt and relocated downwards together with melt. The pellet of the inner rod #1 was intensively dissolved by the metal melt, however partially remained at this elevation (Figure 90). The oxidized melt contains relative large voids, which were presumably formed as parts of gas channels during steam flow (Figure 91). There is also micro scale porosity inside oxide which could be *nitride* formation with following re-oxidation (during reflood). Not dissolved but completely oxidized cladding parts remained in relative cold parts of the bundle (Figure 92).

Unlike 950 mm, small metal pools containing Zr and Fe can be observed at this elevation. Especially between rod #18 and absorber rod #6 (mostly relocated down), the frozen parts of steel absorber cladding were detected (Figure 93). Other metal pools at this elevations were formed by droplets of Mo relocated downwards from elevations above 1024 mm (Mo heaters). Additionally, small zones of zirconium nitrides were observed.

A relatively large oxidized molten pool was formed at the position of the previously downward relocated absorber rod #12 and frozen at this elevation between rods #3, #11, #13 and #14 (Figure 94). Similar to other bundle elevations, the bulk of the frozen pool is very porous.

5.3.5   Elevation 560 mm (grid spacer)

Unfortunately, only low-temperature TFS and TSH thermocouples were installed at the appropriate elevation (550 mm), which failed before the temperatures reached the melting point of Zr alloy (Figure 27). But the fact that these temperatures have been reached is indicated by the TIT G/9 thermocouple inside the corner rod G9 and metallographic observations at this and lower elevations.

Bundle materials relocated from upper elevations collected mostly on the top and inside the grid spacer located between 550 and 595 mm (Figure 95). However, no noticeable blockage of cooling channel was formed due to numerous small channels which developed inside the melt. The shroud is completely oxidized and was partially removed during the test section dismantling. The frozen melt is mostly completely oxidized, but there are metal pools with ceramic precipitates (Figure 96, Figure 99, Figure 103, Figure 104).

In place of the absorber rod #12, parts of its stainless steel cladding and M5 guide tube that formed a eutectic melt were found (Figure 100, Figure 101). At the position of downwards relocated Ag/In/Cd material, almost completely oxidized zirconium melt relocated from above was detected (Figure 102).

In some places of the bundle center, *nitrides* formed at the boundary between the oxide and the gas channel (Figure 97, Figure 98). Re-oxidized separate nitrides were also found in other areas: inside not completely dissolved segments of oxidized cladding of rod #14 (Figure 99) and in the surroundings of downwards relocated absorber rod #12 (Figure 100, Figure 101).

5.3.6 Elevation 350 mm

Similar to the elevation 560 mm, all thermocouples here failed during the temperature escalation in the air ingress stage (Figure 25), however, according to the metallographic investigations, the melting point of Zr alloy was reached.

Only a small part of the bundle – the hottest segment between 0° and 90° - was blocked by the melt (Figure 105). Part of the melt consisted of molybdenum, mixed with W, Zr, Fe, and transferred here during a sharp escalation of temperatures at the flooding stage from elevations above 1050 mm (Figure 106). Unlike higher elevations, where most of the thick shroud was either completely oxidized or melted, the shroud at this elevation was only partially oxidized. As result of steam and oxygen starvation stages (with formation of α-Zr(O) layer at the ZrO_2 surface [22]) and simultaneous nitrogen ingress, *nitrides* were formed at the inner shroud surface (reaction of N_2 with α-Zr(O) [9]) (Figure 107). These nitrides were re-oxidized during the following reflood stage. Not completely re-oxidized *nitrides* remained in outer parts or internal cracks of many oxidized claddings (Figure 108 – Figure 110). The re-oxidized porous structure is similar to the structure of "nitride pockets" formed in strongly oxidized claddings of the QUENCH-10 bundle [4].

Molten particles of absorber rod #12 penetrated through the failed cladding of rod #2, mixed with molten cladding metal and froze in the gap between cladding oxide and pellet (Figure 111 – Figure 113).

5.3.7 Elevation 160 mm

According to Figure 23, the temperature at the outer cladding and shroud surfaces did not reach the melting point of Zr alloy neither during the temperature escalation in the air ingress stage, nor during the following quench stage. Obviously, this is the level at which and below which the melting point of Zr alloy was not reached during the entire experiment. Partially oxidized Zr-O melt blocked only small part of the bundle in the segment between 0° and 45° (Figure 114). However, the Zr bearing melt relocated here from upper elevations. In the rest of the bundle, no melt is observed outside the fuel rod simulators. The claddings of these rods is substantially - but not completely - oxidized and has a rather thick α-Zr(O) layer (Figure 115). The oxide layer thickness for claddings, shroud and corner rods is between 100 and 330 µm, α-Zr(O) thicknesses - between 130 and 480 µm. Corner rods were also partially oxidized, and frozen melt relocated from upper elevations was found inside the corner tubes (Figure 116). Part of melt was relocated inside fuel rod simulators between oxide layer and pellet with formation of voids (Figure 117, Figure 125, Figure 130).

The oxidation of the molten pool occurred not only along its periphery, but also in the bulk (Figure 121, Figure 123, Figure 124, Figure 128). Numerous ZrO_2 precipitates show that the pool oxidation took place not only during cooling, but also at temperature [24]. There are also small outer metal pools containing absorber materials (Figure 126, Figure 127, Figure 129, Figure 132). Both absorber rods are absent also at this elevation. Parts of molten materials of absorber rods were not only mixed with metal melt relocated from above, but also penetrated into the gap between claddings of fuel rod simulators and pellets (Figure 117, Figure 118, Figure 130, Figure 131). In some cases, Ag and In penetrated even into the outer regions of pellets to a depth up to 150 µm (Figure 117- Figure 120).

Traces of Y inside melt indicate relocation of dissolved parts of pellets (Figure 123, Figure 124); it is the lowest elevation with relocated pellet material.

5.3.8 Elevation 65 mm (grid spacer)

The thermocouples closest to this elevation (at 50 mm) showed maximum temperatures, reached at the end of the escalation, of about 1020 K - well below the melting point of Zr alloy (Figure 22). The axial temperature diagram in Figure 41 shows that this elevation corresponds to an almost stepwise decrease in temperatures before flooding.

The claddings, shroud and corner rods are only slightly oxidized. There is a partial blockage of the bundle by (Ag, In, Cd) and Zr-bearing melt formed from parts of absorber rods and relocated from above (Figure 133). Two types of frozen metal pools were formed: pure (Ag, In) and Zr based melt (mixed with Ag, In) (Figure 134, Figure 135). Absorber material relocated outside the guide tube and interacted with M5 grid spacers and claddings (Figure 136). Similar interaction of absorber material, relocated from above, with M5 guide tube was also observed in the gap between absorber cladding and guide tube (Figure 137). The absence of Y traces at this elevation evidences the fact, that no pellet dissolved material was relocated to this elevation.

5.3.9 Elevation -40 mm

The maximum temperatures registered here were about 700 K (Figure 21) and claddings did practically not oxidize. Only materials of absorber rods (including materials of stainless steel absorber cladding and Zr-bearing guide tube) were registered here inside the outer pools (Figure 138). Precipitation of intermetallic phases AgZr, $InZr_2$, and Zr_3Fe inside the (Ag, In, Cd) melt relocated from above was observed (Figure 139-Figure 144). The corresponding binary phase diagrams (taken from [25]) could be seeing in Figure 145.

6 Summary and Conclusions

QUENCH-18 was the first large-scale bundle test including a prototypical experiment stage in air + steam mixture. The bundle contained 20 heated and 2 unheated rods with M5® cladding as well as 2 Ag-In-Cd absorber rods surrounded by stainless steel cladding and M5 guide tube. The test was performed at KIT on September 27, 2017 in the framework of the international ALISA project. Three typical features of QUENCH-18 were: moderate pre-oxidation to ≈ 80 μm of oxide layer (less than in the QUENCH-16 test on air ingress), a long period of oxygen starvation during the air and steam ingress stage (1770 s instead 800 s for the QUENCH-16 test performed without steam injection during air ingress), and reflood initiation at the melting point of the cladding (≈ 2000 K instead of 1700 K for QUENCH-16).

The claddings of unheated pressurized (to 6 MPa) rods burst at 1045 K at a heat-up rate of 0.3 K/s. This burst temperature is lower in comparison to burst temperatures observed during the bundle test QUENCH-L2 (T_{pct} = 1138 ± 34 K) due to lower heat-up rate and thinner cladding wall.

The temperature escalation during the air ingress between elevations 150 and 850 mm was significantly stronger than for QUENCH-16 (performed with the air ingress stage without steam flow) mainly due to higher exothermal cladding oxidation in oxygen, nitrogen and steam (corresponding total chemical power of ≈8 kW that is twice as much as electric power simulating decay energy). The metallographic investigations of the Zry corner rod, withdrawn at the end of escalation, showed formation of ZrN inside an α-Zr(O) layer formed above the oxide layer during oxygen and steam starvation.

Releases of aerosols and helium were registered at the beginning of temperature escalation (failure of absorber rods). Simultaneously, the readings of cladding surface thermocouples below elevation of 550 mm indicated the relocation of absorber melt.

During the starvation period about 100 and 450 g oxygen and steam, respectively, were consumed. During the steam consumption period about 45 g hydrogen were released. In the same time a partial consumption of nitrogen (about 120 g) was registered.

Due to the relatively low heat input (≈3*4 kW=12 kW as a result of electrical heating and exothermal reactions with steam and air), as well as the high specific heat of fusion of zirconium in comparison with its specific heat at the stage of temperature escalation, the escalation stopped when the melting point was reached. The cladding melt appearing at ≈2000 K remained localized between the outer oxide layer and the pellet.

Initiation of reflood with 50 g/s water caused a very strong temperature escalation to about 2430 K at elevations above 550 mm resulting in about 238 g (or 6.3 g/(effective rod)) hydrogen release. It is significantly more, than for QUENCH-16 (128 g, or 4.1 g/(effective rod)) performed also under air ingress conditions, but with the formation of a smaller amount of melt, and a total area of metallic zirconium only 8% less than that of QUENCH-18. Due to the re-oxidation of zirconium nitrides more than 54 g nitrogen and 15 g hydrogen were released. The rest and the largest part of the released hydrogen should be associated with the oxidation of the claddings in the upper part of the bundle and the oxidation of the metal melt in the middle part of the bundle. On the one hand, a catastrophically rapid oxidation of claddings occurred in the upper part of the bundle, the oxide layer of which had disappeared during the stage of oxygen starvation. On the other hand, in the middle part of the bundle, intense oxidation of the melt occurred, which emerged through the rapidly dissolved oxide layer of the claddings at temperatures above 2400 K. Final quench was achieved after about 800 s, which is noticeably longer than in most previous tests, when the cooling occurred in 300-400 seconds.

The metallographic investigations of the bundle show that no remaining nitrides or nitrides re-oxidized during reflood were indicated at upper elevations between 1150 and 1430 mm. Probably, they were dissolved by relocated melt. First indication of re-oxidized nitrides was found at the bundle elevation of 950 mm. The nitrides themselves were observed at elevations between 350 and 750 mm.

Strong cladding oxidation and Zr melt formation below the elevation of 1430 mm was detected. This melt relocated downwards as far as 350 mm, was completely oxidized, and mostly collected inside the grid spacer at 550 mm. Partially oxidized Zr-bearing melt was found down to elevation 160 mm. This elevation was the lowest with evidence of relocated pellet material. For the bundle elevation 65 mm only two kinds of frozen pools were detected: 1) Zr based metal mixed with Ag, In and Cd, and 2) (Ag, In, Cd) melt reacted with Zr bearing spacer grids. Part of this metal melt was relocated downwards as far as elevation -40 mm.

The test data are available for code validation for interested (non-commercial) institutions.

7   Acknowledgments

8   References

1. J. Stuckert, M. Steinbrueck, M. Grosse, "Experimental program QUENCH at KIT on core degradation during reflooding under LOCA conditions and in the early phase of a severe accident," *Proceedings of Meeting on Modelling of Water Cooled Fuel Including Design Basis and Severe Accidents*, Chengdu/China, 28 October–1 November 2013, IAEA-TECDOC-CD-1775, pp. 281-297,2013, https://www-pub.iaea.org/MTCD/Publications/PDF/TE-1775_CD_web.pdf.

2. T. Haste, M. Steinbrück, M. Barrachin, O. de Luze, M. Grosse, J. Stuckert, "A comparison of core degradation phenomena in the CORA, QUENCH, Phébus SFD and Phébus FP experiments," *Nuclear Engineering and Design*, 283, pp. 8–20, 2015, https://doi.org/10.1016/j.nucengdes.2014.06.035.

3. M. Steinbrück, M. Große, L. Sepold, J. Stuckert. "Synopsis and outcome of the QUENCH experimental program", *Nuclear Engineering and Design*, 240 (7), pp. 1714-1727, 2010, https://doi.org/10.1016/j.nucengdes.2010.03.021.

4. G. Schanz, M. Heck, Z. Hózer, L. Matus, I. Nagy, L. Sepold, U. Stegmaier, M. Steinbrück, H. Steiner, J. Stuckert, P. Windberg, "Results of the QUENCH-10 experiment on air ingress, "*Scientific Report FZKA-7087*," Karlsruhe, 2006, http://bibliothek.fzk.de/zb/berichte/FZKA7087.pdf.

5. J. Stuckert, M. Steinbrück, "Experimental results of the QUENCH-16 bundle test on air ingress," *Progress in Nuclear Energy*, 71, pp. 134-141, 2014, https://doi.org/10.1016/j.pnucene.2013.12.001.

6. J. Stuckert; Z. Hózer; A. Kiselev; M. Steinbrück, "Cladding oxidation during air ingress. Part I: Experiments on air ingress," *Annals of Nuclear Energy*, 93, pp. 4–17, 2016, http://dx.doi.org/10.1016/j.anucene.2015.12.034

7. M. Steinbrück, "Prototypical experiments relating to air oxidation of Zircaloy-4 at high temperatures, *Journal of Nuclear Materials*, 392 (3), pp. 531-544, 2009, https://doi.org/10.1016/j.jnucmat.2009.04.018.

8. M. Steinbrück, M. Böttcher, "Air oxidation of Zircaloy-4, M5® and ZIRLO™ cladding alloys at high temperatures", *Journal of Nuclear Materials*, 414 (2), pp. 276-285, 2011, https://doi.org/10.1016/j.jnucmat.2011.04.012.

9. M. Steinbrück, "High-temperature reaction of oxygen-stabilized α-Zr(O) with nitrogen, *Journal of Nuclear Materials*, 447 (1-3), pp. 46-55, https://doi.org/10.1016/j.jnucmat.2013.12.024 (2014).

10. M. Steinbrück, M. Grosse, "Deviations from parabolic kinetics during oxidation of zirconium alloys", *ASTM Special Technical Publication*, STP 1543, pp. 979-1001, 2015, https://doi.org/978-0-8031-7580-8.

11. M. Steinbrück, S. Schaffer, "High-Temperature Oxidation of Zircaloy-4 in Oxygen–Nitrogen Mixtures", *Oxidation of Metals*, 85 (3-4), pp. 245-262, 2016, https://doi.org/10.1007/s11085-015-9572-1.

12. M. Steinbrück, , F.O. da Silva, M. Grosse, „Oxidation of Zircaloy-4 in steam-nitrogen mixtures at 600–1200 °C", *Journal of Nuclear Materials*, 490, pp. 226-237, 2017, https://doi.org/10.1016/j.jnucmat.2017.04.034.

13. L. Sepold, T. Lind, A. Pintér Csordás, U. Stegmaier, M. Steinbrück, J. Stuckert, "AgInCd control rod failure in the QUENCH-13 bundle test", *Annals of Nuclear Energy*, 36, pp. 1349-1359, 2009, https://doi.org/10.1016/j.anucene.2009.06.020.

14. T. Lind, A.P. Csordás, I. Nagy, J. Stuckert, "Aerosol behavior during SIC control rod failure in QUENCH-13 test", *Journal of Nuclear Materials*, 397 (1–3), pp. 92-100, 2010, https://doi.org/10.1016/j.jnucmat.2009.12.013.

15. J. Stuckert, M. Große, C. Rössger, M. Steinbrück, M. Walter. „Results of the LOCA bundle test QUENCH-L2 with M5® claddings", *Scientific report SR-7677*, July 2018, https://publikationen.bibliothek.kit.edu/1000083069/13760741.

16. J. Stuckert, M. Grosse, M. Steinbrueck, M. Walter, A. Wensauer, "Results of the QUENCH-LOCA experimental program at KIT", *Journal of Nuclear Materials*, 534, paper 152143, 2020, https://doi.org/10.1016/j.jnucmat.2020.152143.

17. Jarmo Kalilainen, Terttaliisa Lind, Juri Stuckert, Thomas Bergfeldt, Olli Sippula , Jorma Jokiniemi. "The measurement of Ag/In/Cd release under air-ingress conditions in the QUENCH-18 bundle test", *Journal of Nuclear Materials* 517 (2019), 315-327, https://doi.org/10.1016/j.jnucmat.2019.02.021.

18. J. Kalilainen, T. Lind, J. Stuckert, U. Stegmaier. „Aerosol results from the QUENCH-18 bundle test", The 9th European Review Meeting on Severe Accident Research (*ERMSAR2019*), Prague, March 2019, Paper 019.

19. P. Hofmann, J. Stuckert, A. Miassoedov, M. S. Veshchunov, A. V. Berdyshev, A. V. Boldyrev. "ZrO$_2$ dissolution by molten zircaloy and cladding oxide shell failure. New experimental results and modelling", *Scientific report FZKA-6383*, Karlsruhe, 1999, https://doi.org/10.5445/IR/270046616.

20. J. Stuckert, J. Birchley, M. Grosse, B. Jaeckel, M. Steinbrück. „Experimental and calculation results of the integral reflood test QUENCH-14 with M5® cladding tubes", *Annals of Nuclear Energy* 37 (2010), 1036-1047, https://doi.org/10.1016/j.anucene.2010.04.015

21. J. Stuckert, J. Birchley, M. Grosse, B. Jaeckel, M. Steinbrück. „Experimental and calculation results of the integral reflood test QUENCH-15 with ZIRLO™ cladding tubes in comparison with results of previous QUENCH tests", *Nuclear Engineering and Design* 241 (2011), 3224-3233, https://doi.org/10.1016/j.nucengdes.2011.05.004.

22. J. Stuckert, M. Veshchunov, "Behaviour of Oxide Layer of Zirconium-Based Fuel Rod Cladding under Steam Starvation Conditions", *Scientific report FZKA-7373*, Karlsruhe, April 2008. https://doi.org/10.5445/IR/270071587.

23. J. Stuckert, W. Hering, V. Sánchez-Espinoza, W. Tromm. „Effect of core reflood on melt relocation", *Final report Ares(2019)5357622*, IVMR identification D3.14, 2019, https://ec.europa.eu/research/participants/documents/downloadPublic?documentIds=080166e5c5a07064&appId=PPGMS.

24. M.S. Veshchunov, J. Stuckert, A.V. Berdyshev. "Modelling of Zr-O and U-Zr-O melts oxidation and new crucible tests", *Scientific report FZKA-6792*, Karlsruhe, 2002, https://doi.org/10.5445/IR/270053667.

25. *TAPP*: "A Database of Thermochemical and Physical Properties," E.S. Microware Inc., Hamilton, Ohio 1994.

Tables and Figures

Table 1   QUENCH Test Matrix 1997 – 2018

Test	Quench medium and injection rate	Temp. at onset of flooding[1]	Max. ZrO$_2$ before transient[2]	Max. ZrO$_2$ (X s) before flooding[2]	Posttest average ZrO$_2$ thickness[3]	H$_2$ production before / during cooldown	Remarks, objectives
QUENCH-00 Oct. 9 - 16, 97	Water 80 g/s	≈ 1800 K			completely oxidized		Commissioning tests.
QUENCH-01 Febr 26, 98	Water 52 g/s	≈ 1830 K	312 µm		500 µm at 913 mm	36 / 3	COBE Project; partial fragmentation of pre-oxidized cladding.
QUENCH-02 July 7, 98	Water 47 g/s	≈ 2400 K			completely oxidized	20 / 140	COBE Project; no additional pre-oxidation; quenching from high temperatures.
QUENCH-03 January 20, 99	Water 40 g/s	≈ 2350 K			completely oxidized	18 / 120	No additional pre-oxidation, quenching from high temperatures.
QUENCH-04 June 30, 99	Steam 50 g/s	≈ 2160 K	82 µm		280 µm	10 / 2	Cool-down behavior of slightly pre-oxidized cladding by cold steam injection.
QUENCH-05 March 29, 2000	Steam 48 g/s	≈ 2020 K	160 µm		420 µm	25 / 2	Cool-down behavior of pre-oxidized cladding by cold steam injection.
QUENCH-06 Dec 13 2000	Water 42 g/s	≈ 2060 K	207 µm[5]	300 µm, (60 s), SVECHA modeling	630 µm[4]	32 / 4	OECD-ISP 45; prediction of H$_2$ source term by different code systems.
QUENCH-07 July 25, 2001	Steam 15 g/s	≈ 2100 K	230 µm		completely oxidized	66 / 120	COLOSS Project; impact of B$_4$C absorber rod failure on H$_2$, CO, CO$_2$, and CH$_4$ generation.
QUENCH-09 July 3, 2002	Steam 49 g/s	≈ 2100 K			completely oxidized	60 / 400	As QUENCH-07, steam-starved conditions prior to cooldown.
QUENCH-08 July 24, 2003	Steam 15 g/s	≈ 2090 K	274 µm		completely oxidized	46 / 38	As QUENCH-07, no absorber rod.

Test	Quench medium and injection rate	Temp. at onset of flooding[1]	Max. ZrO_2 before transient[2]	Max. ZrO_2 ($X s$) before flooding[2]	Posttest average ZrO_2 thickness[3]	H_2 production before / during cooldown	Remarks, objectives
QUENCH-10 July 21, 2004	Water 50 g/s	≈ 2200 K	514 µm	613 µm (at 850 mm)	completely oxidized	48 / 5	LACOMERA Project; Air ingress.
QUENCH-11 Dec 08, 2005	Water 18 g/s	≈ 2040 K		170 µm	completely oxidized	9 / 132	LACOMERA Project; Boil-off.
QUENCH-12 Sept 27, 2006	Water 48 g/s	≈ 2100 K	160 µm, breakaway	300 µm, (110 s), breakaway	completely oxidized	34 / 24	ISTC Project #1648.2; VVER bundle with E110 claddings.
QUENCH-13 Nov 7, 2007	Water 52 g/s	≈ 1820 K		400 µm,after AgInCd rod failure	750 µm	42 / 1	SARNET; impact of AgInCd absorber rod failure on aerosol generation.
QUENCH-14 July 2, 2008	Water 41 g/s	≈ 2100 K	170 µm[6]	470 µm[6] (30 s)	900 µm	34 / 6	ACM series: M5® cladding
QUENCH-15 May 27, 2009	Water 48 g/s	≈ 2100 K	145 µm[6]	380 µm[6] (30 s)	620 µm	41 / 7	ACM series: ZIRLO™ cladding.
QUENCH-16 July 27, 2011	Water 53 g/s	≈ 1870 K*	135 µm	130 µm at 450-950 mm, breakaway	1075 µm at 550-650 mm	144 / 128	LACOMECO Project; Air ingress.
QUENCH-17 Jan. 31, 2013	Water 10 g/s	≈ 1800 K		completely oxidized	completely oxidized	110 / 1	SARNET-2; Debris formation and coolability.
QUENCH-18 Sept. 27, 2017	Water 53 g/s	≈ 1950 K	80 µm	completely oxidized	completely oxidized	57/238	ALISA Project; air ingress; AgInCd absorber rods

[1] Maximum measured bundle temperature at 950 mm elevation.
[2] Measured (or calculated for LOCA tests) at the withdrawn corner rod at 950 mm elevation.
[3] Measured posttest at the bundle elevation of maximum temperature, i.e. 950 mm.
[4] Some claddings were completely oxidized at 950 mm elevation.
[5] Oxide thickness during transient stage.
[6] Zircaloy-4 corner rods.   Revised: Mai 2018

Table 2　　Design characteristics of the QUENCH-18 test bundle

Bundle type		PWR
Bundle size		24 rods: 20 heated rods, 2 unheated rods, 2 neutron absorber rods
Effective number of rods (+surface of shroud and corner rods)		24 + (9 + 5) = 38
Pitch		12.6 mm
Coolant channel area		33.55 cm^2
Hydraulic diameter		11.71 mm
Cladding material		M5®
Cladding outside / inside diameter / thickness		9.50 / 8.36 / 0.57 mm
Cladding length (elevations)		2278 mm (-593 to 1685 mm)
Full length of rods(levels)	heated	2480 mm (-690 to 1790 mm)
	unheated	2140 mm (-250 to 1890)
Material of middle heater		Tungsten (W)
	surface roughness	Ra = 1.6 µm
Tungsten heater length (elevations)		1024 mm (0 to 1024 mm)
Tungsten heater diameter		5 mm
Annular pellet	material	$ZrO_2;Y_2O_3$-stabilized
	dimensions	OD = 8.2 mm; ID = 5.2 mm (2.4 mm for unheated rods); L=10 mm
Pellet stack		0 mm to 1020 mm
Internal rod pressure at room temperature (gas)	heated	0.23 MPa abs. (Kr)
	unheated	6.0 MPa (He)
	absorber	0.12 MPa (He)
Absorber pin	material composition	wt%: 80 Ag, 15 In, 5 Cd
	density	10.2 g/cm³
	dimensions (elevations)	OD = 8.60 mm; L = 1068 mm (-15 mm to 1053 mm)
	roughness	Ra = 1.6 µm
Absorber cladding	material	stainless steel 316L
	dimensions	OD = 9.70 mm; ID = 8.75 mm
Absorber guide tube	material	M5®
	dimensions	OD = 12.45 mm; ID = 11.25 mm; L = 1187 mm (-42 mm to 1145 mm)
Corner rod (8)	material	Zircaloy-4
	instrumented (A, C, E, G)	tube ∅ 6x0.9 (bottom: -1140 mm)
		rod ∅ 6 mm (top: +1300 mm)
	not instrumented (B, D, F, H)	rod ∅ 6 mm (-1350 to +1155 mm)
Grid spacer	designation	AREVA AH 32715
	height	45.5
	location of lower edge	-200; 50; 550; 1050, 1410 mm
Shroud	material	Zirconium 702 (flange: Zry-4)
	wall thickness	3.05 mm
	outside diameter	88.9 mm
	length (extension)	1600 mm (-300 mm to 1300 mm)
Shroud insulation	material	ZrO_2 fiber
	insulation thickness	34 mm
	elevation	-300 mm to ~1000 mm
Molybdenum heaters and Copper electrodes	length of upper part	766 mm (576 Mo, 190 mm Cu)
	length of lower part	690 mm (300 Mo, 390 mm Cu)
	diameter:	
	- prior to coating	7.6 mm
	- after coating with ZrO_2	8.0 mm
	coating surface roughness	Ra = 6- 12 µm
Cooling jacket	Material: inner/outer tube	Inconel 600 (2.4816) / SS (1.4571)
	inner tube	ID = 158.3 mm, OD = 168.3 mm
	outer tube	ID = 181.7 mm, OD = 193.7 mm

Table 3   Main characteristics of the ZrO$_2$ pellet material, yttria-stabilized (type ZYK3)

Property	Data
Y$_2$O$_3$ content	5 %
Density	6.07 ± 0.03 g/cm^3
Open porosity	0
Average crystallite size	0.8 μm
Specific heat at 20 °C	400 J/kg K
Thermal conductivity at 100 °C	2.5 W/m K
Linear expansion, 20-1000 °C	11 x 10^{-6}/K
Vickers Hardness HV10	> 12000 N/mm^2
Bending strength	> 1150 MPa
Elastic modulus	> 200 GPa
Weibull modulus	20
Fracture toughness K$_{1C}$	12 MPa•m$^{1/2}$

According to Barat Ceramics GmbH, 07955 Auma

Table 4   QUENCH-18; Electrical resistances of heated rods at 20 °C

Rod #	1	2	3	4	5	7	8	10	11	13	ave-rage	10 rods parallel
Pre-test [mΩ]	4.5	4.5	4.4	4.5	4.3	4.5	4.5	4.5	4.5	4.4	4.46	**0.45**
Post-test [Ω]	13.5	27.0	39.1	6.4	2.0	1.9	1.9	8.6	7.8	14.1		

Rod #	14	16	17	18	19	20	21	22	23	24	ave-rage	10 rods parallel
Pre-test [mΩ]	4.4	4.5	4.5	4.1	4.4	4.4	4.4	4.4	4.4	4.5	4.4	0.44
Post-test [Ω]	4.2	0.3	155.5	2.1	4.1	33.0	*4.3 kΩ*	*4.6 kΩ*	1.8	0.167		

Table 5   Properties of zirconia fiber insulating boards of type ZYFB3

Chemical composition

Oxide	ZrO_2	Y_2O_3	HfO_2	TiO_2	SiO_2	CaO	MgO	Fe_2O_3	Al_2O_3	Na_2O
typical wt%	88	10	2	0.14	0.12	0.09	0.03	0.04	0.01	0.01

Physical properties

bulk density	porosity	shrinkage		thermal expansion coefficient @298-1453K	melting point	max service temperature	flexural strength	compressive strength @10% compression
		(1 hour @1925 K)	(24 hours @1925 K)					
g/cm³	%	%		1/K	K	K	MPa	MPa
0.48	92	1.2	2.8	$10.7*10^{-6}$	2866	2500	0.59	0.29

Thermal conductivity

temperature, K	673	1073	1373	1673	1923
conductivity, W/(m*K)	0.08	0.11	0.14	0.19	0.24

Specific heat capacity

temperature, K	366	2644
specific heat capacity, J/(kg*K)	544	754

According to specifications of manufacturer ZIRCAR PRODUCTS

Table 6   List of instrumentation for the QUENCH-18 test

Chan-nel	Designation	Instrument, location	Output in
0	TCC 9/13	TC (W/Re) fuel rod simulator 9 (type), 950 mm, center	K
1	TFS 1/13	TC (W/Re) fuel rod simulator 1 (type), 950 mm, °	K
2	TFS 9/13	TC (W/Re) fuel rod simulator 9 (type), 950 mm, °	K
3		TC (W/Re) Reserve	K
4	TFS 18/13	TC (W/Re) fuel rod simulator 18 (type), 950 mm, °	K
5	TSH 14/90	TC (W/Re) shroud outer surface, 1050 mm, °, TC legs behind shroud insulation	K
6	TFS 2/12	TC (W/Re) fuel rod simulator 2 (type), 850 mm, °	K
7	TFS 2/14	TC (W/Re) fuel rod simulator 2 (type), 1050 mm, °	K
8	TFS 5/14	TC (W/Re) fuel rod simulator 5 (type), 1050 mm, °	K
9	TFS 14/14	TC (W/Re) fuel rod simulator 14 (type), 1050 mm, °	K
10	TFS 19/14	TC (W/Re) fuel rod simulator 19 (type), 1050 mm, °	K
11	TFS 4/15	TC (W/Re) fuel rod simulator 4 (type), 1150 mm, °	K
12		TC (W/Re) Reserve	K
13	TFS 9/15	TC (W/Re) fuel rod simulator 9 (type), 1150 mm, °	K
14	TFS 11/15	TC (W/Re) fuel rod simulator 11 (type), 1150 mm, °	K
15	TFS 16/13	TC (W/Re) fuel rod simulator 16 (type), 950 mm, °	K
16		TC (W/Re) Reserve	K
17	TSH 14/270	TC (W/Re) shroud outer surface, 1050 mm, °, TC legs behind shroud insulation	K
18	TSH 13/90	TC (W/Re) shroud outer surface, 950 mm, °, TC legs behind shroud insulation	K
19	TSH 13/270	TC (W/Re) shroud outer surface, 50 mm, °, TC legs behind shroud insulation	K
20	TSH 12/0	TC (W/Re) shroud outer surface, 850 mm, °, TC legs behind shroud insulation	K
21	TSH 12/180	TC (W/Re) shroud outer surface, 850 mm, °, TC legs behind shroud insulation	K
22	TSH 3/180	TC (NiCr/Ni) shroud	K
23	TSH 4/270	TC (NiCr/Ni) shroud	K
24		Reserve flow rate CALDOS(20 mA)	
25	Fm 401 Krohne	Ar flow rate (20 mA) (channel #164 is more precise)	g/s
26..31		TC (W/Re) Reserve	K
32	TIT A/12	TC (W/Re) corner rod A, center, 850 mm	K
33	TCC 15/13	TC (W/Re) fuel rod simulator 15 (type), 950 mm, center	K
34	TIT C/11	TC (W/Re) corner rod C, center, 750 mm	K
35	TSH 5/180	TC (NiCr/Ni) shroud	K
36	TSH 5/0	TC (NiCr/Ni) shroud	K
37	TFS 3/17	TC (W/Re) fuel rod simulator 3 (type), 1350 mm, °	K
38	TFS 1/7	TC (NiCr/Ni) fuel rod simulator 1 (type), 350 mm, °	K

Chan-nel	Designation	Instrument, location	Output in
39	TFS 21/7	TC (NiCr/Ni) fuel rod simulator 21 (type), 350 mm, °	K
40	TIT E/10	TC (W/Re) corner rod E, center, 650 mm	K
41	TIT G/9	TC (W/Re) corner rod G, center, 550 mm	K
42	TSH 6/270	TC (NiCr/Ni) shroud	K
43	TSH 6/90	TC (NiCr/Ni) shroud	K
44	TSH 7/180	TC (NiCr/Ni) shroud	K
45	T 304	TC (NiCr/Ni) outer surface of pipe after V302	K
46	TFS 3/3	TC (NiCr/Ni) fuel rod simulator 3 (type), -50 mm, °	K
47	TFS 8/16	TC (W/Re) fuel rod simulator 8 (type), 1250 mm, °	K
48	TFS 13/16	TC (W/Re) fuel rod simulator 13 (type), 1250 mm, °	K
49	TFS 6/17	TC (W/Re) fuel rod simulator 6 (type), 1350 mm, °	K
50		TC (W/Re) Reserve	K
51	TFS 8/12	TC (W/Re) fuel rod simulator 8 (type), 850 mm, °	K
52	TSH 11/0	TC (W/Re) shroud outer surface, 750 mm, °, TC legs behind shroud insulation	K
53	TSH 11/180	TC (W/Re) shroud outer surface, 750 mm, °, TC legs behind shroud insulation	K
54	TSH 10/90	TC (W/Re) shroud outer surface, 650 mm, °, TC legs behind shroud insulation	K
55	TSH 10/270	TC (W/Re) shroud outer surface, 650 mm, °, TC legs behind shroud insulation	K
56	TFS 13/12	TC (W/Re) fuel rod simulator 13 (type), 850 mm, °	K
57	TFS 22/12	TC (W/Re) fuel rod simulator 22 (type), 850 mm, °	K
58	TSH 7/0	TC (NiCr/Ni) shroud outer surface, 350 mm, °, TC legs behind shroud insulation	K
59	TFS 1/11	TC (W/Re) fuel rod simulator 1 (type), 750 mm, °	K
60	TFS 14/11	TC (W/Re) fuel rod simulator 14 (type), 750 mm, °	K
61	T 206	Temperature before steam flow instrument location 1 g/s	K
62	P 206	Pressure at steam flow instrumentation location 1 g/s	bar
63	R001 air	Flow rate air 0.08…2 g/s	g/s
64	T 402b	Temperature of the tube surface after gas heater	K
65	TFS 3/10	TC (W/Re) fuel rod simulator 3 (type), 650 mm, °	K
66	TFS 6/10	TC (W/Re) fuel rod simulator 6 (type), 650 mm, °	K
67		TC (W/Re) Reserve	K
68	T 512	Gas temperature bundle outlet	K
69		TC (W/Re) Reserve	K
70		TC (W/Re) Reserve	K
71	Ref. T 01	Reference temperature 1	K
72	TFS 11/9	TC (NiCr/Ni) fuel rod simulator 11 (type), 550 mm, °	K
73	TFS 2/9	TC (NiCr/Ni) fuel rod simulator 2 (type), 550 mm, °	K
74	TFS 5/9	TC (NiCr/Ni) fuel rod simulator 5 (type), 550 mm, °	K
75	TFS 9/8 defect	TC (NiCr/Ni) fuel rod simulator 9 (type), 450 mm, °	K

Chan-nel	Designation	Instrument, location	Output in
76	TFS 6/8	TC (NiCr/Ni) fuel rod simulator 6 (type), 450 mm, °	K
77	TFS 3/8	TC (NiCr/Ni) fuel rod simulator 3 (type), 450 mm, °	K
78	TFS 5/6	TC (NiCr/Ni) fuel rod simulator 5 (type), 250 mm, °	K
79	TFS 11/6	TC (NiCr/Ni) fuel rod simulator 11 (type), 250 mm, °	K
80	TFS 2/5	TC (NiCr/Ni) fuel rod simulator 2 (type), 150 mm, °	K
81	TFS 17/5	TC (NiCr/Ni) fuel rod simulator 17 (type), 150 mm, °	K
82	TFS 7/4	TC (NiCr/Ni) fuel rod simulator 8 (type), 50 mm, °	K
83	TFS 13/4	TC (NiCr/Ni) fuel rod simulator 14 (type), 50 mm, °	K
84	TFS 1/2	TC (NiCr/Ni) fuel rod simulator 1 (type), -150 mm, °	K
85	TFS 4/1 F	TC (NiCr/Ni) fuel rod simulator 4 (type), -250 mm, °	K
86	TSH 16/0	TC (NiCr/Ni) shroud outer surface, 1250 mm, 26°	K
87	TSH 16/180	TC (NiCr/Ni) shroud outer surface, 1250 mm, 206°	K
88	TSH 15/0	TC (NiCr/Ni) shroud outer surface, 1150 mm, 26°	K
89	TSH 15/180	TC (NiCr/Ni) shroud outer surface, 1150 mm, 206°	K
90	TSH 9/0	TC (NiCr/Ni) shroud outer surface, 550 mm, 26°	K
91	TCI 9/270	TC (NiCr/Ni) cooling jacket inner tube wall, 550 mm, 270°	K
92	TCI 10/270	TC (NiCr/Ni) cooling jacket inner tube wall, 650 mm, 270°	K
93	TCI 11/270	TC (NiCr/Ni) cooling jacket inner tube wall, 750 mm, 270°	K
94	TCI 13/270	TC (NiCr/Ni) cooling jacket inner tube wall, 950 mm, 270°	K
95	TSH 9/180	TC (NiCr/Ni) shroud outer surface, 550 mm, 206°	K
96	TCI 1/180	cooling jacket inner tube wall, -250 mm, 180°	K
97	TCI 4/180	cooling jacket inner tube wall, 50 mm, 180°	K
98	TCI 7/180	cooling jacket inner tube wall, 350 mm, 180°	K
99	TCI 11/180	TC (NiCr/Ni) cooling jacket inner tube wall, 750 mm, 180°	K
100	TCI 12/180	TC (NiCr/Ni) cooling jacket inner tube wall, 850 mm, 180°	K
101	TCI 13/180	TC (NiCr/Ni) shroud outer surface, 50 mm, 296°	K
102	TCI 15/180	TC (NiCr/Ni) cooling jacket inner tube wall, 1150 mm, 180°	K
103	T002 inlet	Cooling water, inlet of off-gas tube	K
104	T 309	Ar bundle top	K
105	TSH 8/90	TC (NiCr/Ni) shroud outer surface, 450 mm, 116°	K
106	TSH 4/90	TC (NiCr/Ni) shroud outer surface, 50 mm, 116°	K
107	TCI 13/90	TC (NiCr/Ni) cooling jacket inner tube wall, 950 mm, 90°	K
108	T 305 flange	TC (NiCr/Ni) bundle inlet flange	K
109	TCI 1/0	TC (NiCr/Ni) cooling jacket inner tube wall, -250 mm, 0°	K
110	TCI 4/0	TC (NiCr/Ni) cooling jacket inner tube wall, 50 mm, 0°	K
111	TCI 7/0	TC (NiCr/Ni) cooling jacket inner tube wall, 350 mm, 0°	K
112	TCI 11/0	TC (NiCr/Ni) cooling jacket inner tube wall, 750 mm, 0°	K
113	TCI 12/0	TC (NiCr/Ni) cooling jacket inner tube wall, 850 mm, 0°	K
114	TCI 13/0	TC (NiCr/Ni) cooling jacket inner tube wall, 950 mm, 0°	K
115	TCI 15/0	TC (NiCr/Ni) cooling jacket inner tube wall, 1150 mm, 0°	K
116	T003	Cooling water, outlet of off-gas tube	K
117		Reserve (NiCr/Ni) defect	K

Chan-nel	Designation	Instrument, location	Output in
118	TSH 8/270	TC (NiCr/Ni) shroud outer surface, 450 mm, 296°	K
119	T 306 foot	TC (NiCr/Ni) outer surface of bundle foot	K
120	TCO 1/0	TC (NiCr/Ni) cooling jacket outer tube surface, -250 mm, 0°	K
121	TCO 7/0	TC (NiCr/Ni) cooling jacket outer tube surface, 350 mm, 0°	K
122	TCO 13/0	TC (NiCr/Ni) cooling jacket outer tube surface, 950 mm, 0°	K
123	T 601	Temperature before off-gas flow instrument (orifice) F 601	K
124	T 513	Outer wall of bundle head	K
125	T 514	Cooling water bundle head	
126	T307 off-gas	TC (NiCr/Ni) inner surface of inlet of off-gas pipe	K
127	TFS 20/9 defect	TC (NiCr/Ni) fuel rod simulator 20 (type 4), 550 mm, 225°	K
128	T 104	Temperature quench water	K
129	T 201	Temperature steam generator heating pipe	K
130	T 204	Temperature before steam flow instrument location 50 g/s	K
131	T 205	Temperature before steam flow instrument location 10 g/s	K
132	T 301A	Temperature behind superheater	K
133	T 302	Temperature superheater heating pipe	K
134	T 303	Temperature before total flow instrument (orifice) location	K
135	T 401	Temperature before gas flow instrument (orifice) location	K
136	T 403	Temperature of Ar at inlet cooling jacket	K
137	T 404	Temperature of Ar at outlet cooling jacket	K
138	T 501 cont-t	Temperature in containment (near from bundle head)	K
139	T 502	Temperature at outer surface of containment, 0°, 2.4 m	K
140	T 503	Temperature at outer surface of containment, 270°, 2.2 m	K
141	T 310	TC (NiCr/Ni) aerosol extraction tube in off-gas pipe	K
142	T 505	Temperature at outer surface of containment, 90°, 3.2 m	K
143	T 506	Temperature at outer surface of containment, 270°, 3.6 m	K
144	TSH 2/90	TC (NiCr/Ni) shroud outer surface, -150 mm, 116°	K
145	TSH 1/0	TC (NiCr/Ni) shroud outer surface, -250 mm, 26°	K
146		TC (NiCr/Ni) reserve (defect)	K
147	T 510	Temperature at outer surface of containment, 270°, 4.4 m	K
148	T 511	Gas temperature at bundle inlet	K
149		TC (NICr/Ni) reserve	K
150		TC (NICr/Ni) reserve	K
151	Ref. T 02	Reference temperature 2	K
152	P 201	Pressure steam generator	bar
153	P 09	Rod 9 pressure	bar
154	P 205	Pressure at steam flow instrument location 10 g/s	bar
155	P 303	Pressure before total flow instrument (orifice) location	bar
156	P 401	Pressure before gas flow instrument location	bar
157	P 511	Pressure at bundle inlet	bar
158	P 512	Pressure at bundle outlet	bar

Chan-nel	Designation	Instrument, location	Output in
159	P 601	Pressure before off-gas flow instrument (orifice) F 601	bar
160	P 15	Rod 15 pressure	bar
161	L 201	Liquid level steam generator	mm
162	L 501	Liquid level quench water	mm
163	L 701	Liquid level condensation vessel	mm
164	Fm 401	Argon flow rate	g/s
165	P 411	Pressure Kr supply	bar
166	P 403	Pressure Ar cooling of cooling jacket	bar
167	P 406	Pressure insulation shroud/cooling jacket	bar
168	Fm 104	Flow rate quench water	l/h
169	Fm 206	Steam flow rate 1 g/s	g/s
170	Fm 205	Flow rate steam 10 g/s	g/s
171	F 303	Flow rate at bundle inlet (steam + argon), orifice	mbar
172	F 401	Argon gas flow rate	Nm³/h
173	F 403	Flow rate cooling gas	Nm³/h
174	F 601	Flow rate off-gas (orifice)	mbar
175	Fm 406	Flow rate argon into room between shroud and cooling jacket	g/s
176	E 201	Electric current steam generator	A
177	E 301	Electric current superheater	A
178	E 501	Electric current inner ring of fuel rod simulators	A
179	E 502	Electric current outer ring of fuel rod simulators	A
180	E 503	Electric voltage inner ring of fuel rod simulators	V
181	E 504	Electric voltage outer ring of fuel rod simulators	V
182	Hub_V302	Gas supply valve lift	%
183	Ref. T 03	Reference temperature 3	K
:			
250	E 505	Electric power inner ring of fuel rod simulators	W
251	E 506	Electric power outer ring of fuel rod simulators	W

Indications:

TFS – TC at the surface of fuel rod simulators;

TCC – TC at the surface of the central rod;

TSH – TC at the outer surface of shroud;

TIT – TC inside corner rods.

Table 7 QUENCH-18; map of TFS and TCC thermocouples

elevation, mm	-250	-150	-50	50	150	250	350	450	550	650	750	850	950	1050	1150	1250	1350
elev. No. / rod No.	1	2	3	4	5	6	7	8	9	10	11	12	13	14	15	16	17
1		N					N				W		W				
2					N				N			W		W			
3			N					N		W							N
4	N														W		
5						N			N					W			
6								N		W							N
7																	
8				N								W				N	
9								N		W			W, <u>W</u>		W		
10																	
11						N			N						W		
12																	
13												W				N	
14				N							W			W			
15													<u>W</u>				
16													W				
17					N												
18													W				
19														W			
20																	
21							N			W							
22												W					
TC quantity:	1	1	1	2	2	2	2	1 2	1 2	4	2	4	4+2	4	3	2	2

| heated rods |
| unheated rod |

- TC to bottom: **10 W/Re**+**13 NiCr/Ni**
- TC to top: **13 W/Re 4 NiCr&Ni**

N NiCr/Ni (totally 17)
W W/Re (totally 21)
<u>W</u> W/Re TCC (2)

25

Table 8 Diameters of the materials used for the QUENCH High-Temperature Thermocouples [mm]

Material	As-received	Final
W/Re wires	0.254	
HfO$_2$ insulation OD (see drawing below)	1.1	
Ta tube OD / ID	2.15 / 1.65	1.4 / 0.94
Zr tube OD / ID	2.5 / 1.65 ± 0.05	2.2-2.3 / ~1.4
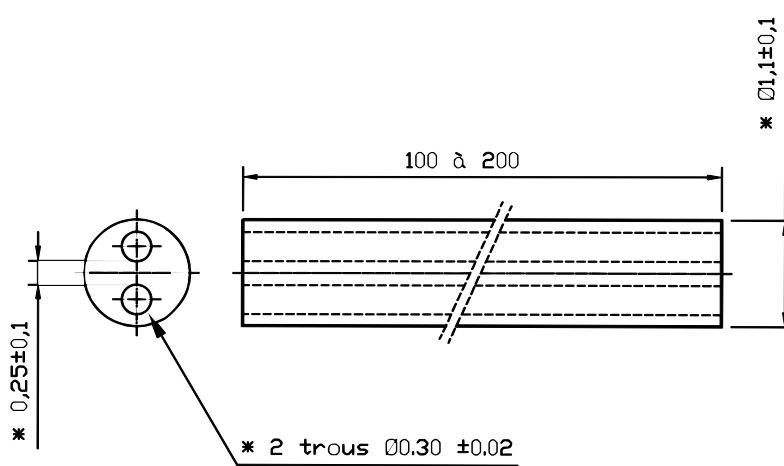
Table 9 Main characteristics of the HfO$_2$ thermocouple insulator

Property	Data
Composition of basic material	99 % HfO$_2$
Melting temperature	2840 °C
Max. use temperature	2500 °C
Density	8.4 g/cm^3
Thermal conductivity at 20-1000 °C	1.14 W/m K
Linear expansion	5.8 x 10^{-6}/K

According to Saint-Gobain ceramics, 1997

Table 10   QUENCH-18; Sequence of events

Time [s]	Event
0 (11:54:08h)	Start data recording; el. power at 4.1 kW; flow rates 3 g/s Ar, 3.3 g/s
20…6309	Increase of electrical power from 7.7 to 9.1 kW
481	Burst of cladding #9 (internal pressure drop), first He peak
558	Burst of cladding #15 (internal pressure drop), second He peak
6309	Temporary cool-down (reduction of electrical power from 9.1 to 3.8 kW)
7263	Corner rod D withdrawn
7387	Steam reduction
7422	Ar reduction, beginning of cladding temperature increase
7537	**Air ingress initiation**; flow rates 1 g/s Ar, 0.3 g/s steam, 0.046 O_2 + 0.168 N_2
10000	Accelerated oxygen consumption
10470	First indication of hydrogen release (oxygen starvation)
10537 (14:49:45h)	First Cd aerosol release (absorber cladding failure)
10539…12329	Continuous small helium release from failed absorber rods
10570	Accelerated steam consumption
10612, 11392, 11992	Aerosol collections with filters 1, 2, 3
10600	***Start of sharp temperature increase at 650…850 mm from ≈1400 K***
10660	Beginning of nitrogen consumption
10681	Intensive absorber cladding failure (TFS 6/8, TFS 3/8, TFS 5/6, TFS 11/6)
10687	Absorber melt relocation to 250 mm for rod #12, (Figure 45)
10703	Absorber melt relocation to 350 mm for rod #6, (Figure 45)
10730	Massive cladding failures (Kr release)
10850	***Reach of melting point of Zr-bearing materials at 650…850 mm***
11000	Steam starvation
11014	Corner rod H withdrawn
11045	Relocation of of first Zr-bearing molten rivulets to 150 mm (TFS 2/5)
11253	Shroud failure (Fm 406)
11500	***Start of sharp temperature increase at 150 m***
11632, 12172	Aerosol collections with BLPI1, BLPI2
12329 (15:19:37h)	**Reflood initiation: start of the quench pump**
12333	Filling of bundle foot with water (quick water injection)
12367	Increase of TCI readings
12452	*Maximum temperature 2430 K (TCC 15/13)*
13276	Failure of cooling jacket feedthrough for TCs - water release to containment
(15:42:44h)	Switch-off

Table 11   QUENCH-18; mass and elemental concentrations of the Nuclepore filters and BLPI samples. The mass obtained from the samples is compared against the average ELPI measurement during the sampling.

	ICP-OES average mass conc. during the sampling [g/Nm³]	ELPI average during sampling with 95% confidence interval [g/Nm³]	Mass % from the ICP-OES		
			Ag	Cd	In
Filter 1 (10612 s)	5.21	2.96 ± 0.28	0.3	99.6	0.1
Filter 2 (11392 s)	7.40	4.83 ± 0.09	46.3	45.9	7.8
BLPI 1 (11632 s)	9.48	7.61 ± 0.14	43.2	47.8	9.0
Filter 3 (11992 s)	6.83	3.27 ± 0.04	49.4	42.2	8.4
BLPI 2 (12172 s)	6.32	2.99 ± 0.07	44.4	46.1	9.5

Table 12   QUENCH-18; release of Cd, In, Ag

Element	Total mass of sampled aerosol, g	Approximate mass of released aerosol (including losses 28%)	Fraction of total mass in control rods, %
Cadmium	7.1 ± 0.1	9.0	14.3
Indium	1.0 ± 0.1	1.2	0.7
Silver	5.1 ± 0.1	6.6	0.6
Total	*13.2*	*16.8*	*1.3*

Table 13   Cross sections of the QUENCH-18 bundle (upper part) for metallographic examination

		bottom (mm)	top (mm)
remainder		1484	
cut	4		
QUE-18-1	16	1464	**1480**
cut	4		
QUE-18-a	26	1434	1460
cut	4		
QUE-18-2	16	1414	**1430**
cut	4		
QUE-18-b	56	1354	1410
cut	4		
QUE-18-3	16	1334	**1350**
cut	4		
QUE-18-c	76	1254	1330
cut	4		
QUE-18-4	16	1234	**1250**
cut	4		
QUE-18-d	76	1154	1230
cut	4		
QUE-18-5	16	1134	**1150**
cut	4		
remainder			1130

Table 14   Cross sections of the QUENCH-18 bundle (lower part) for metallographic examination

		bottom (mm)	top (mm)
remainder	176	954	1130
cut	4		
QUE-18-6	22	928	**950**
cut	4		
QUE-18-e	170	754	924
cut	4		
QUE-18-7	22	728	**750**
cut	4		
QUE-18-f	138	586	724
cut	4		
QUE-18-8	22	**560**	582
cut	4		
QUE-18-g	202	354	556
cut	4		
QUE-18-9	22	328	**350**
cut	4		
QUE-18-h	160	164	324
cut	4		
QUE-18-10	22	138	**160**
cut	4		
QUE-18-i	43	91	134
cut	4		
QUE-18-11	22	**65**	87
cut	4		
QUE-18-j	75	-14	61
cut	4		
QUE-18-12	22	**-40**	-18
remainder	4		-44
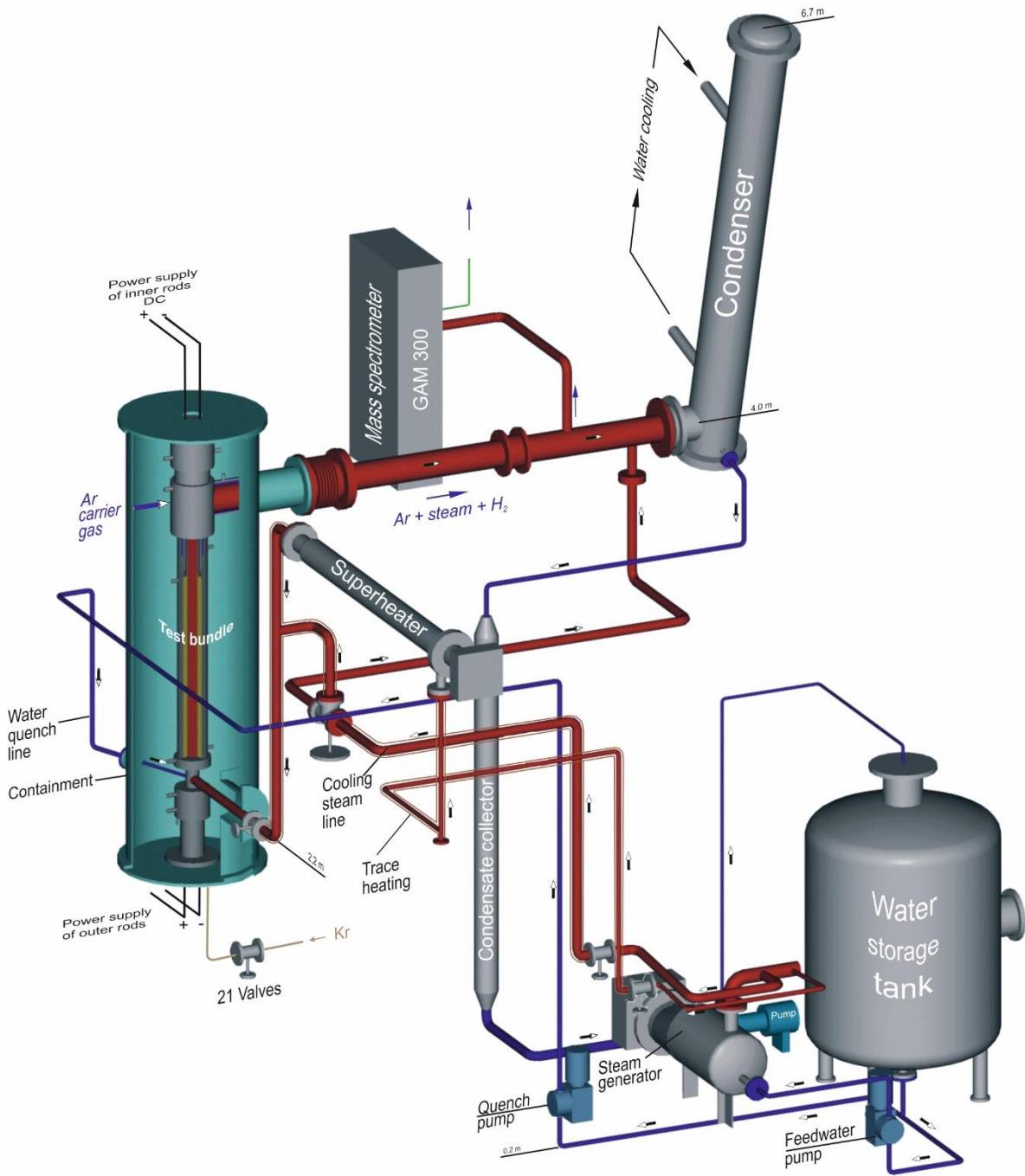
Figure 1   QUENCH Facility - Main components.
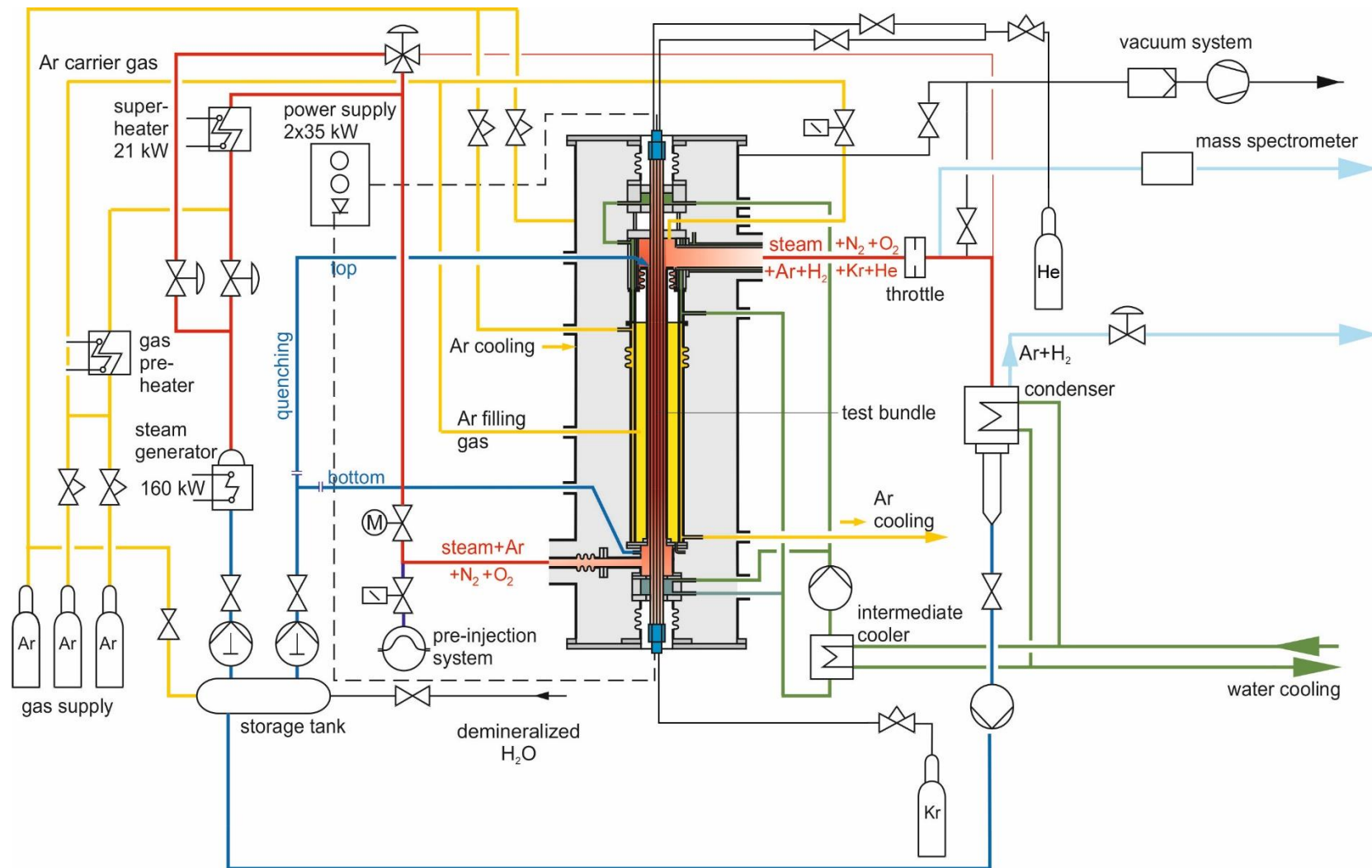
Figure 2   QUENCH-18; flow diagram of the QUENCH facility.
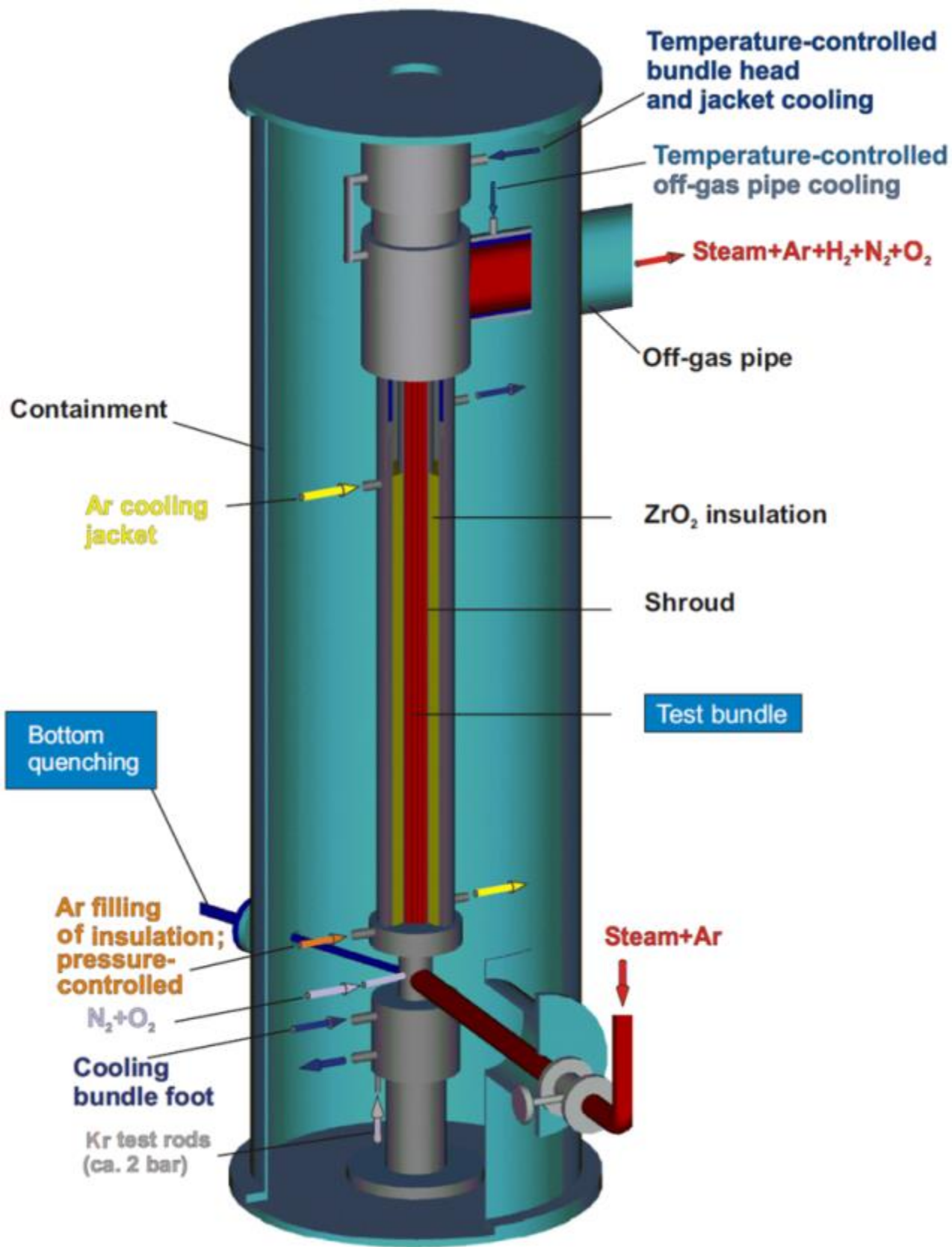
Figure 3 QUENCH-18; containment and test section.
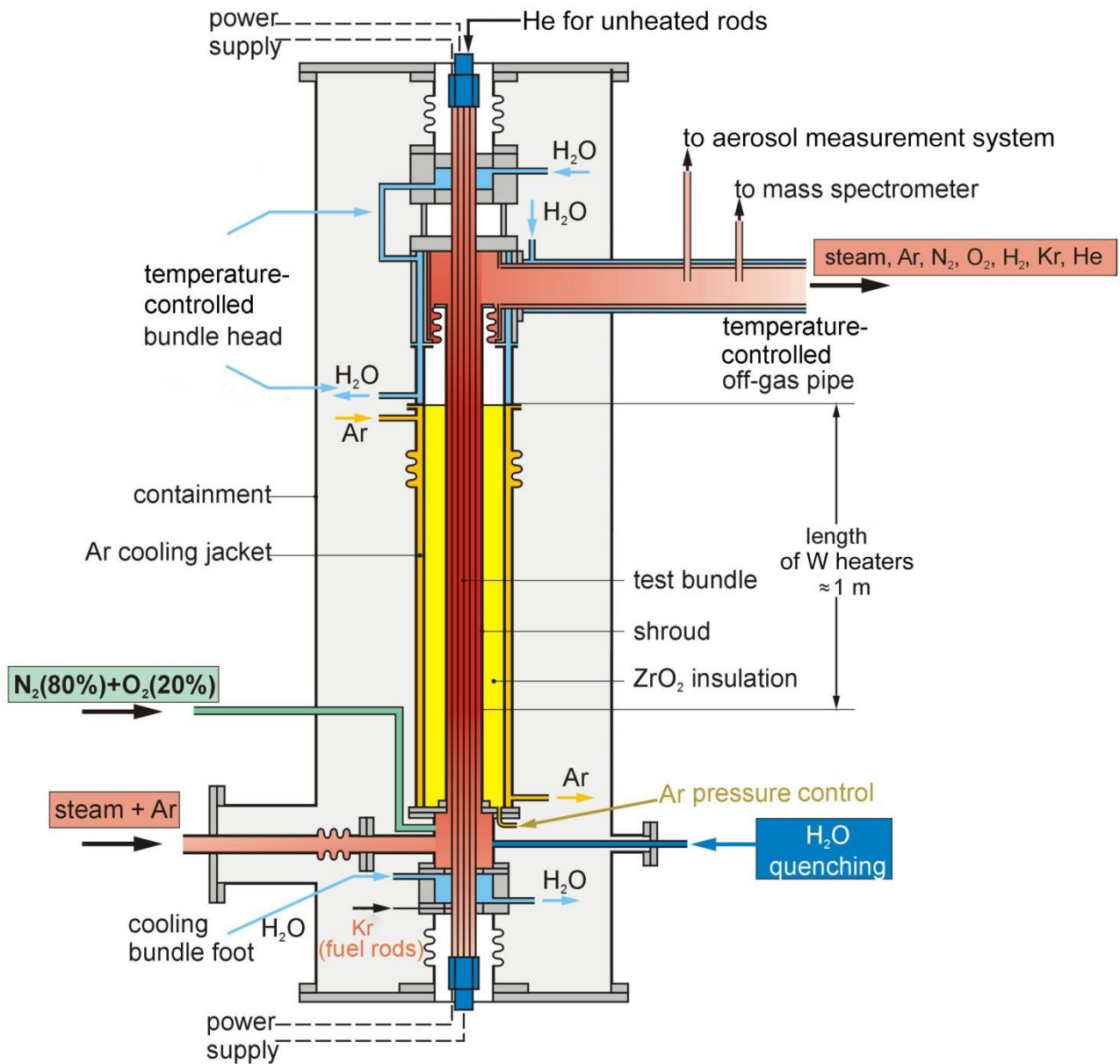
Figure 4   QUENCH-18; test section with flow lines.
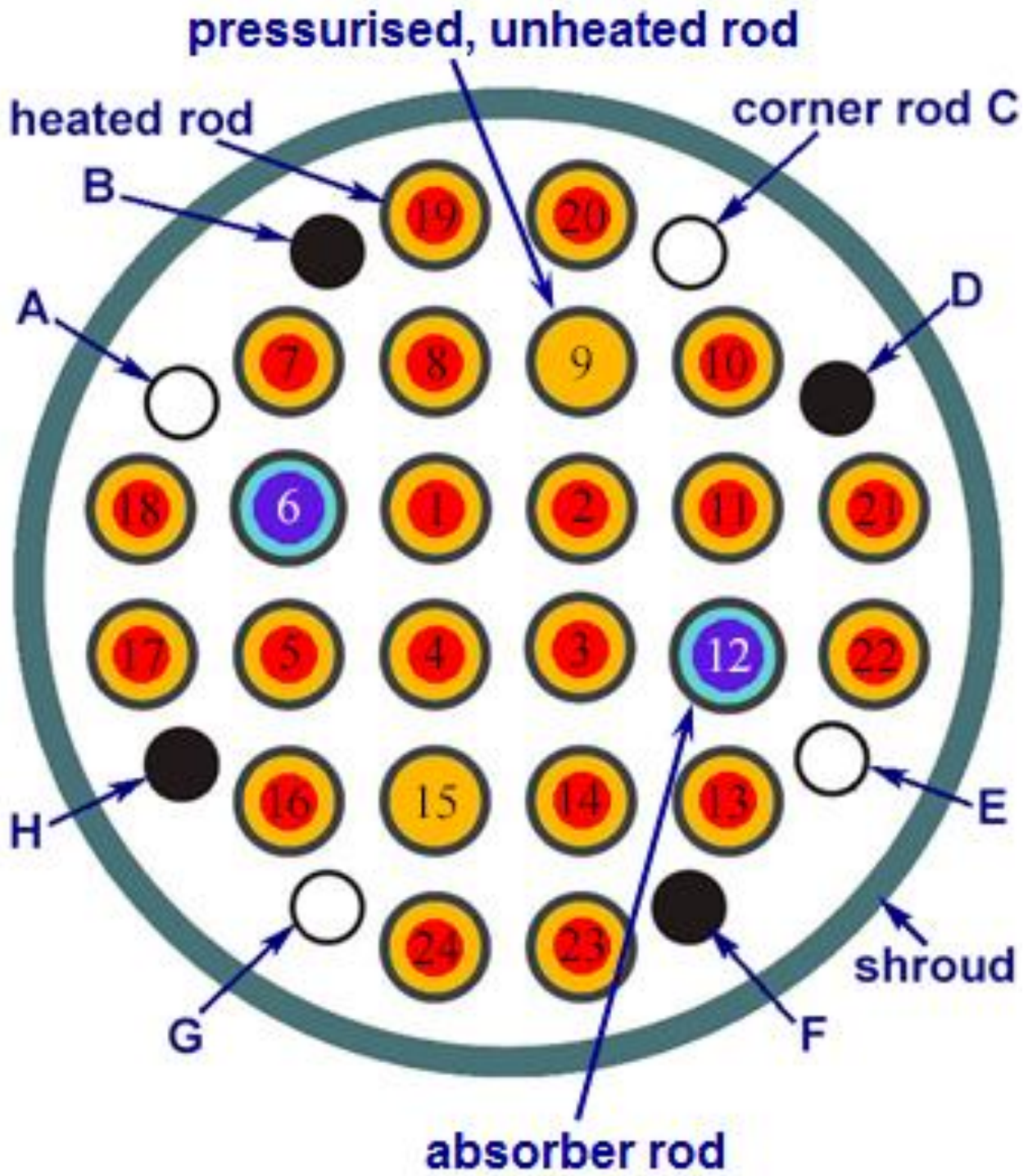
Figure 5 QUENCH-18; cross section of test bundle.
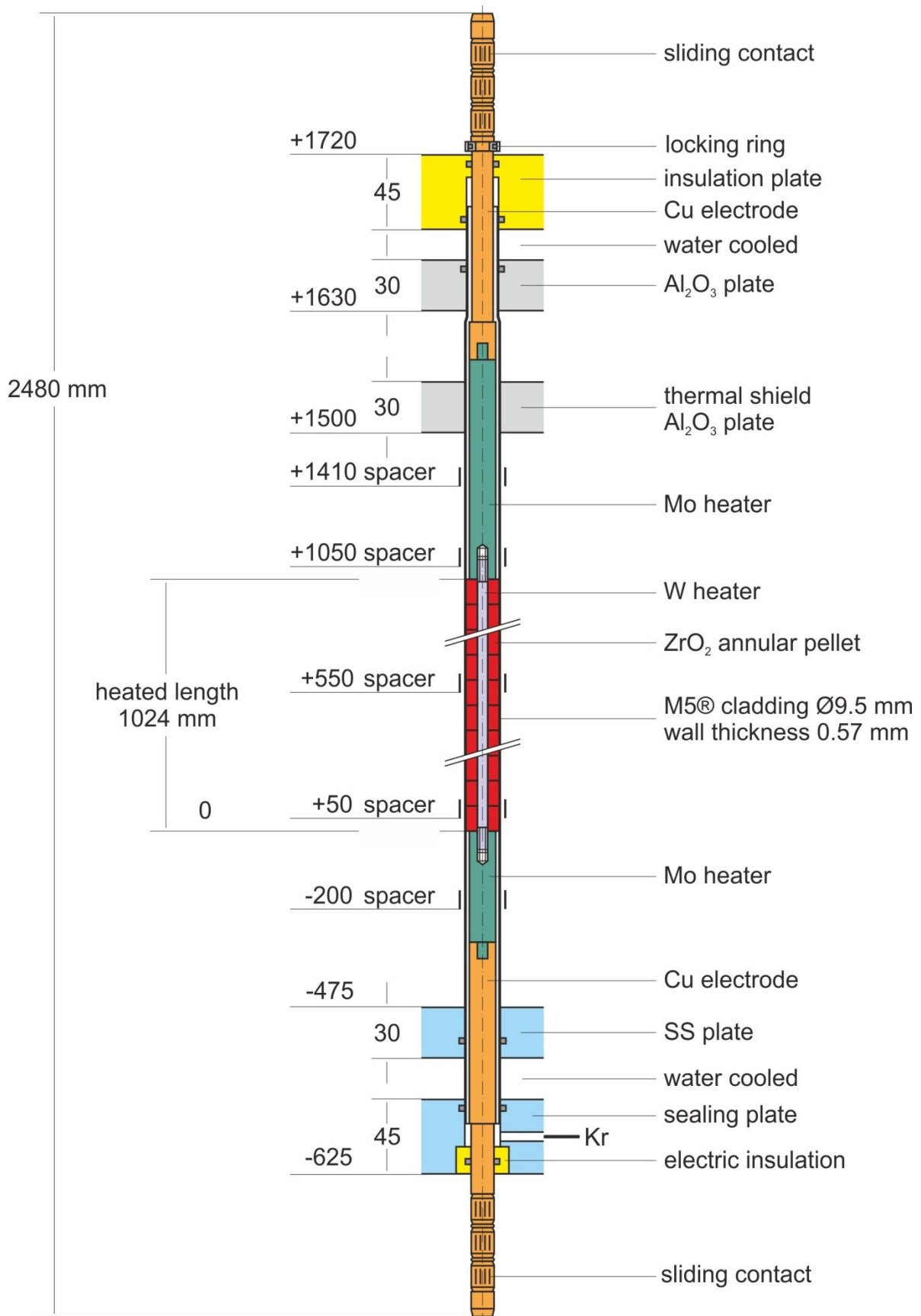
Figure 6   QUENCH-18; heated rod.
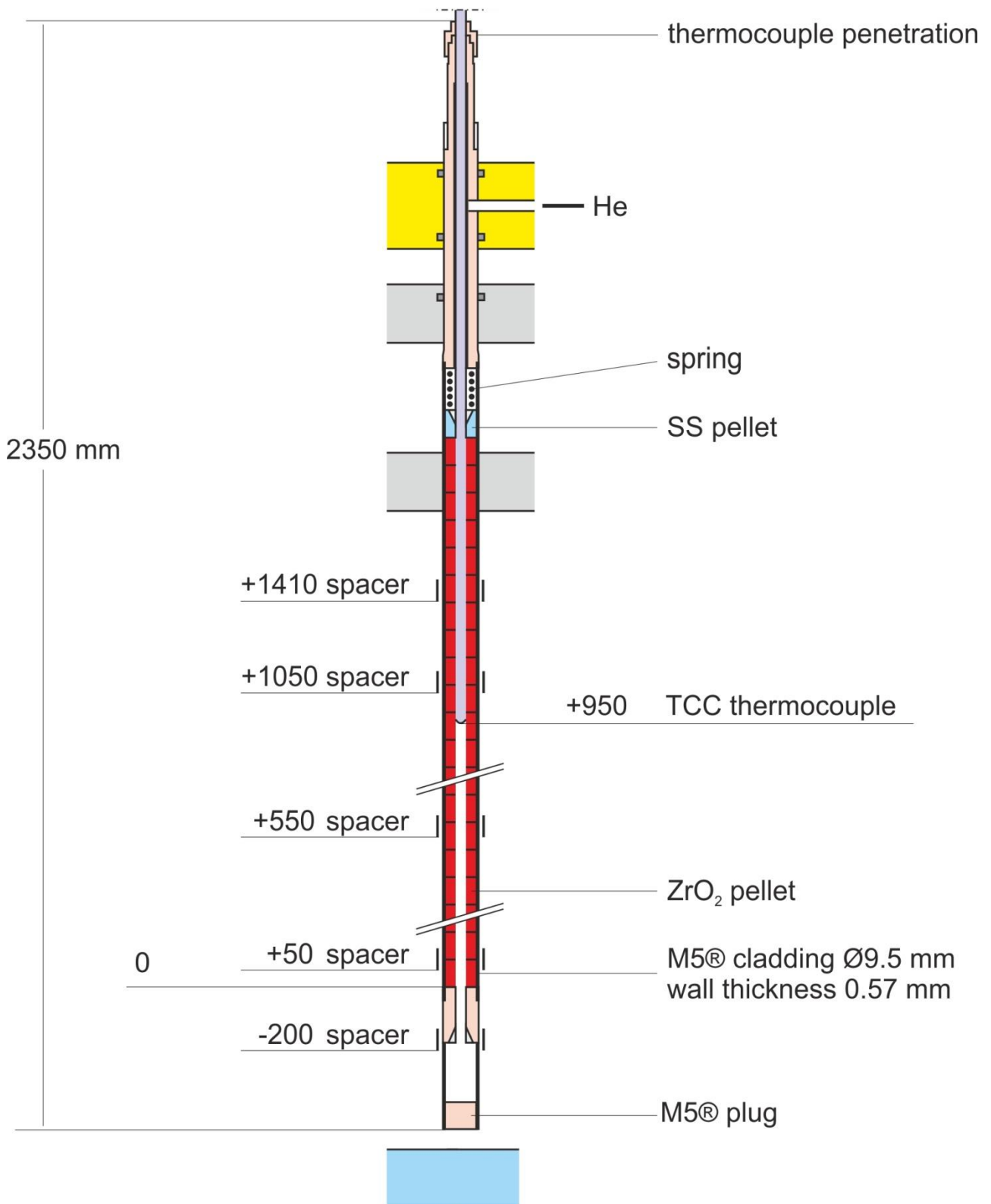
Figure 7 QUENCH-18; unheated rod.
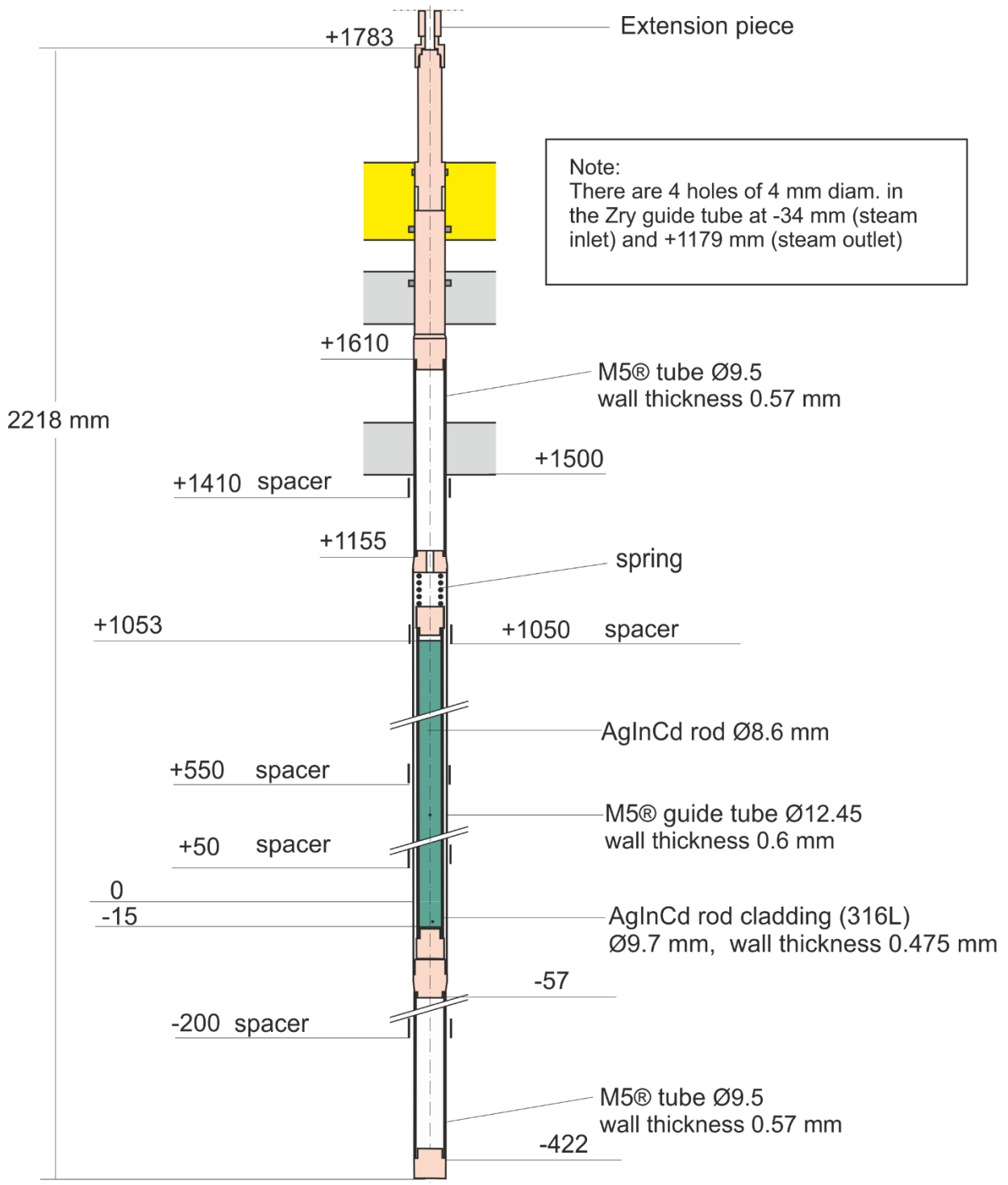
Figure 8 QUENCH-18; absorber rod.

	material	80 Ag, 15 In, 5 Cd (wt-%)
Absorber rod	dimensions	∅ 8.60 mm, L=1068 mm (Elev. -15 to 1053 mm), **M ≈ 633 g**
Cladding of absorber rod		**SS**, ∅ 9.70 / 8.75 mm
		L = 1083 mm (Elev. -20 to 1063 mm)
Guide tube of absorber rod		**M5®** , ∅ 12.45 / 11.25 mm
		L = 1187 mm (Elev. -42 to 1145 mm)
		Holes for coolant penetration (2x4): ∅4 mm (Elev. -34 and +1137 mm)
Internal rod pressure of absorber rod		0.12 MPa abs. (**He**)

Figure 9   QUENCH-18; absorber rod features.
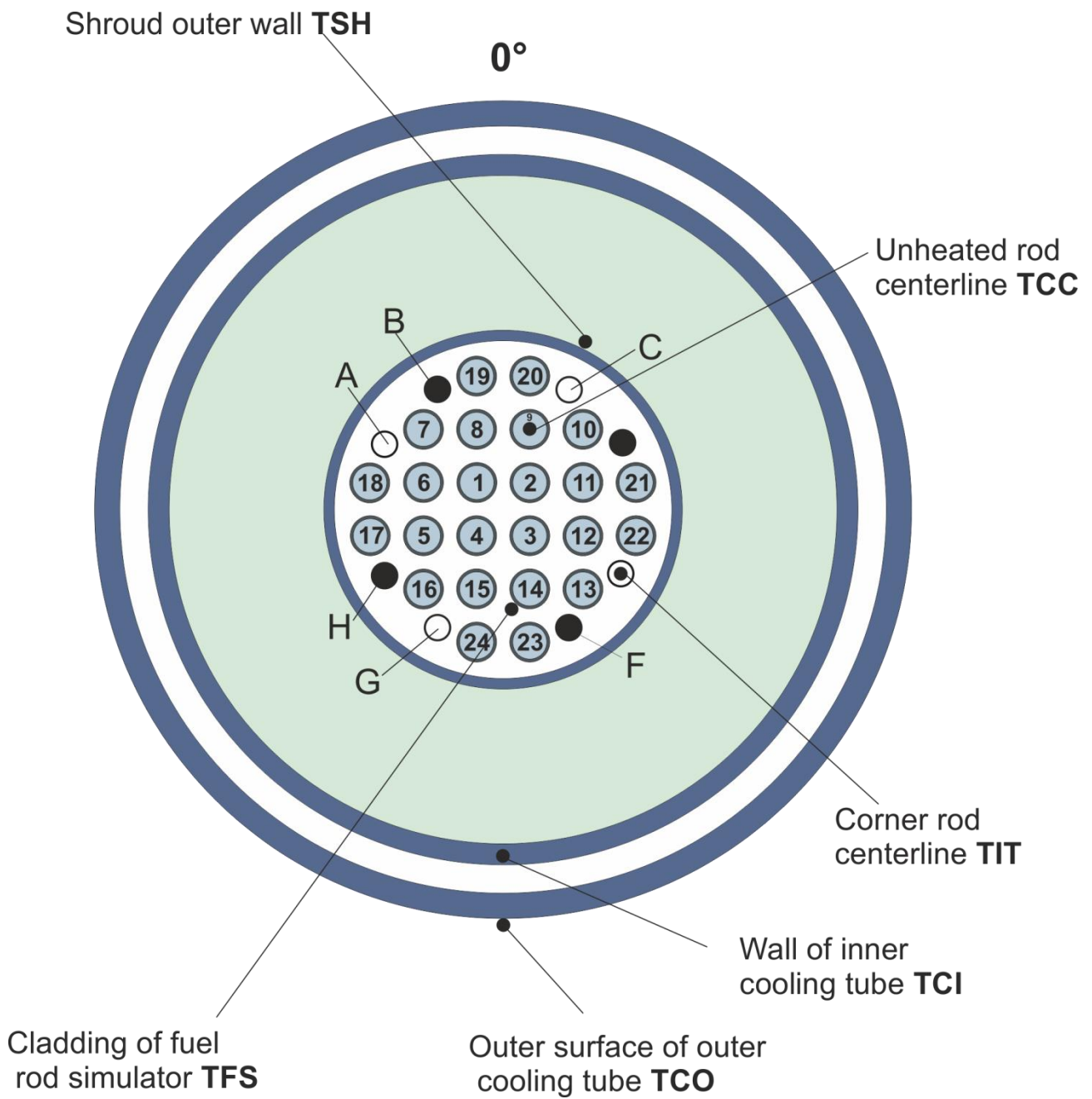
Figure 10   QUENCH-18; designation of the various thermocouples.
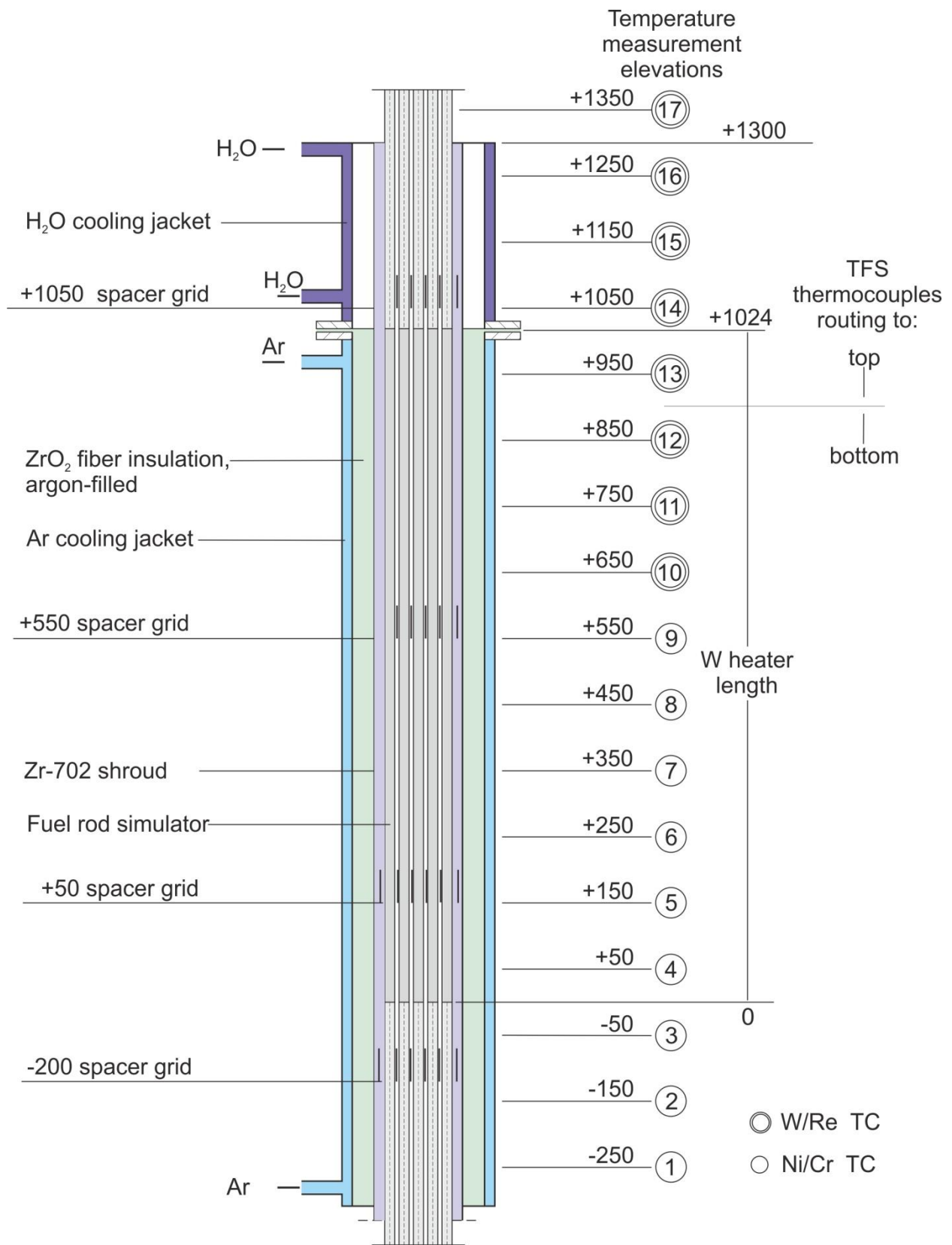
Figure 11   QUENCH-18; axial locations of thermocouples.

W/Re thermocouple

transition piece

SS compensation cable Ø 1 mm

connector

Ø 3.4 mm

L$^{*)}$

30

1000

Laser weld

Zr sheath Ø 2.2-2.3 mm
wall thickness 0.35 mm

disc

Hot junction
laser welded

W26%Re wire

W5%Re wire

Zircaloy cap

HfO_2 insulation

Ta sheath
Ø 1.4 mm
wall thickness 0.23 mm
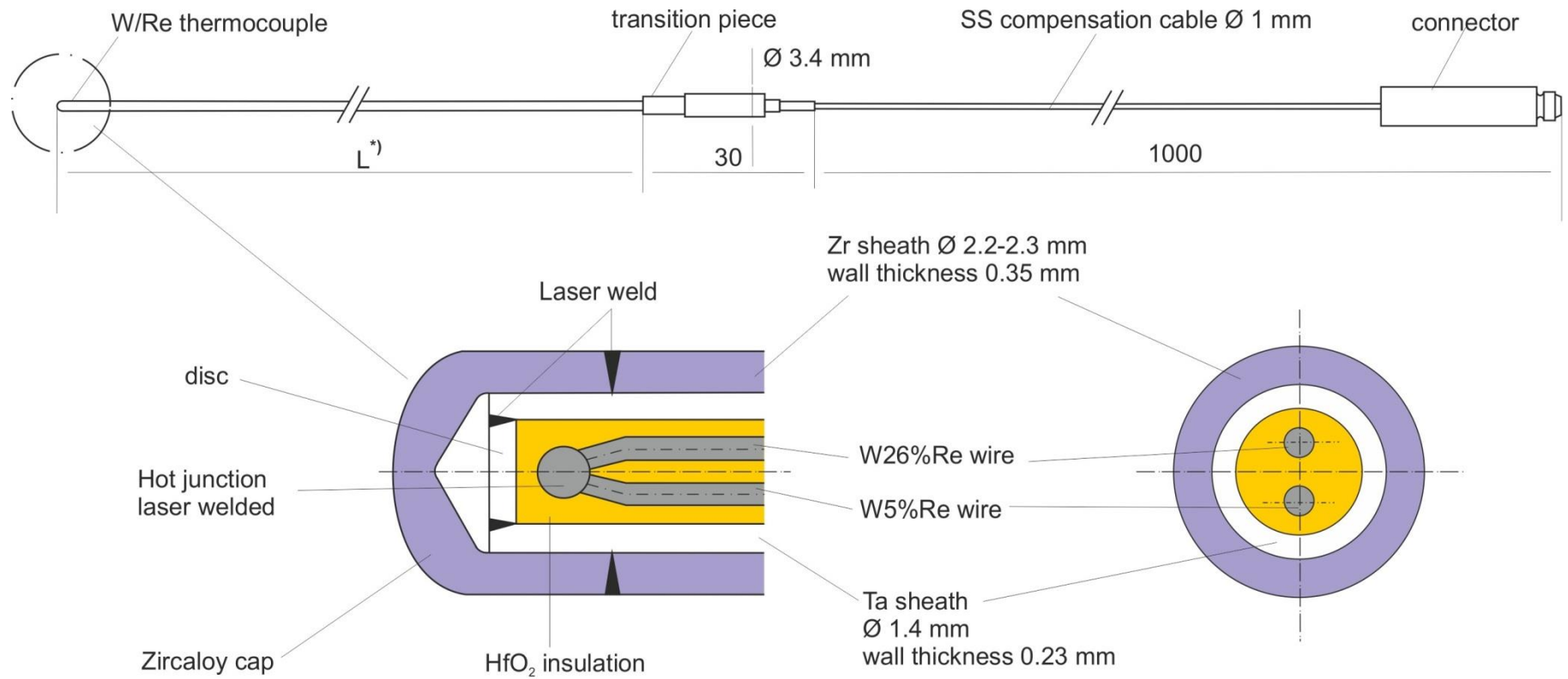
$^{*)}$ L: high-temperature section length dependent on the TC position in the test bundle: 500-1700 mm

Figure 12   QUENCH-18; high temperature thermocouple.
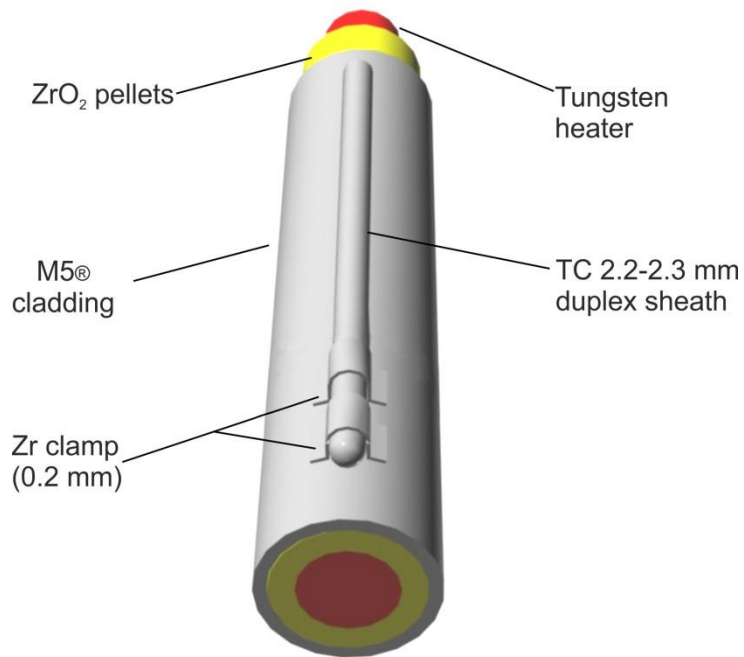
Figure 13   QUENCH-18; TC fastening at the cladding.
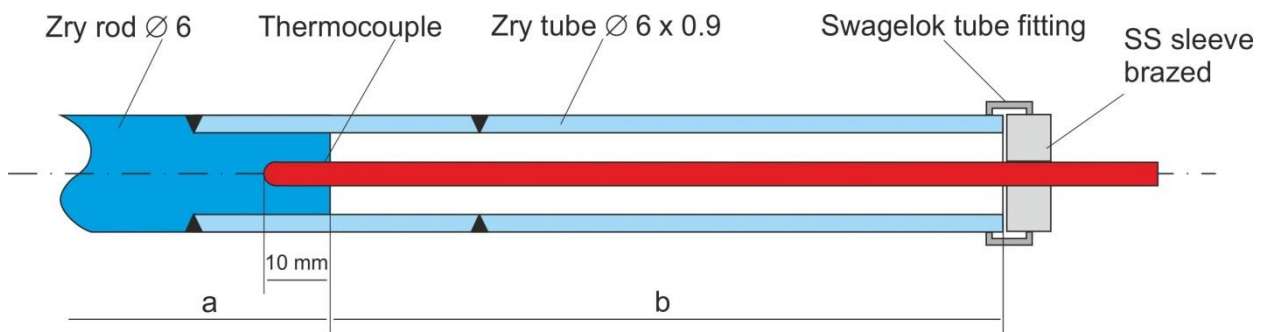
Rod A: TIT/ A12 (850 mm), W/Re, $\varnothing$ 2.1 mm, a = 460 mm, b = 1980 mm

Rod C: TIT/ C11 (750 mm), W/Re, $\varnothing$ 2.1 mm, a = 560 mm, b = 1880 mm

Rod E: TIT/ E10 (650 mm), W/Re, $\varnothing$ 2.1 mm, a = 660 mm, b = 1780 mm

Rod G: TIT G/9 (550 mm), W/Re, $\varnothing$ 2.1 mm, a = 760 mm, b = 1680 mm

Figure 14   QUENCH-18; arrangement of the thermocouples inside the corner rods.
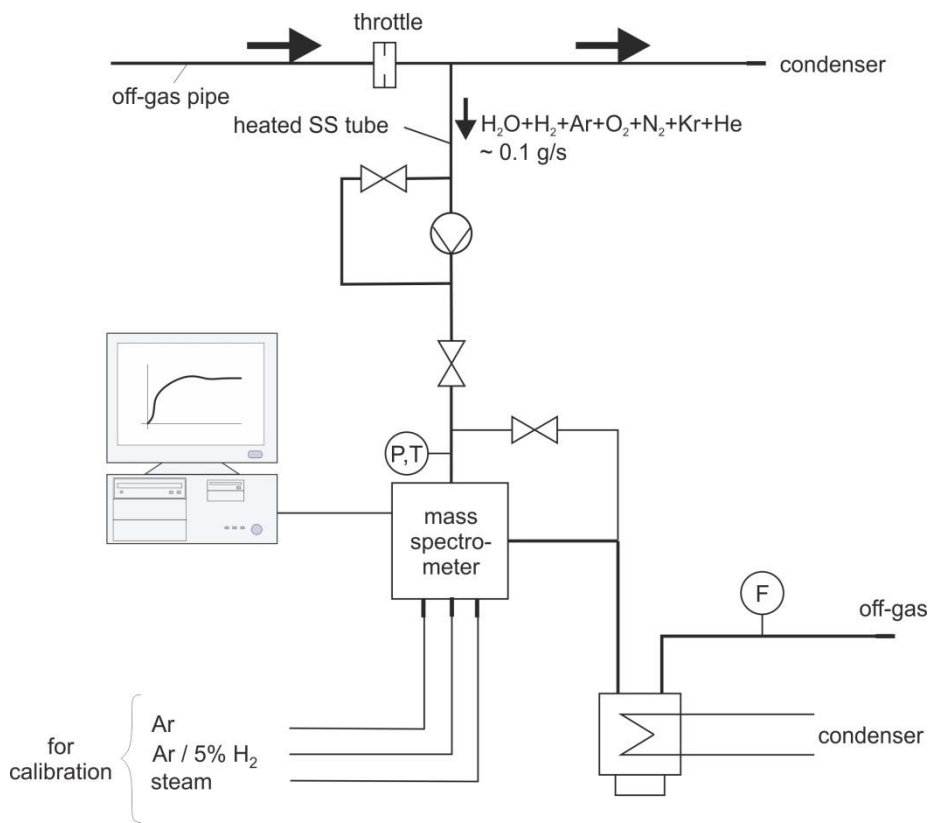
Figure 15   QUENCH-18; gas measurement with the GAM 300 mass spectrometer.
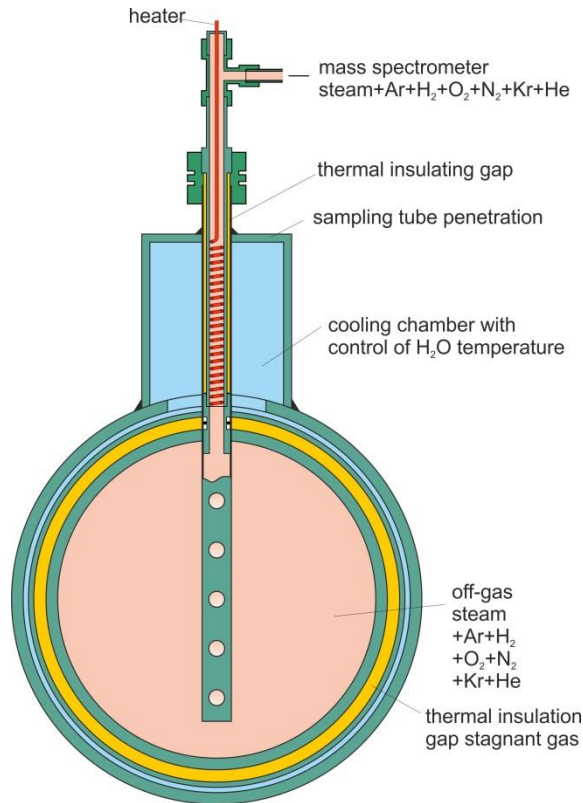
Figure 16   QUENCH-18; mass spectrometer sampling position at the off-gas pipe.
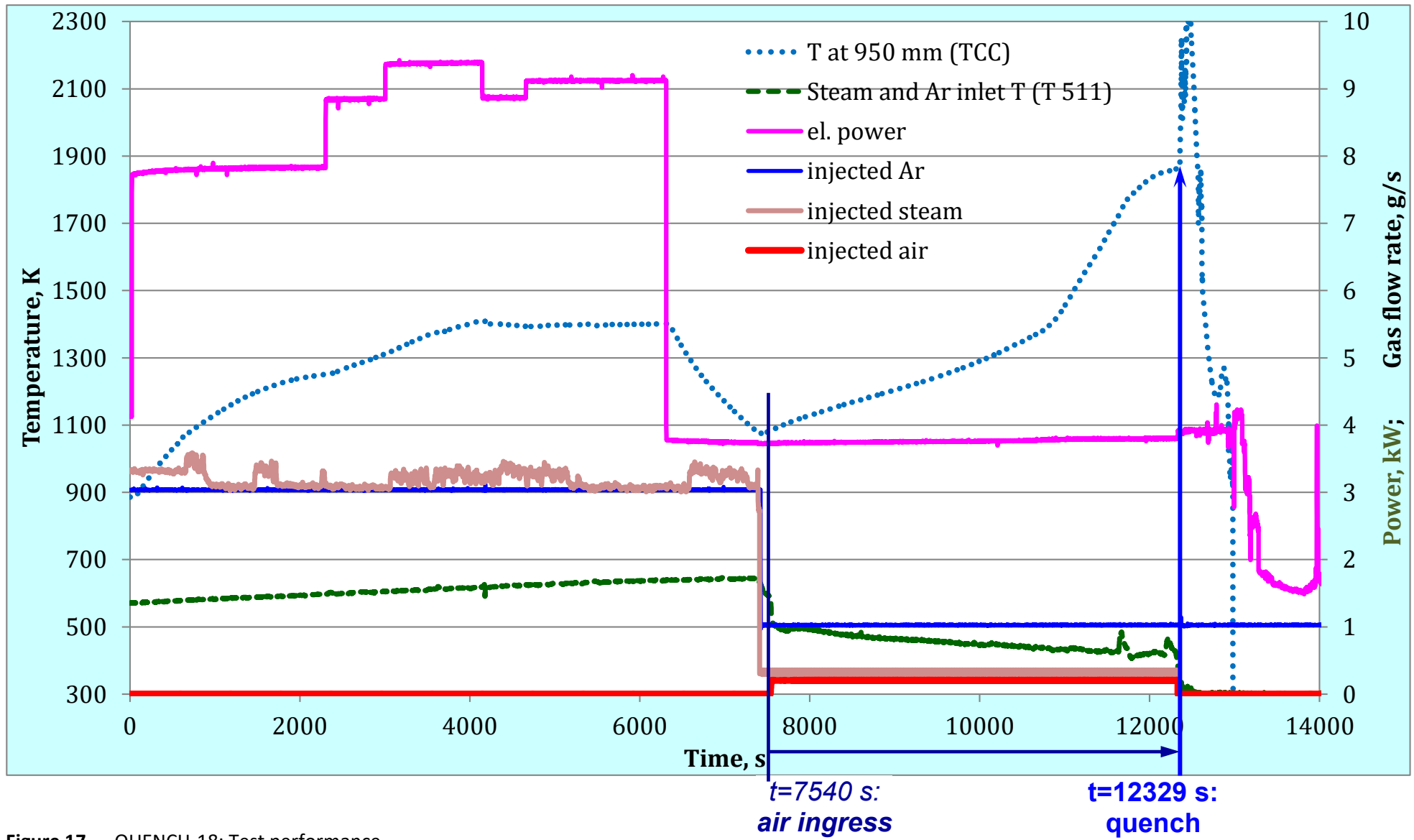
Figure 17   QUENCH-18; Test performance.
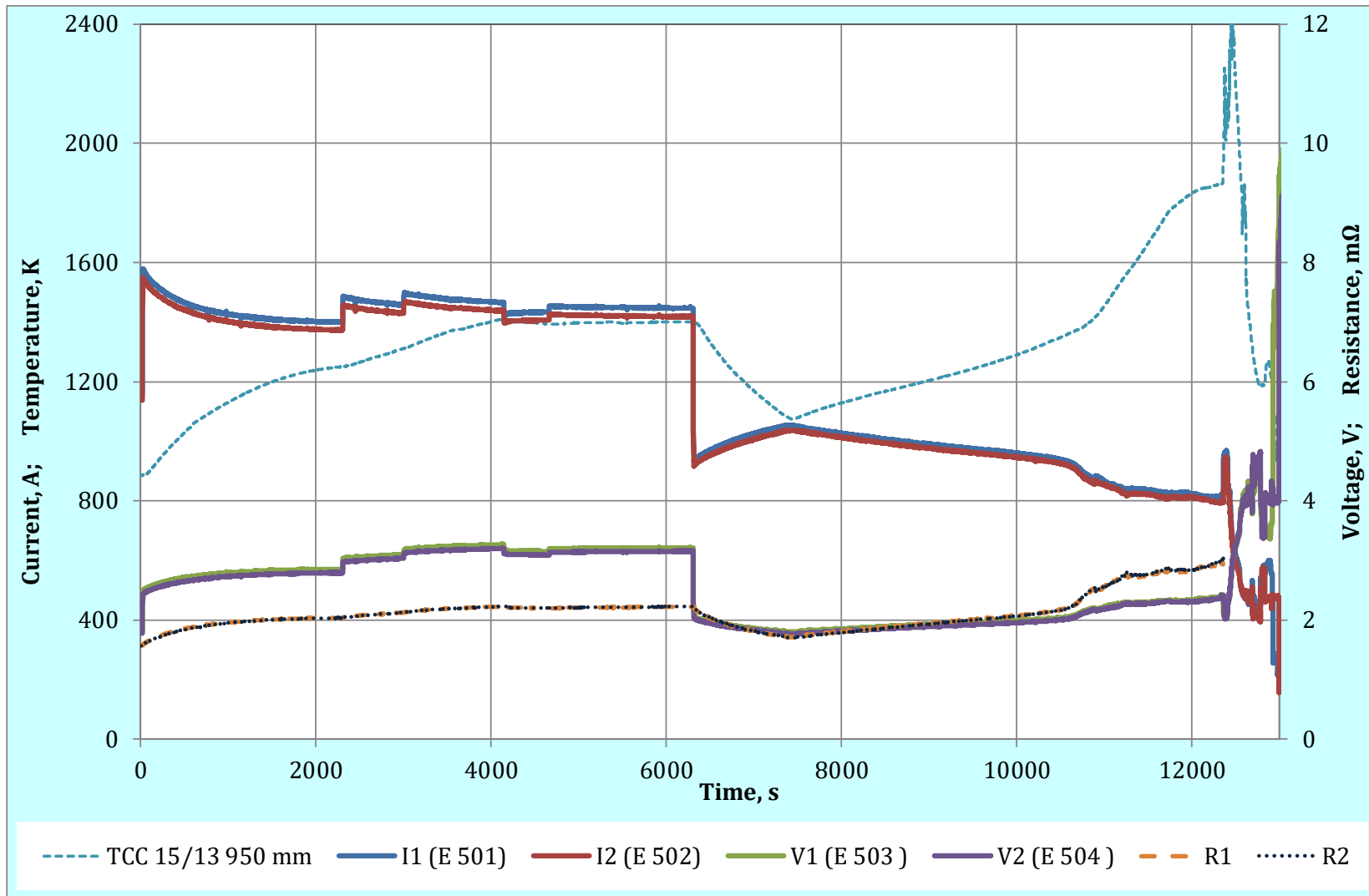
Figure 18   QUENCH-18; Electrical current I and voltage V of two DC generators, resistance R=V/I of two bundle halves.
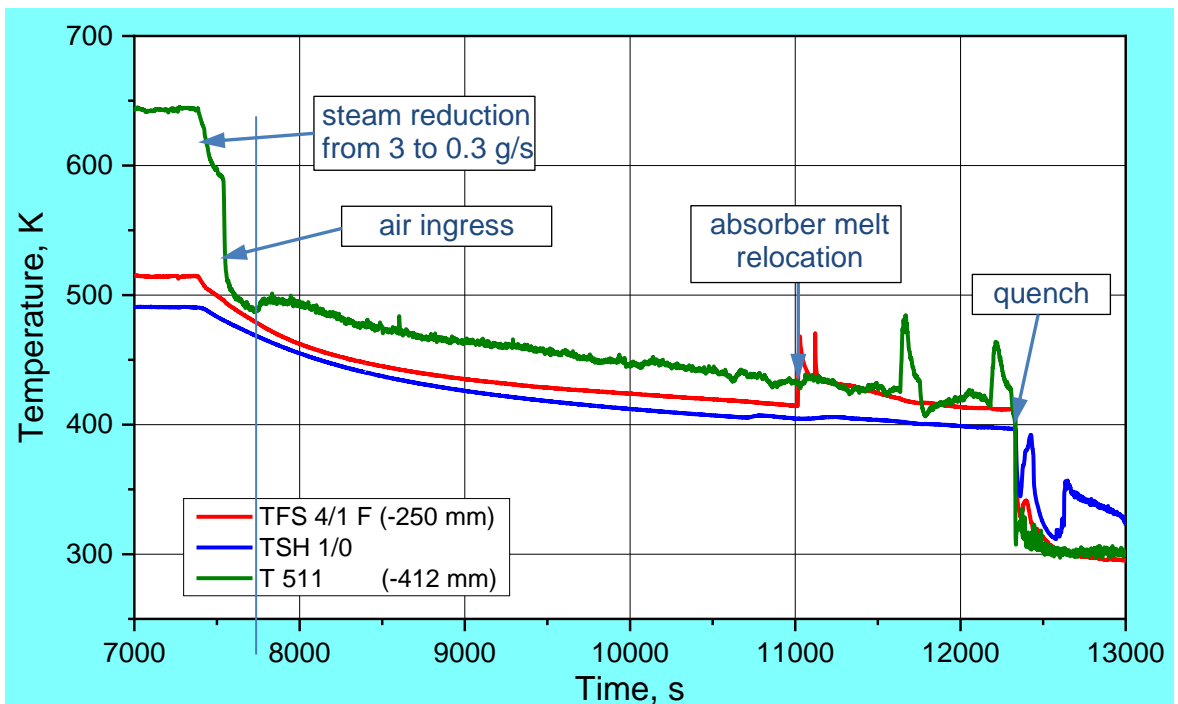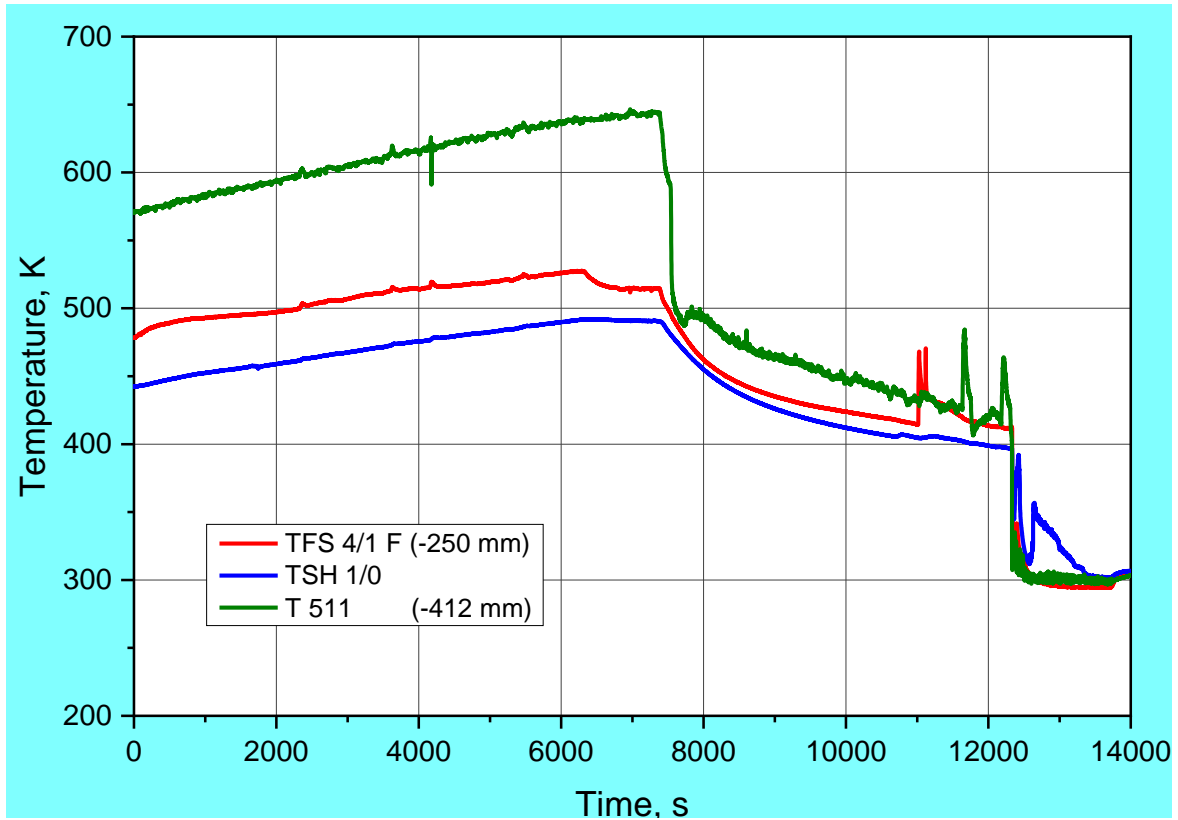
Figure 19   QUENCH-18; Temperatures measured by gas inlet thermocouple (T 511) at -412 mm, rod cladding thermocouple (TFS 4/1F) and shroud (TSH 1/0) thermocouples at -250 mm elevation.
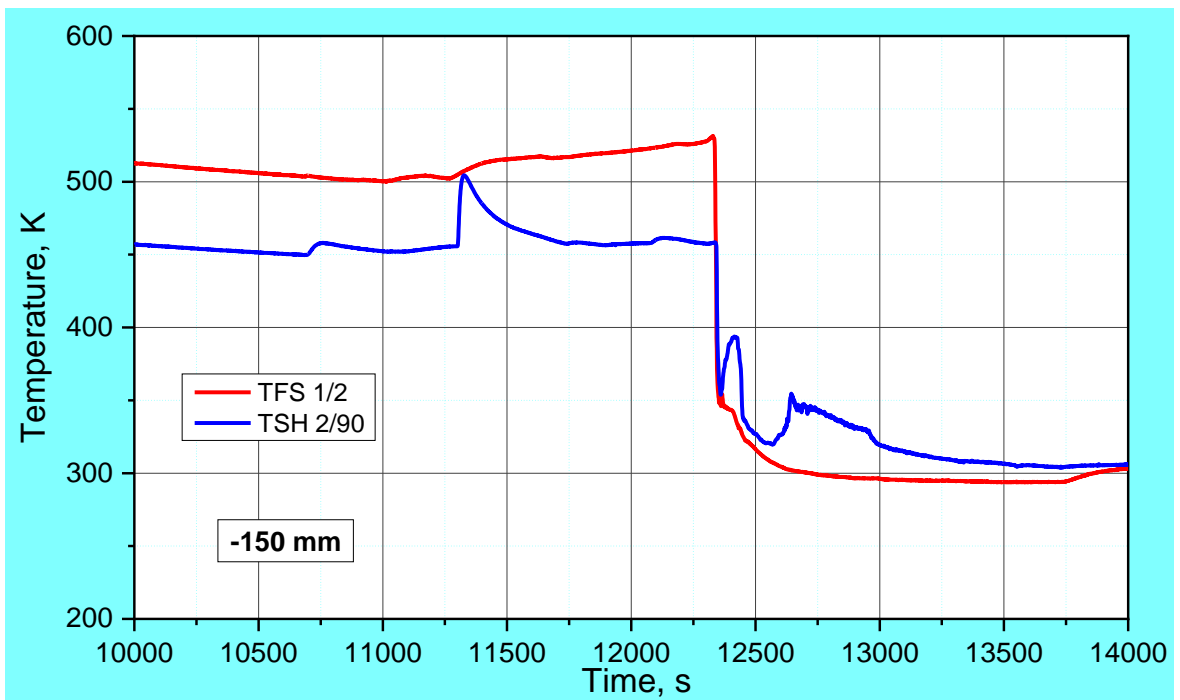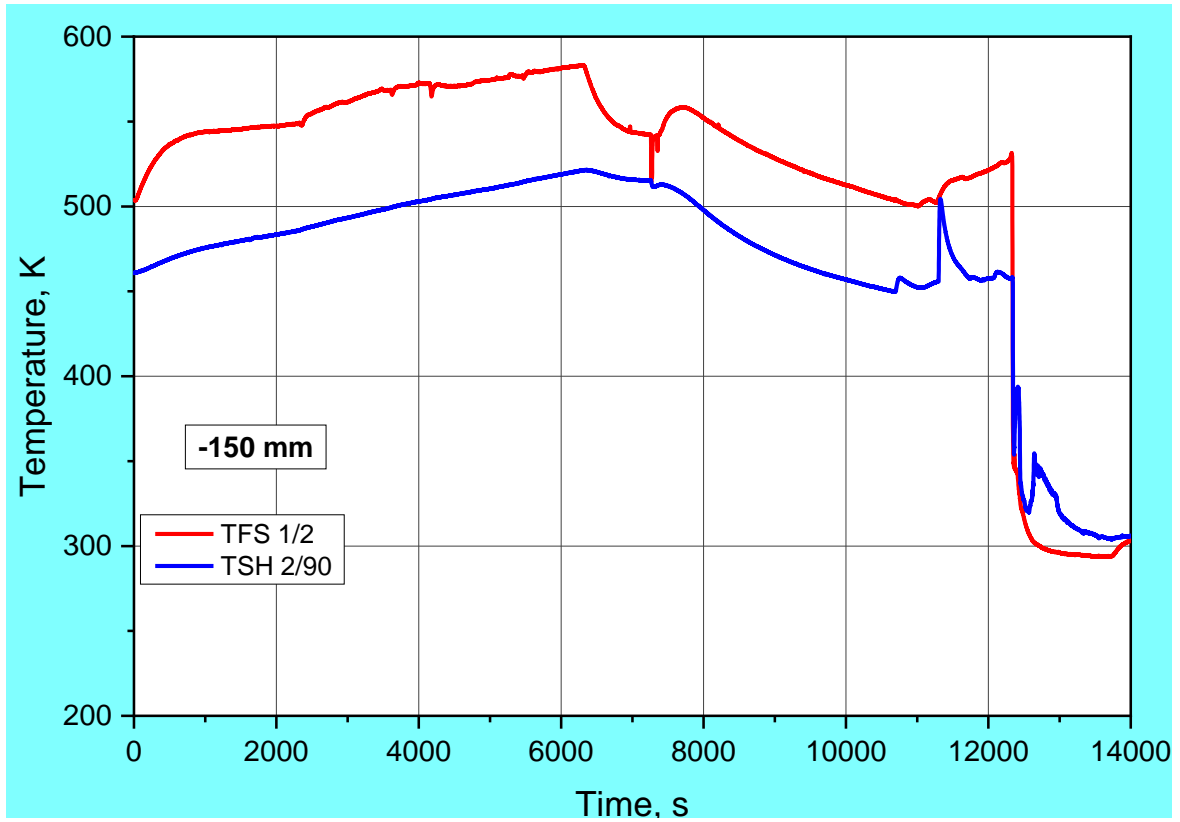
Figure 20   QUENCH-18; Temperatures measured by rod cladding (TFS 1/2) and shroud (TSH 2/90) thermocouples thermocouple at -150 mm elevation.
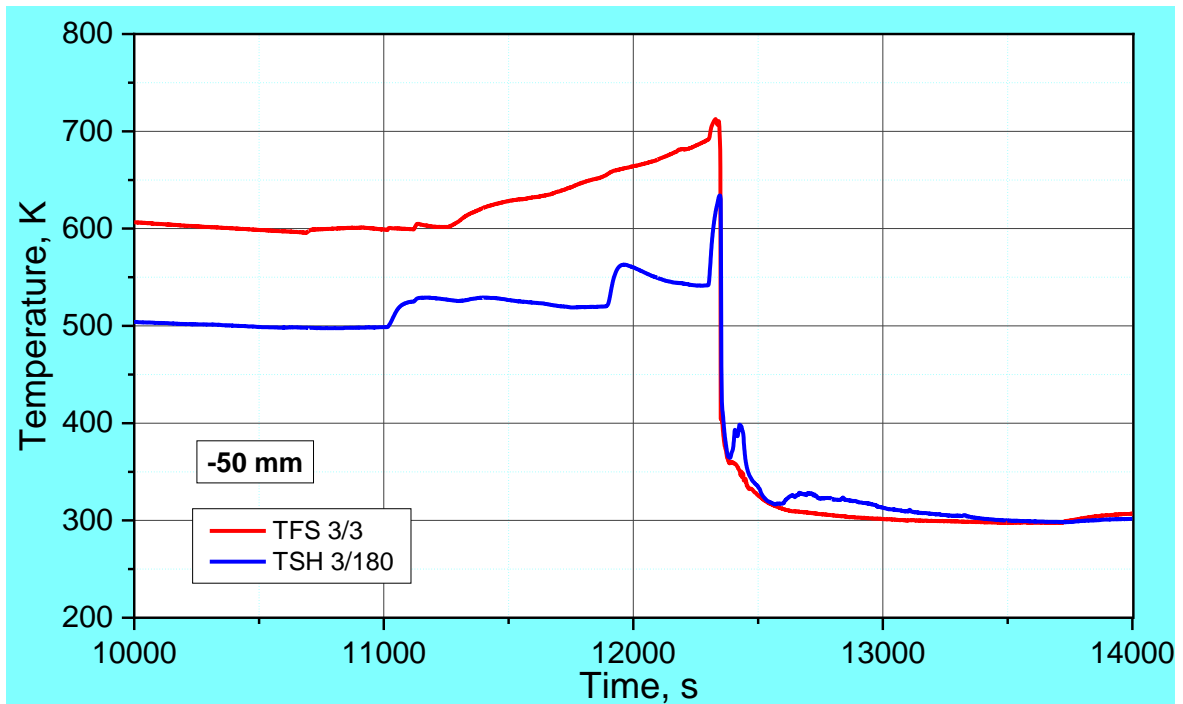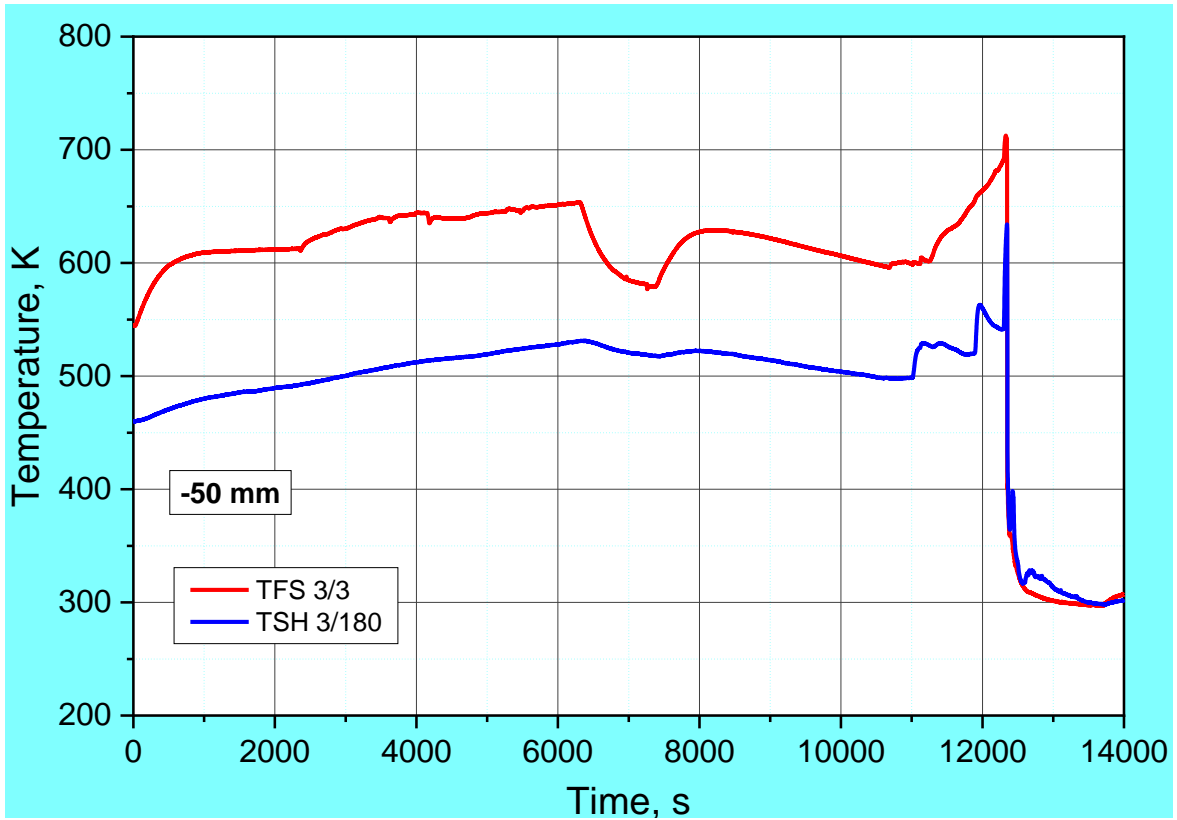
Figure 21 QUENCH-18; Temperatures measured by rod cladding (TFS 3/3) and shroud (TSH 3/180) thermocouples at -50 mm elevation.
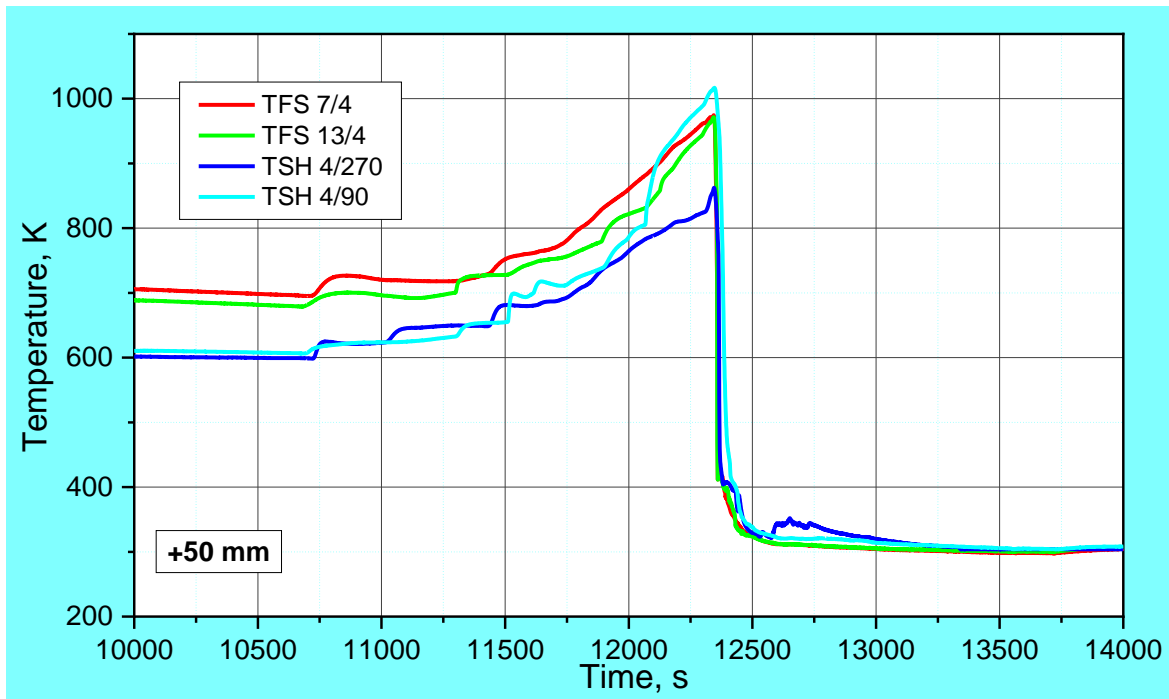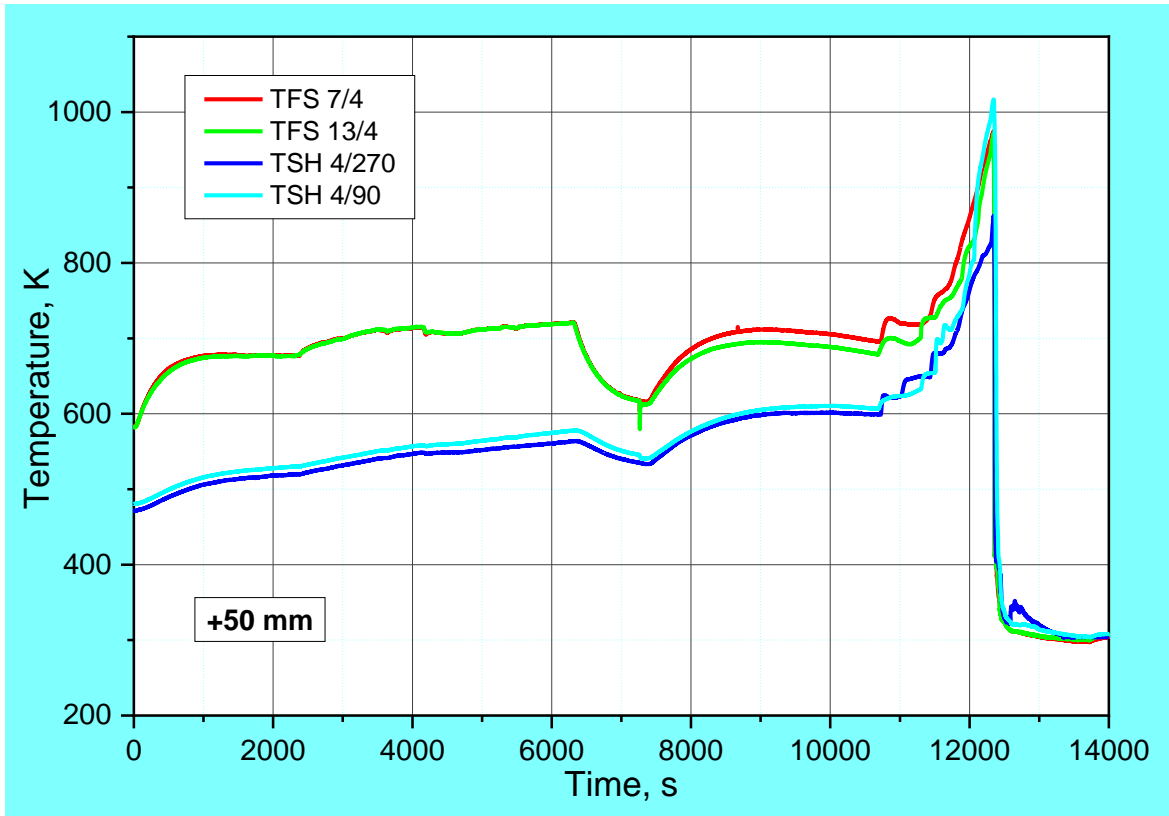
Figure 22   QUENCH-18; Temperatures measured by rod cladding (TFS) and shroud (TSH) thermocouples at 50 mm elevation.
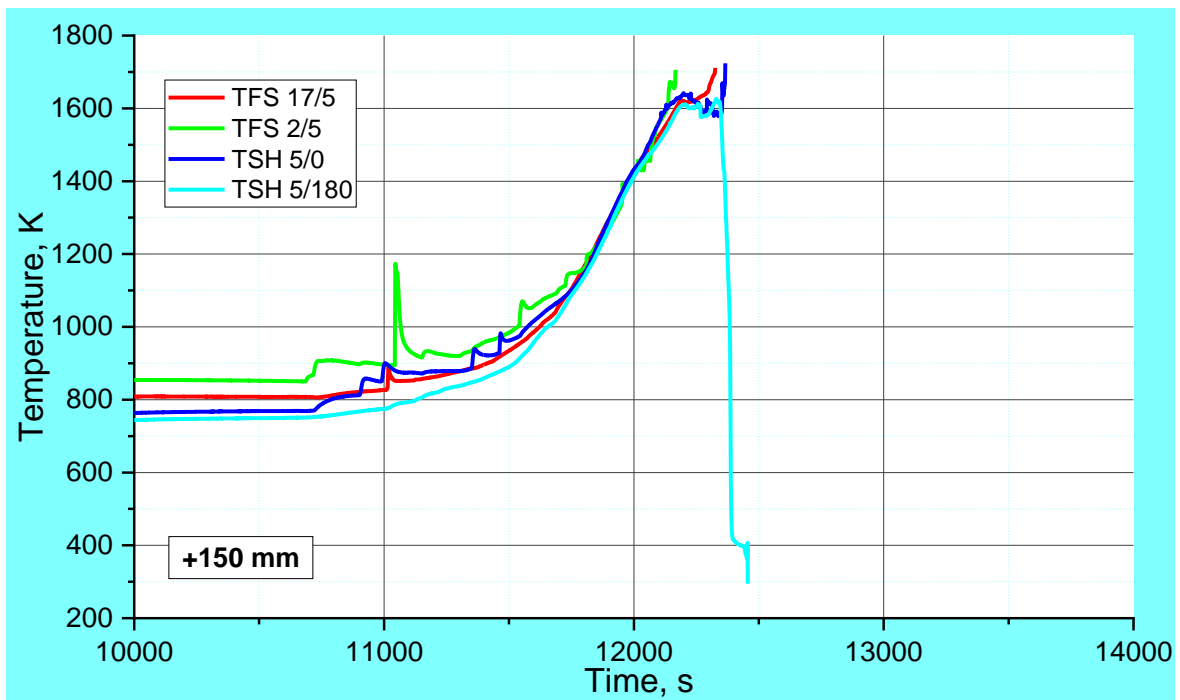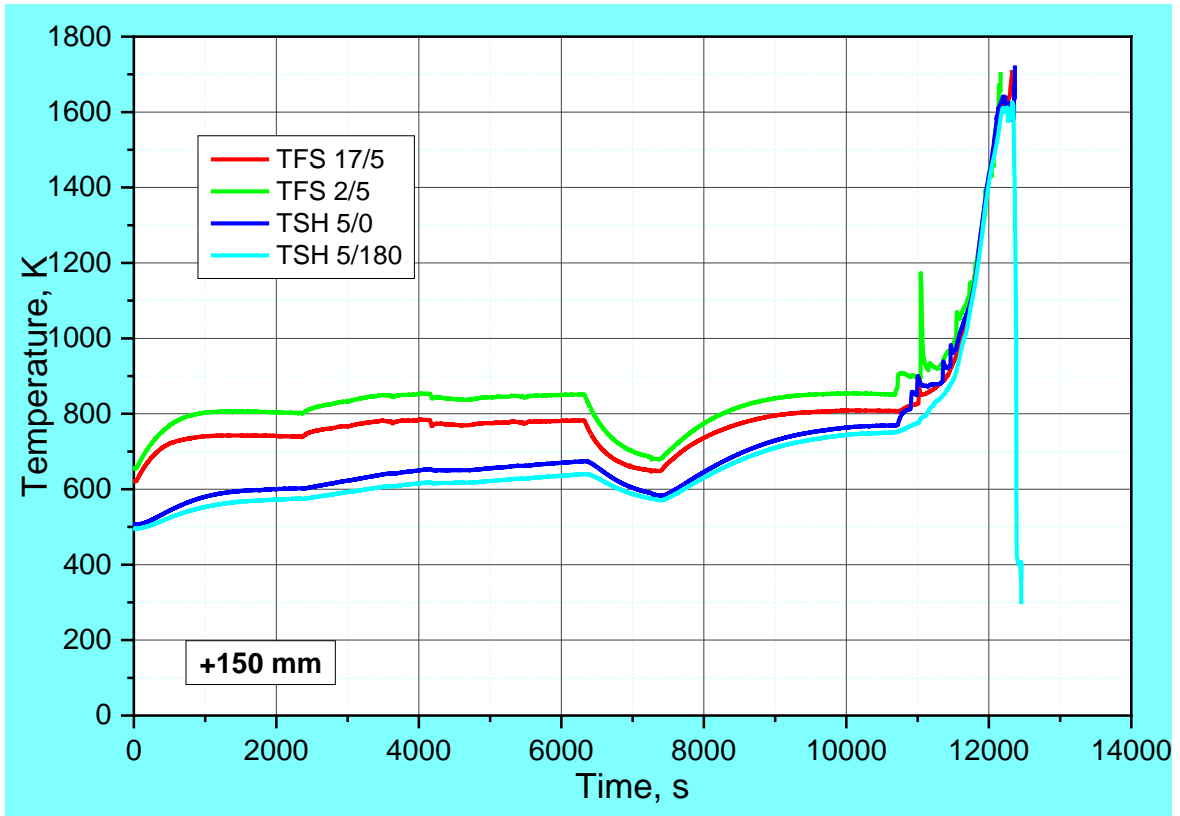
Figure 23   QUENCH-18; Temperatures measured by rod cladding (TFS) and shroud (TSH) thermocouples at 150 mm elevation.
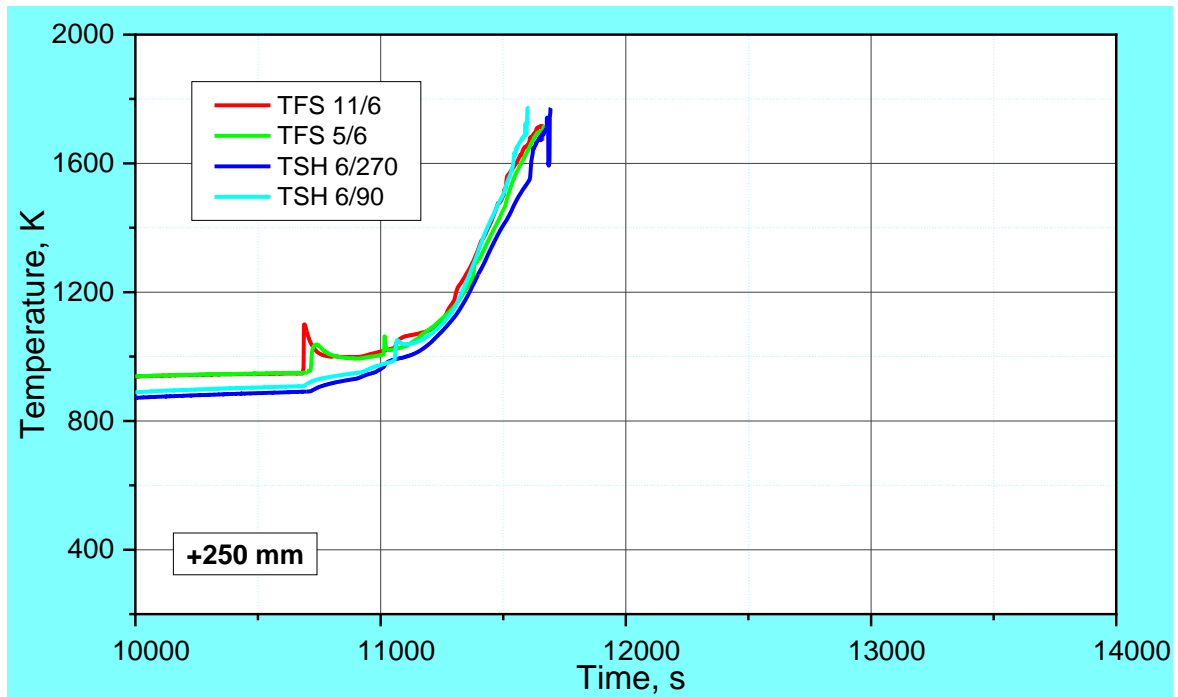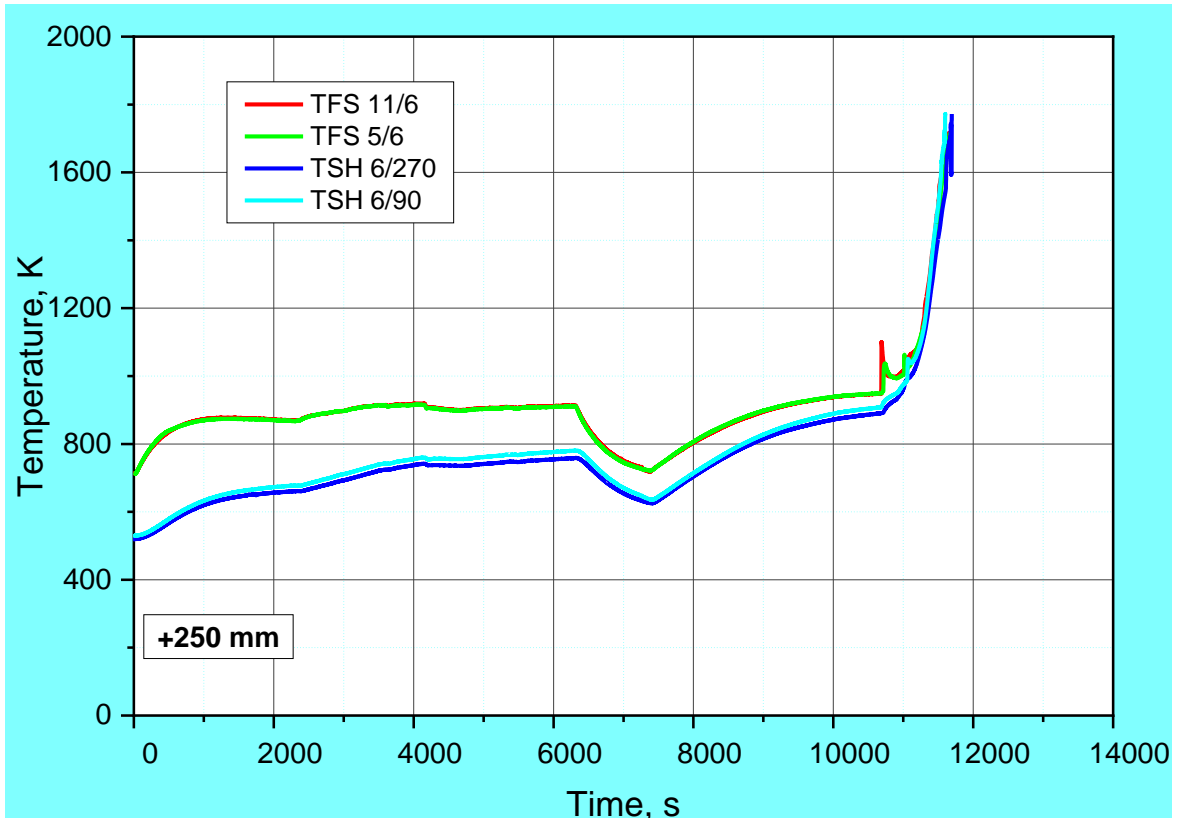
Figure 24 QUENCH-18; Temperatures measured by rod cladding (TFS) and shroud (TSH) thermocouples at 250 mm elevation.
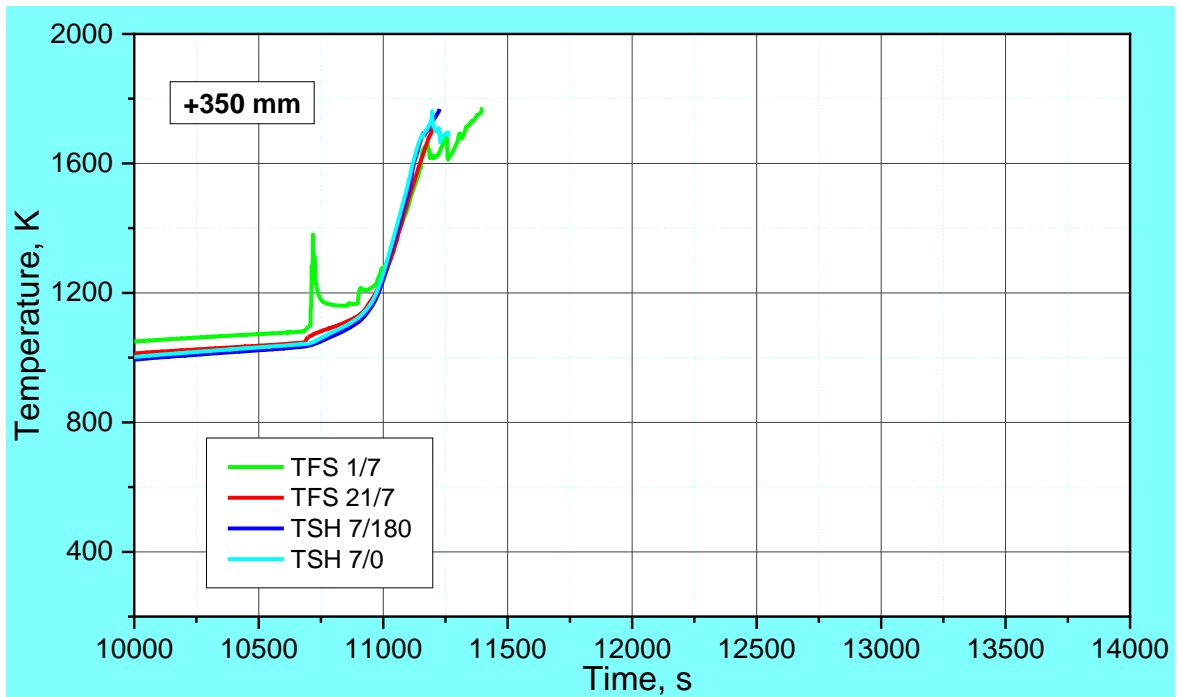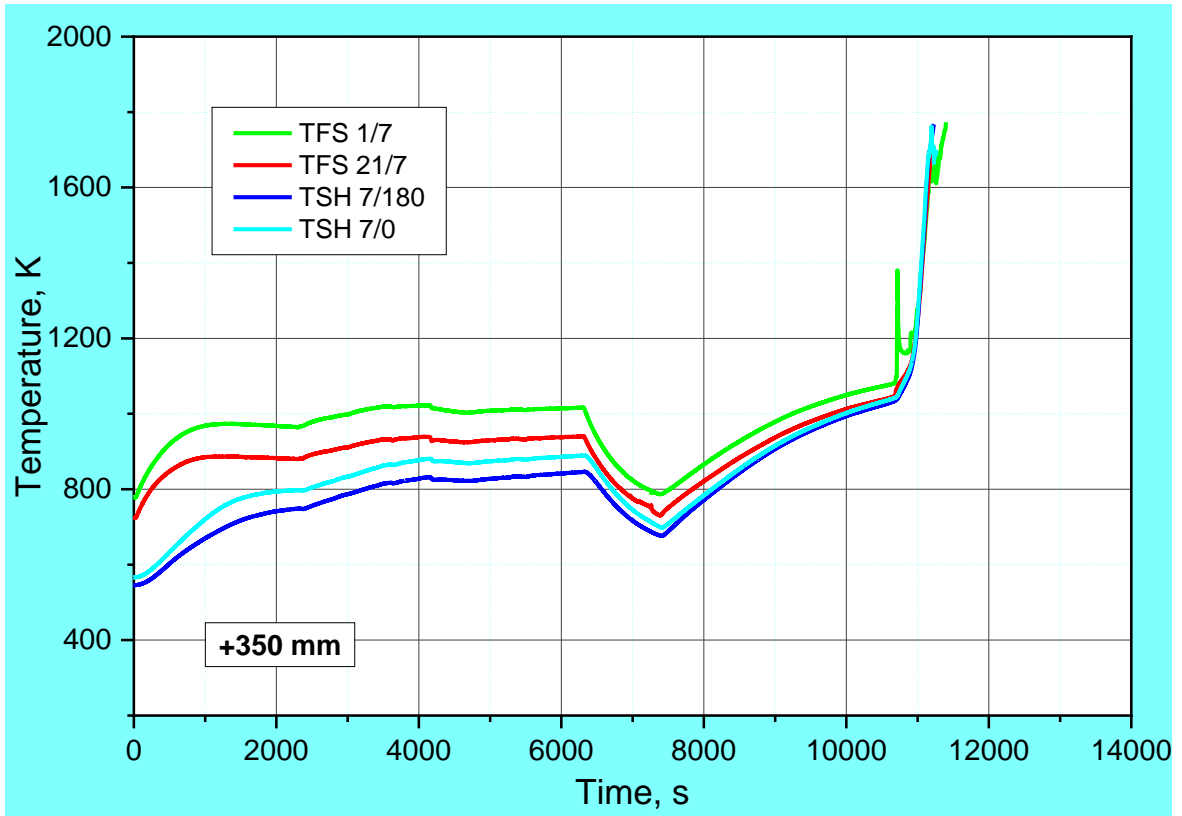
Figure 25 QUENCH-18; Temperatures measured by rod cladding (TFS) and shroud (TSH) thermocouples at 350 mm elevation.
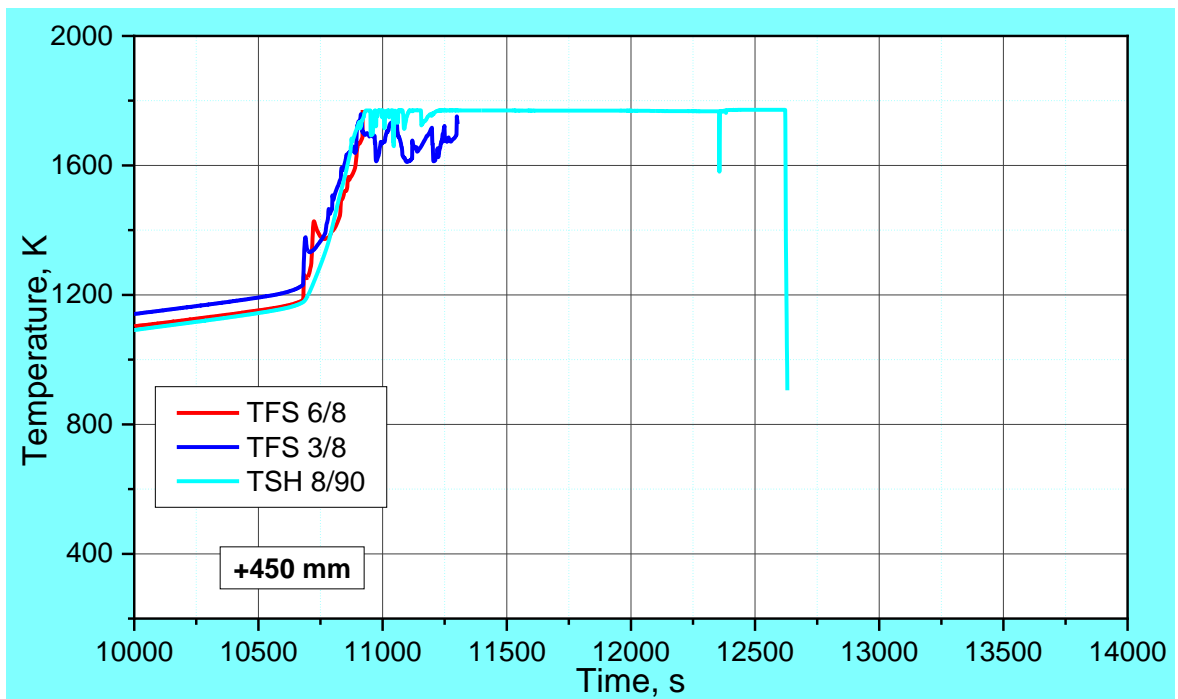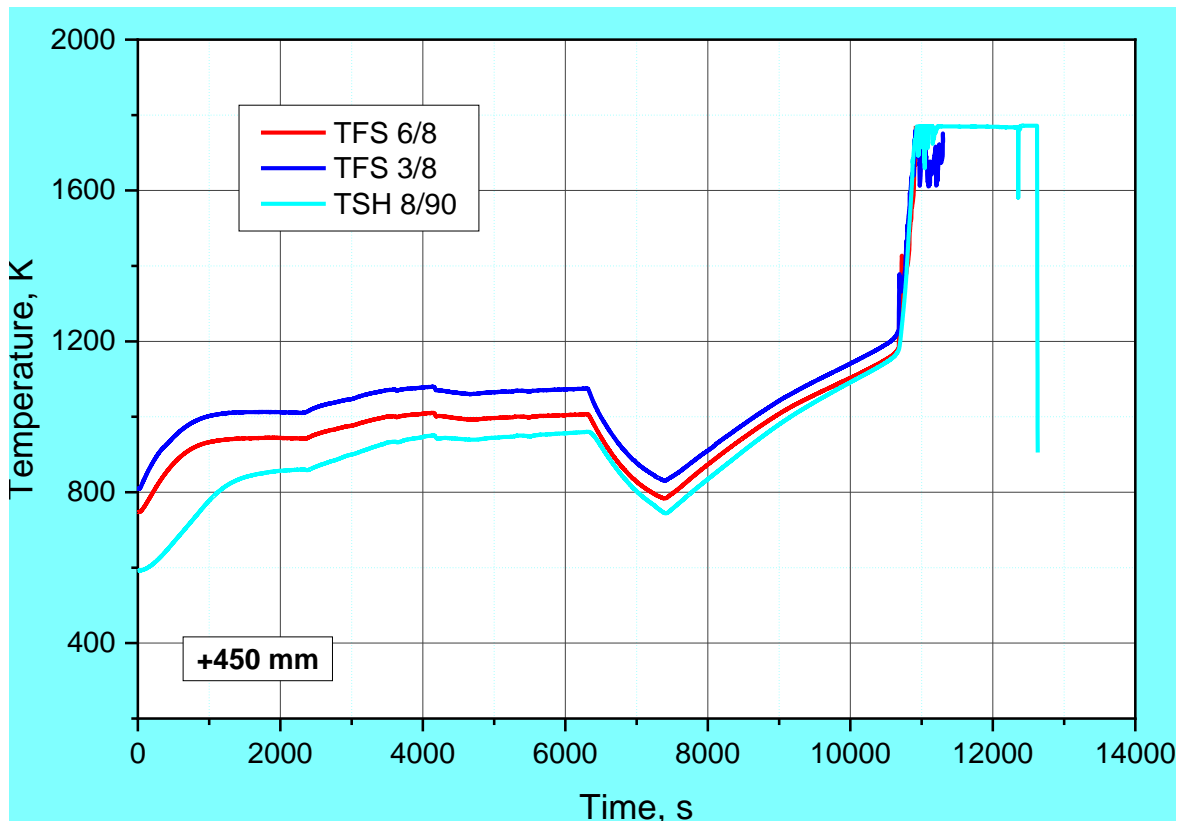
Figure 26 QUENCH-18; Temperatures measured by rod cladding (TFS) and shroud (TSH) thermocouples at 450 mm elevation.
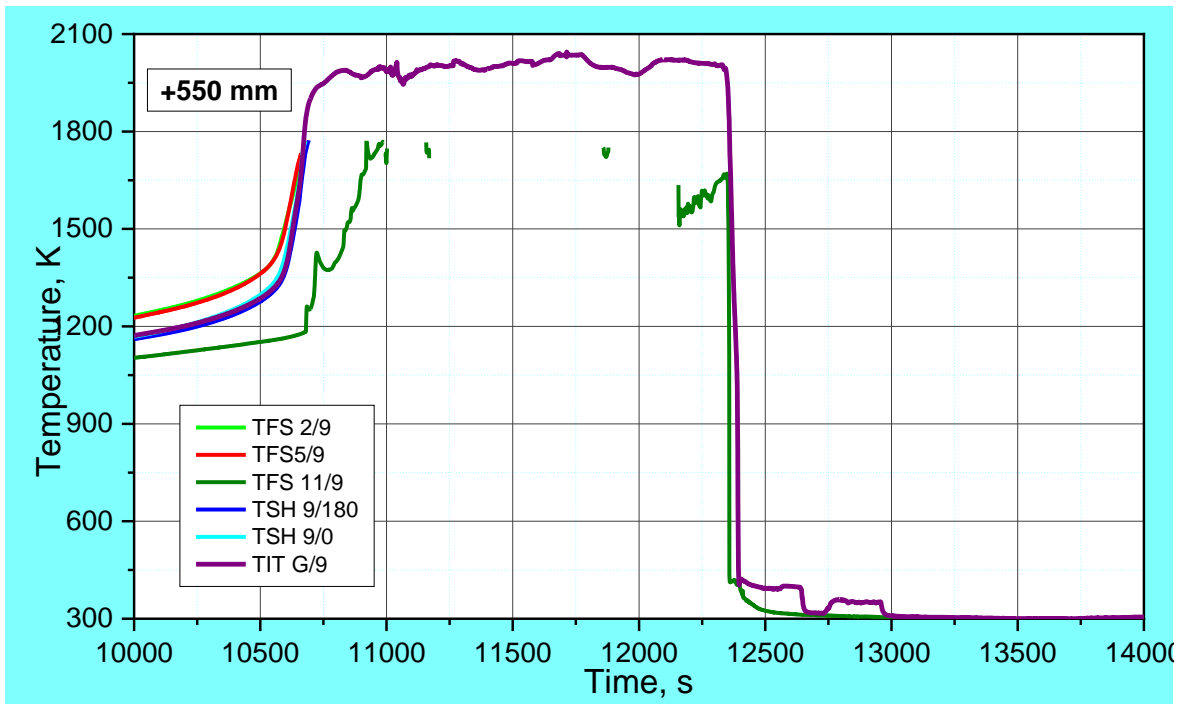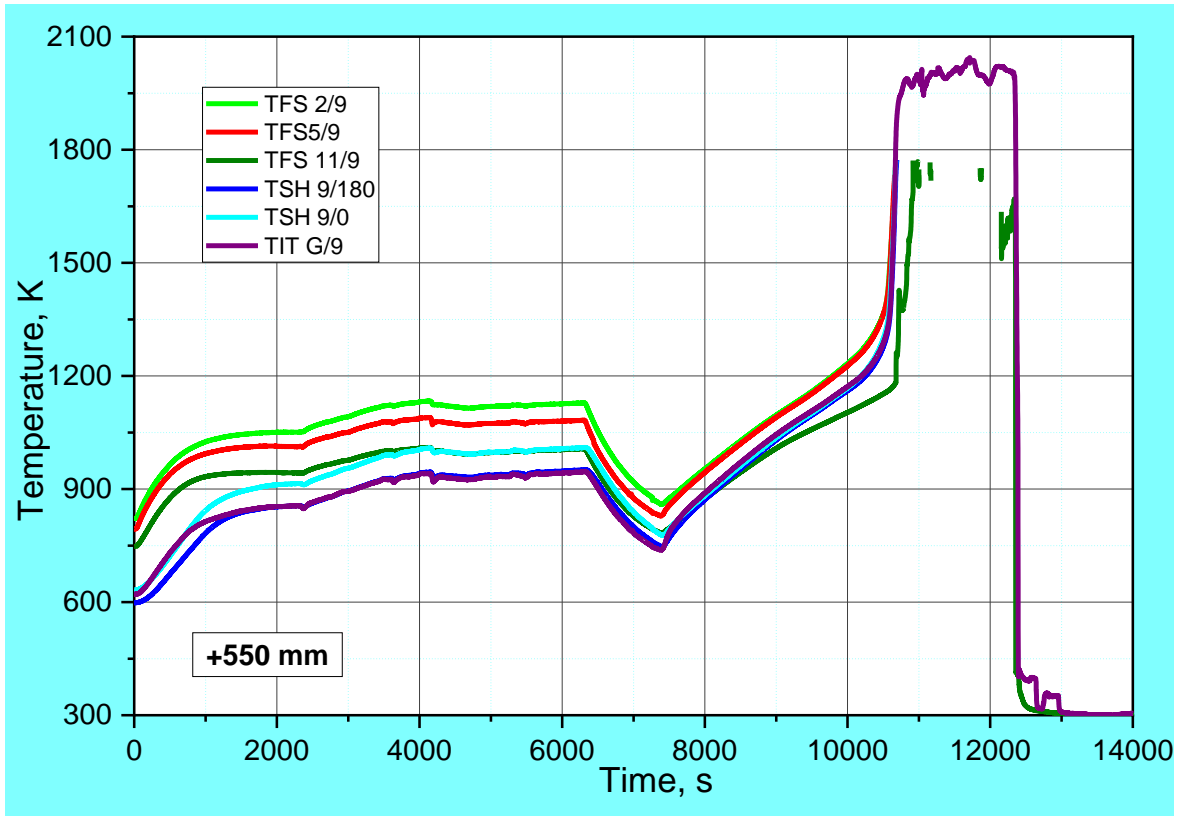
Figure 27 QUENCH-18; Temperatures measured by rod cladding (TFS) and shroud (TSH) thermocouples at 550 mm elevation.
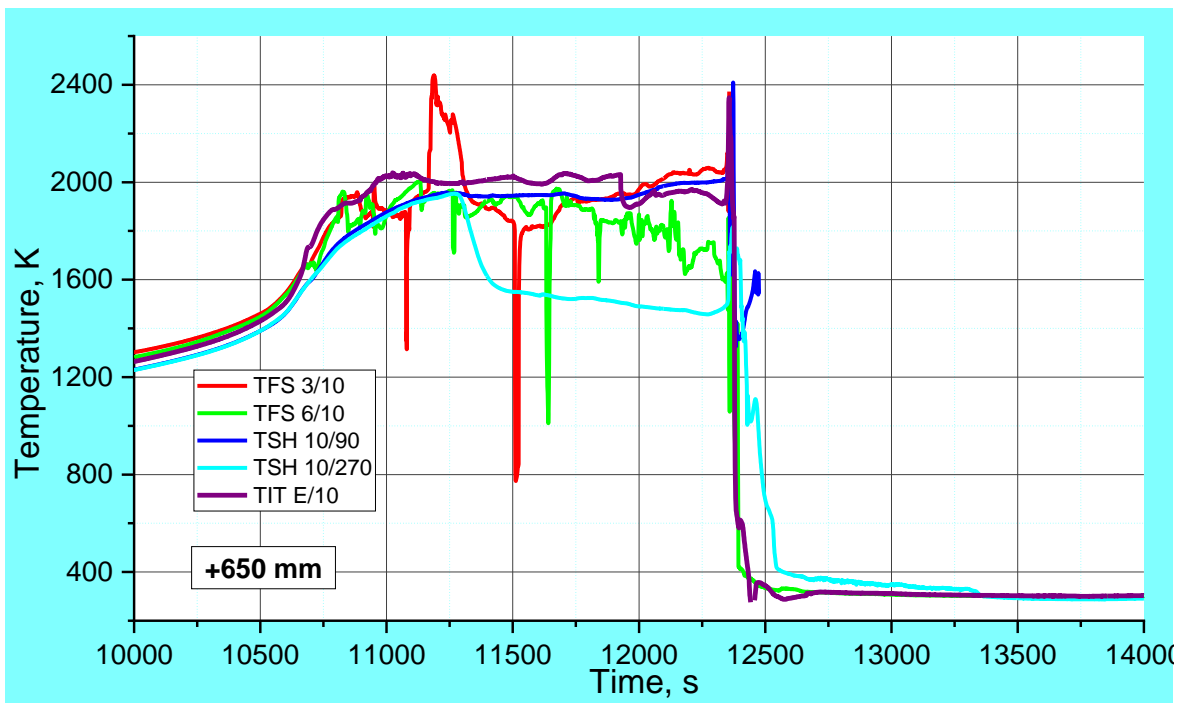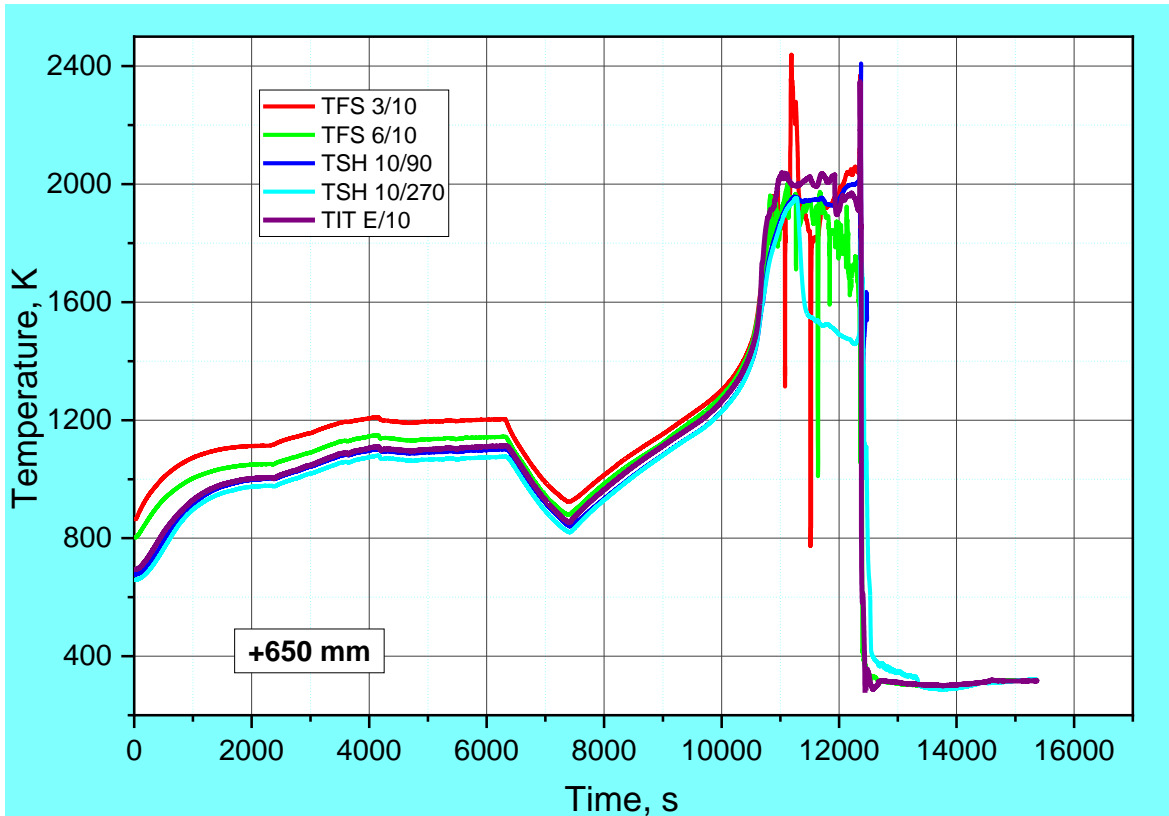
Figure 28 QUENCH-18; Temperatures measured by rod cladding (TFS) and shroud (TSH) thermocouples at 650 mm elevation.
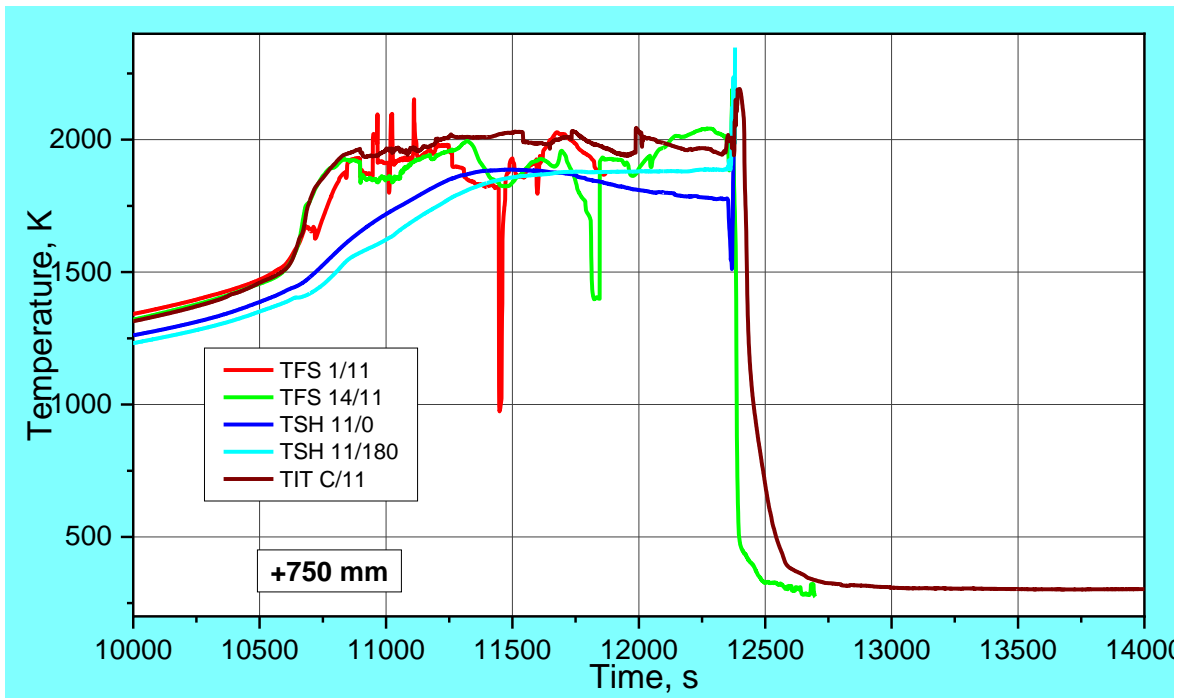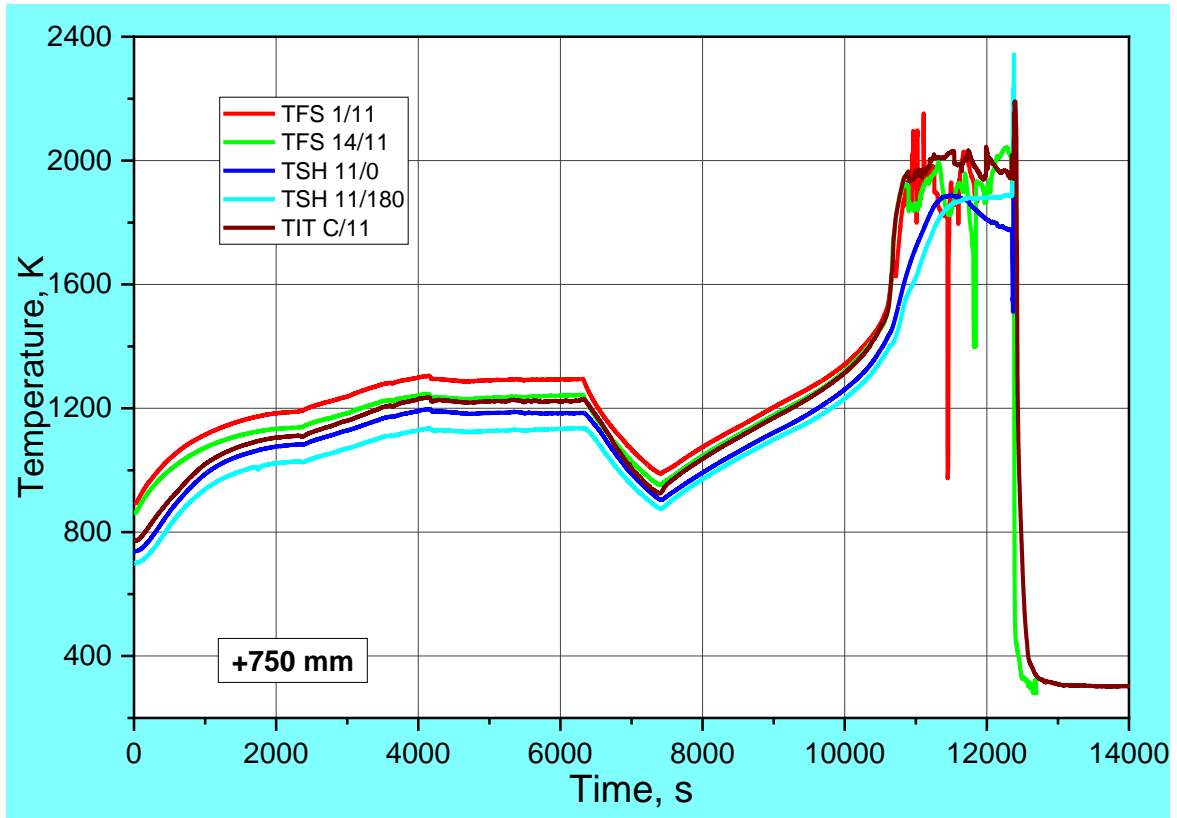
Figure 29   QUENCH-18; Temperatures measured by rod cladding (TFS) and shroud (TSH), and corner rod internal (TIT C/11) thermocouples at 750 mm elevation.
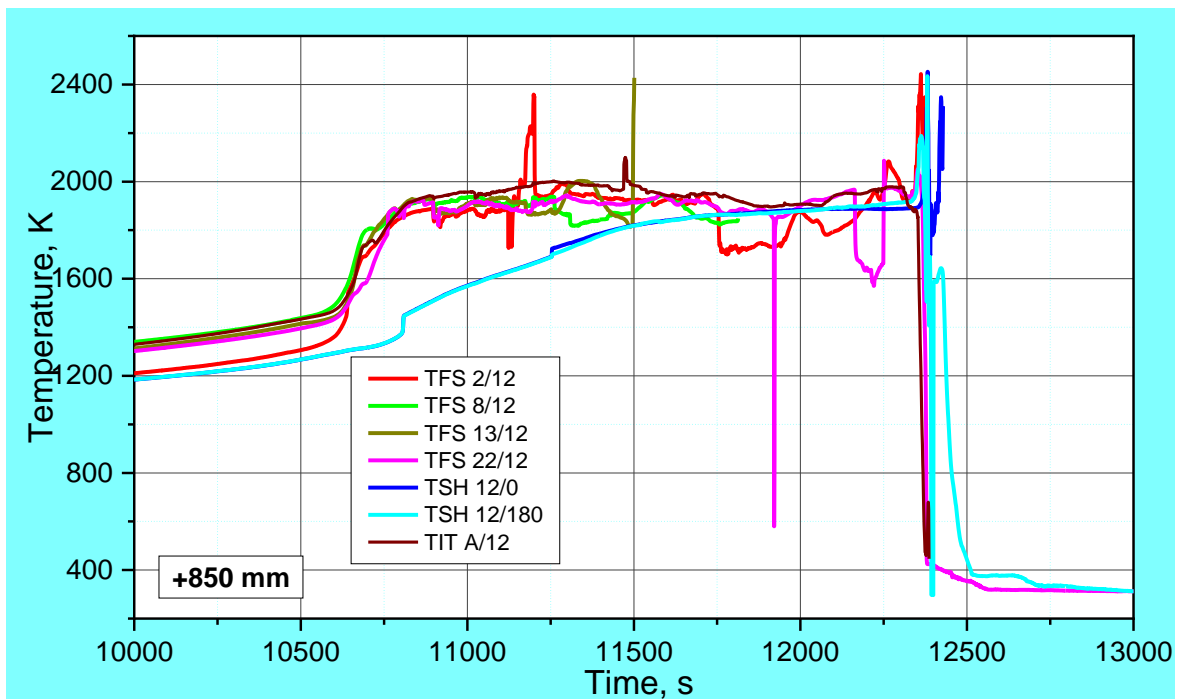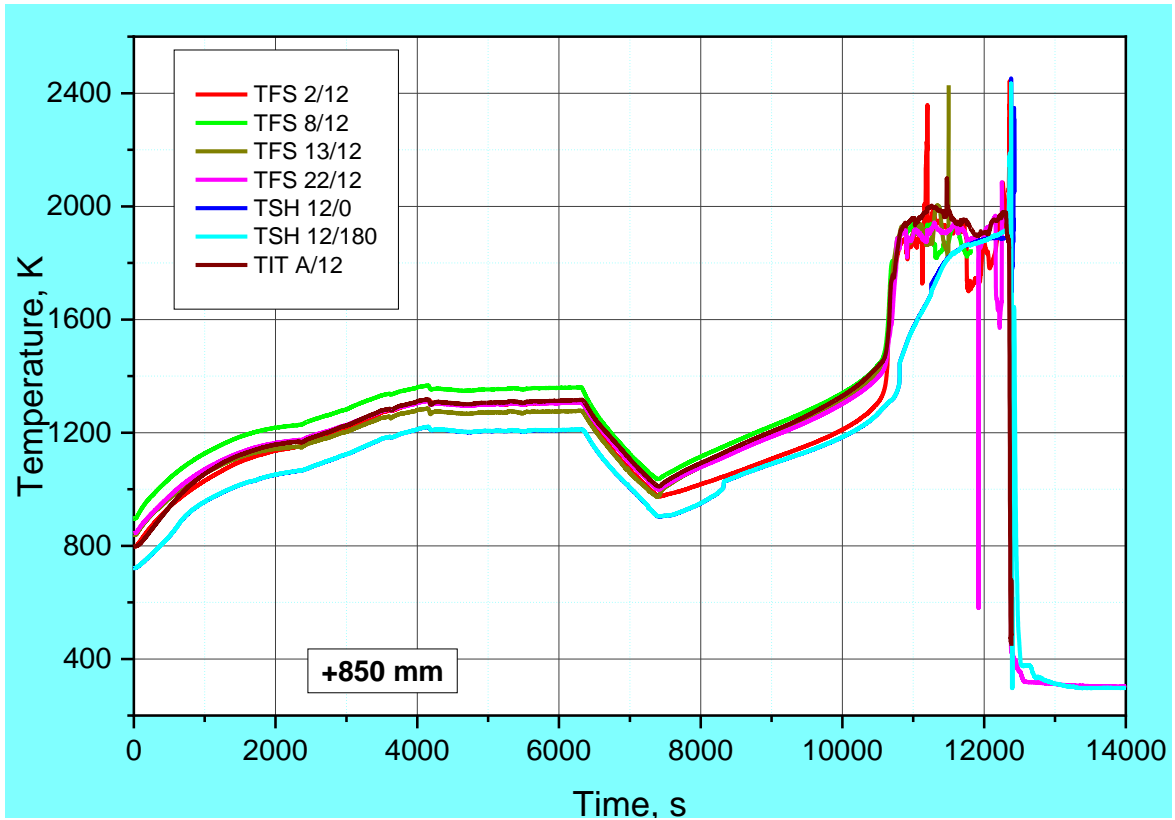
Figure 30   QUENCH-18; Temperatures measured by rod cladding (TFS) and shroud (TSH), and corner rod internal (TIT A/12) thermocouples at 850 mm elevation.
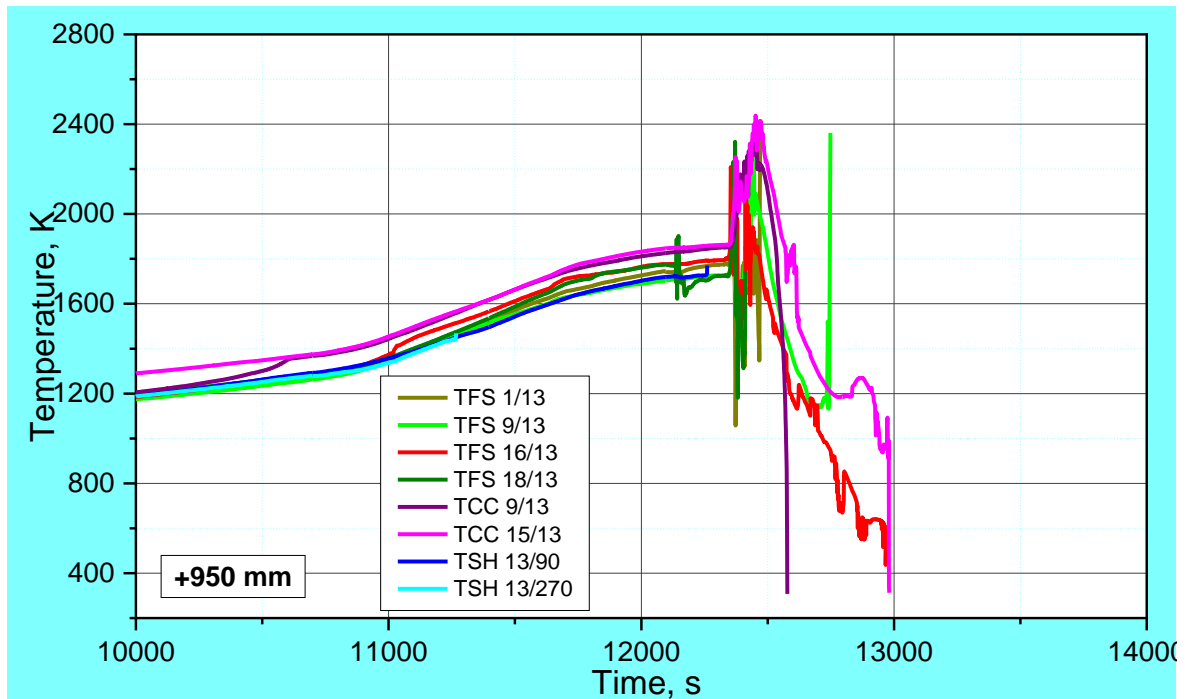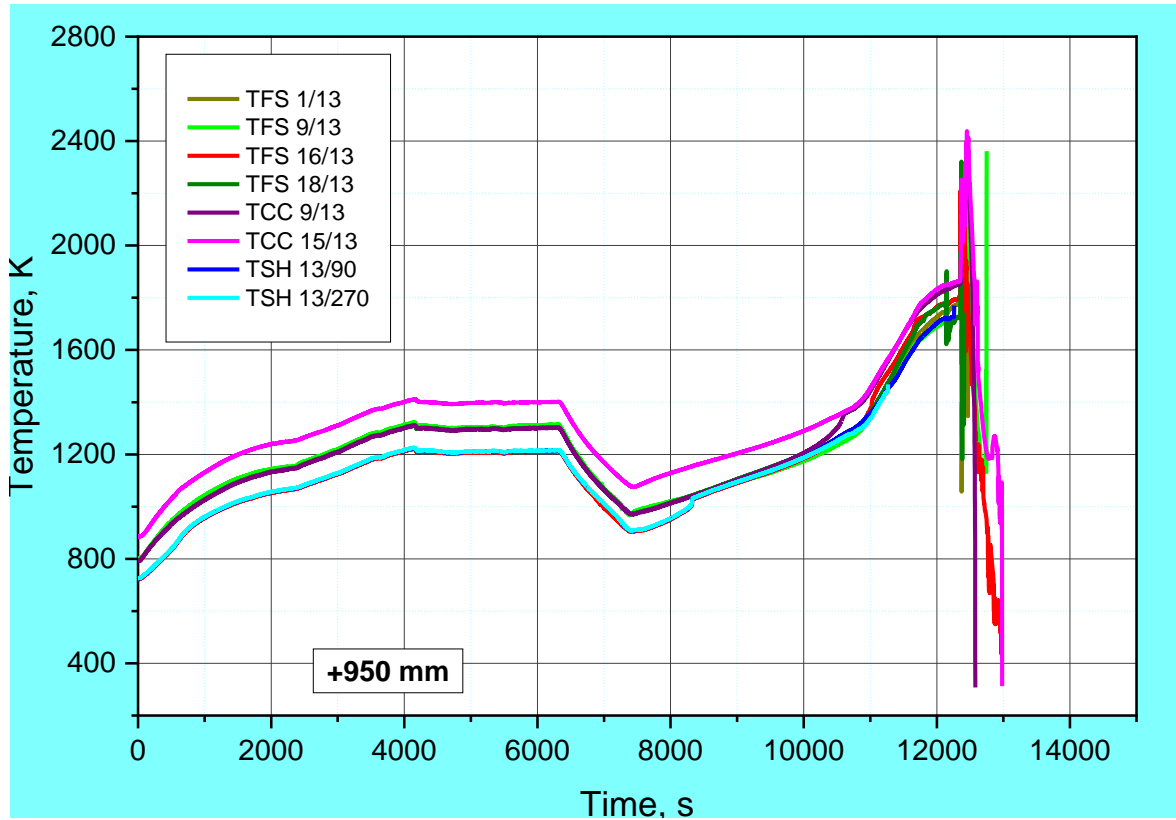
Figure 31   QUENCH-18; Temperatures measured by rod cladding (TFS) and shroud (TSH), and corner rod internal (TIT A/13) thermocouples at 950 mm elevation.
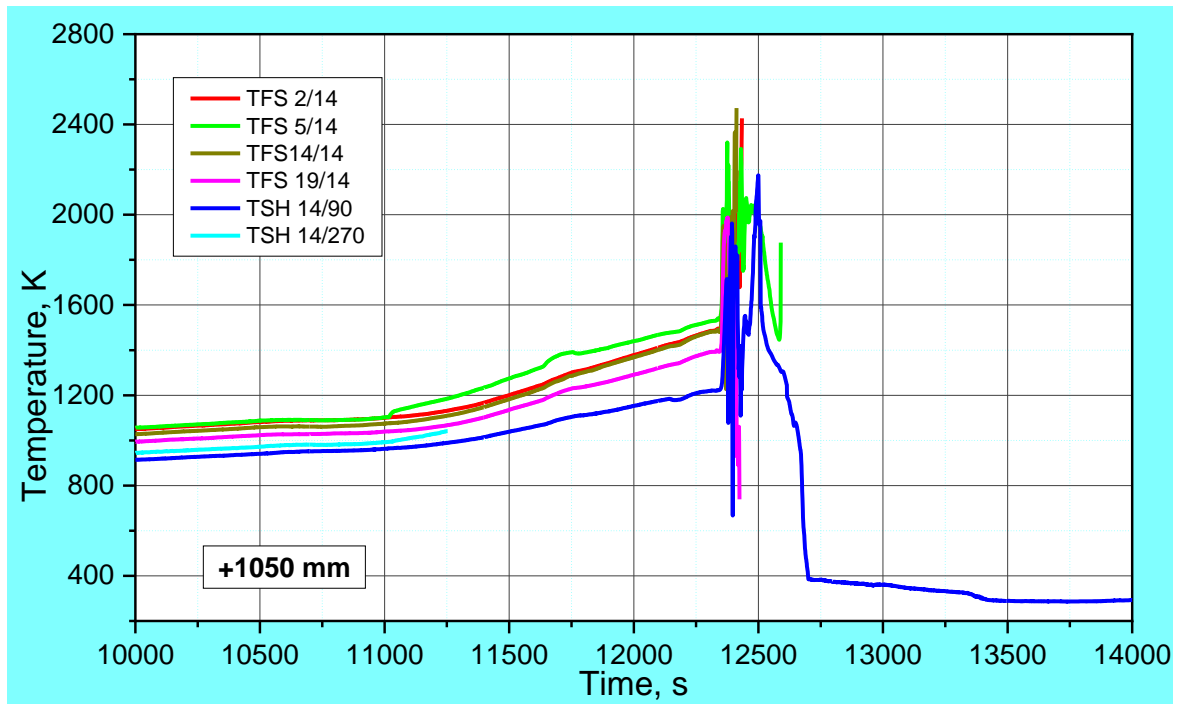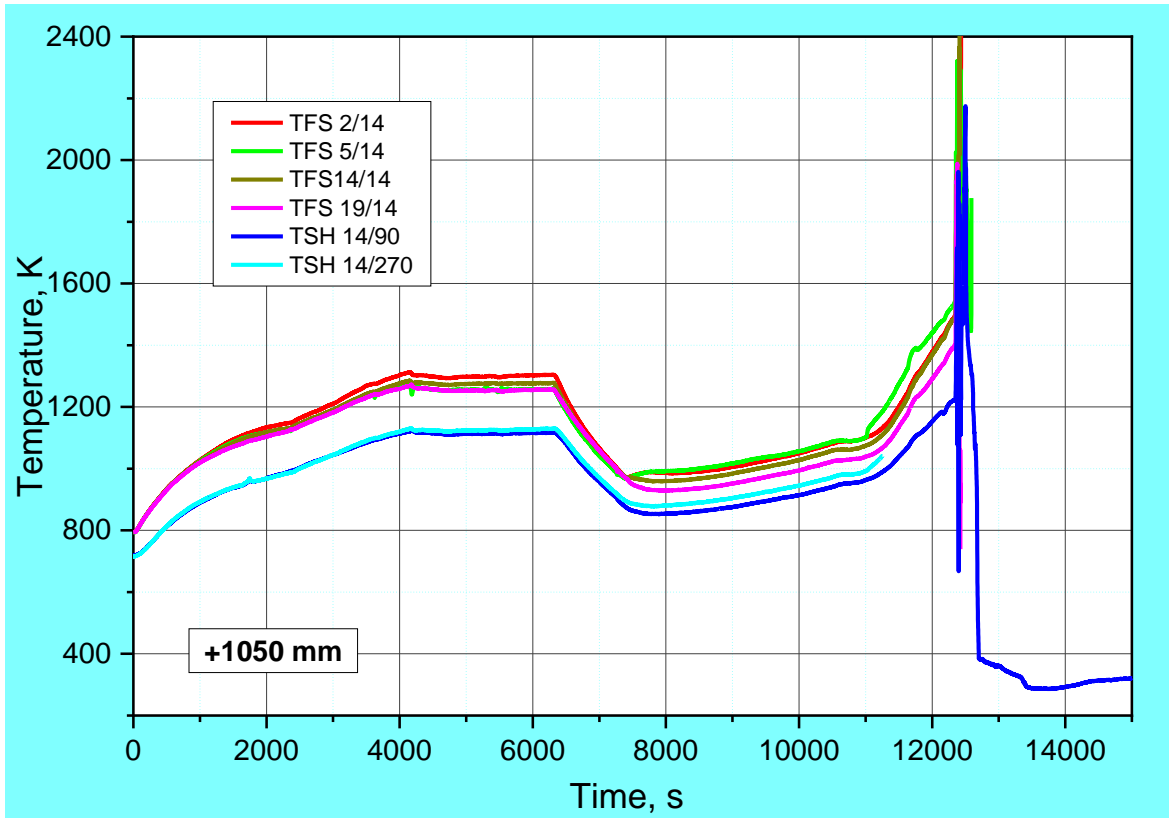
Figure 32 QUENCH-18; Temperatures measured by rod cladding (TFS) and shroud (TSH) thermocouples at 1050 mm elevation.
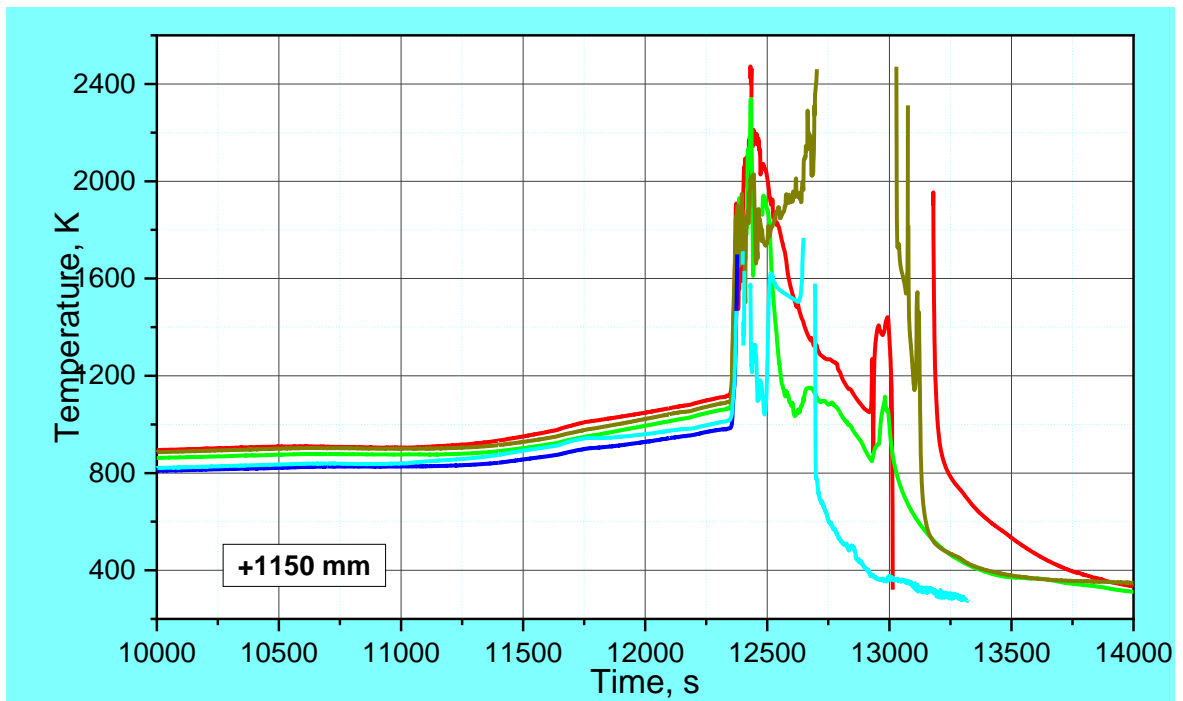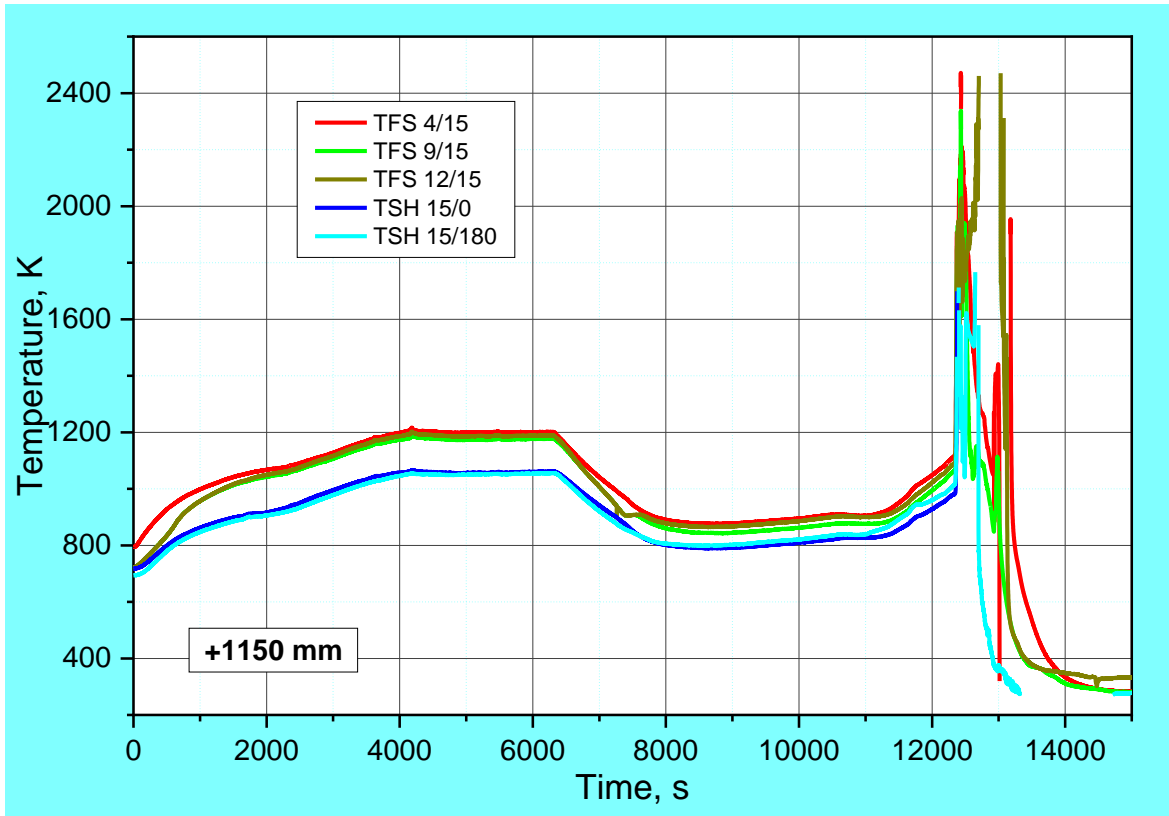
Figure 33 QUENCH-18; Temperatures measured by rod cladding (TFS) and shroud (TSH) thermocouples at 1150 mm elevation.
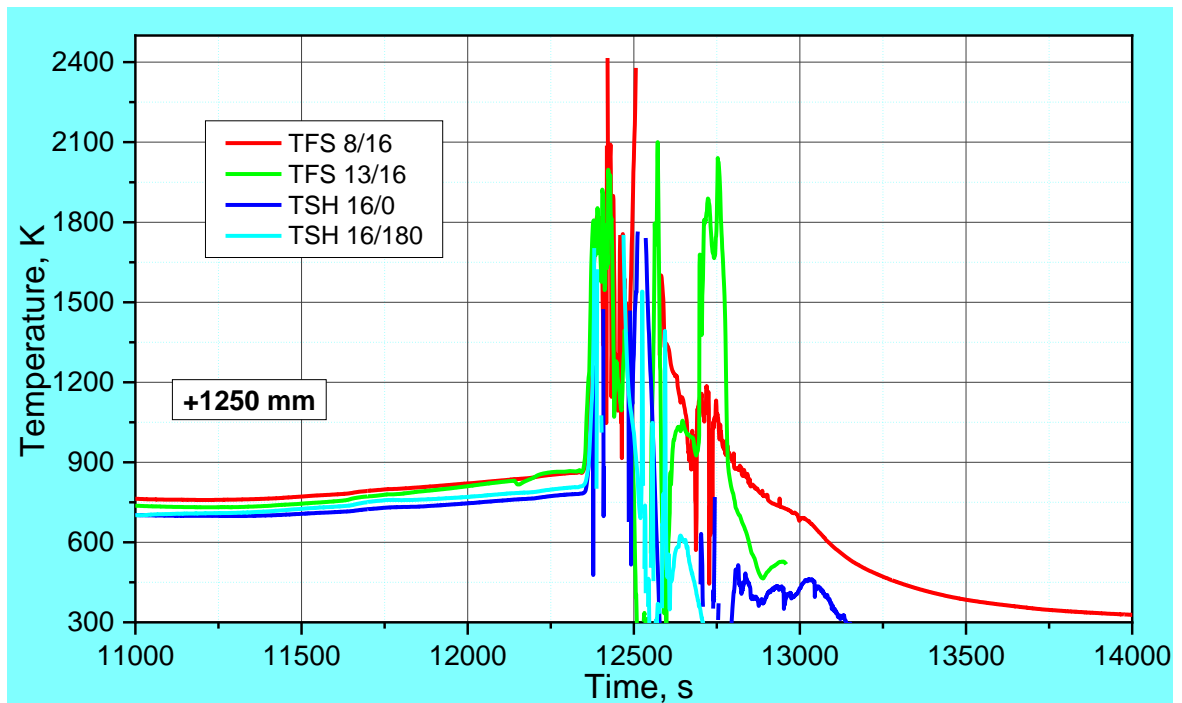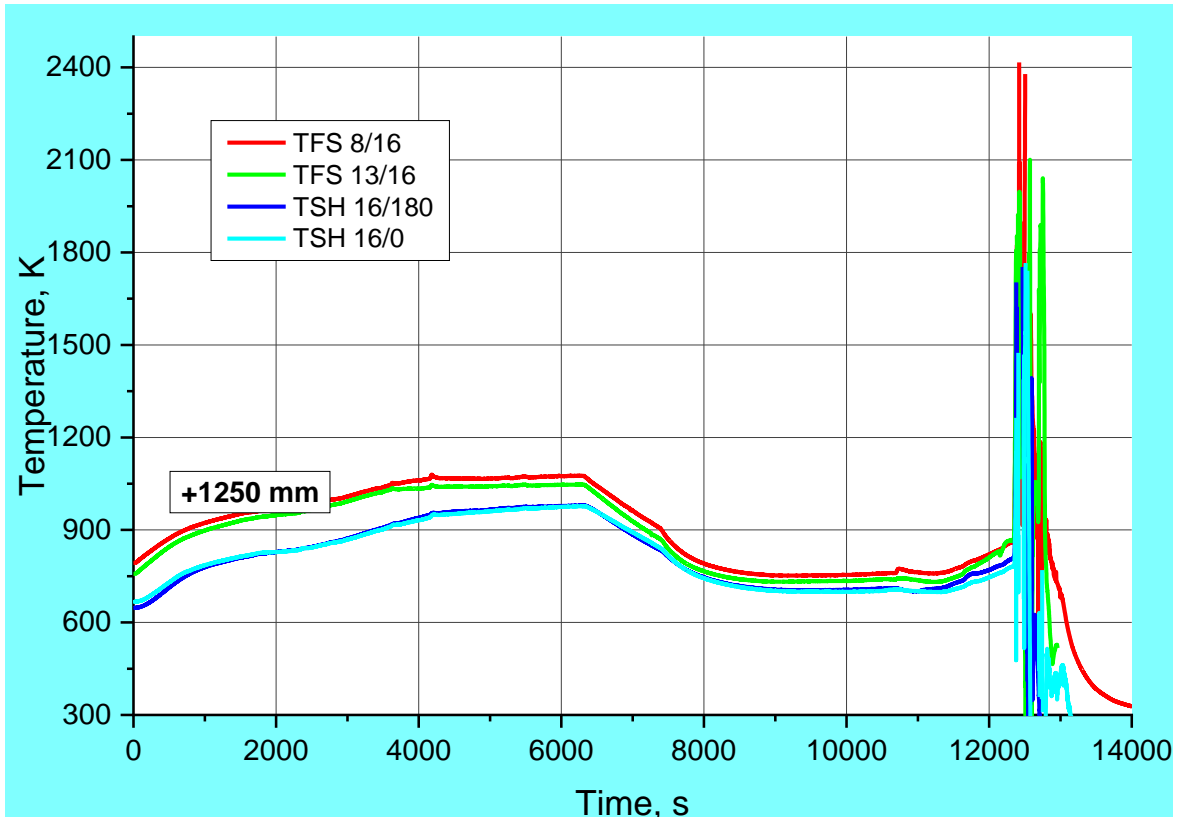
Figure 34 QUENCH-18; Temperatures measured by rod cladding (TFS) and shroud (TSH) thermocouples at 1250 mm elevation.
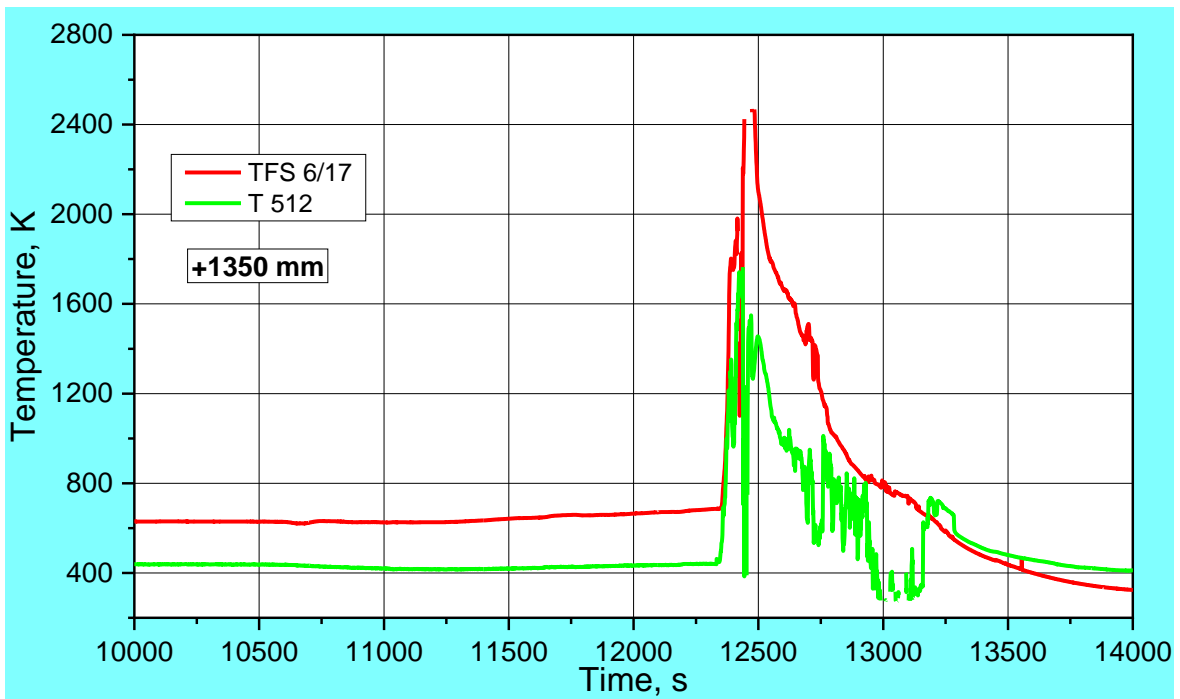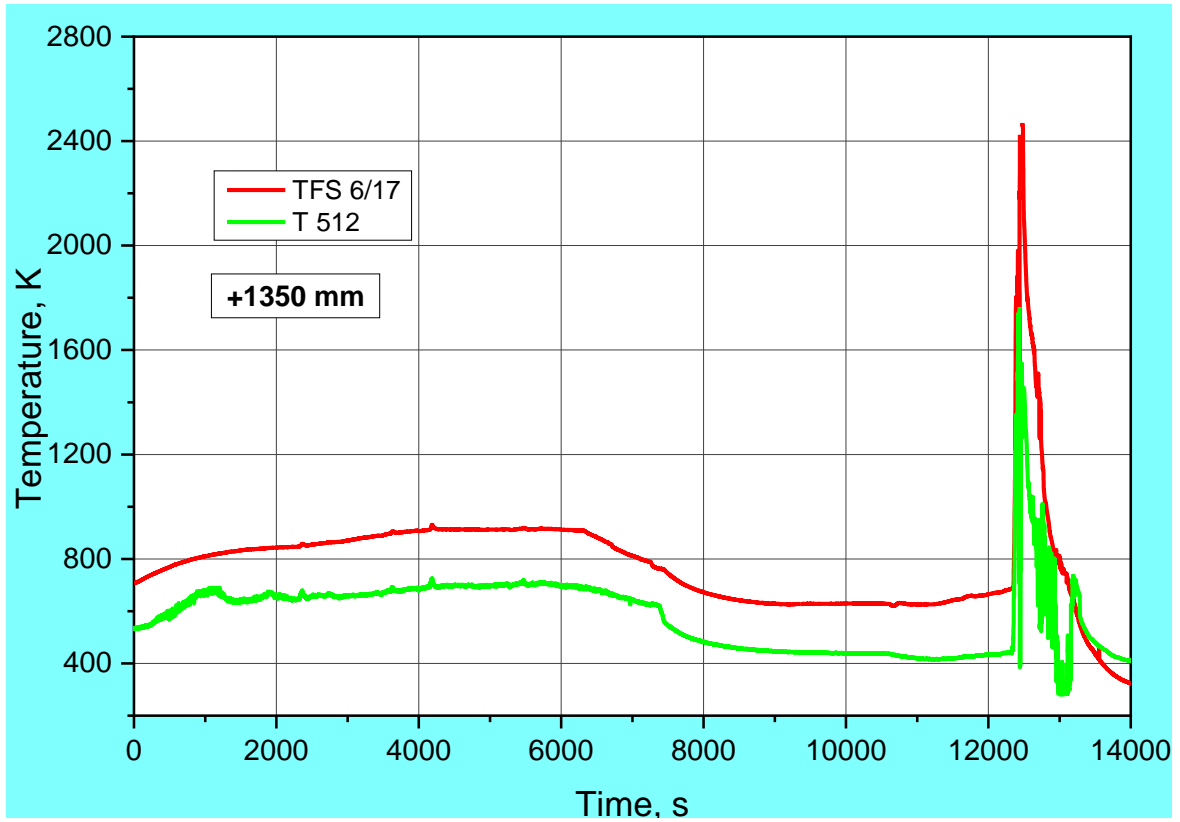
Figure 35 QUENCH-18; Temperatures measured by rod cladding thermocouple at 1350 mm elevation (TFS 7/17) and gas temperature (T 512) at 1360 mm between shroud and rod #20.
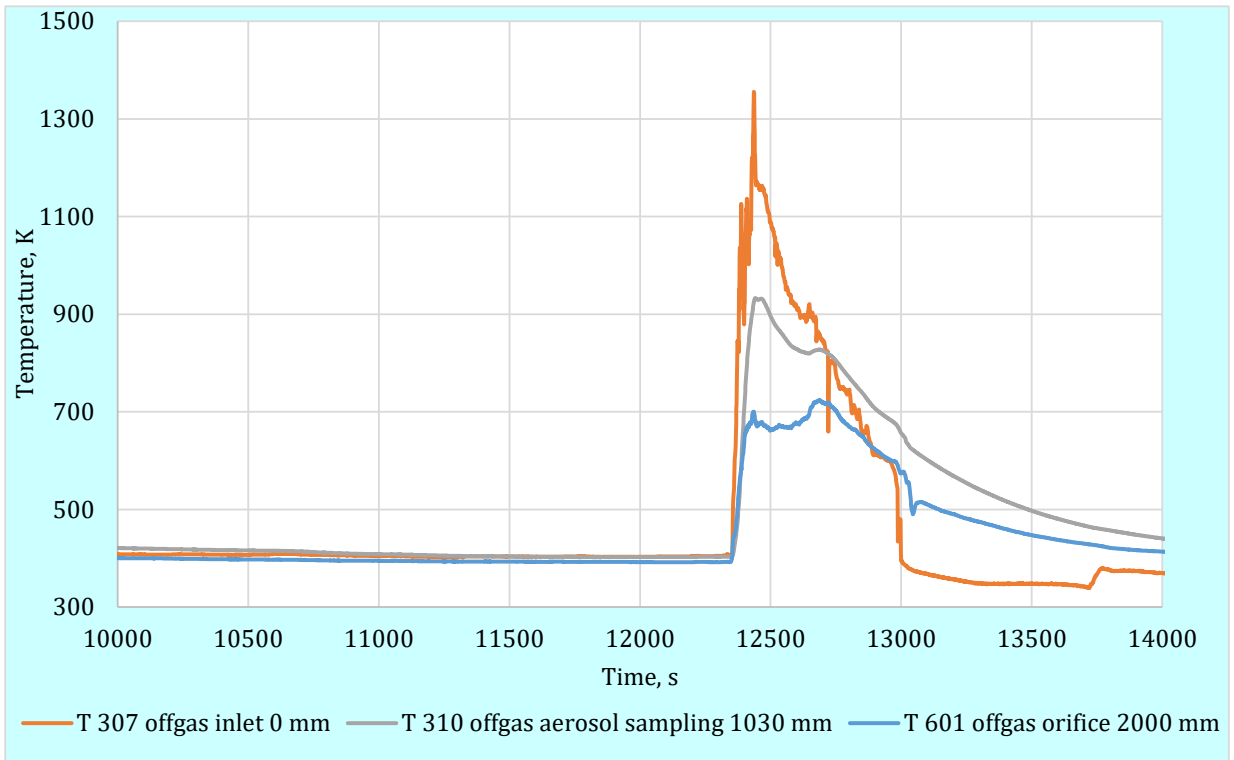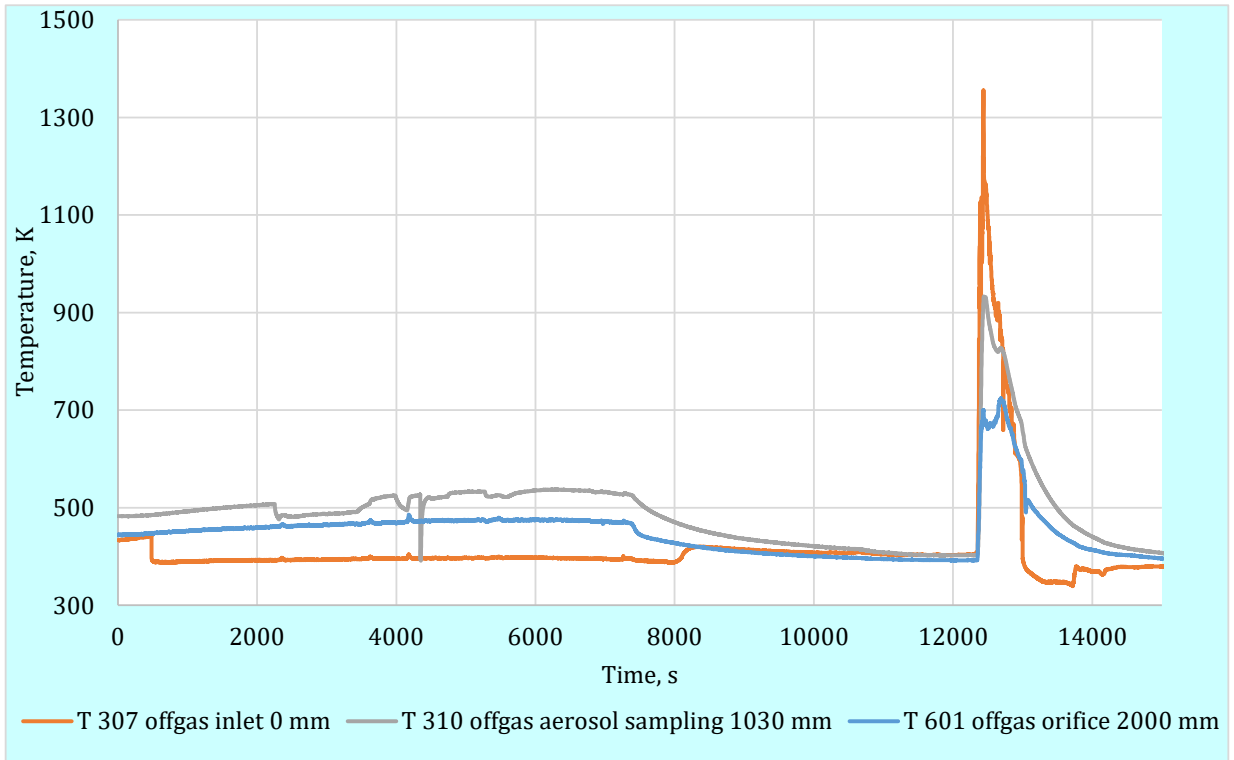
Figure 36   QUENCH-18; Temperatures, measured inside the off-gas pipe.
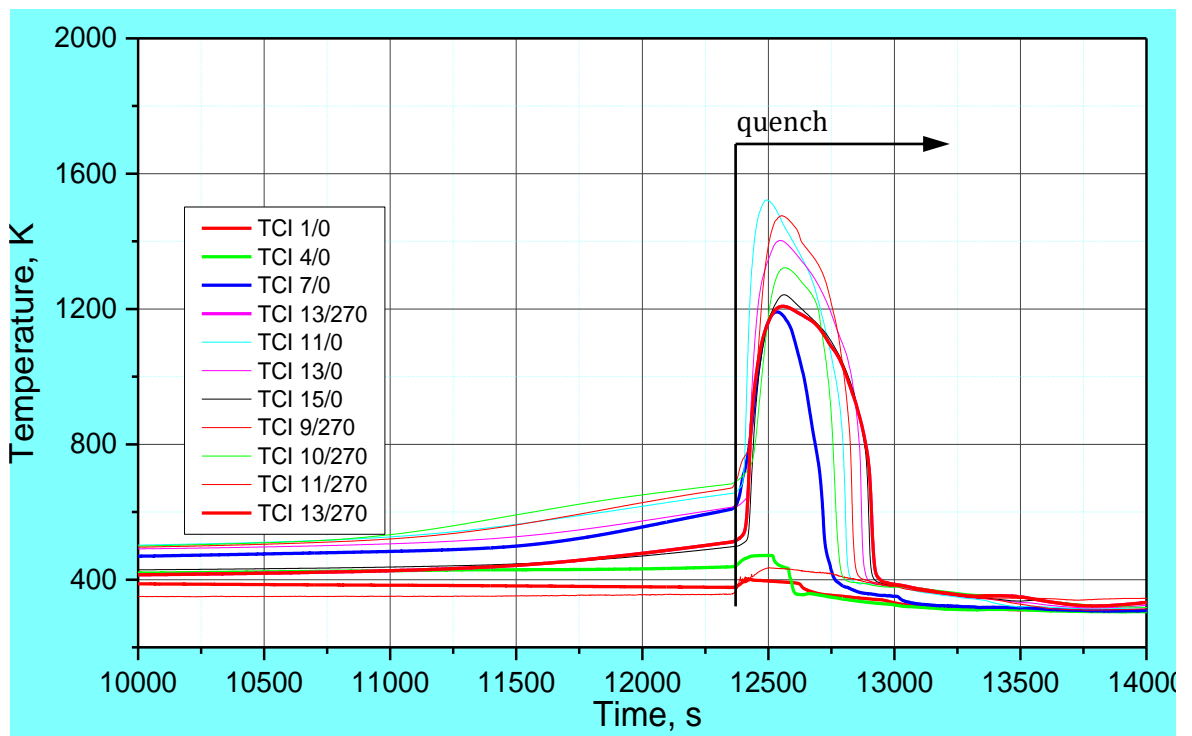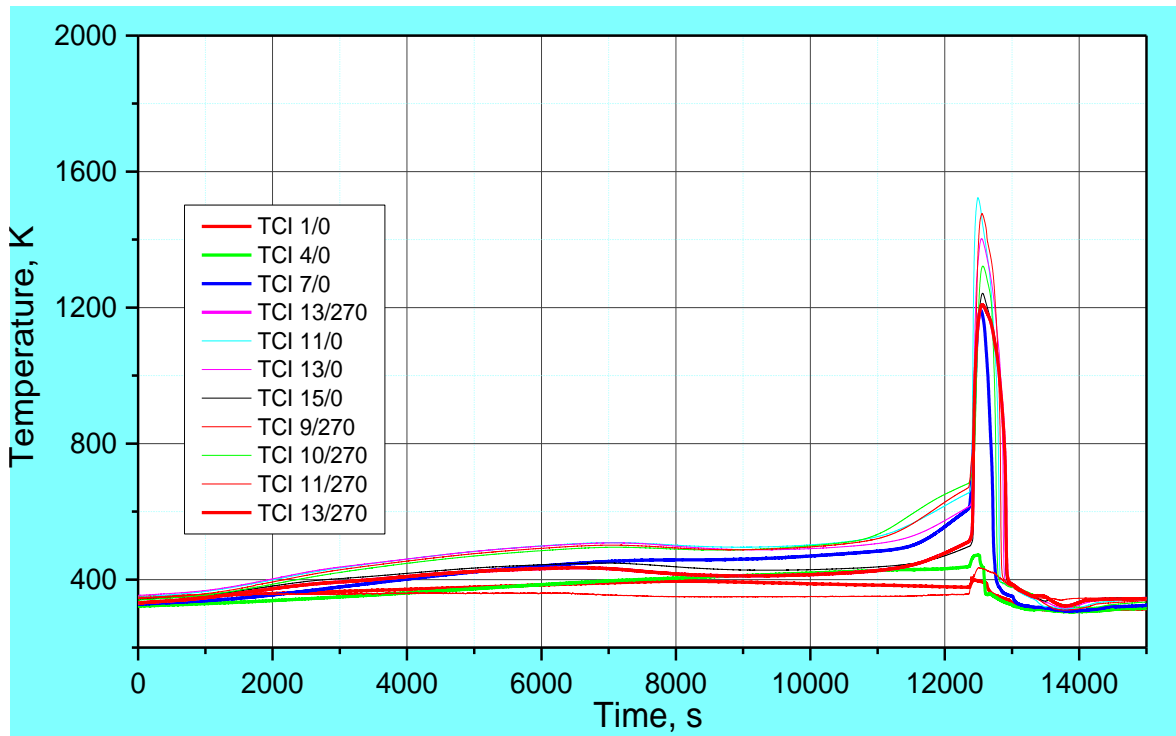
Figure 37   QUENCH-18; Overview of the TCI (inner cooling jacket).
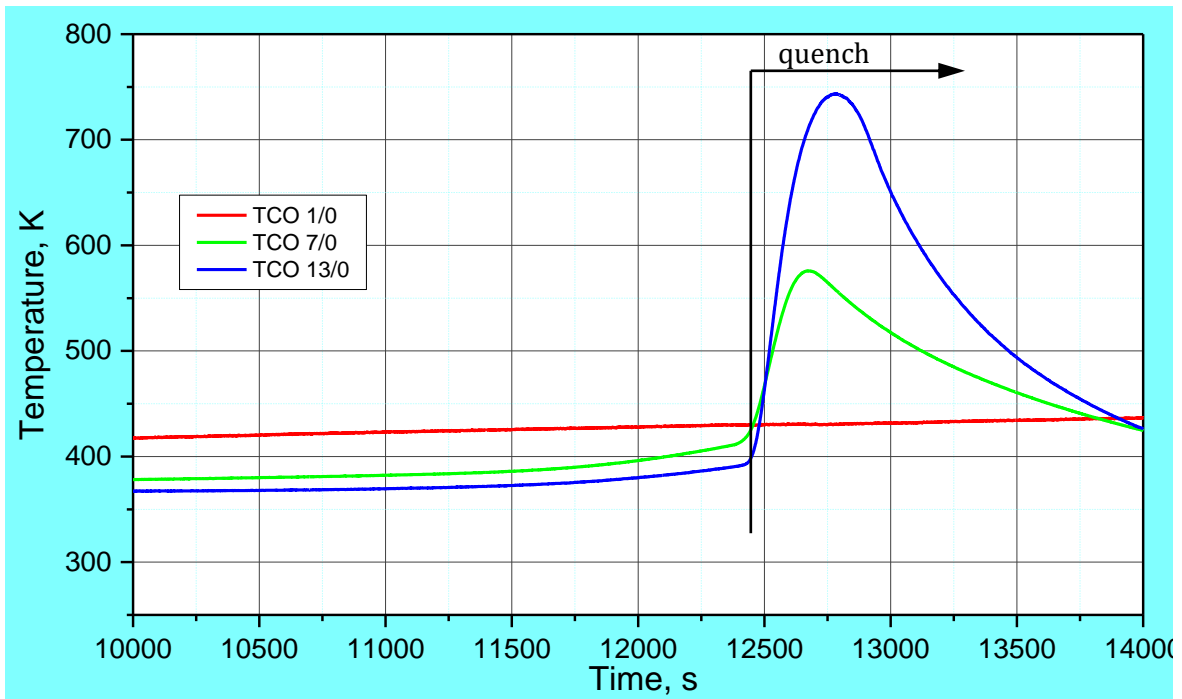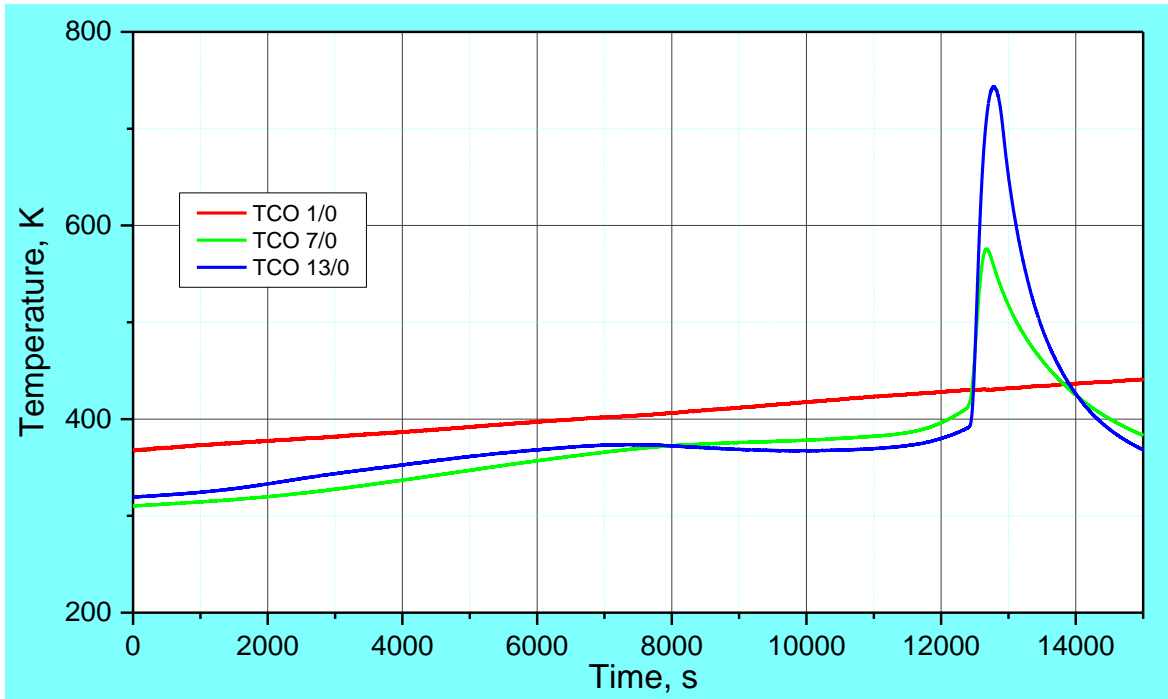
Figure 38   QUENCH-18; Overview of the TCO (outer cooling jacket).
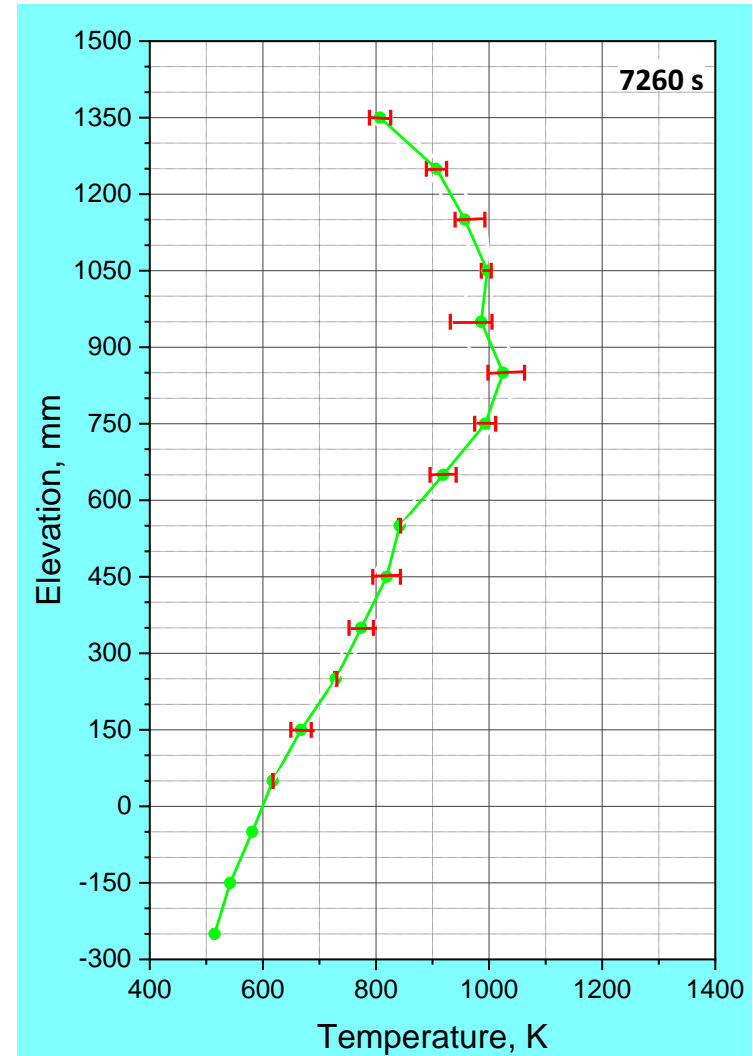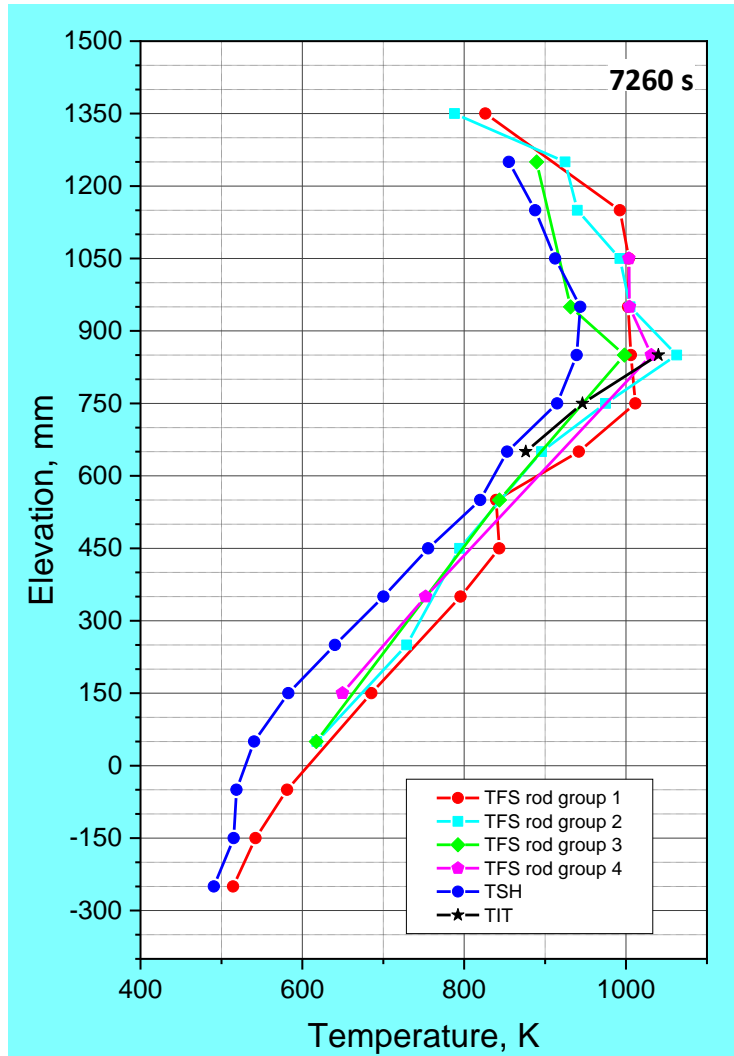
Figure 39 QUENCH-18; Axial temperature profile TFS rod groups together with TSH, left, and mean axial temperature profile of all TFS, right, at 7260 s (end of cool-down, drawing of corner rod D).
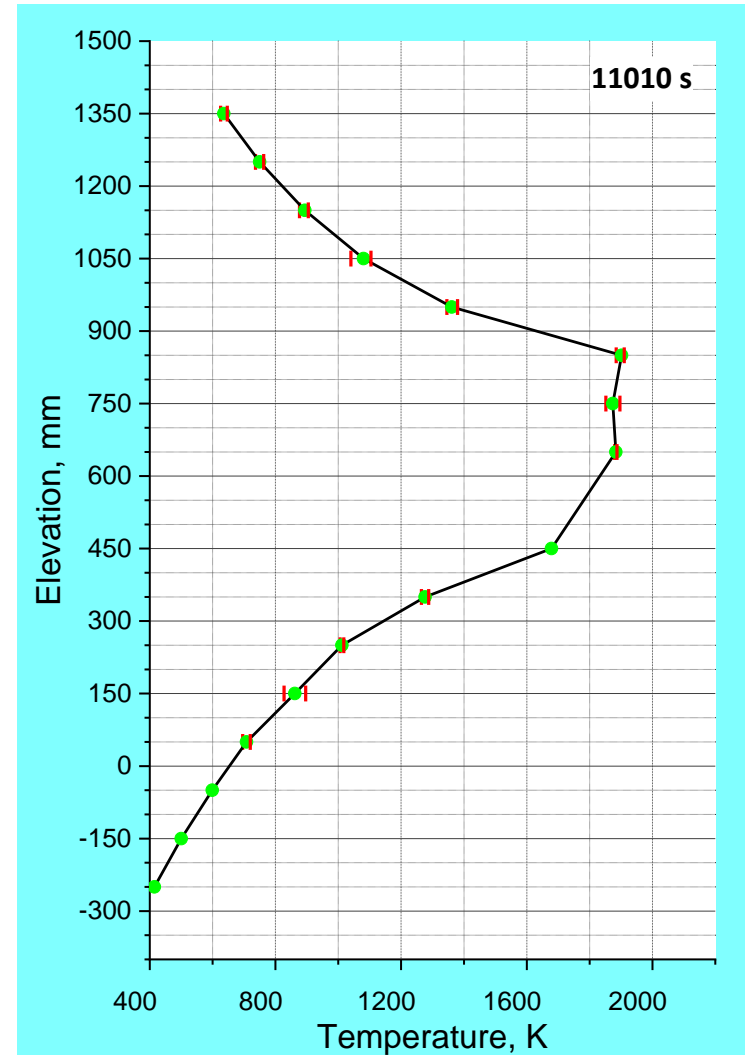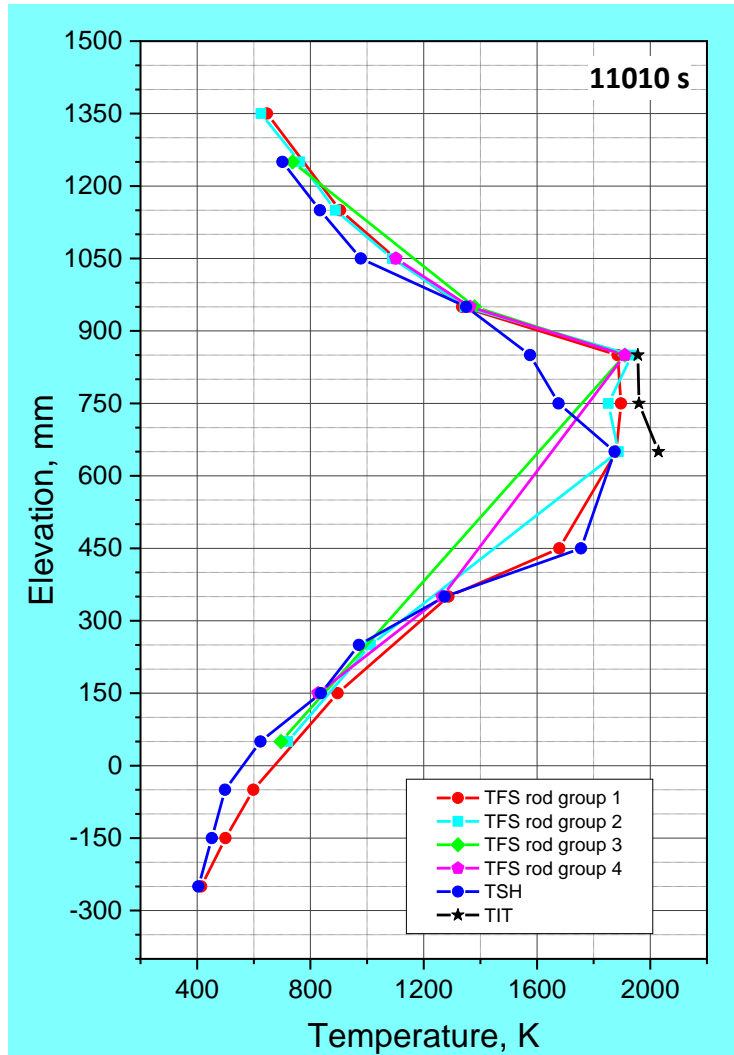
Figure 40 QUENCH-18; Axial temperature profile TFS rod groups together with TSH, left, and mean axial temperature profile of all TFS, right, at 11010 s (end of temperature escalation, drawing of corner rod H).
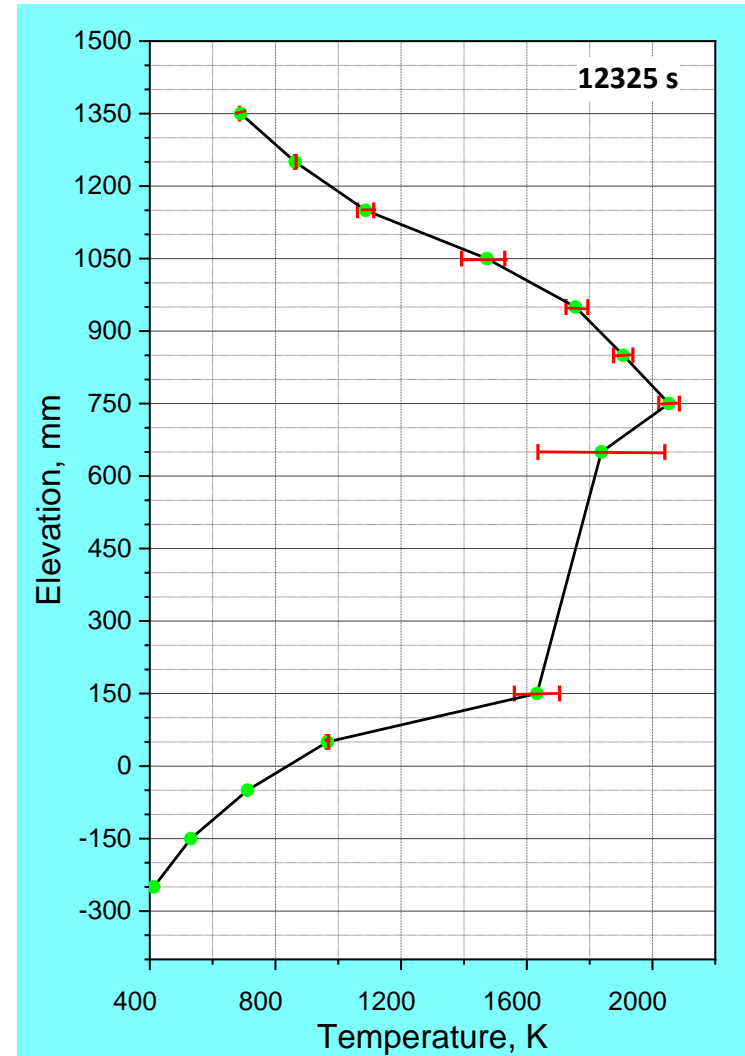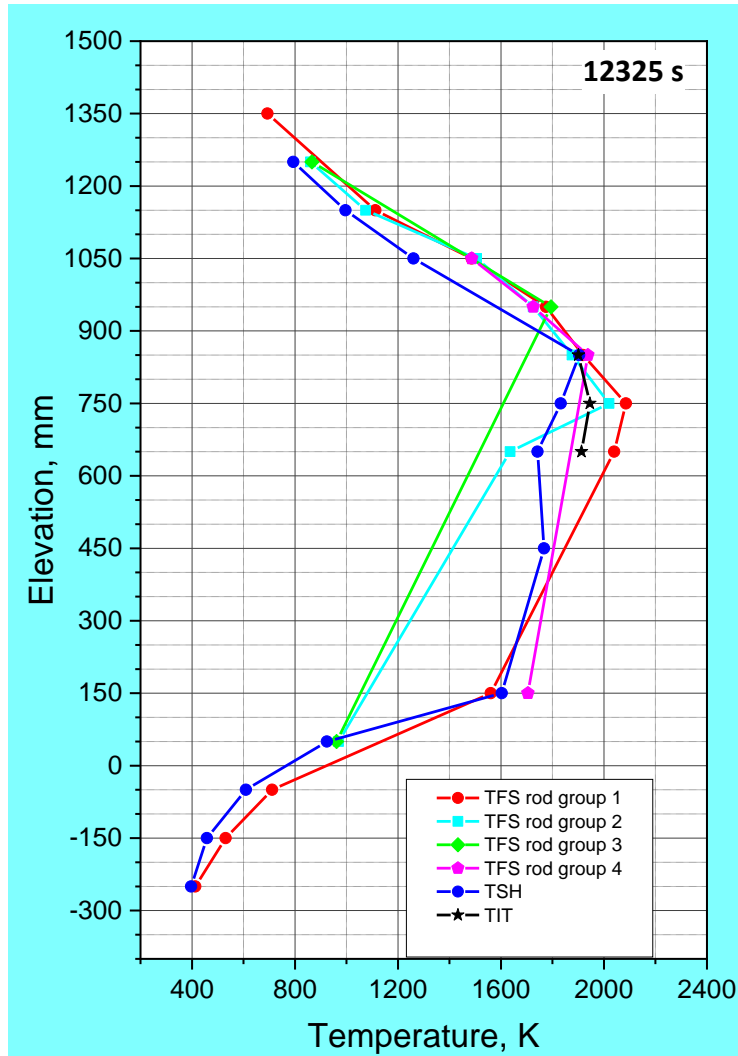
Figure 41 QUENCH-18; Axial temperature profile TFS rod groups together with TSH, left, and mean axial temperature profile of all TFS, right, at 12325 s (shortly before quench initiation).
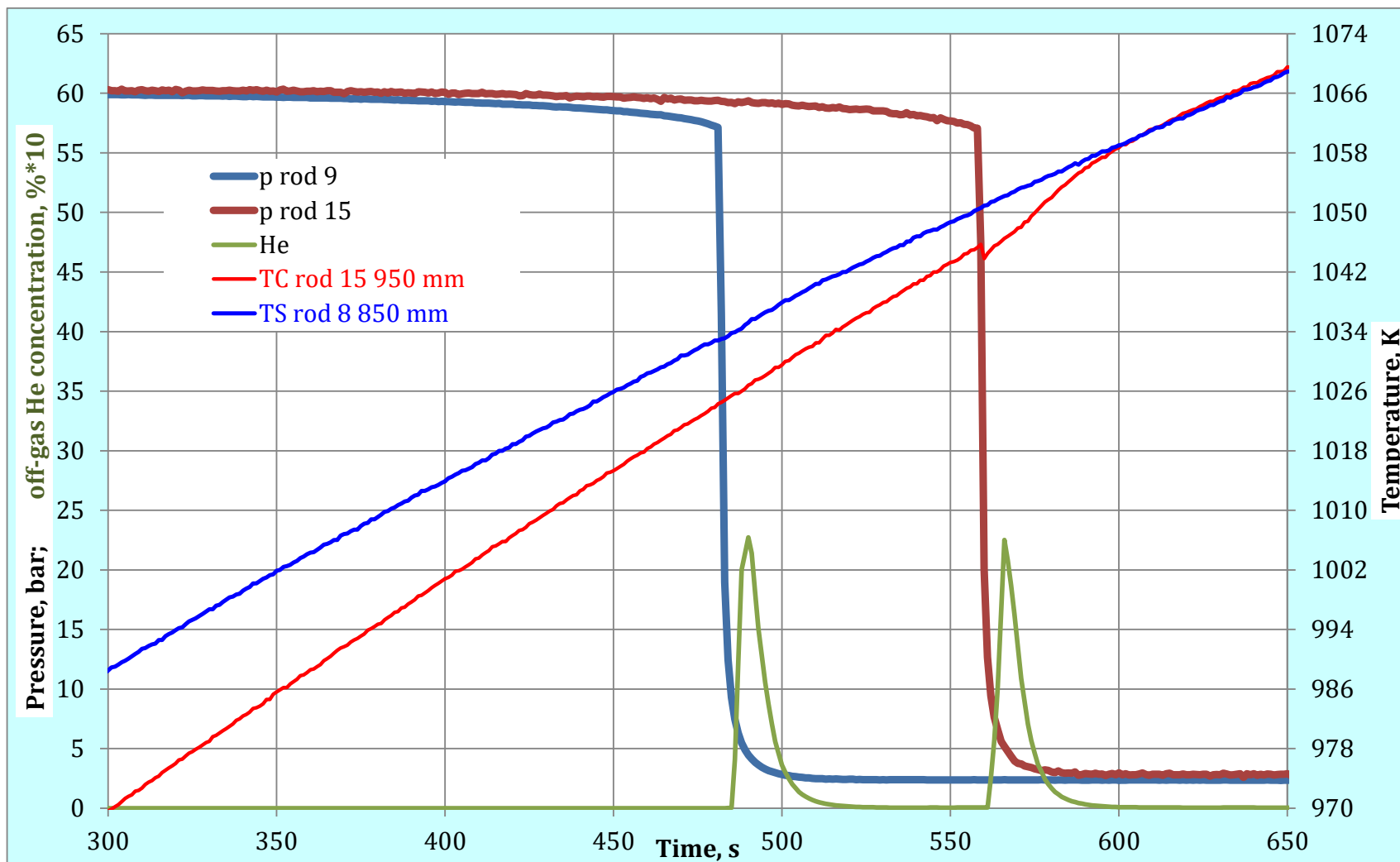
Figure 42 QUENCH-18; burst of pressurized rods #9 (at ≈ 850 mm) and #15 (at 950 mm); burst temperature: 1045 K (rod #15) at heat-up rate 0.3 K/s.
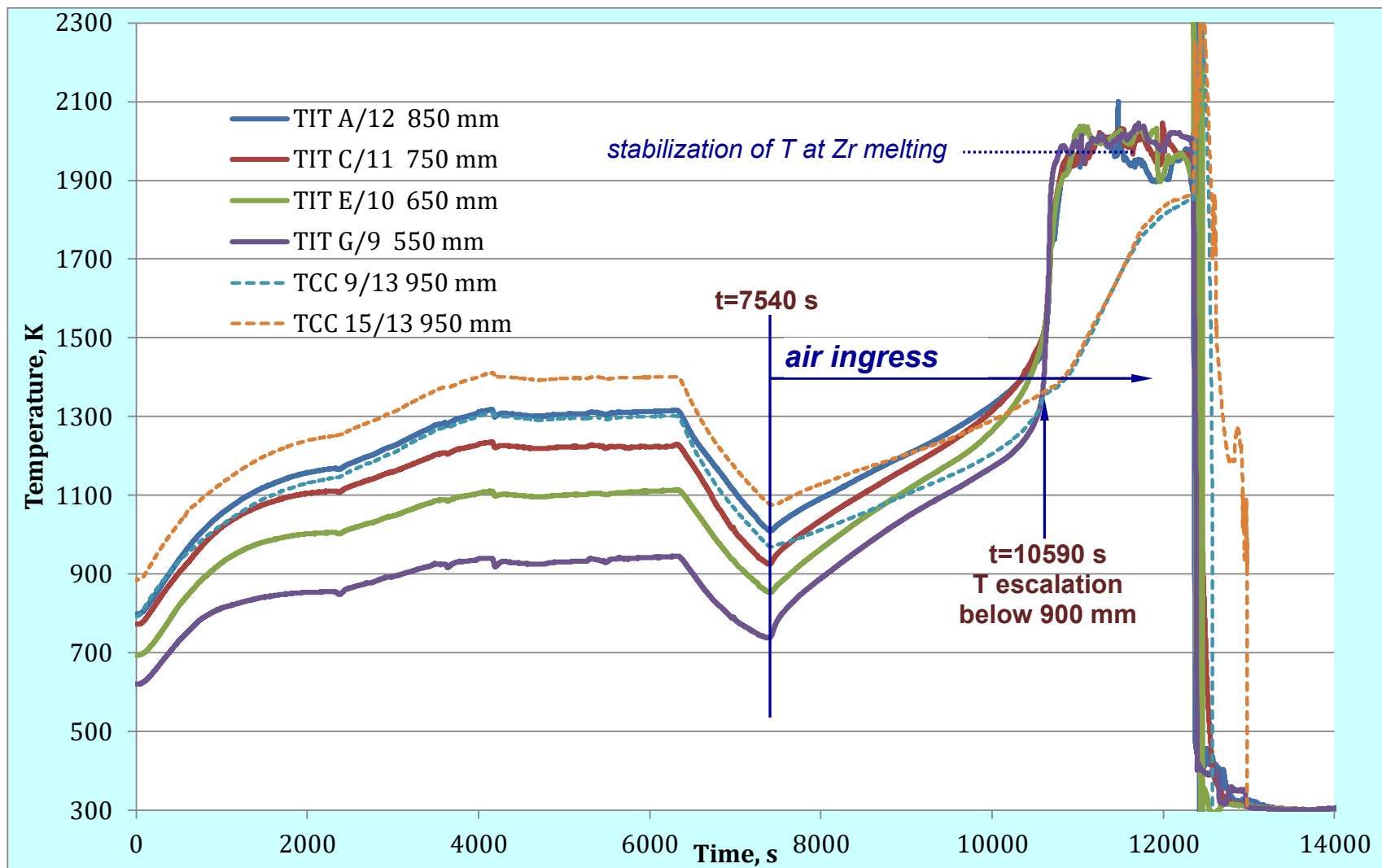
Figure 43   QUENCH-18; readings of sheathed thermocouples (TIT in corner rods and TCC inside pellets): temperature escalation during air ingress.
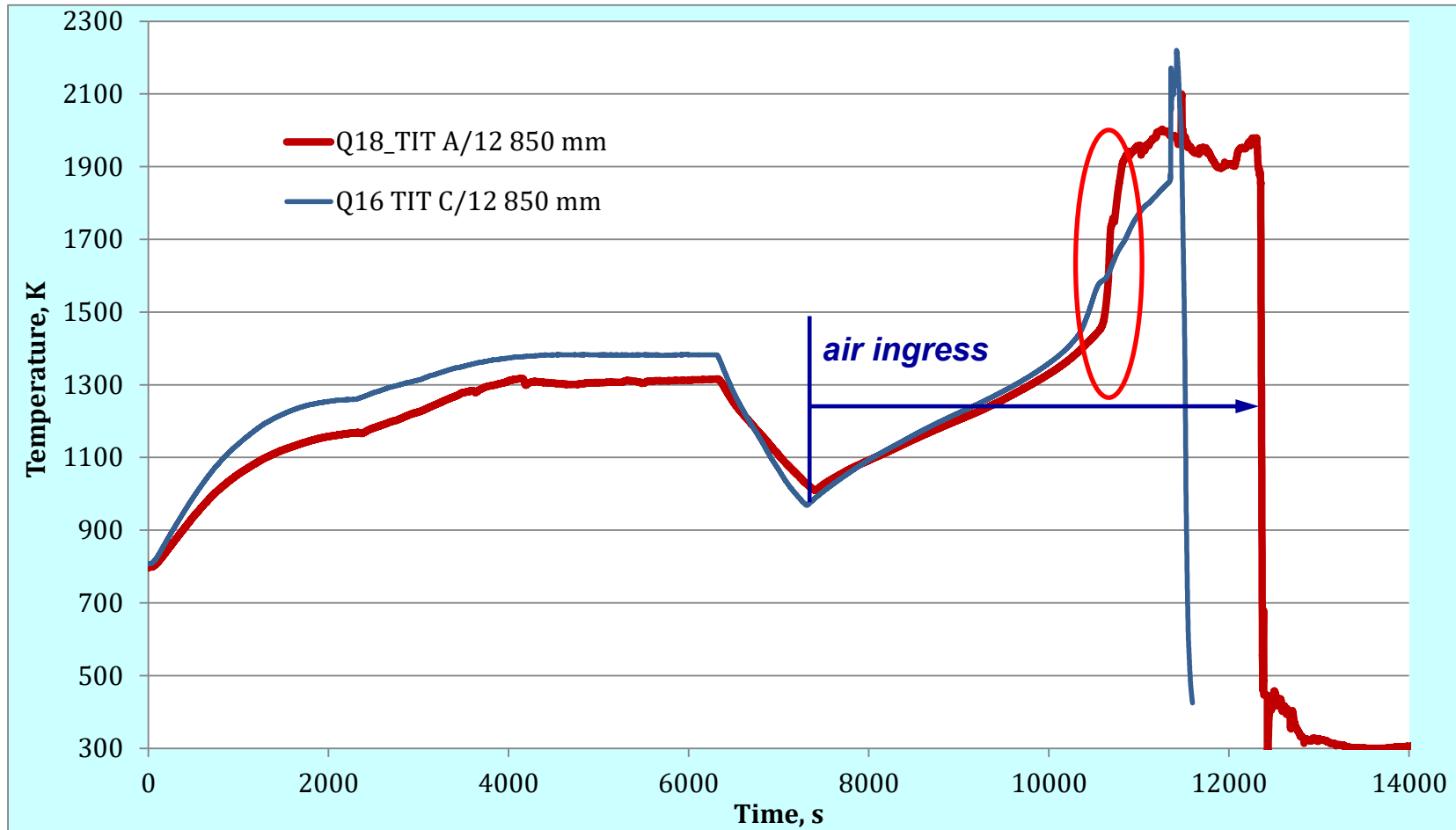
Figure 44 QUENCH-18 (air + steam) vs. QUENCH-16 (only air): accelerated temperature escalation during air ingress stage.
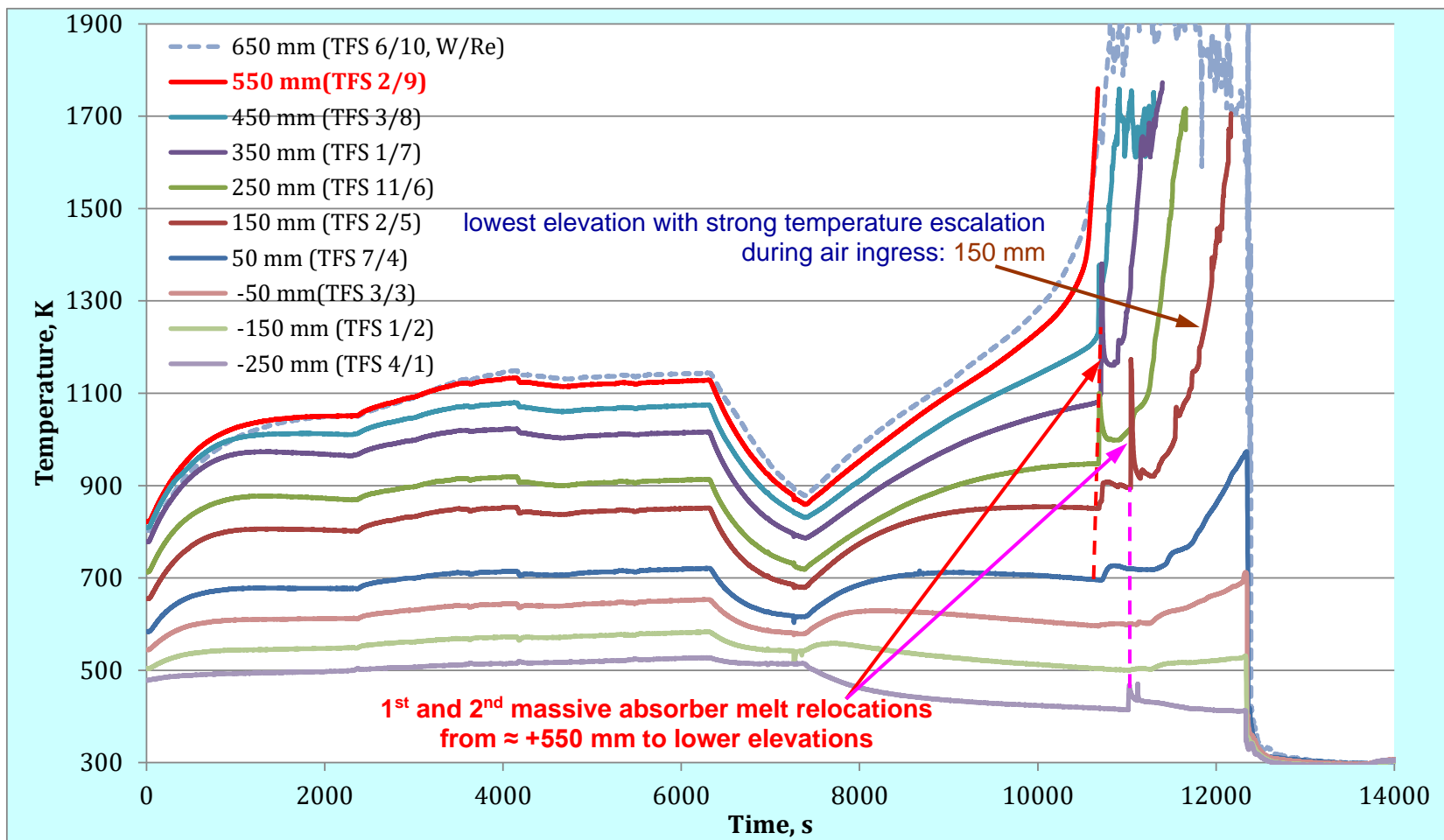
Figure 45 QUENCH-18; readings of clad surface thermocouples (Ni/CrNi) at lower elevations.
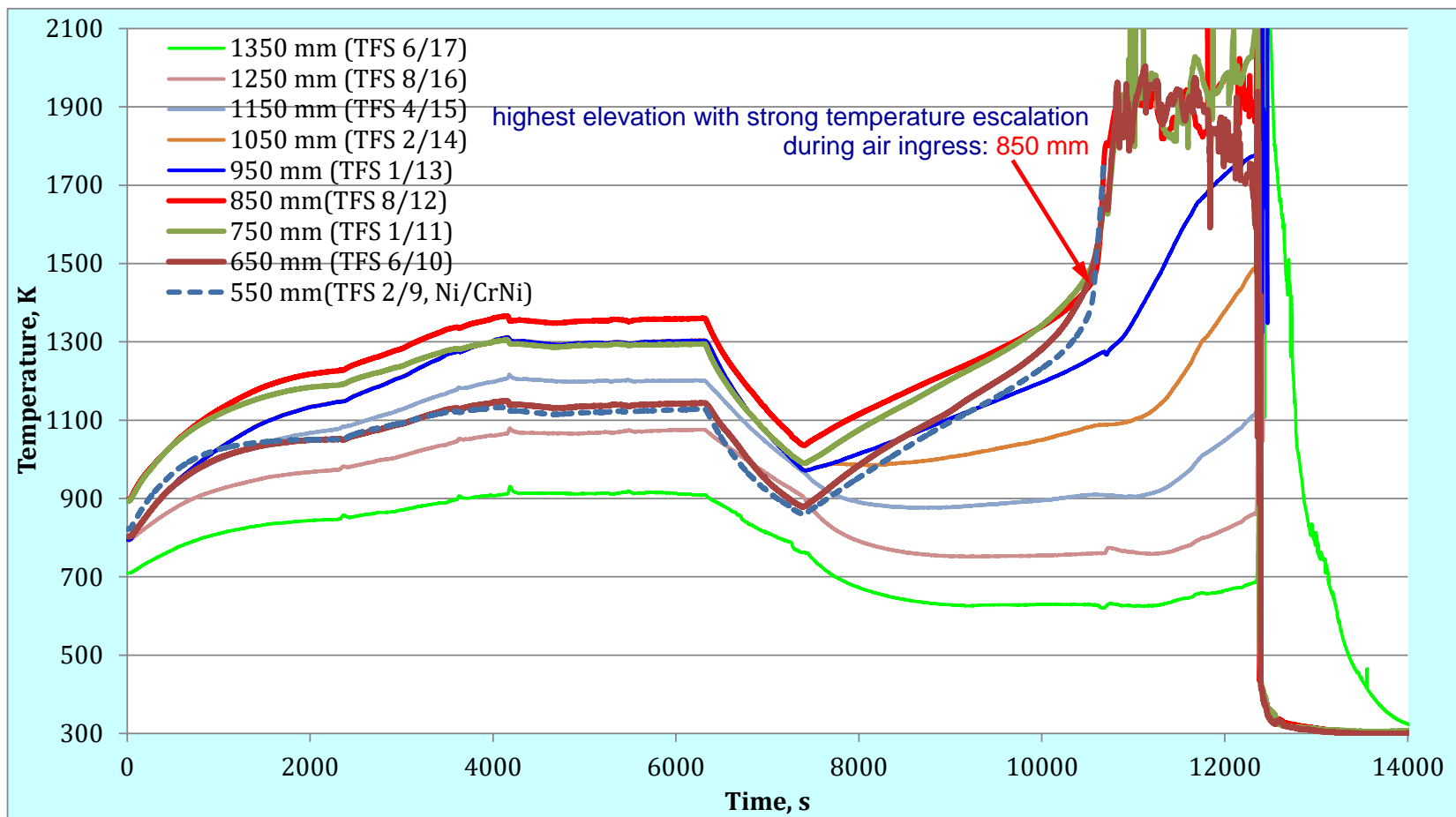
Figure 46 QUENCH-18; readings of clad surface thermocouples (W/Re) at upper elevations.
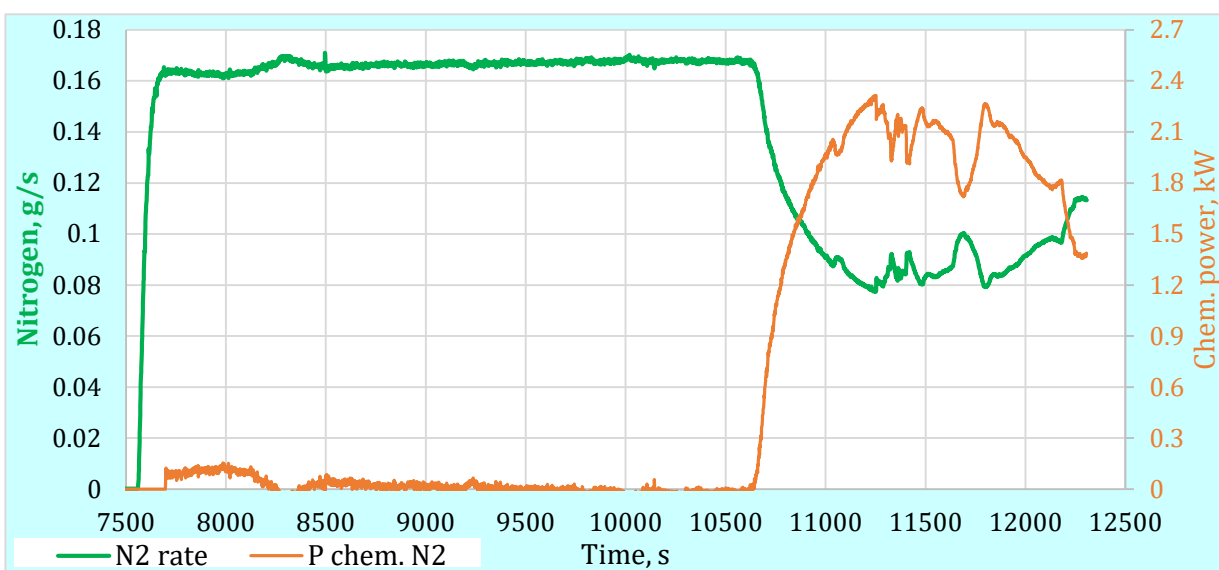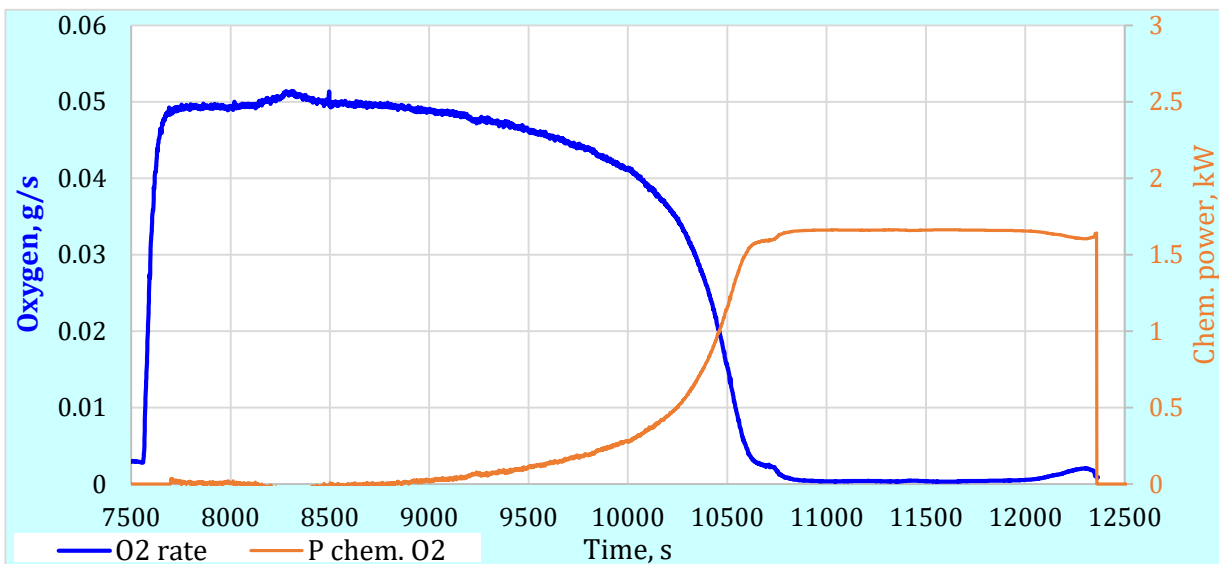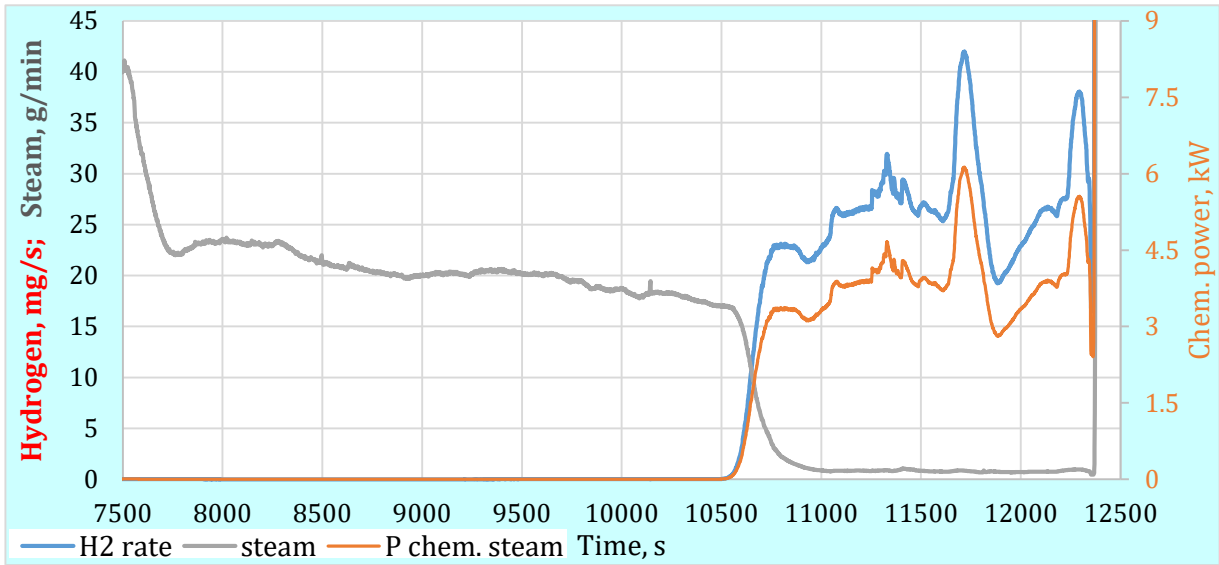
Figure 47   QUENCH-18; mass spectrometer measurement results: release of chemical energy due to consumption of steam, oxygen and nitrogen.
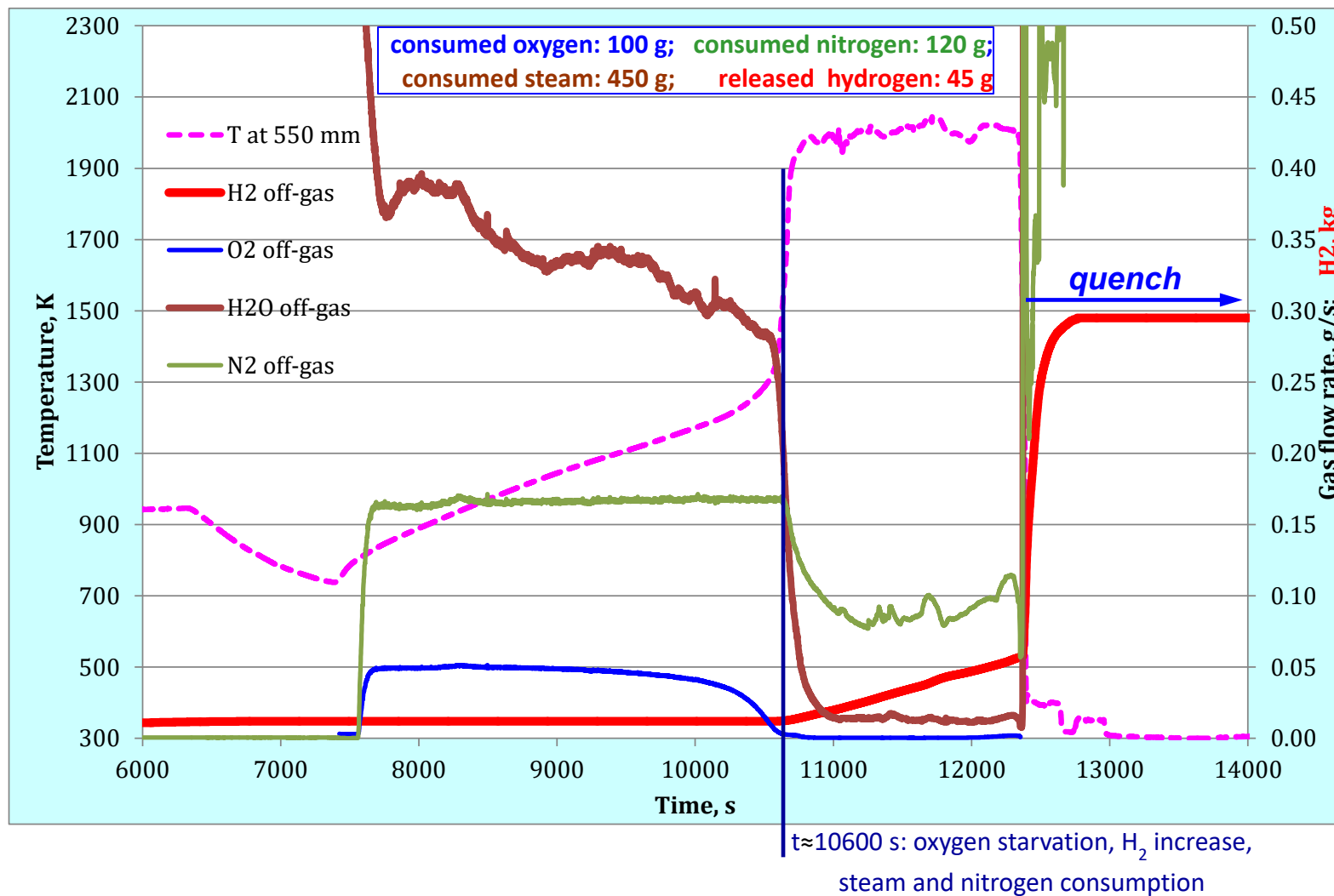
Figure 48 QUENCH-18; outlet gas behavior during air ingress: starvation phenomena.
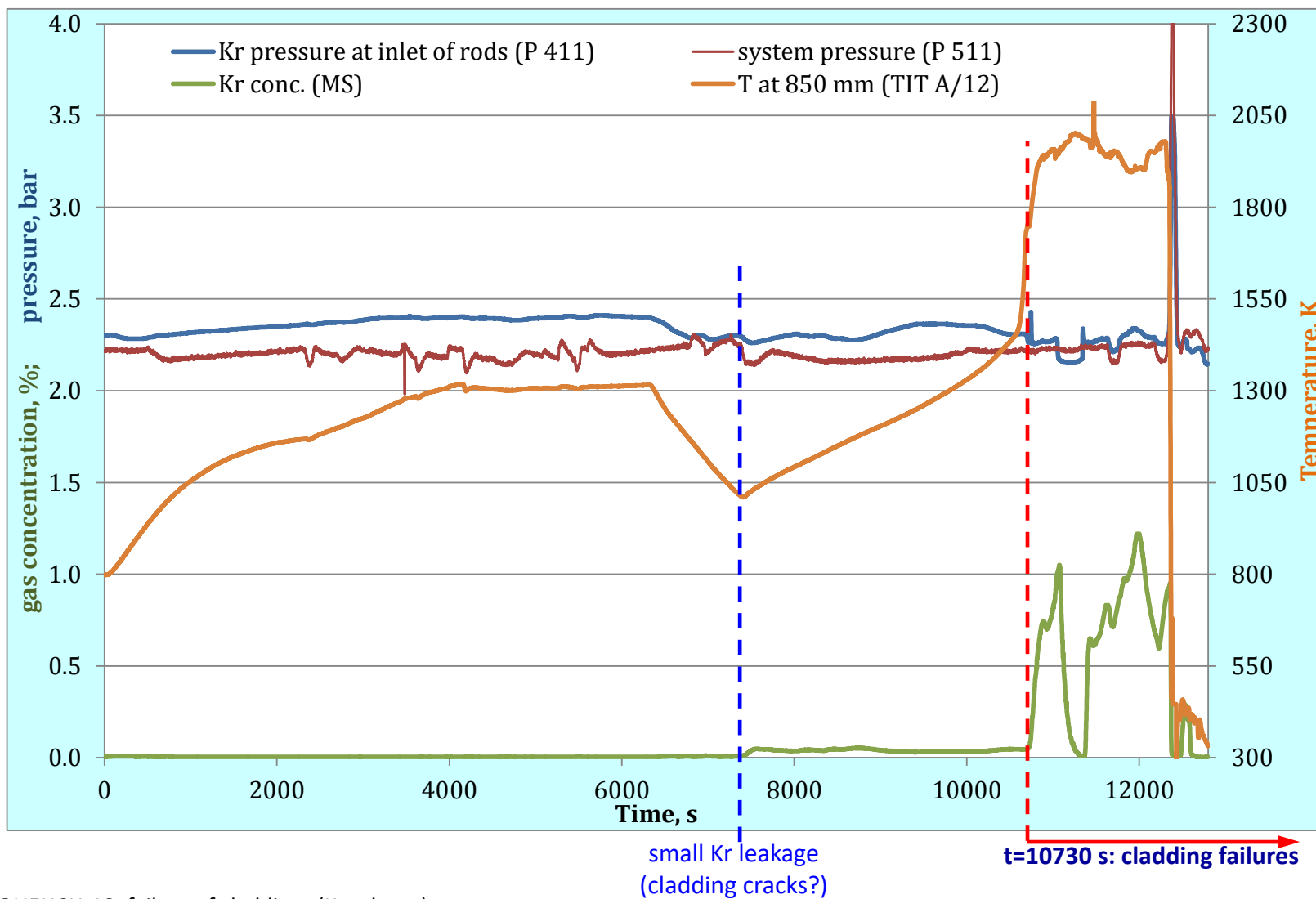
Figure 49   QUENCH-18; failure of claddings (Kr release).

Figure 50 QUENCH-18; failure of shroud (Ar flow through shroud breach).
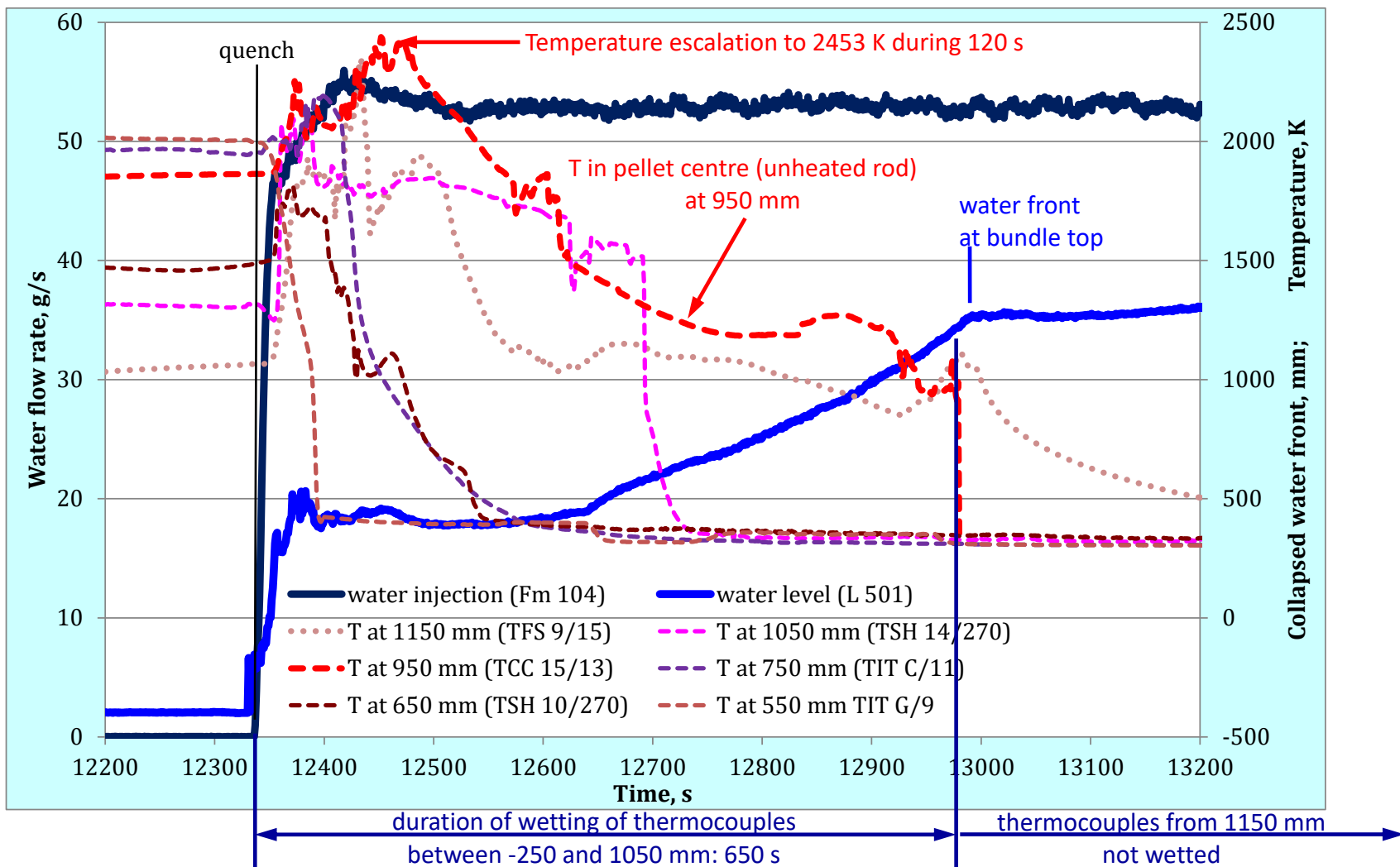
Figure 51 QUENCH-18; water and temperatures during the quench stage.
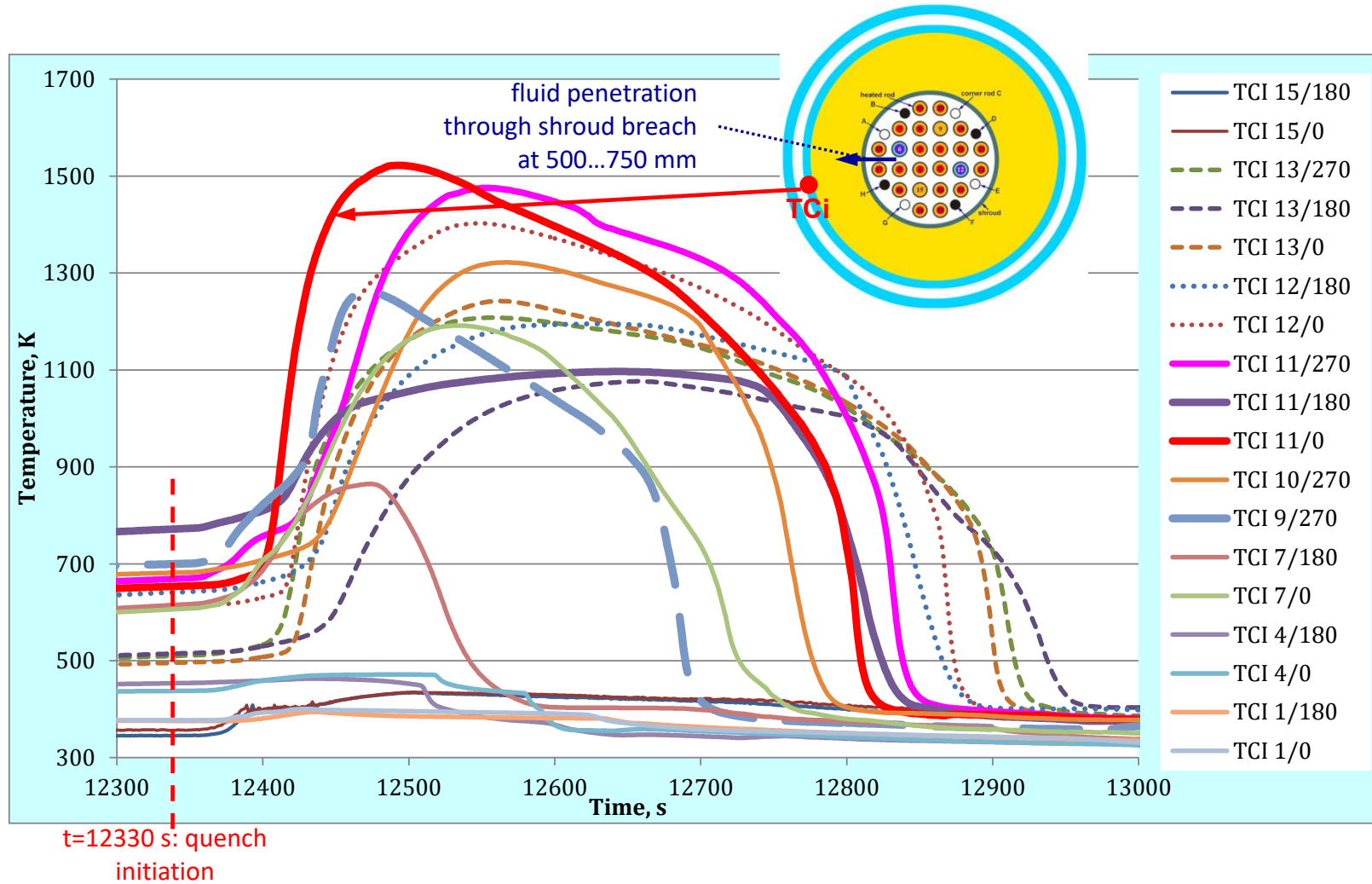
Figure 52   QUENCH-18; Readings of thermocouples at inner surface of cooling jacket after quench initiation.
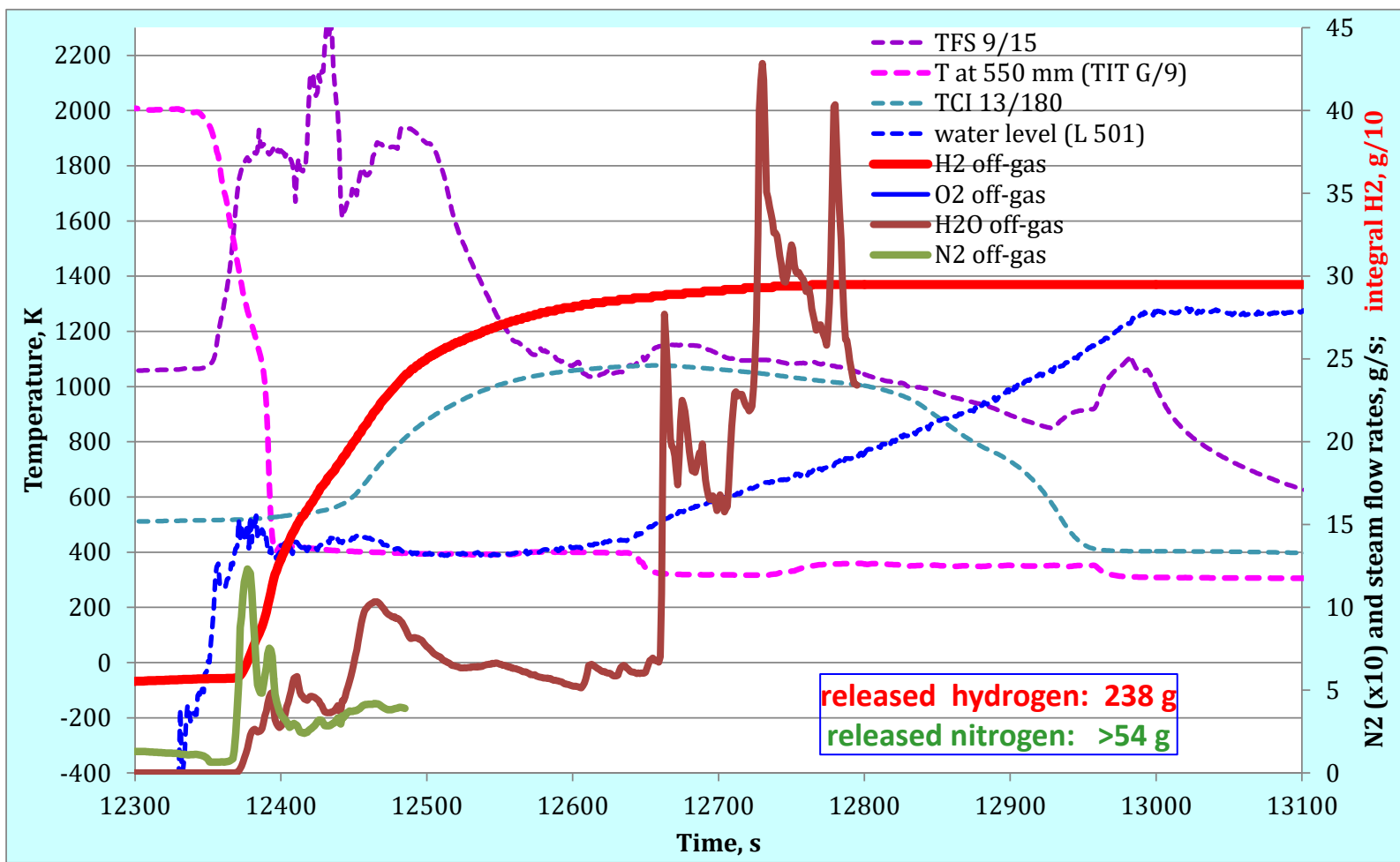
Figure 53   QUENCH-18; Gas release during the quench stage.

QUENCH off-gas pipe

5 nlpm

Cycl

70 nlpm — N₂ → CO → D1 — Exhaust 70/64 nlpm

Filter

70 nlpm — N₂ → CO → D2 — BLPI

70 nlpm — N₂ → CO → D3 — Exhaust 70/25 nlpm

Exhaust 65 nlpm

10 nlpm — CO

ELPI — Vacuum pump — 10 nlpm → Exhaust

Vacuum pump — 45 nlpm → Exhaust
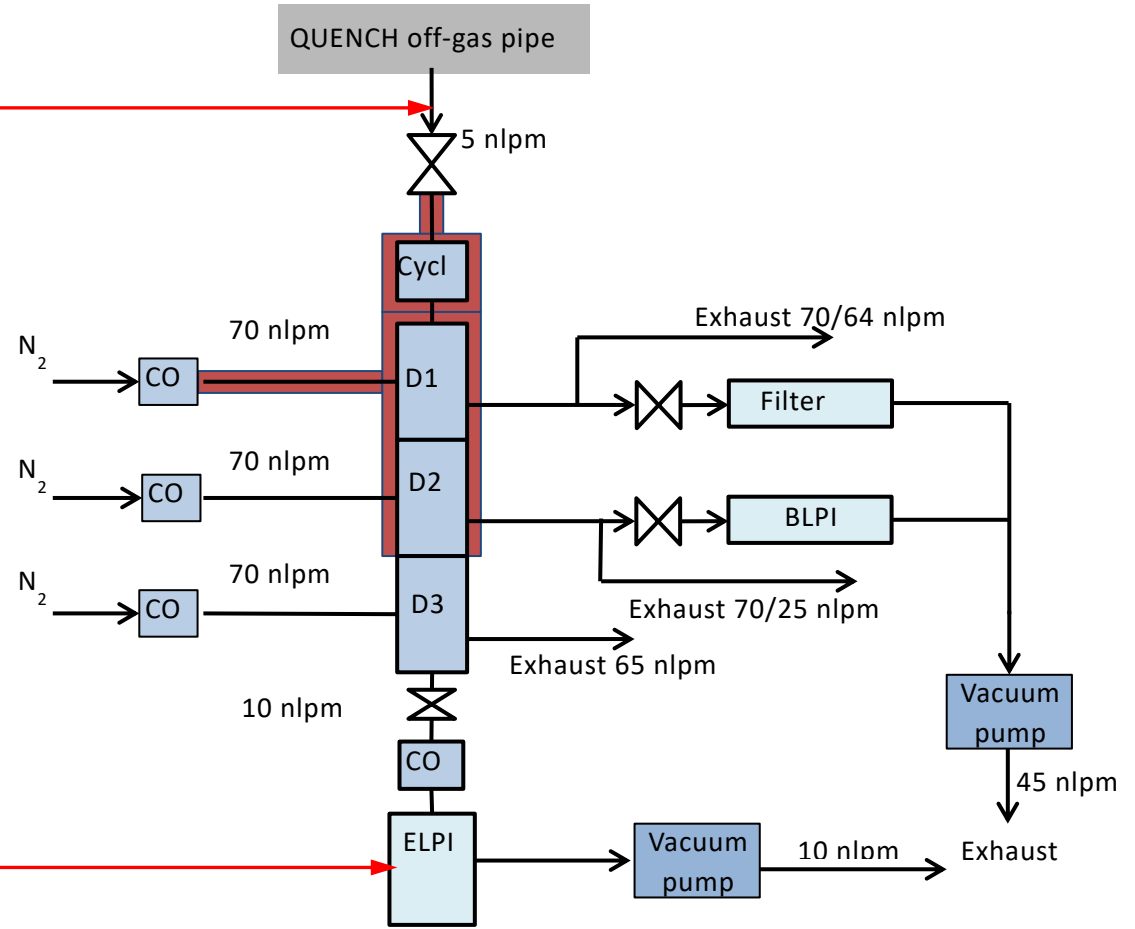
Figure 54 QUENCH-18; Aerosol measurement setup.
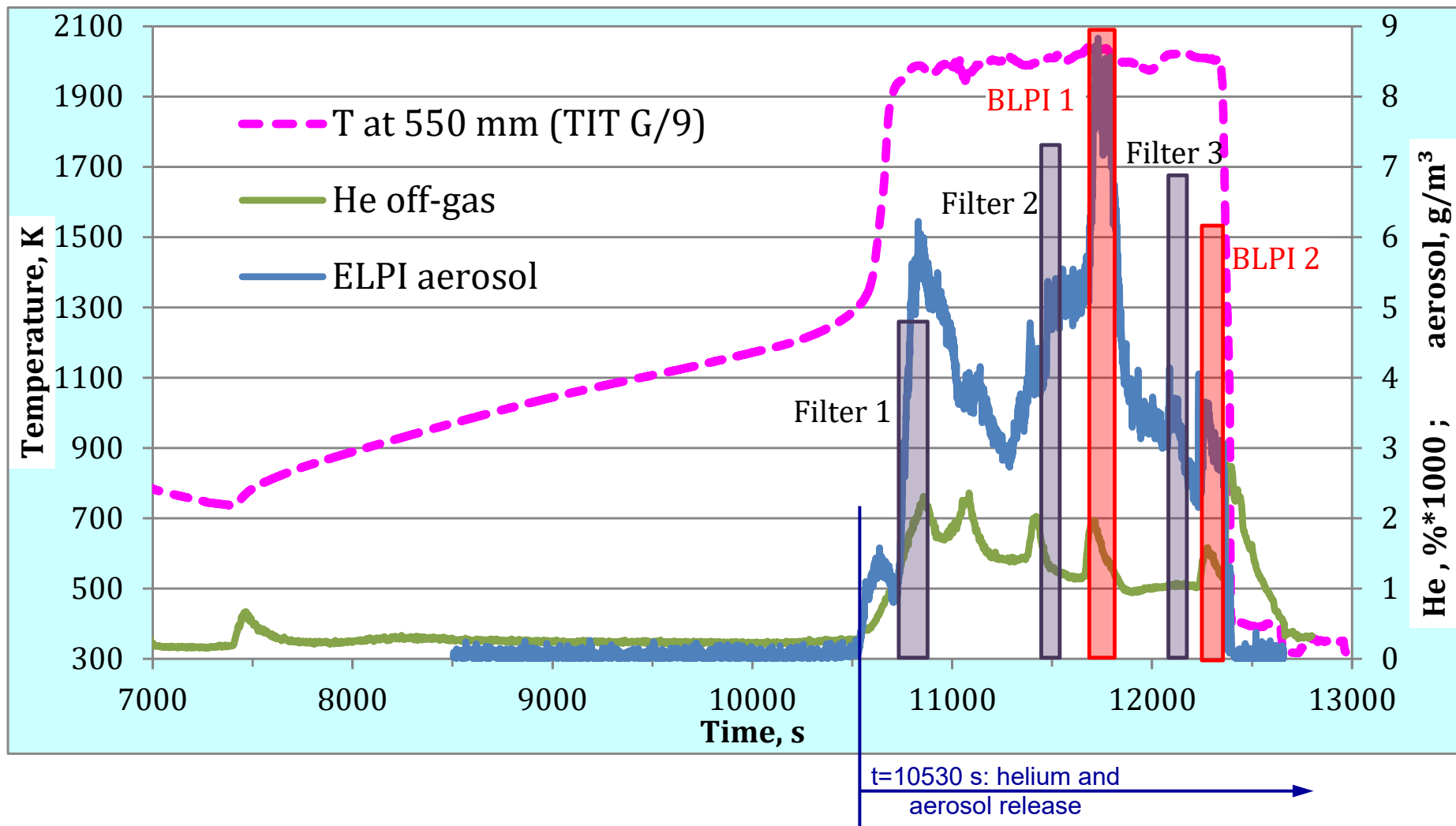
Figure 55   QUENCH-18; Failure of absorber rods indicated by He release and aerosol release measured by ELPI with indication of time periods for taking of filter and BLPI samples.
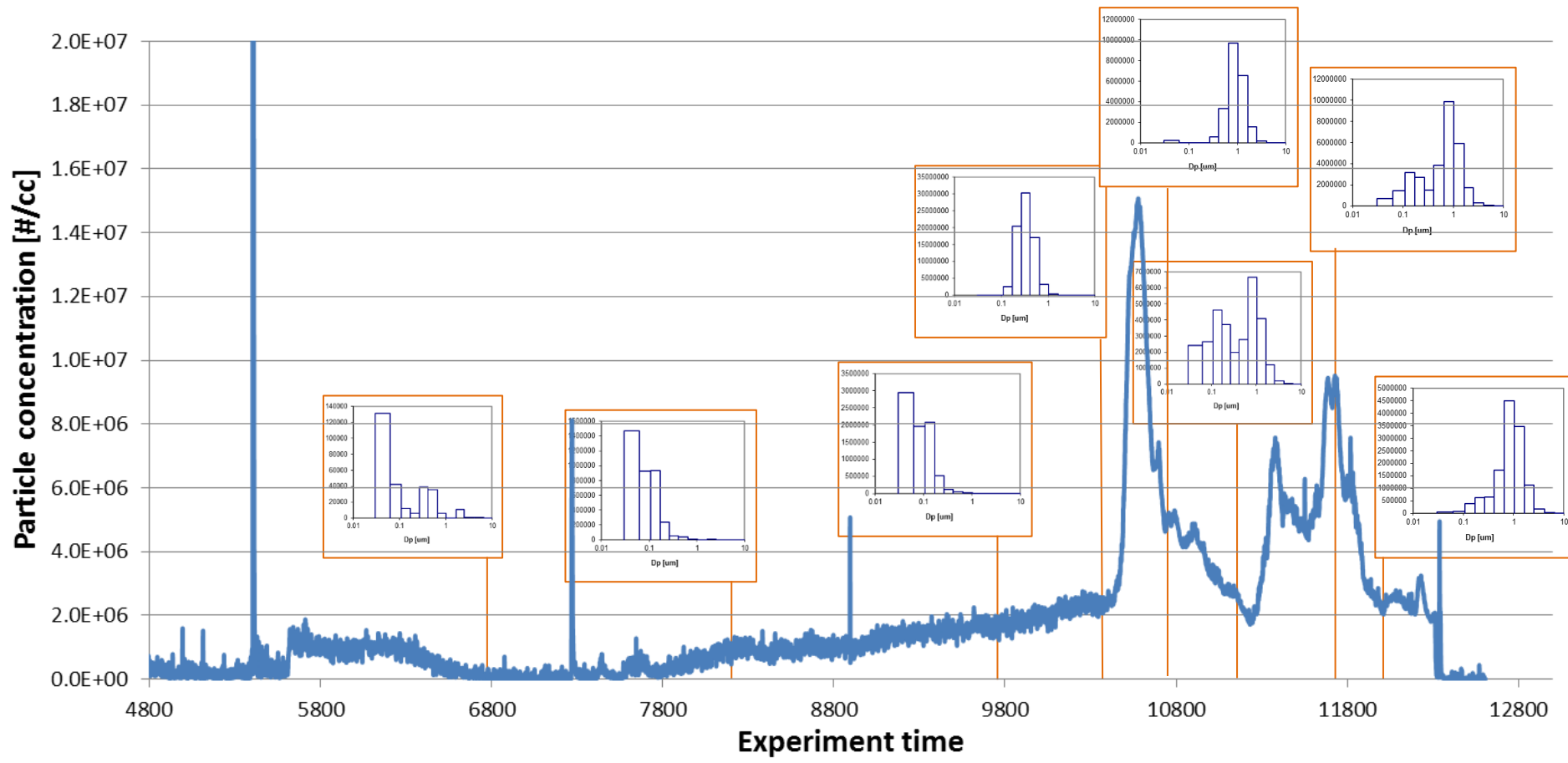
Figure 56   QUENCH-18; Number size distributions of aerosol particles registered by ELPI.
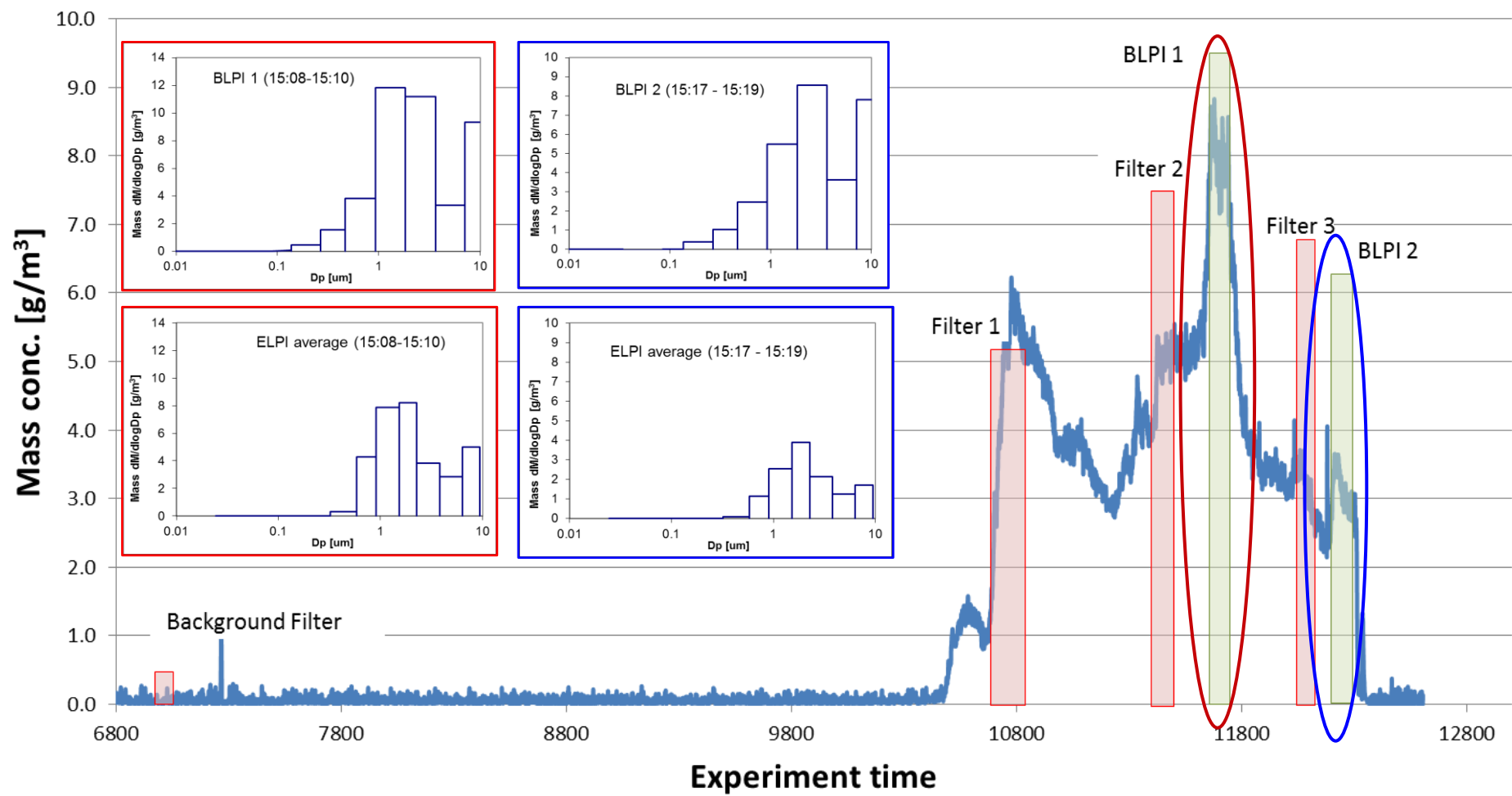
Figure 57 QUENCH-18; Mass/size distribution of aerosols: comparison of BLPI and ELPI measurements during two time intervals of high temperature stage.
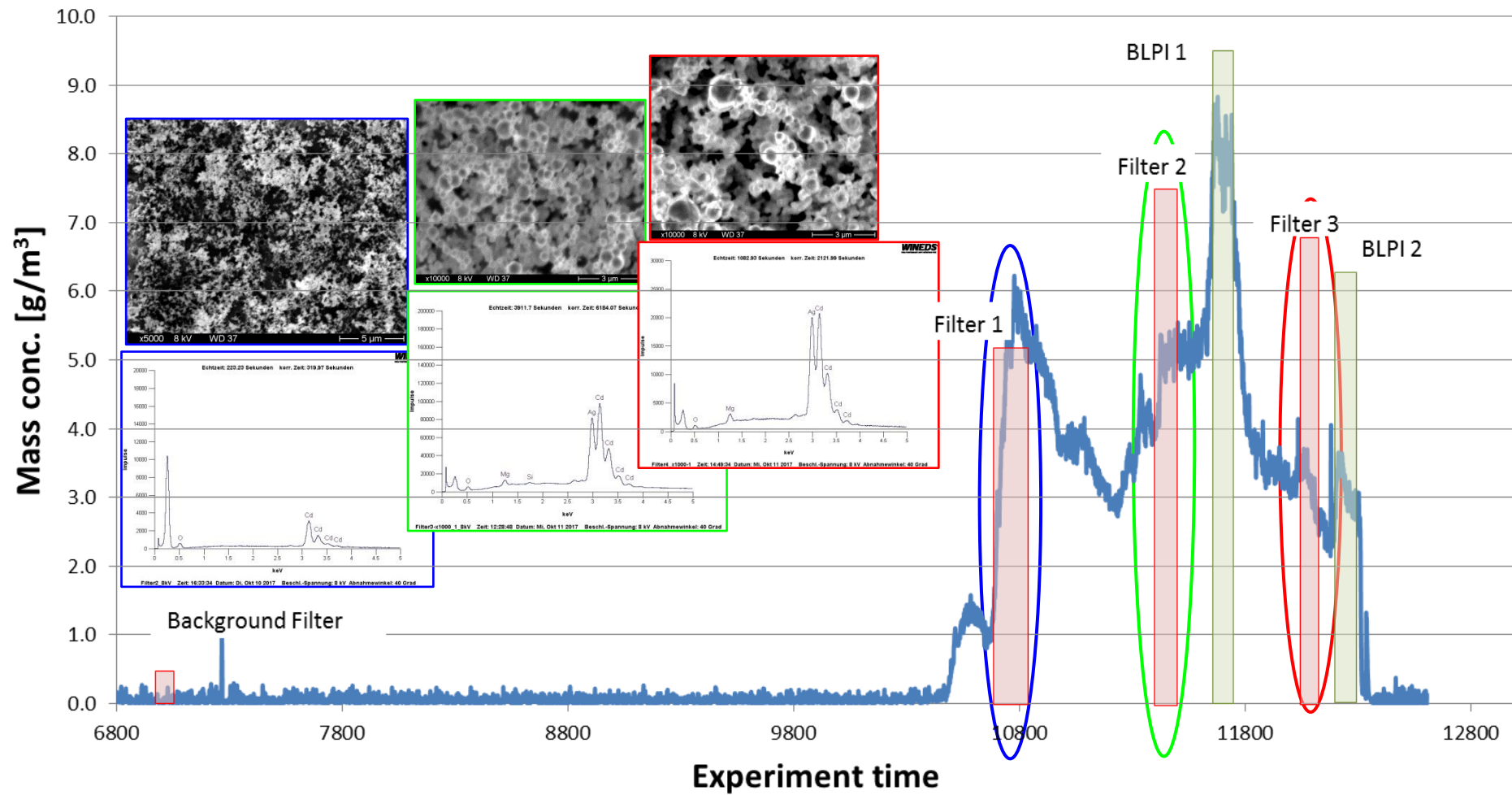
Figure 58 QUENCH-18; Results of SEM/EDX analysis of aerosols collected by filters 1, 2, 3.
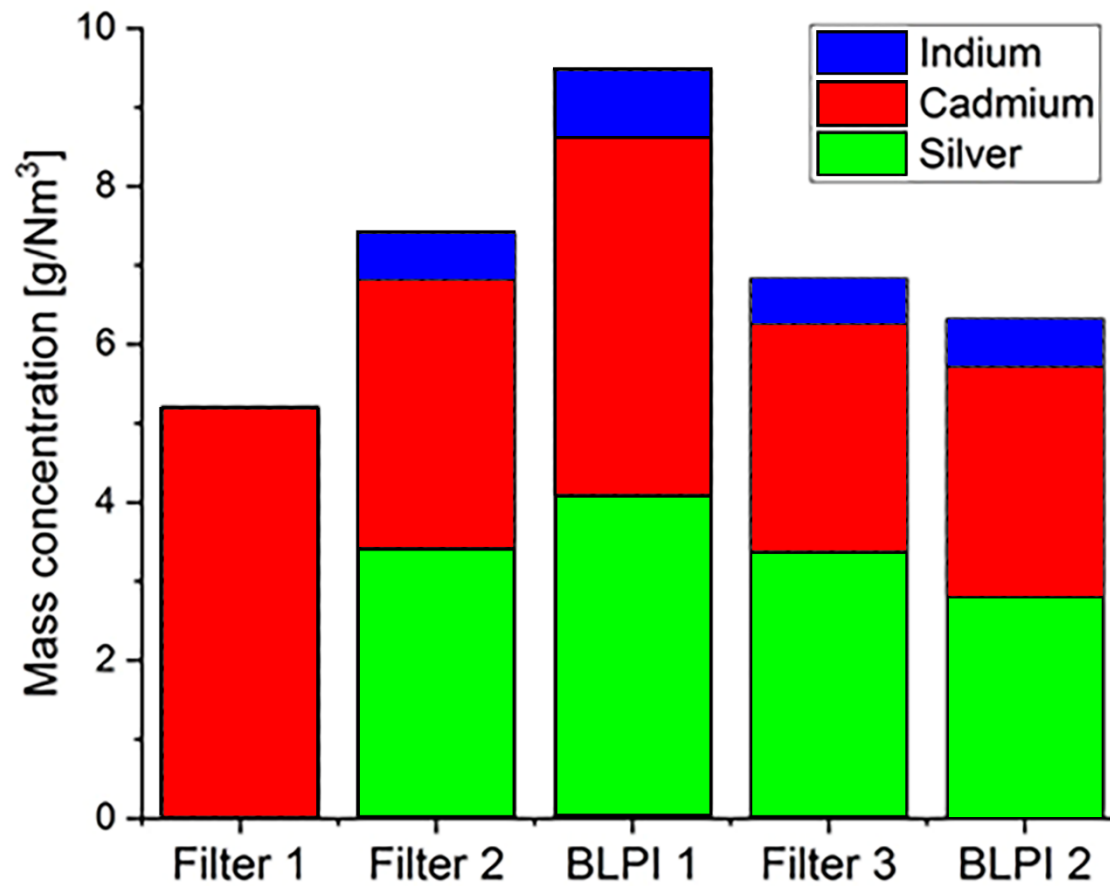
Figure 59 QUENCH-18; fraction of absorber materials in the atmosphere based on the ICP-OES analysis of the filter samples.
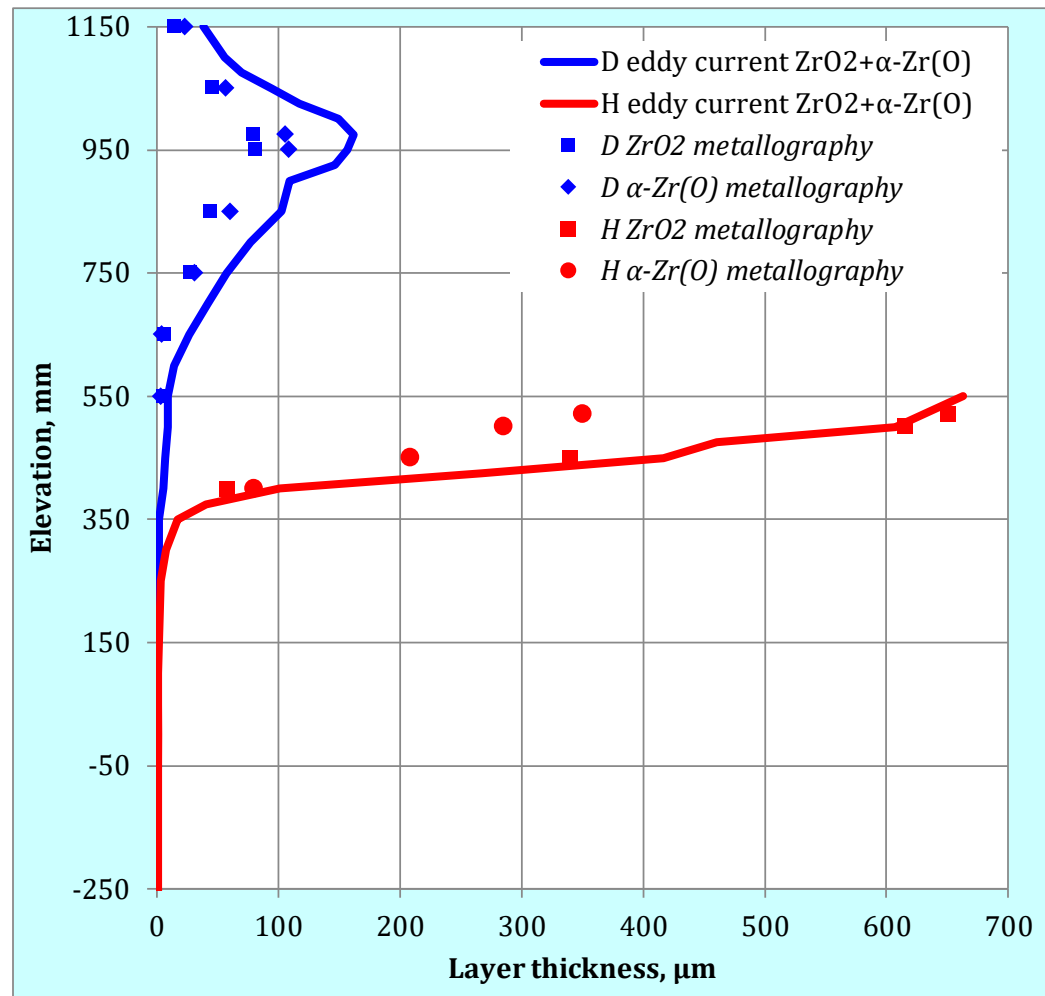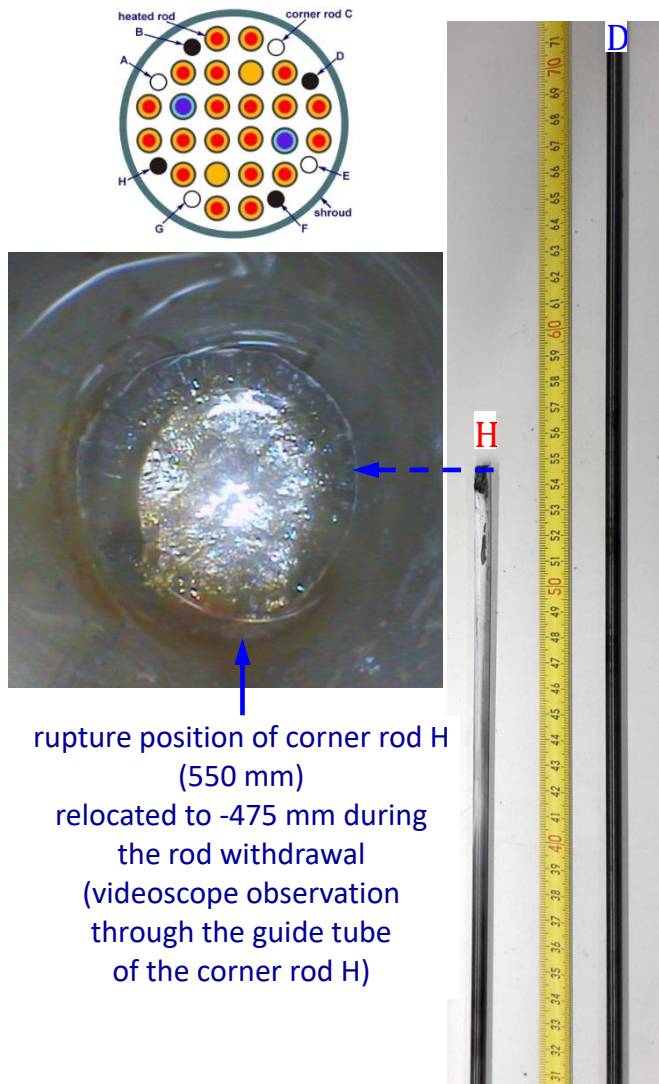
Figure 60 QUENCH-18; eddy current and metallography measurements at corner rods D (withdrawn before air ingress) and H (withdrawn at the end of temperature escalation).
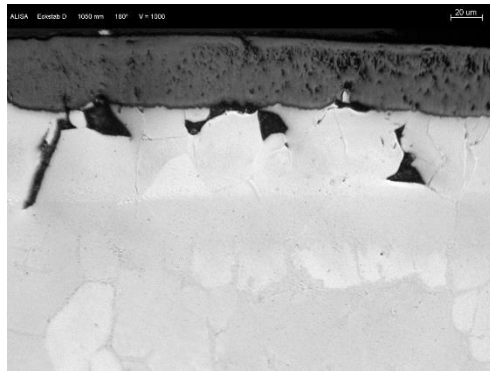
1050 mm: ZrO$_2$ 45 µm; α-Zr(O) 56 µm

1150 mm: ZrO$_2$ 15 µm; α-Zr(O) 23 µm

950 mm: ZrO$_2$ 81 µm; α-Zr(O) 108 µm

975 mm: ZrO$_2$ 79 µm; α-Zr(O) 105 µm

750 mm: ZrO$_2$ 27 µm; α-Zr(O) 31 µm

850 mm: ZrO$_2$ 44 µm; α-Zr(O) 60 µm

550 mm: ZrO$_2$ 5 µm; α-Zr(O) 3 µm

650 mm: : ZrO$_2$ 6 µm; α-Zr(O) 4 µm

Figure 61   QUENCH-18; Metallography of corner rod D withdrawn before air ingress: layer structures and thicknesses.
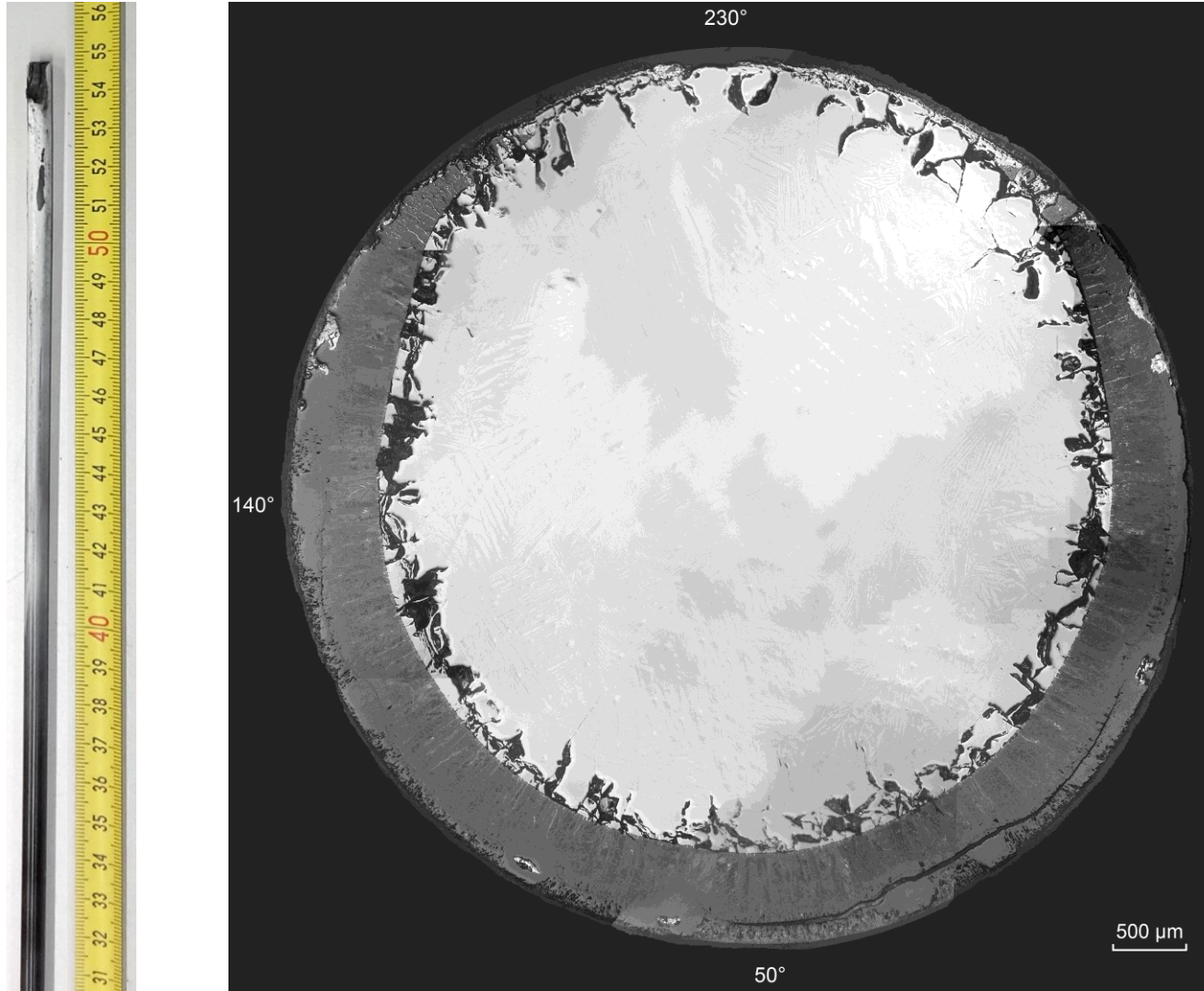
Figure 62 QUENCH-18; Withdrawn part of corner rod H (left); cross section at elevation 500 mm (right), top view, grayscale.
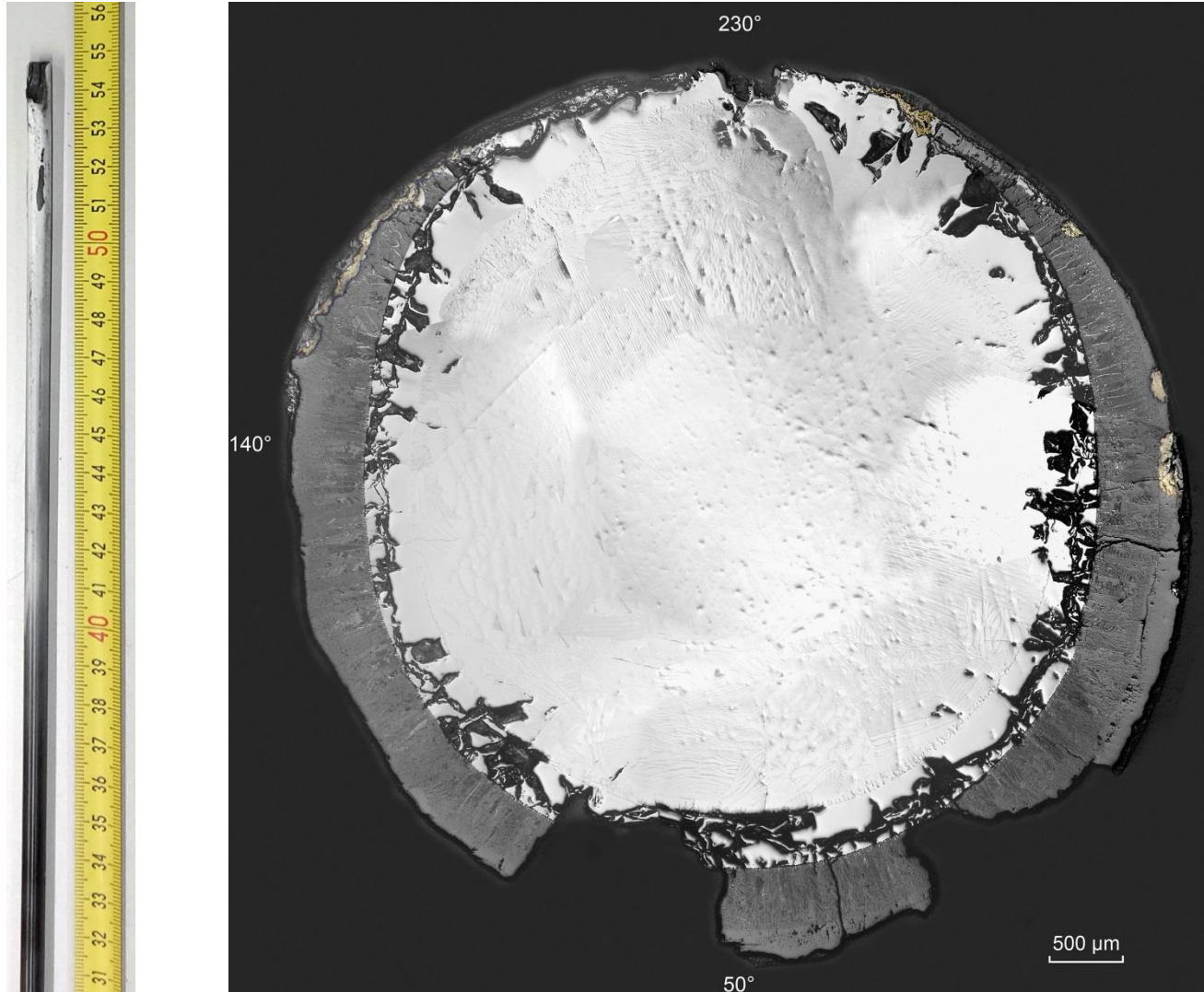
Figure 63 QUENCH-18; Withdrawn part of corner rod H (left); cross section at elevation 520 mm (right), top view: zones of nitrides (yellowish).
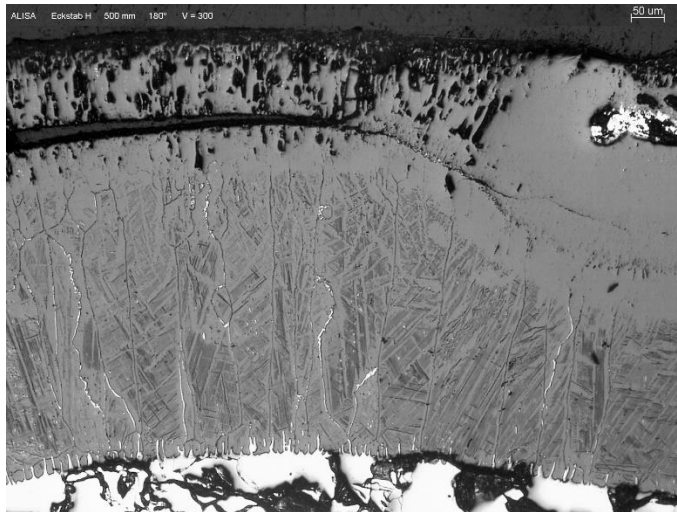
500 mm: nitrides; at 50°: ZrO$_2$ 615 µm, α-Zr(O) 285 µm
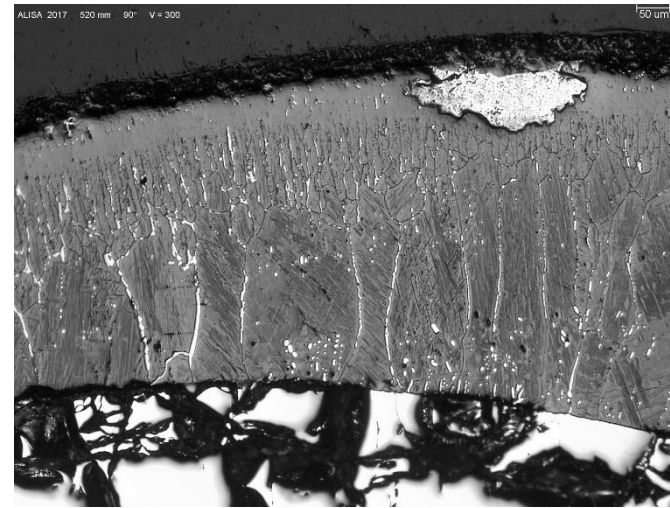
520 mm: nitrides; at 50°: ZrO$_2$ 650 µm, α-Zr(O) 350 µm
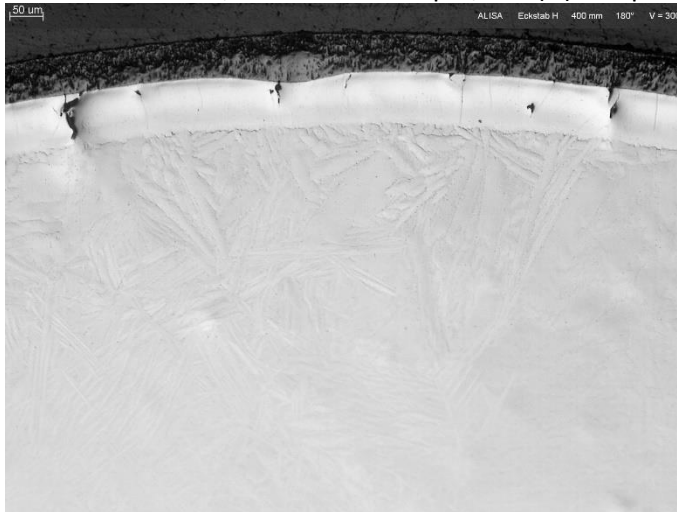
400 mm: no nitrides, ZrO$_2$ 58 µm, α-Zr(O) 80 µm

450 mm: no nitrides, ZrO$_2$ 340 µm, α-Zr(O) 208 µm

Figure 64   QUENCH-18; Metallography of lower part of corner rod H withdrawn after temperature escalation during air ingress: nitrides above 500 mm.
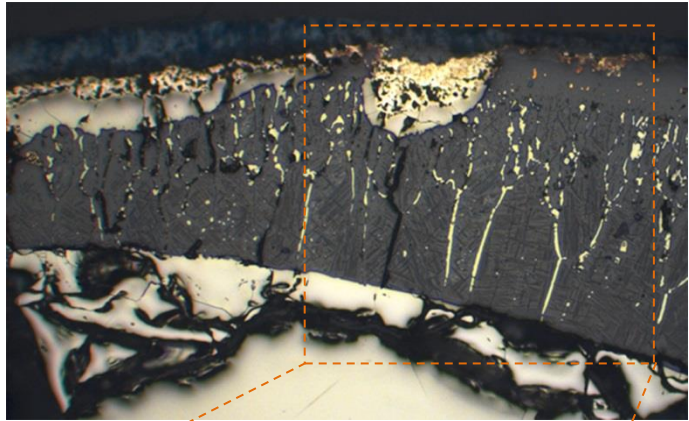
optical view of oxidized and nitrided rod surface
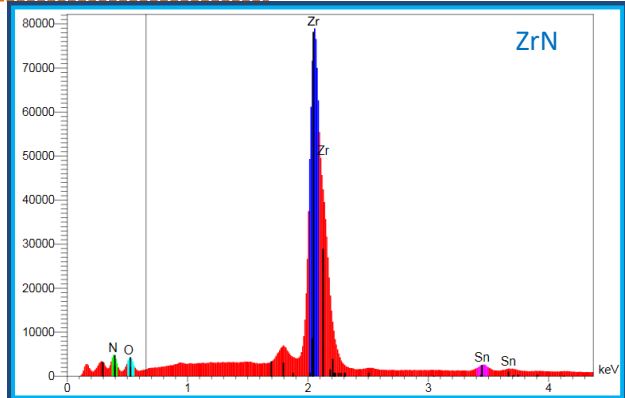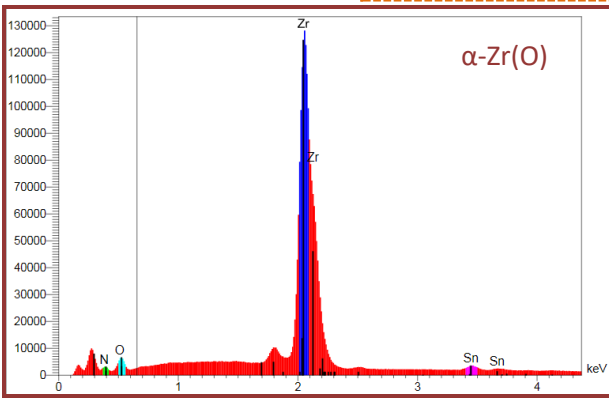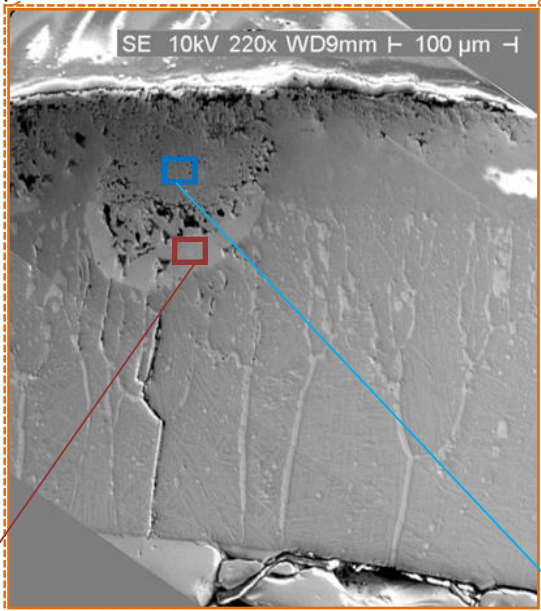
Element	α-Zr(O) / ZrN, **wt%**	α-Zr(O) / ZrN, **at%**
N	0.00 / 8.02	0.00 / 33.47
O	3.23 / 2.77	16.15 / 10.12
Zr	91.97 / 83.83	80.62 / 53.76
Sn	4.80 / 5.39	3.23 / 2.65

Figure 65   QUENCH-18; Corner rod H, elevation 520 mm, top view: EDX analysis.

elevation 640 mm

elevation 670 mm

elevation 580 mm

elevation 610 mm

550 – 700 mm
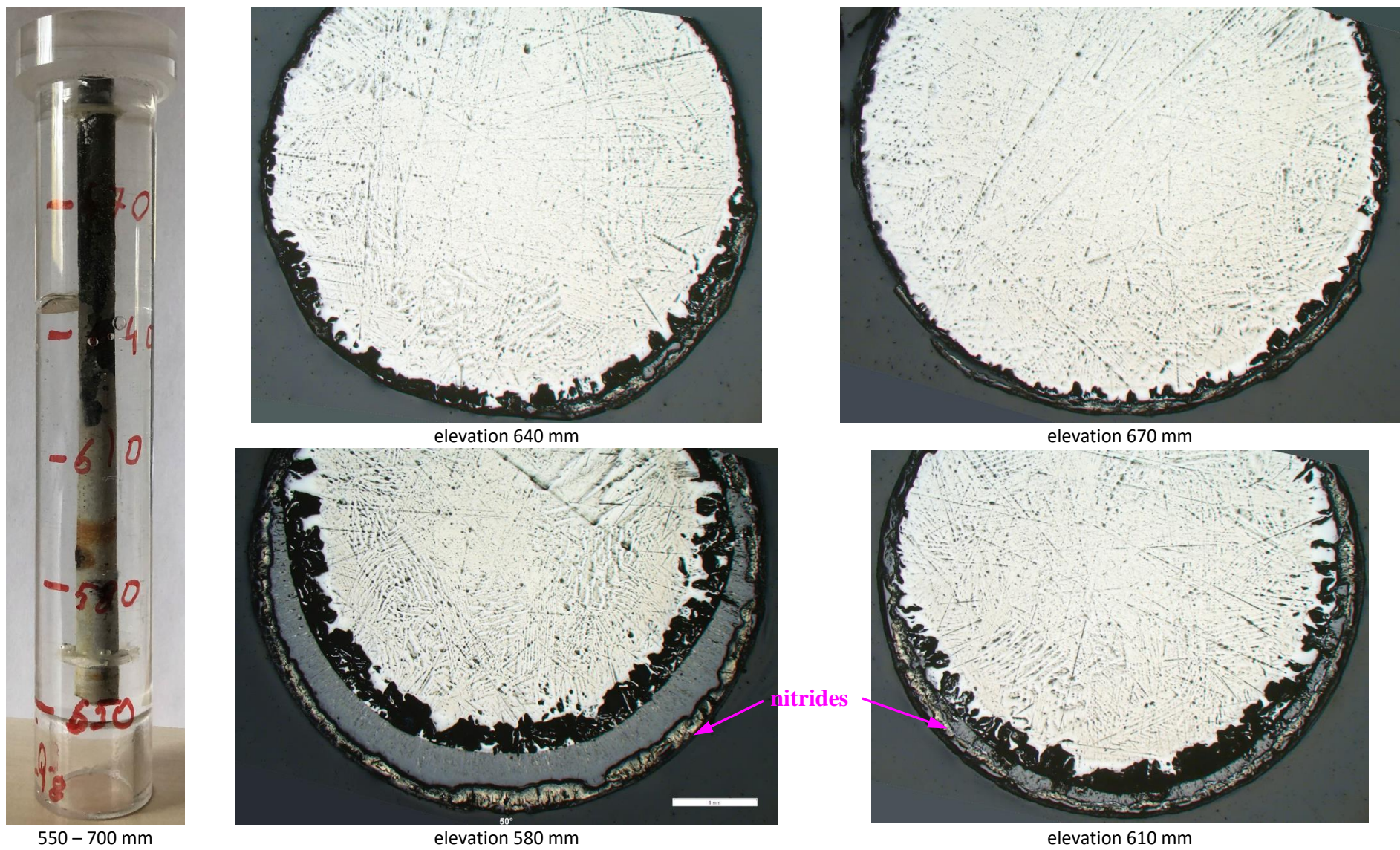
nitrides

Figure 66   QUENCH-18; Corner rod H: formation of thick nitride layer between elevations about 570 and 620 mm.
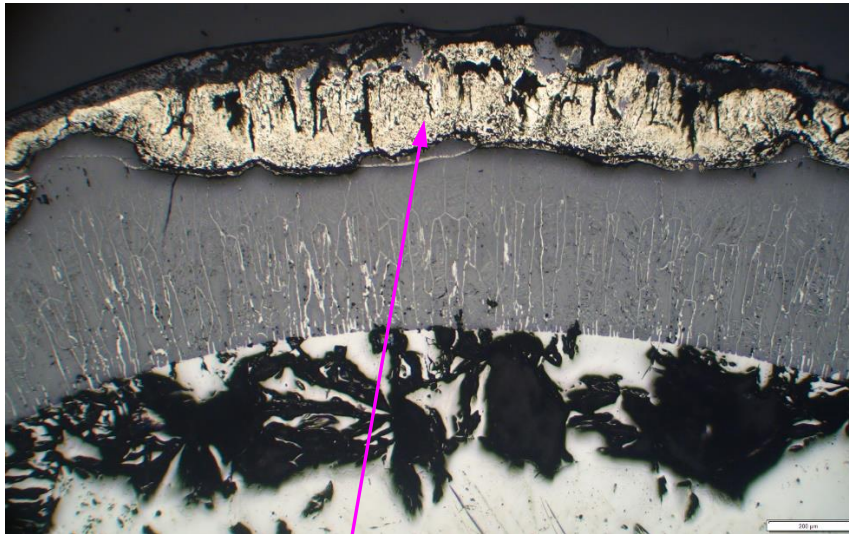
angle 50°: outer ZrO$_2$ 40 µm, ZrN 260 µm, inner ZrO$_2$ 415 µm, α-Zr(O) 460 µm

angle 140°: outer ZrO$_2$ 100 µm, ZrN 120 µm, inner ZrO$_2$ 300 µm, α-Zr(O) 470 µm

angle 230°: ZrO$_2$ 95 µm, ZrN 45 µm, α-Zr(O) 100 µm
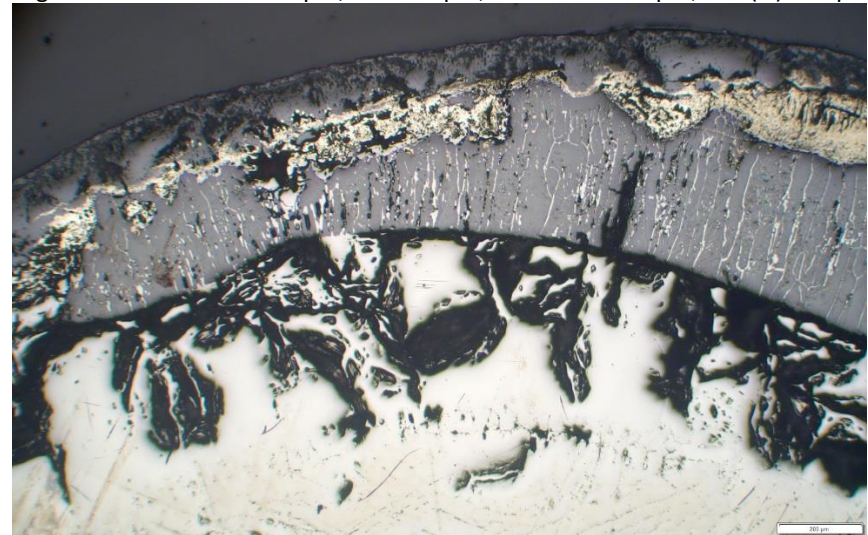
angle 320°: outer ZrO$_2$ 80 µm, ZrN 90 µm, inner ZrO$_2$ 370 µm, α-Zr(O) 400 µm

Figure 67   QUENCH-18; Corner rod H, elevation 580 mm, top view: thin outer oxide layer and thick nitride layer formed under not complete steam starvation outside of segment between 190° and 270°.
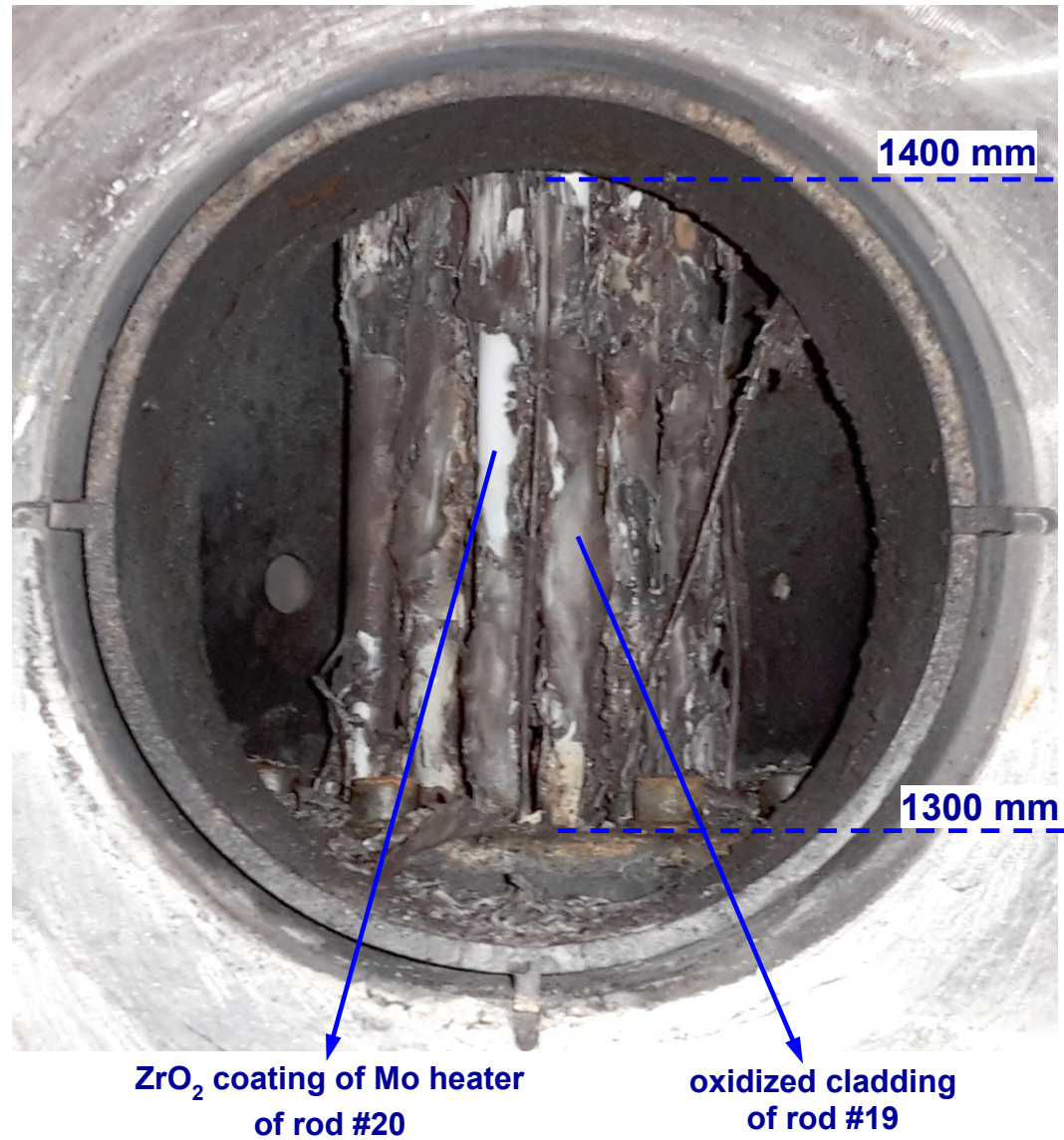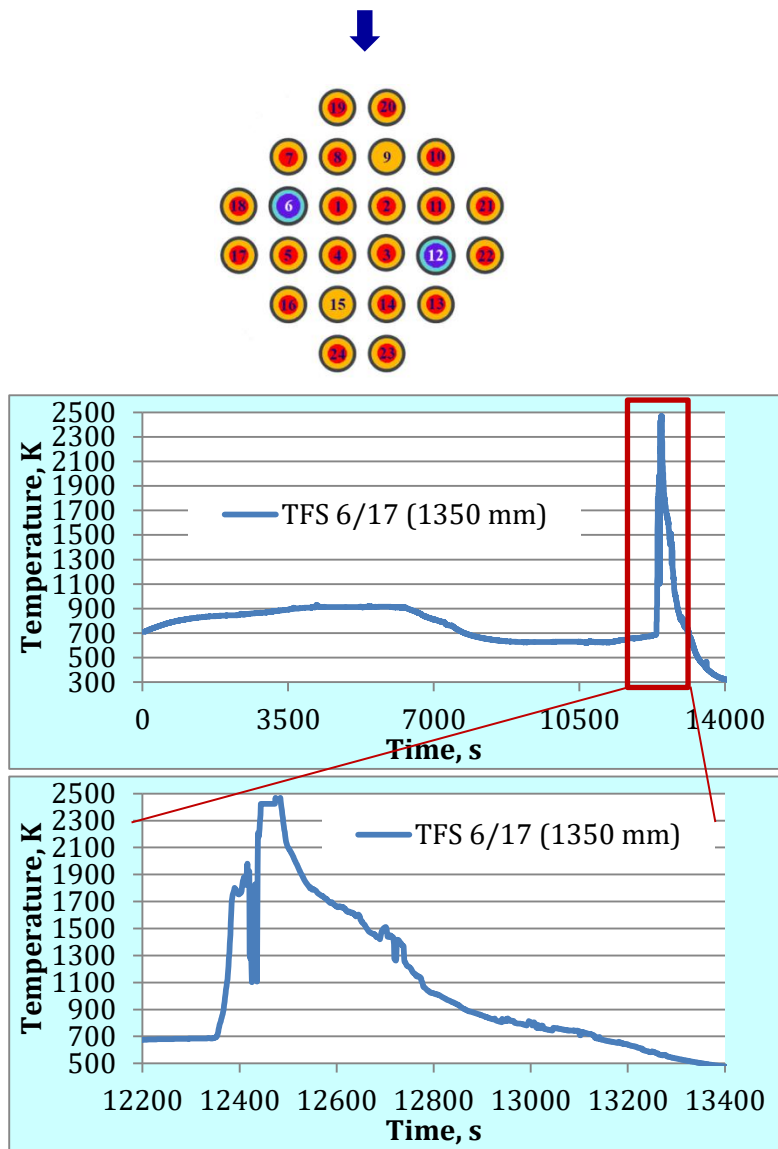
Figure 68   QUENCH-18; View of the bundle top through the off-gas pipe.
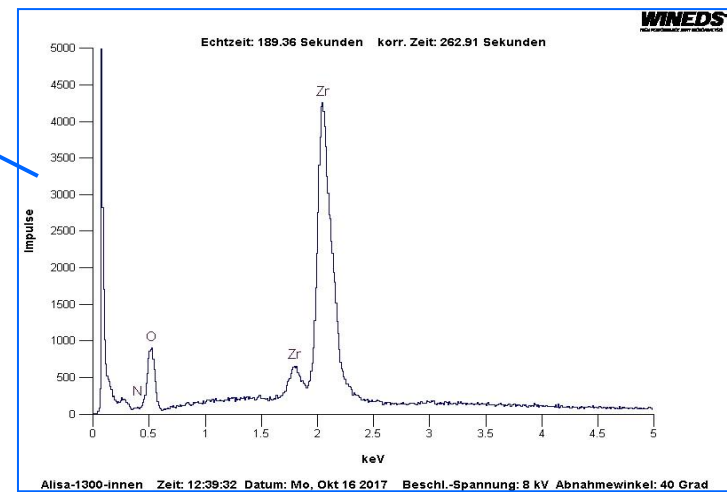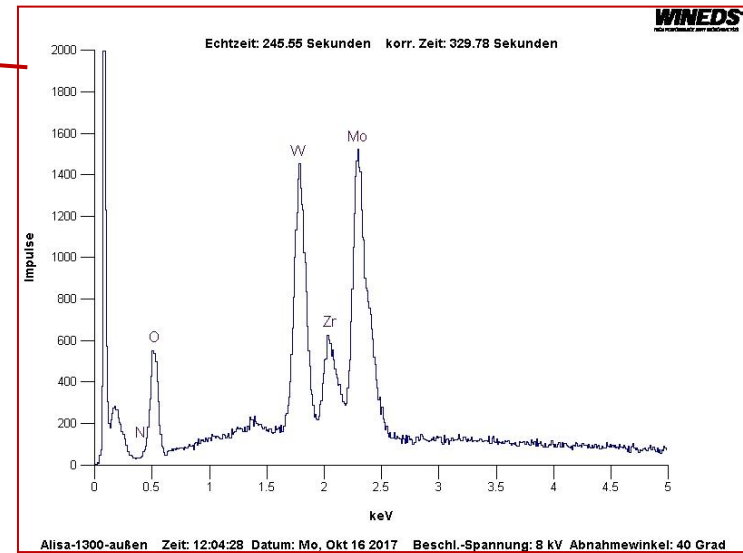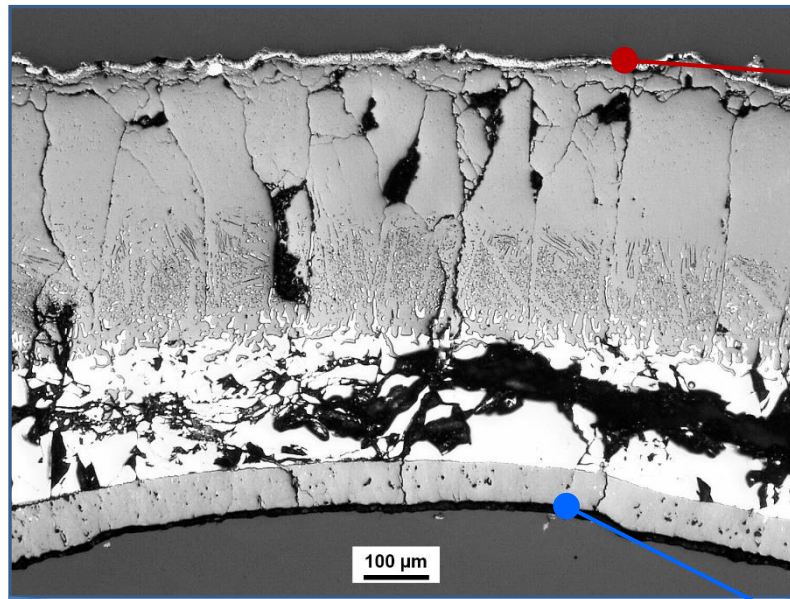
Figure 69 QUENCH-18; EDX analysis of cladding segment spalled at 1350 mm: thin tungsten and molybdenum layer at outer cladding surface (sedimentation from the gas phase of sublimated metals).
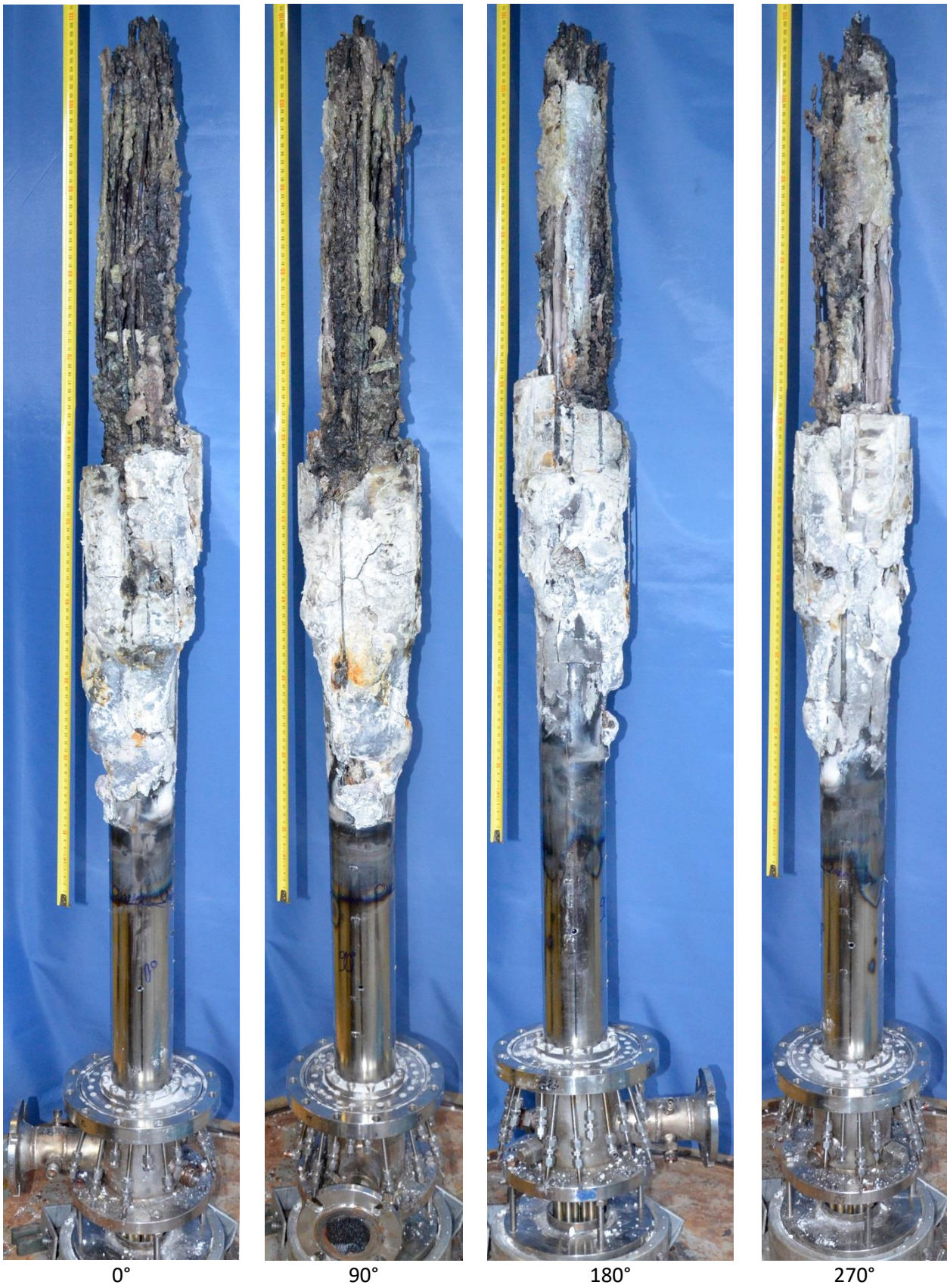
Figure 70   QUENCH-18; Post-test bundle overview (without bundle upper part) at four angle positions.

0°   90°   180°   270°

0°	90°	180°	270°

Figure 71   QUENCH-18; Post-test bundle overview between about 550 and 1100 mm at four angle positions.
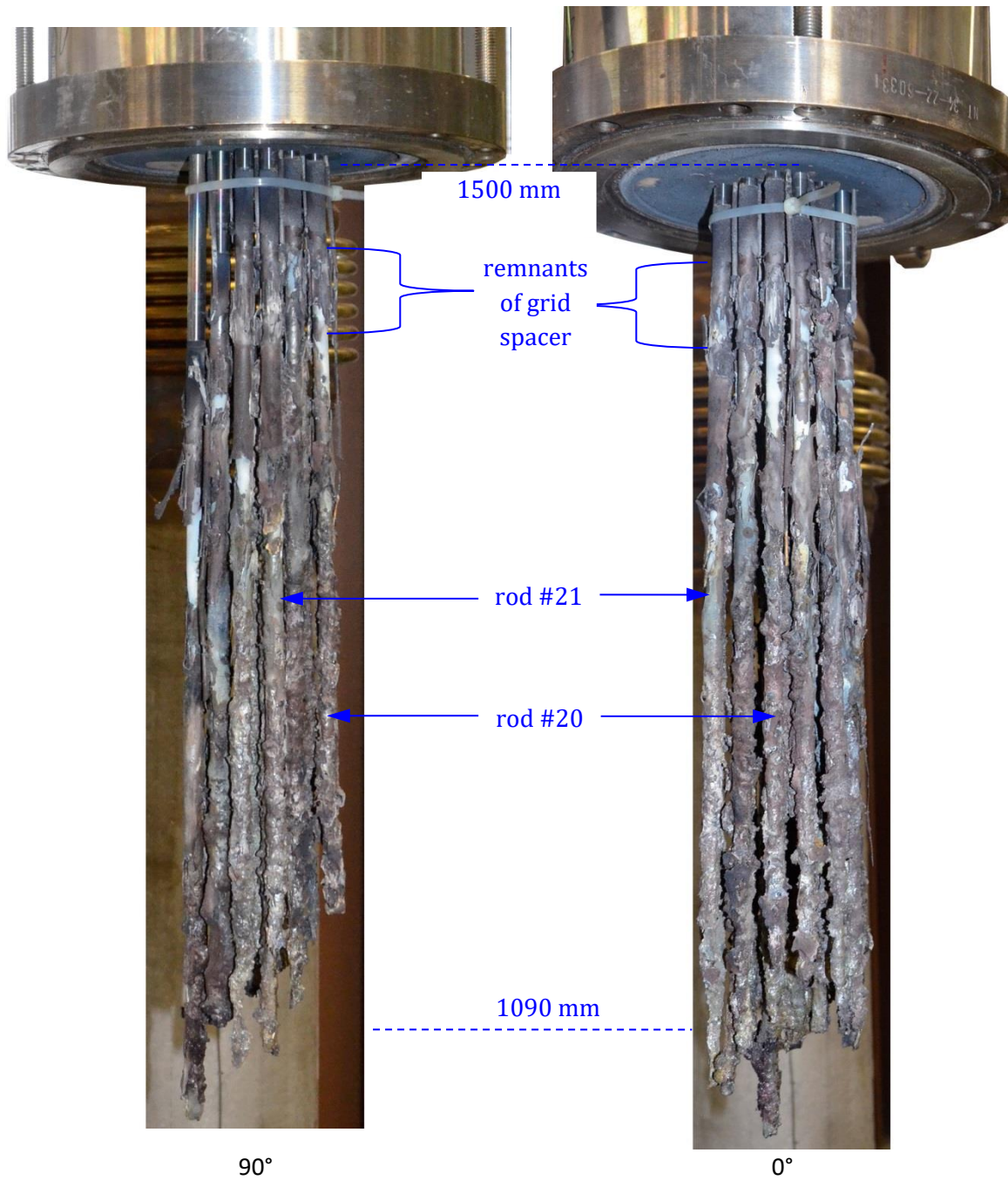
Figure 72   QUENCH-18; Upper part of the bundle between elevations 1090 and 1500 mm.
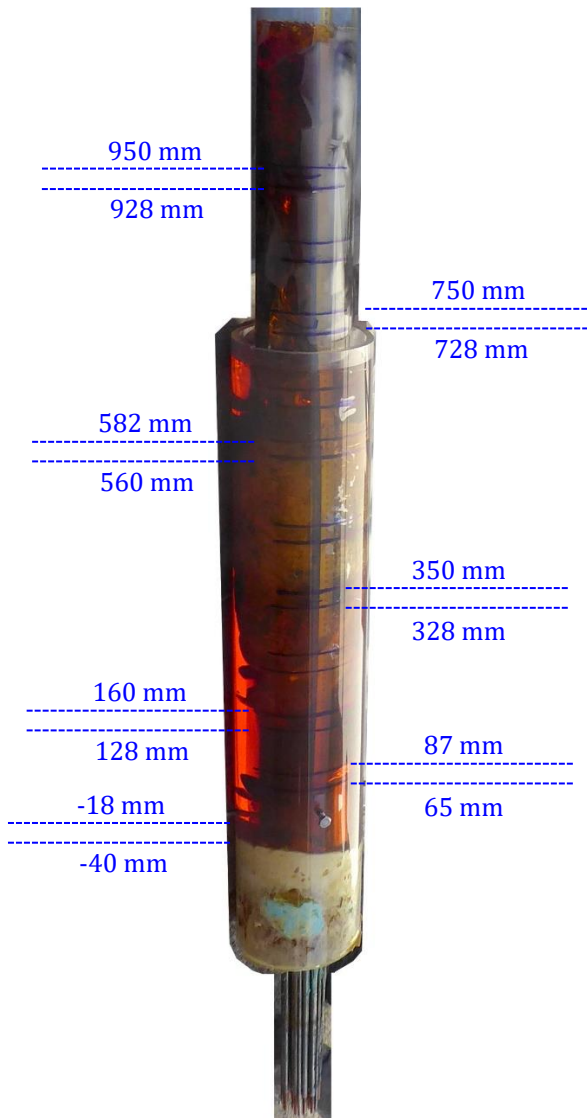
lower bundle part embedded in epoxy with indication of slices chosen for cutting

upper bundle part (without rods 3 and 23) embedded in epoxy

Figure 73   QUENCH-18; embedding of upper and lower parts of bundle in epoxy resin.
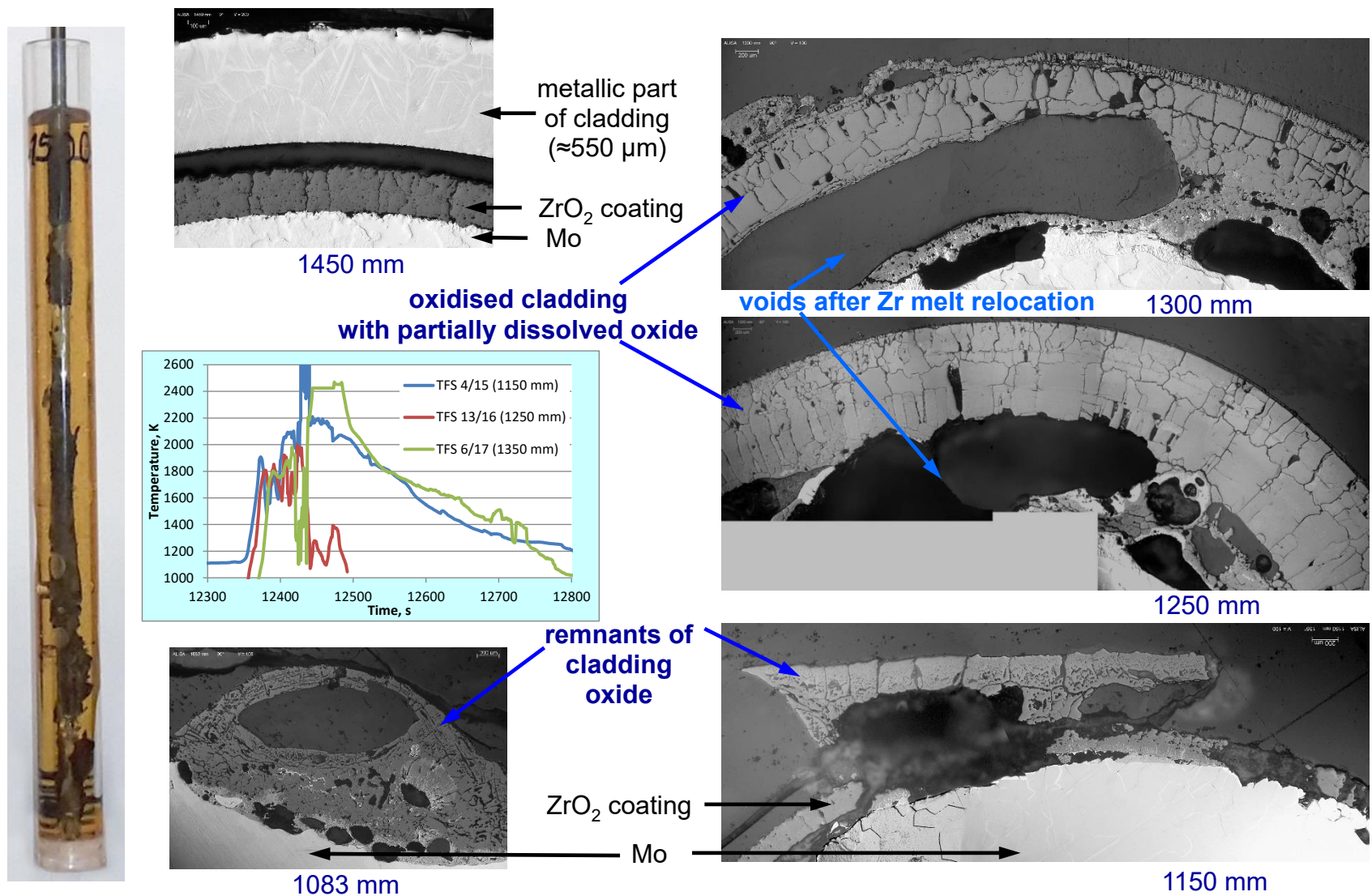
Figure 74 QUENCH-18; Upper part of rod #3 (between 1080 and 1500 mm), broken up during bundle dismounting, and corresponding temperature progressions.
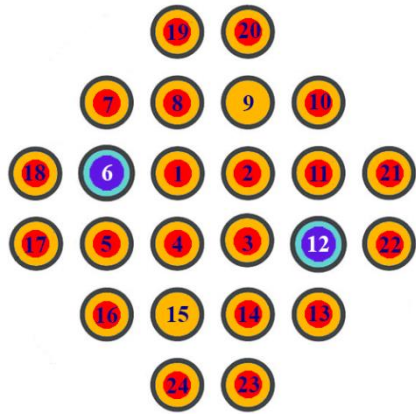
bundle composition at upper elevations

1480 mm: intact rods, slightly oxidized clads
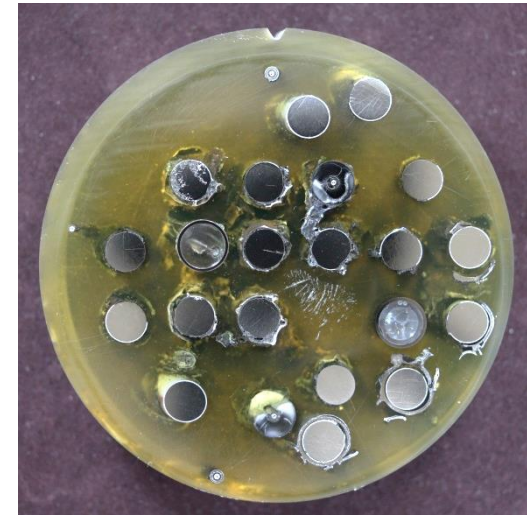
1430 mm (upper grid spacer GS5): loss of clads and GS
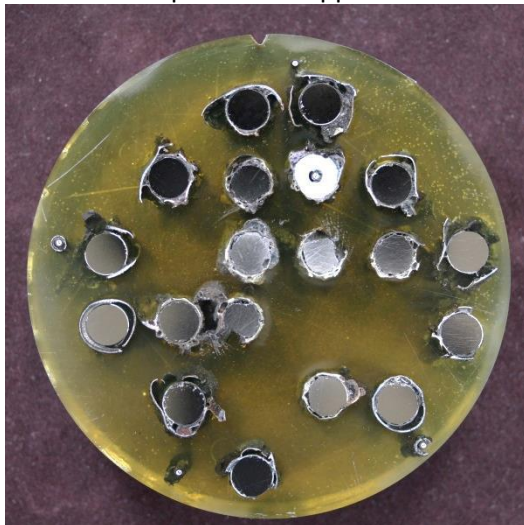
1350 mm: remainders of strongly oxidized clads

1250 mm: remainders of strongly oxidized clads

1150 mm: remainders of strongly oxidized clads

Figure 75   QUENCH-18; Post-test bundle cross-sections (without rods 3 and 23; top view) at upper elevations with coated Mo heaters, as polished.

meaning of signs

1480 mm: low cladding oxidation
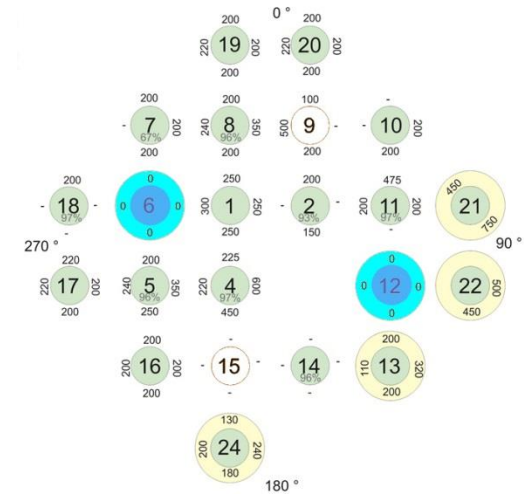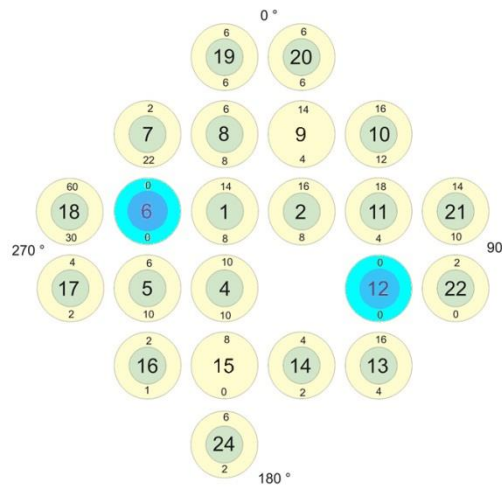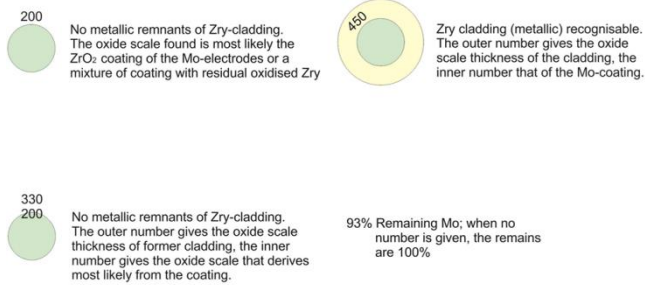
1430 mm: moderate oxidation
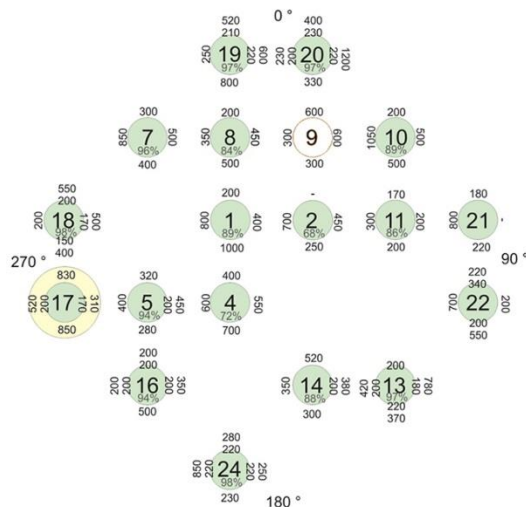
1350 mm: strong oxidation, absence of parts of absorber rods and unheated rod 15
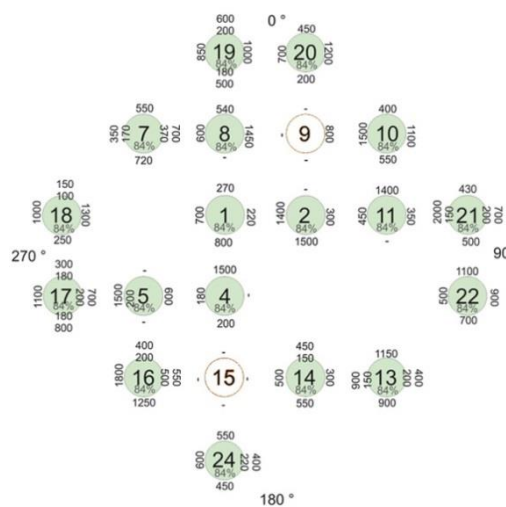
1250 mm: very strong oxidation, absence of parts of absorber rods
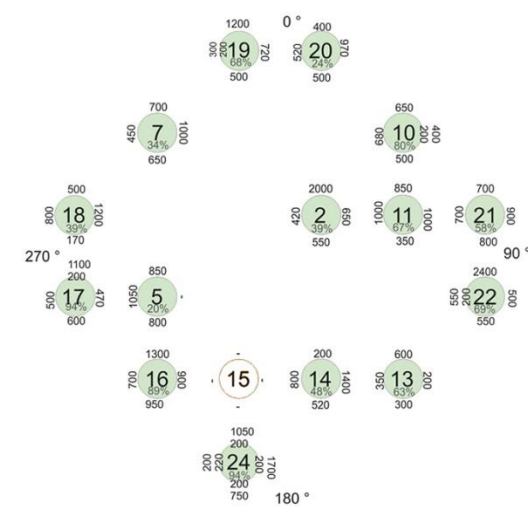
1150 mm: strong oxidation, absence of parts of absorber rods, unheated rod 9, heated rods 1, 4, 8

Figure 76   QUENCH-18; Oxide layer thicknesses at claddings of upper elevations with coated Mo heaters (rods #3 and #23 are withdrawn).
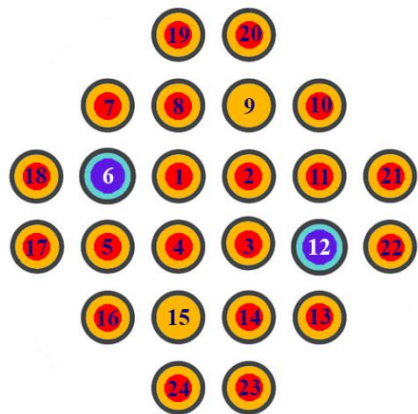
bundle composition
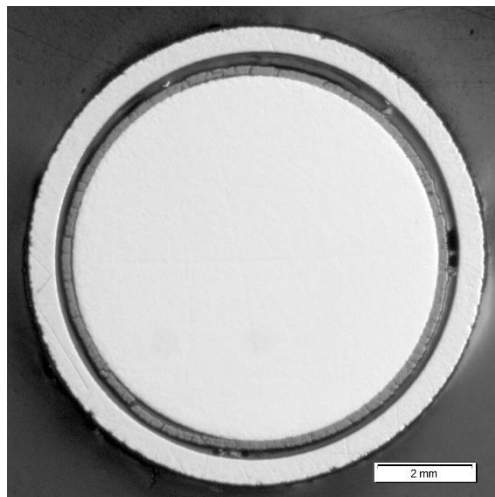
1480 mm: intact rod structure (clad, coating, Mo)
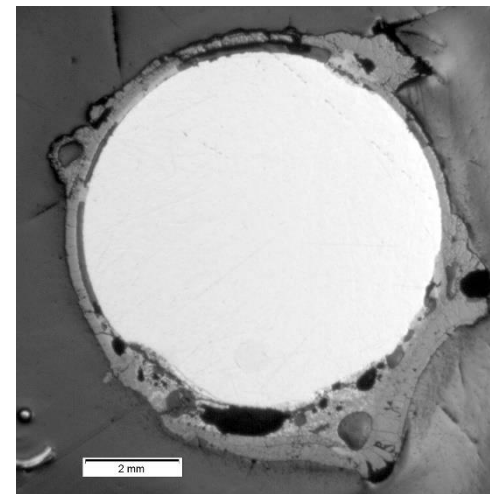
1430 mm: absence of cladding (melted away)
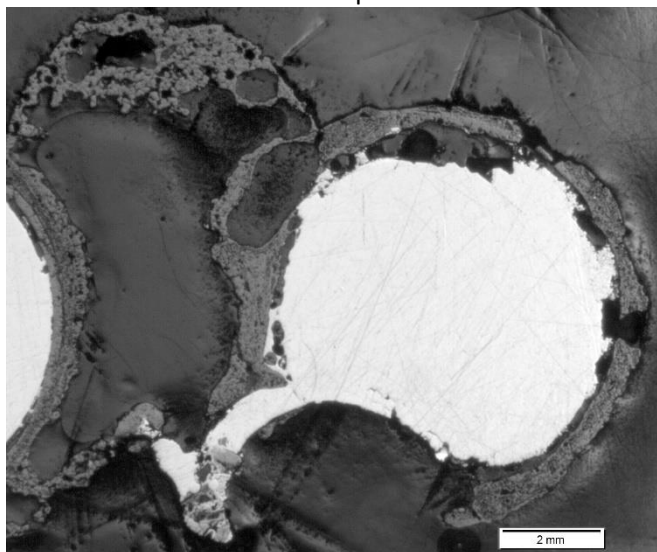
1350 mm: attack of ZrO$_2$ coating (dissolution) and Mo heater (eutectic Mo$_2$Zr at 1550 °C) by molten Zr
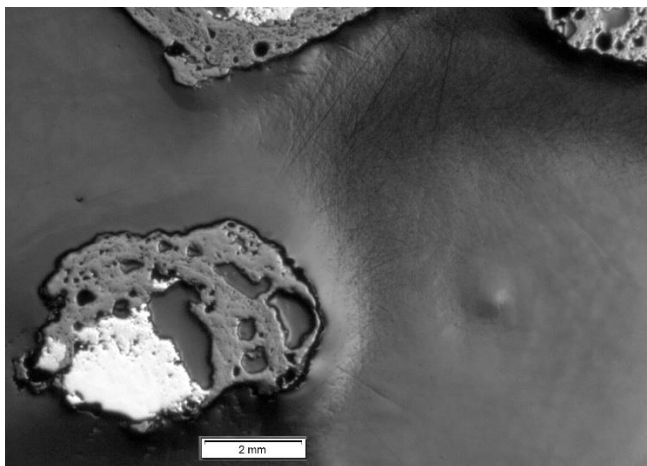
1250 mm: strong degradation of Mo heater

1150 mm

Figure 77 QUENCH-18; cross sections of rod #4 at upper bundle elevations: degradation of Mo heater.
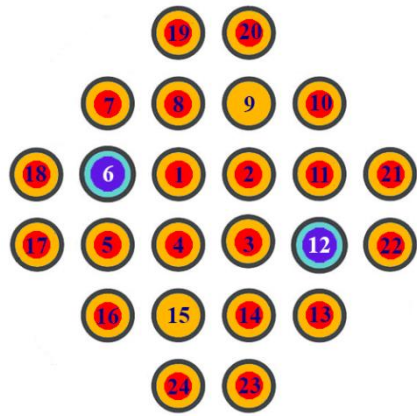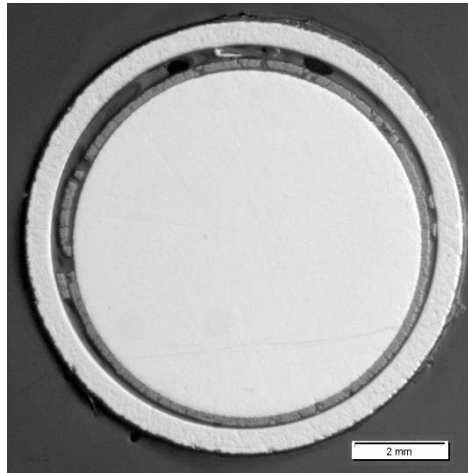
bundle composition

1480 mm: intact rod structure (clad, coating, Mo)
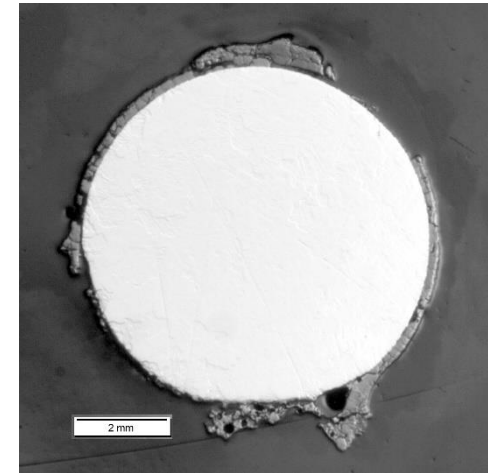
1430 mm: absence of cladding (melted away)
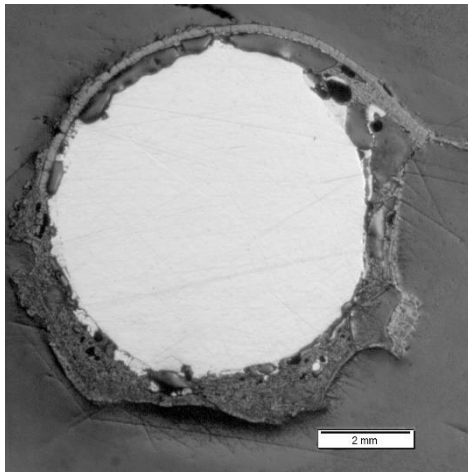
1350 mm: attack of coating and Mo heater by molten Zr cladding (later oxidized)
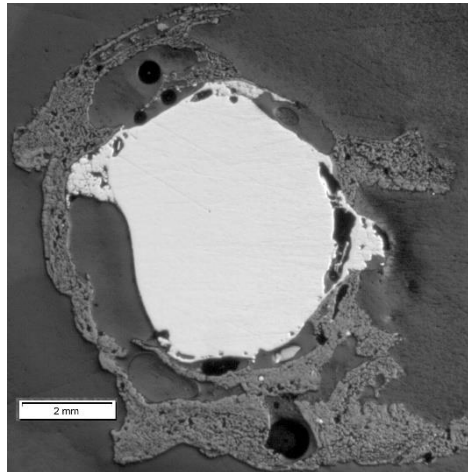
1250 mm: strong Mo degradation and attack of ZrO_2 coating by Zr melt
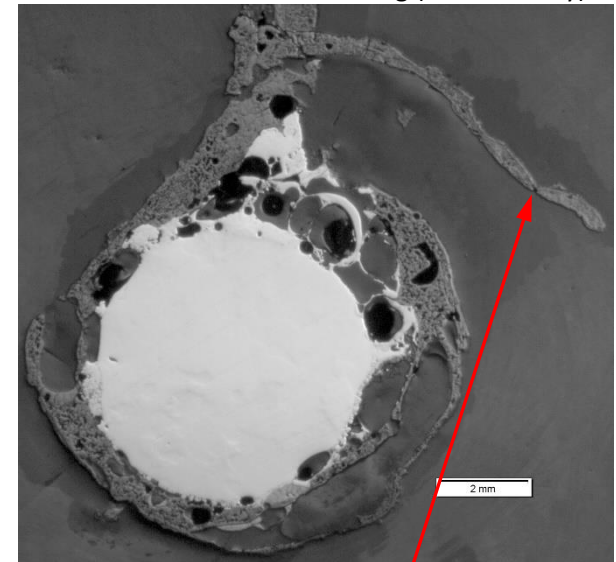
1150 mm: oxidized remnant of cladding

Figure 78   QUENCH-18; cross sections of heated rod #11 at upper bundle elevations: degradation of Mo heater.
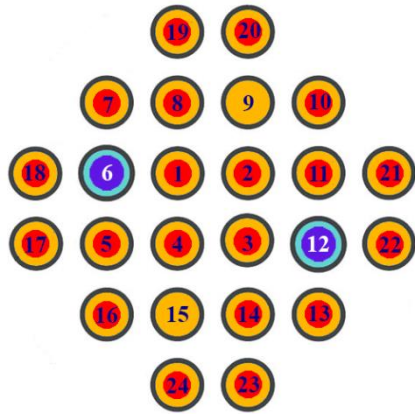
bundle composition
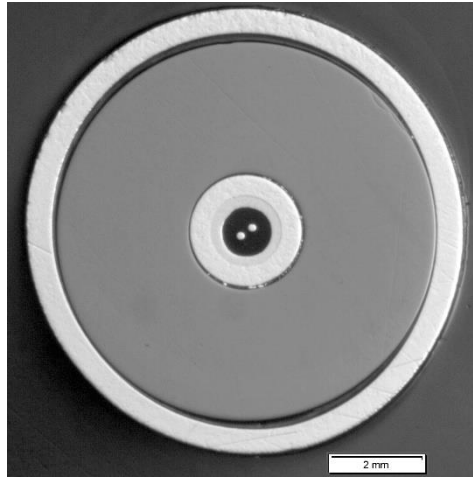
1480 mm: intact rod (clad, pellet, TC with Ta, Zr clads)
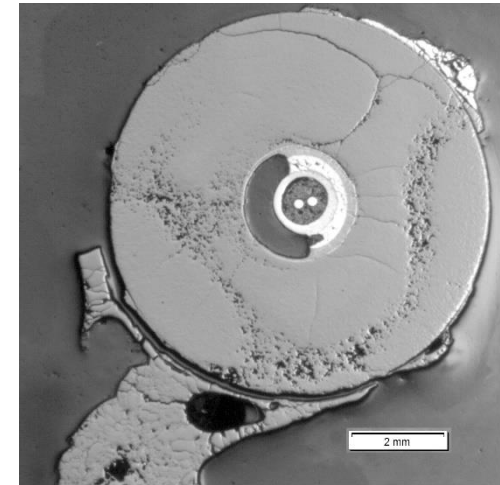
1430 mm: remnants of ox. clad, melted Zr of TC
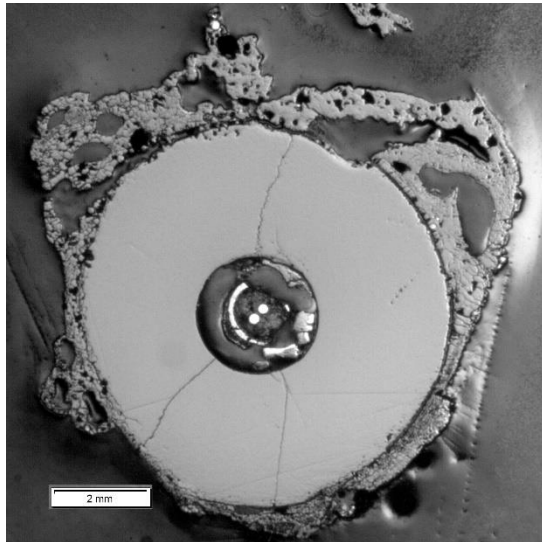
1350 mm: melt attack of pellet
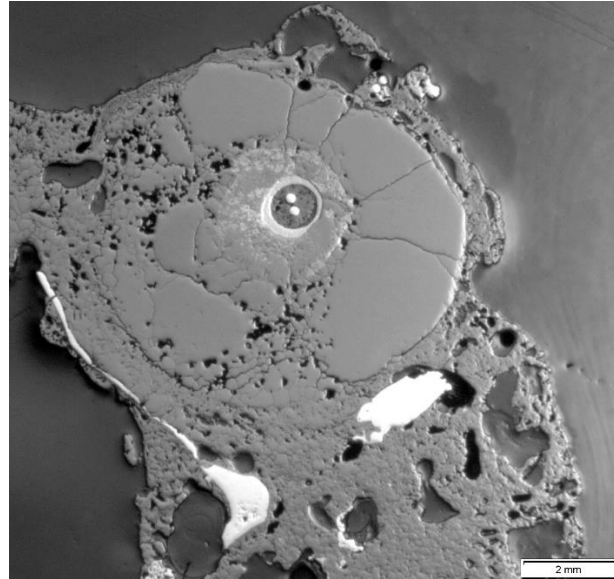
1250 mm: dissolution of pellet by molten Zr cladding

Figure 79   QUENCH-18; cross sections of unheated rod #9 at upper bundle elevations: dissolution of pellet.
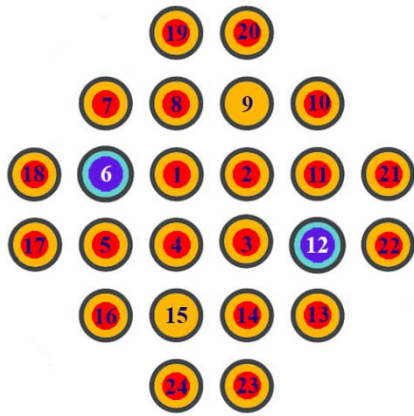
bundle composition
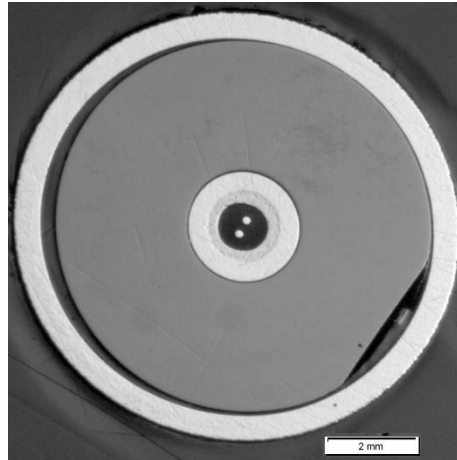
1480 mm: intact rod (clad, pellet, TC with Ta, Zr clads)
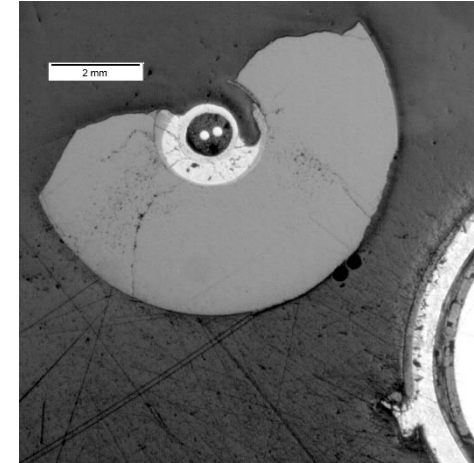
1430 mm: cladding melted away, Zr clad of TC melted
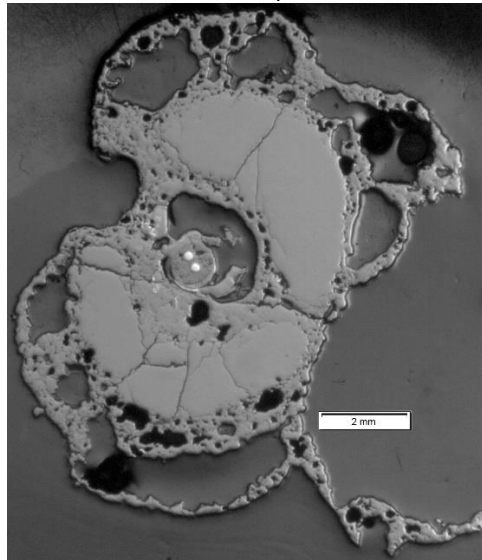
1350 mm

1250 mm: dissolution of pellet by Zr melt
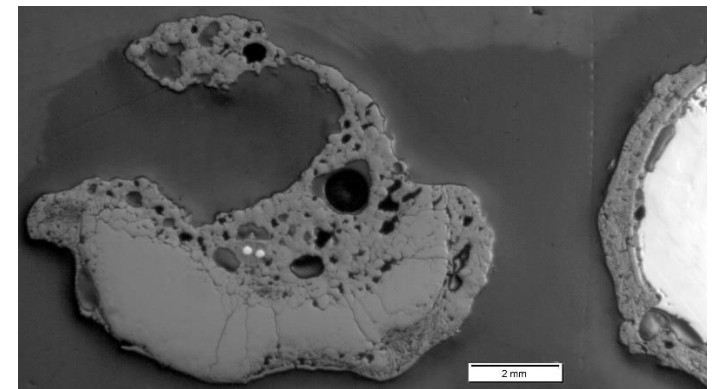
1150 mm: strong dissolution of pellet by melt

Figure 80   QUENCH-18; cross sections of unheated rod #15 at upper bundle elevations: dissolution of pellet.

Mo+W layer from sublimated heaters

outer oxide layer

cladding melt

inner oxide layer

ZrO$_2$ coating of Mo heater

Mo heater

rod #22, 1430 mm

rod #17, 1350 mm: more melt due to relocation from upper elevations
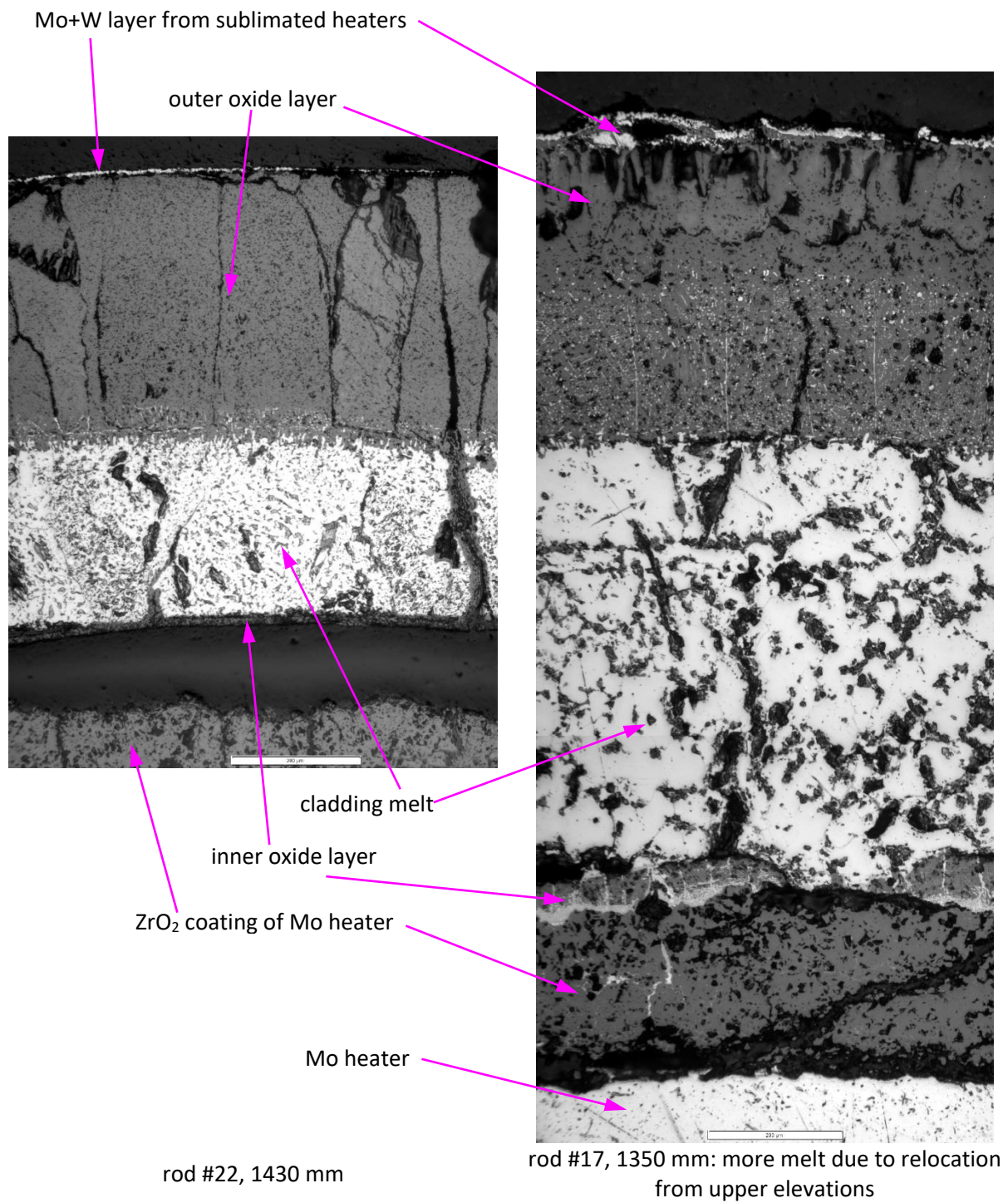
Figure 81   QUENCH-18; structure of cladding layers at elevations 1350 and 1430 mm.
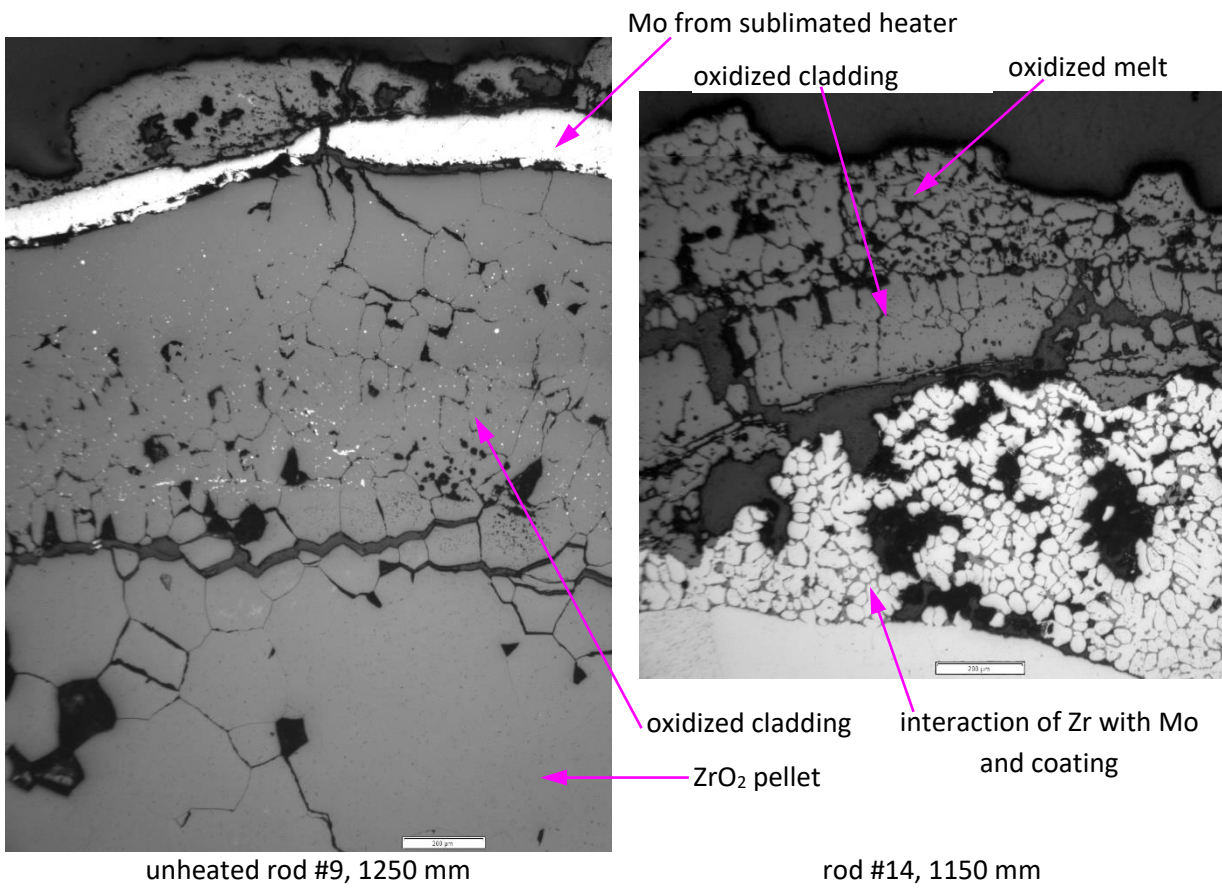
Figure 82   QUENCH-18; structure of cladding and melt layers at elevations 1150 and 1250 mm.

950 mm: local pools of completely oxidized melt

750 mm: local pools of oxidized melt

560 mm: melt collection inside grid spacer

350 mm: local molten pool at bundle periphery formed by relocated molten shroud
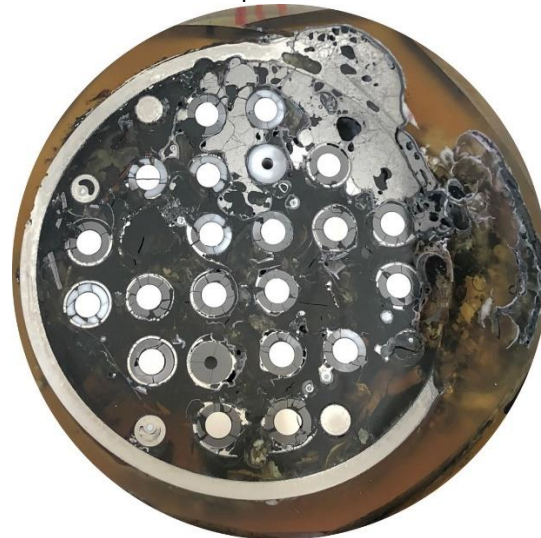
160 mm: local molten pool at bundle periphery formed by relocated molten shroud
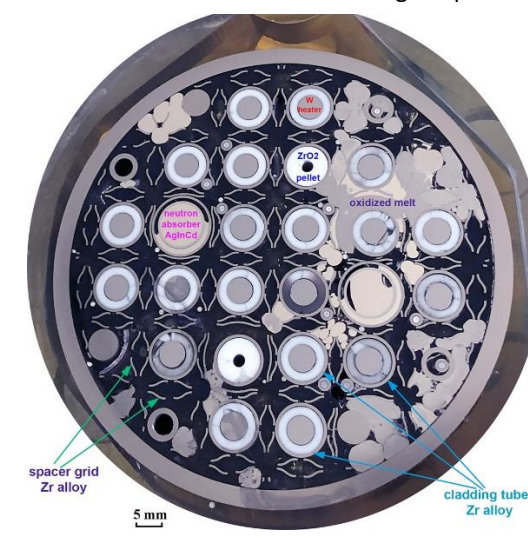
65 mm: absorber molten pools and partially oxidized Zr molten pools

Figure 83 QUENCH-18; redistribution of cladding melt and absorber melt between bundle elevations.
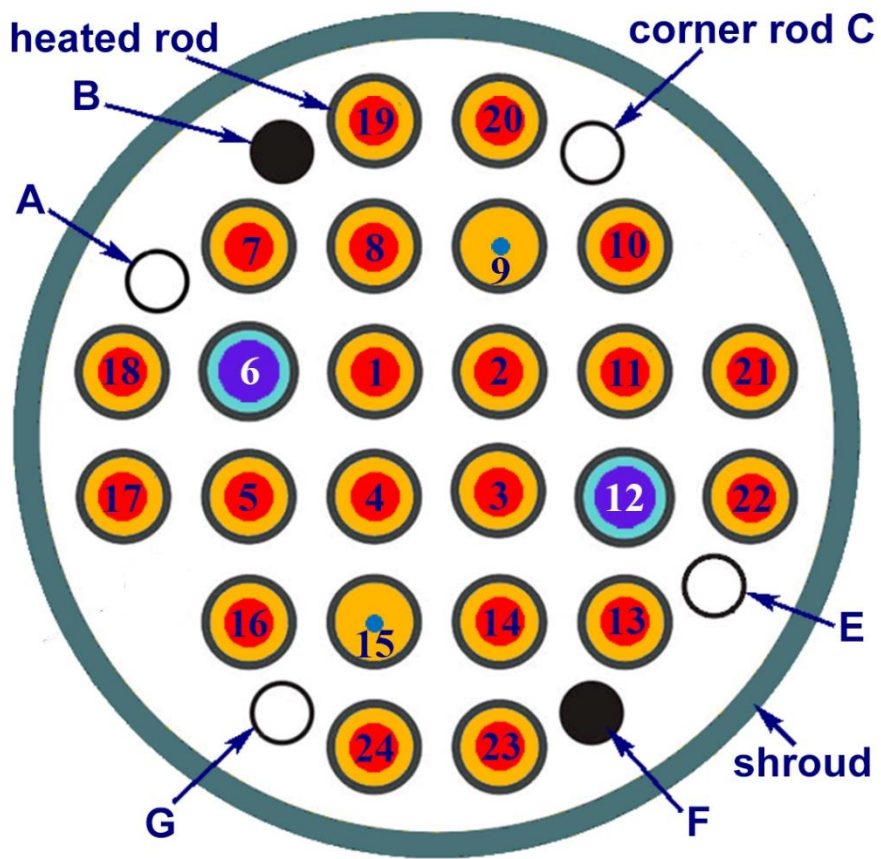
bundle composition, corner rods D and H are withdrawn
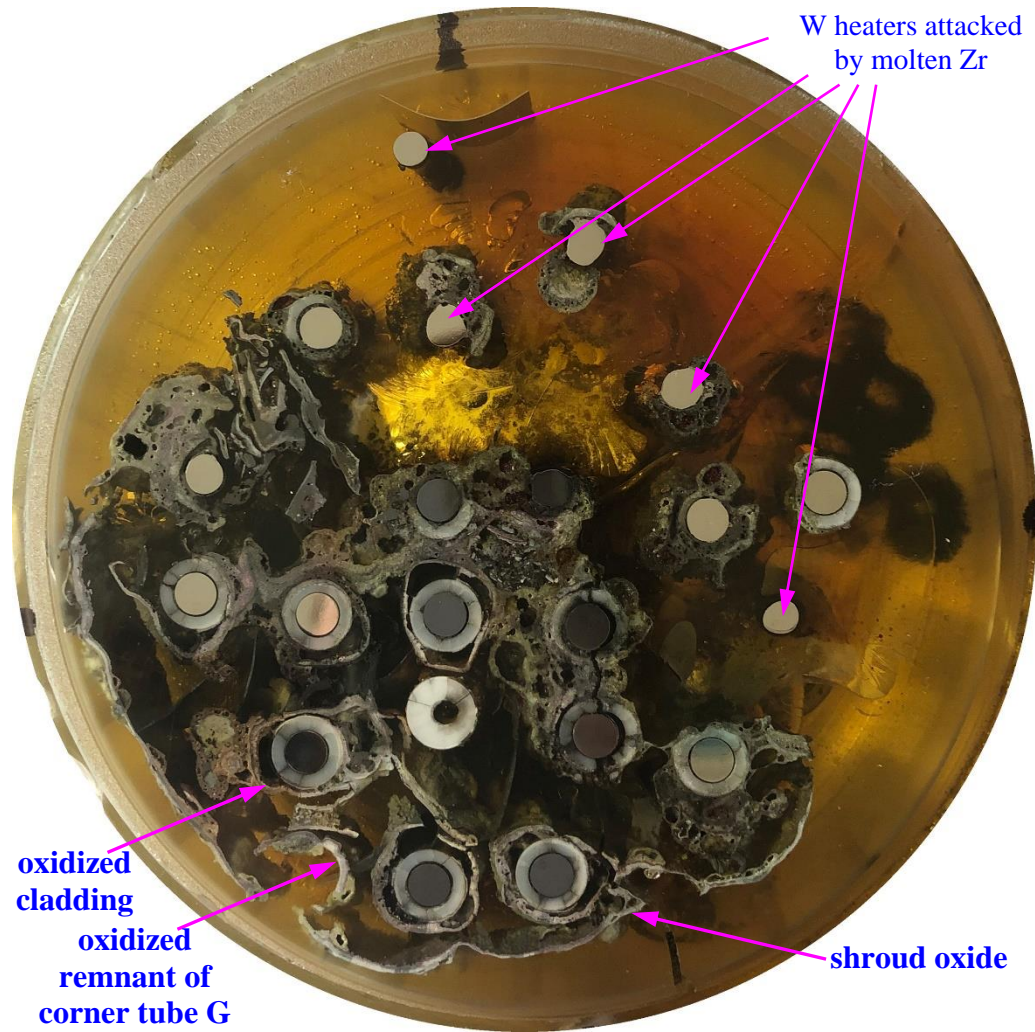
cross section, top view (perspective projection): melt and debris of unheated rod 9 and corner rods relocated downwards

Figure 84   QUENCH-18; cross section at bundle elevation 950 mm.
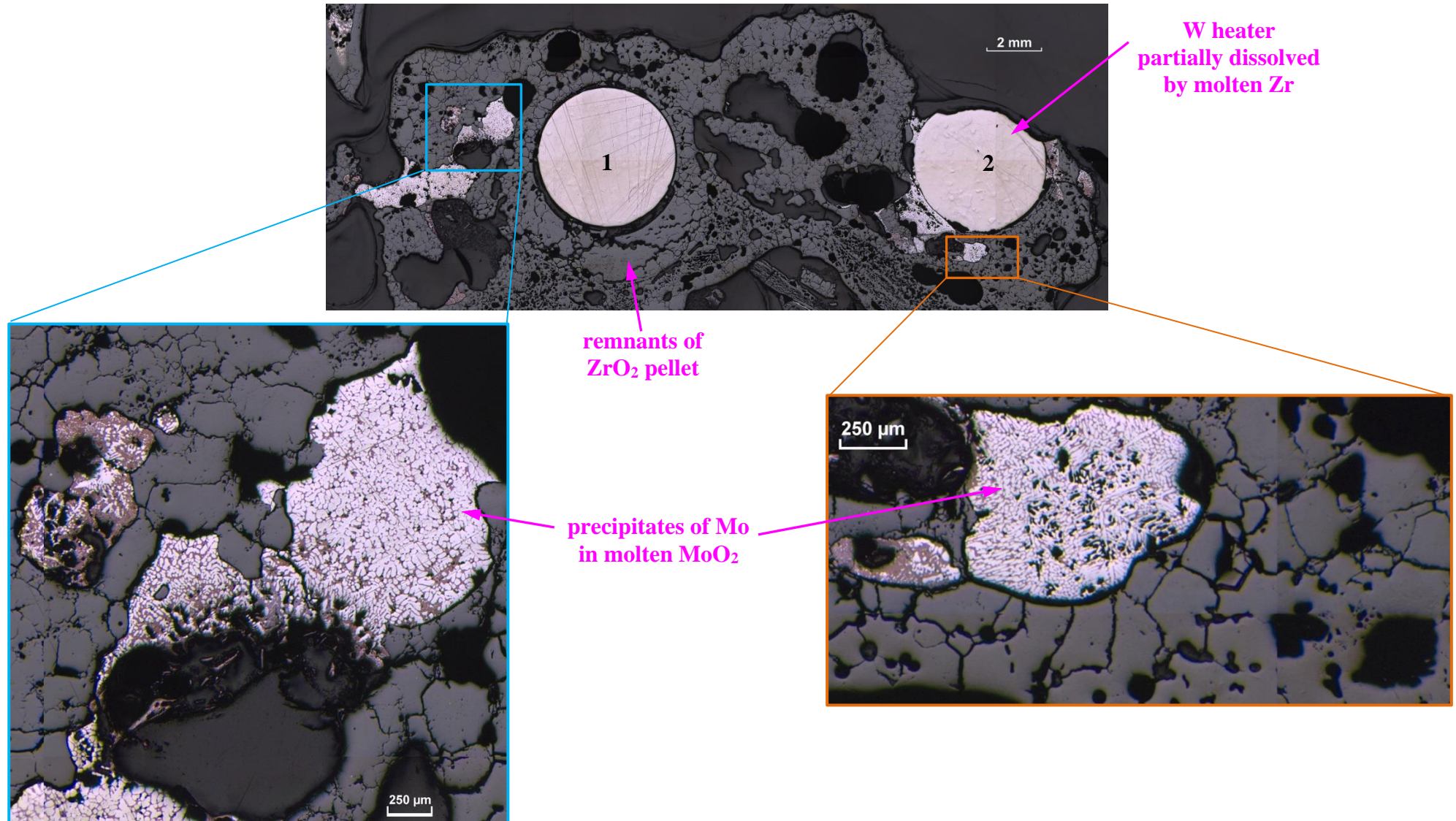
Figure 85 QUENCH-18, elevation 950 mm; completely oxidized very porous ZrO_2 melt between rods #1 and #2 with inclusions of partially oxidized Mo; partial dissolution of pellet #1 and completely dissolved (by molten Zr) pellet #2.
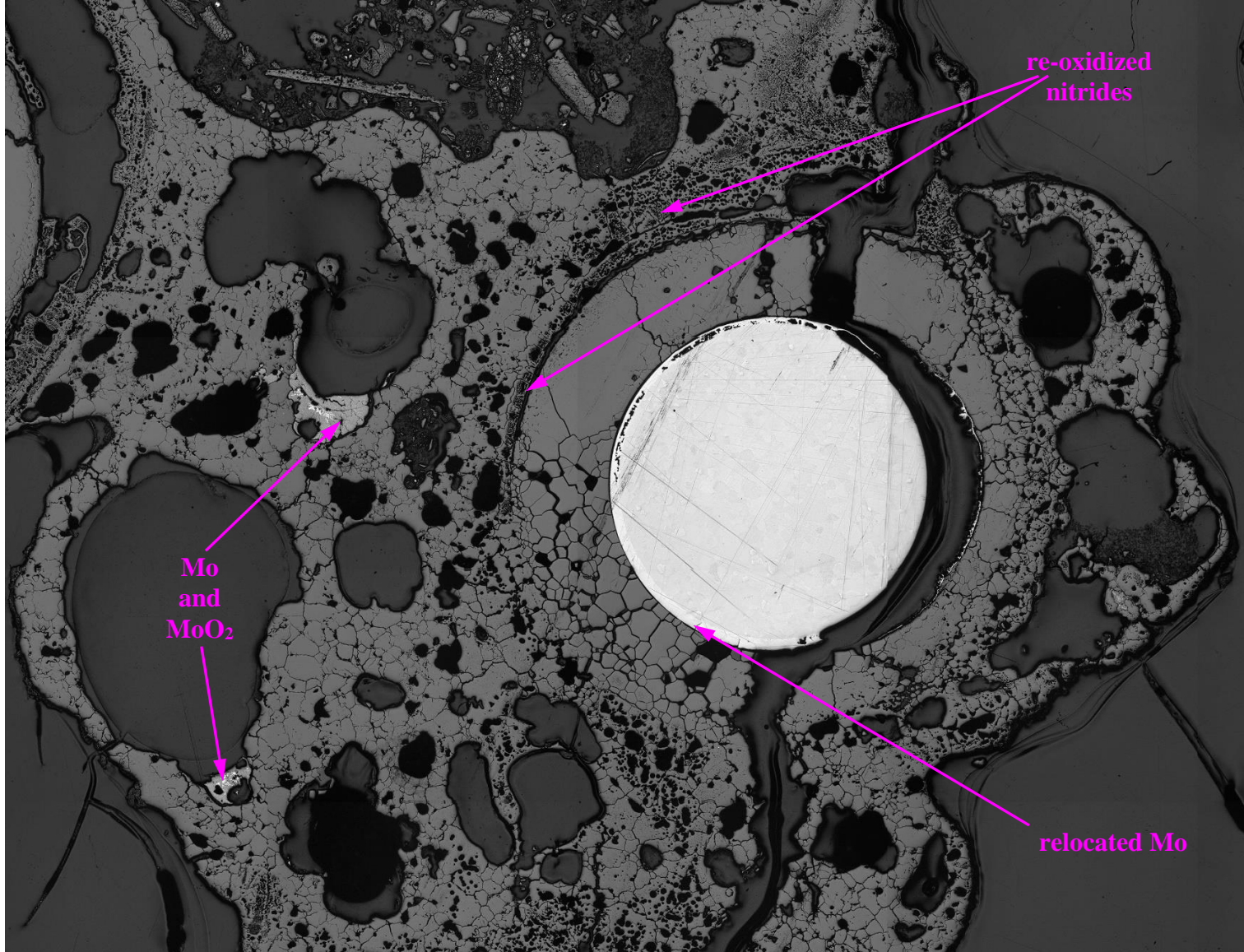
Figure 86   QUENCH-18; oxidized melt around rod #3 at the elevation 950 mm, strong destruction of pellet (partial dissolution by Zr melt).
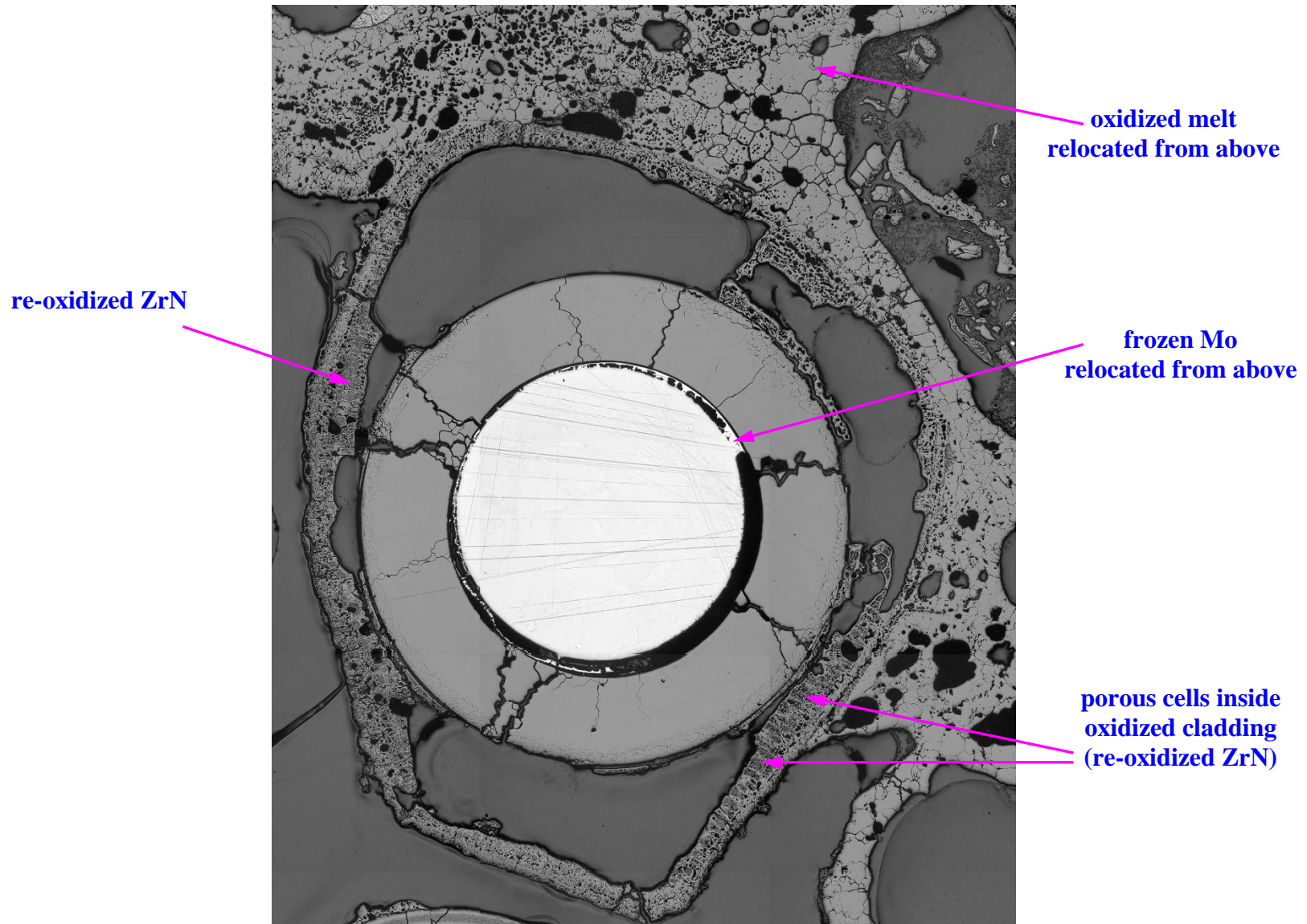
Figure 87   QUENCH-18; elevation 950 mm: oxidized cladding of rod #4 with re-oxidized nitrides at inner cladding surface and oxidized melt in the neighborhood.
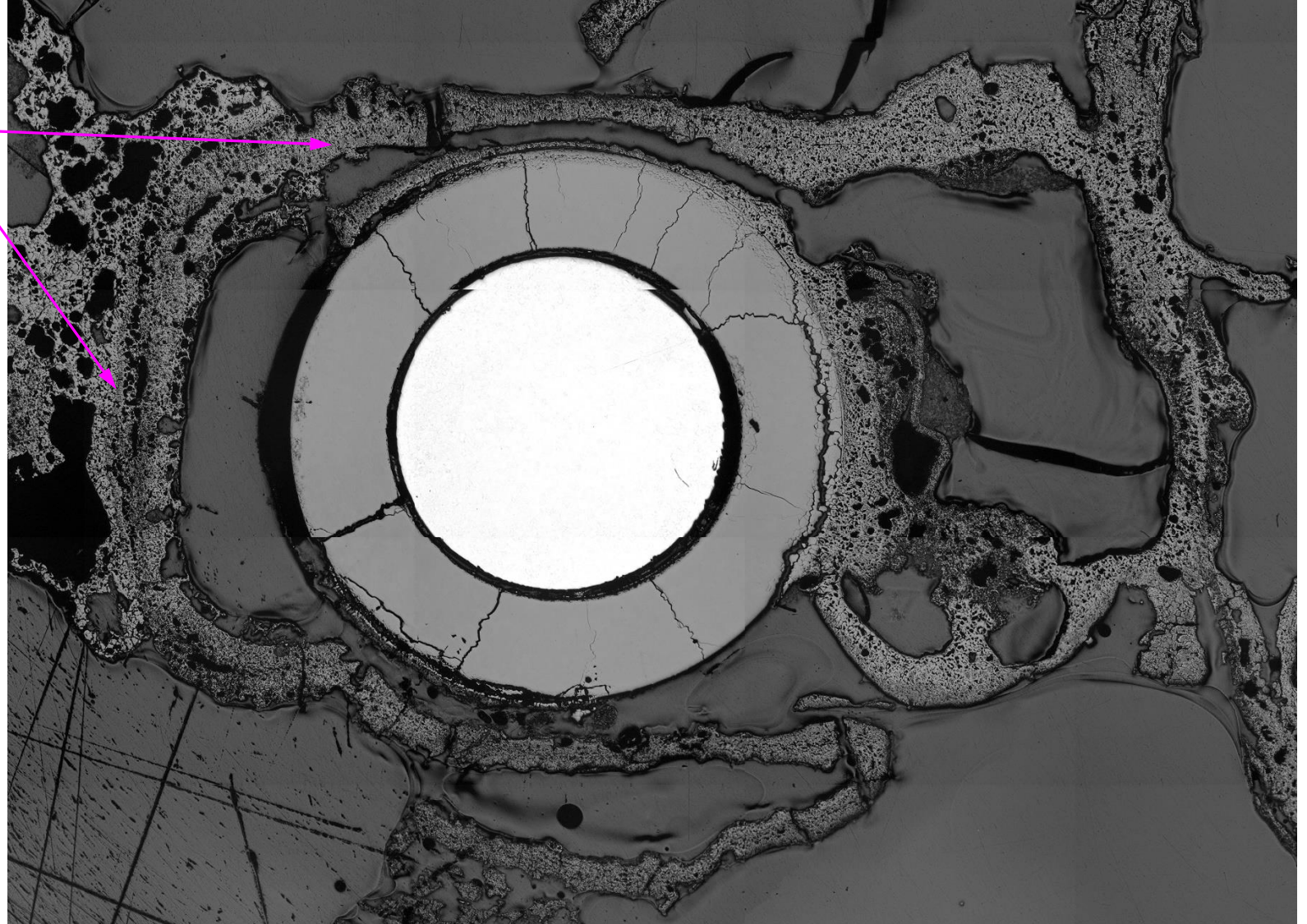
Figure 88   QUENCH-18; oxidized cladding of rod #16 at elevation 950 mm.
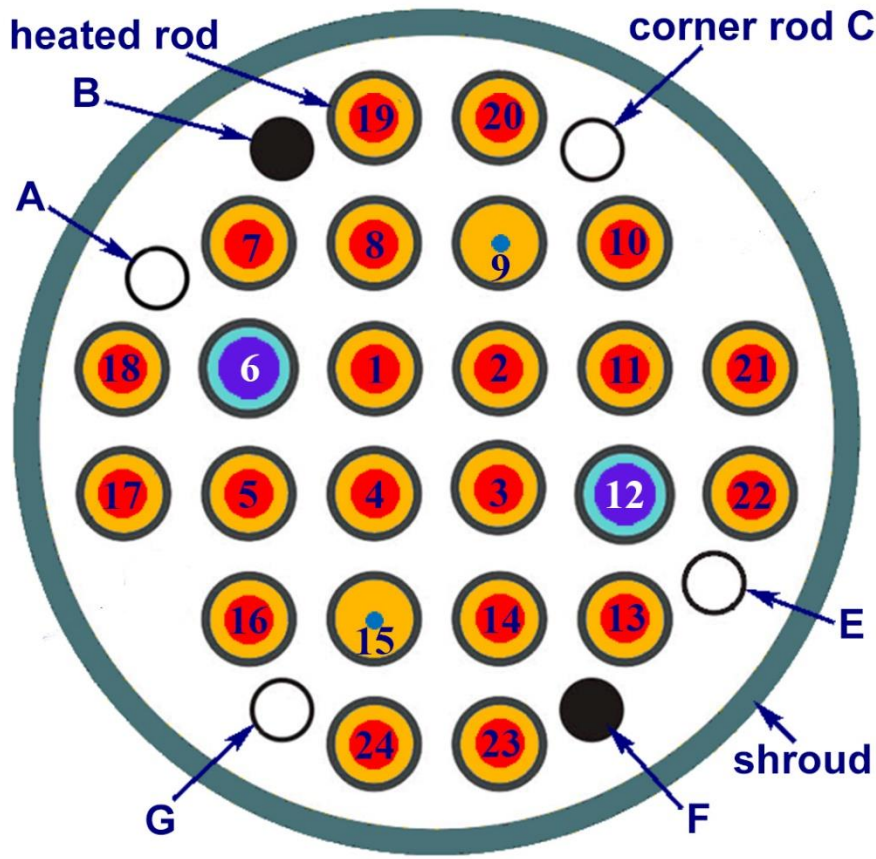
bundle composition, corner rods D and H are withdrawn
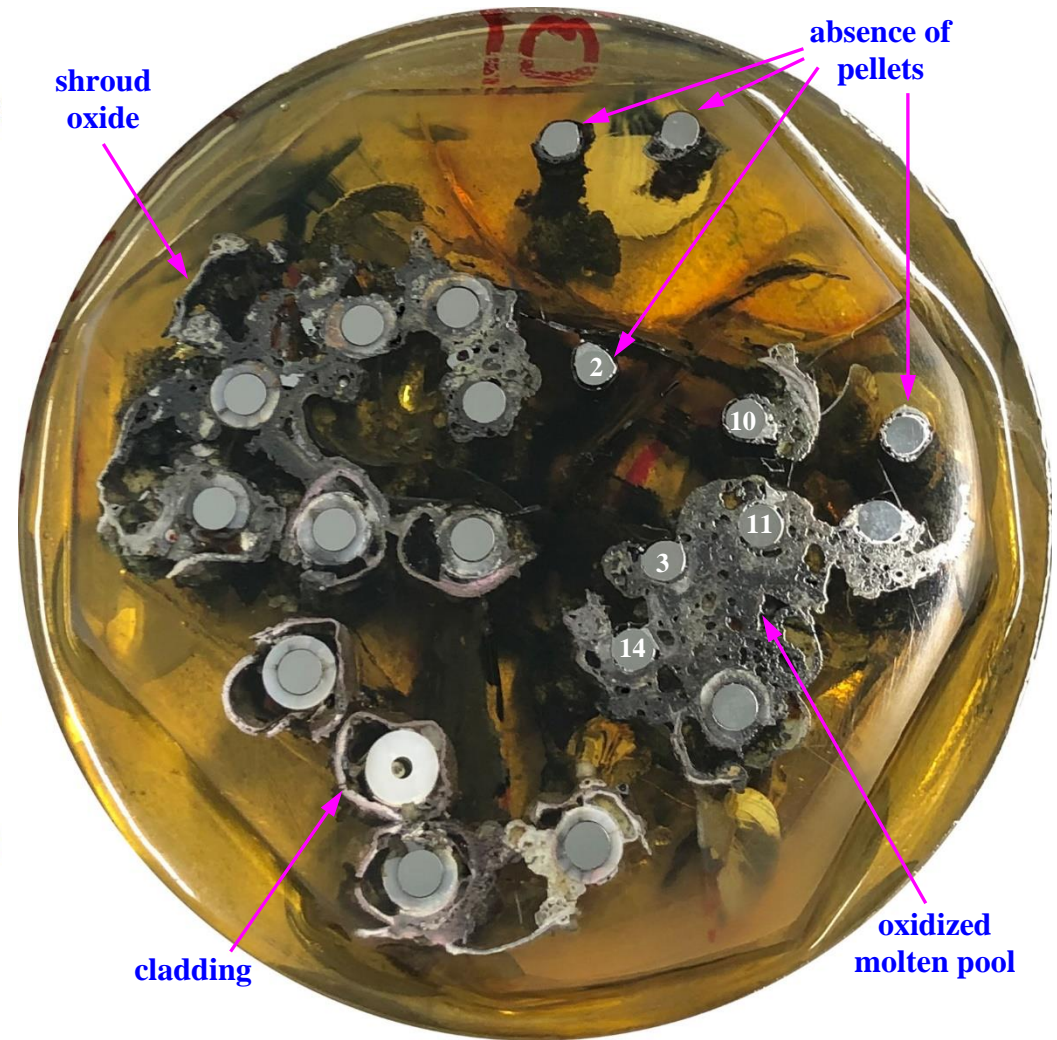
cross section top view (perspective projection): melt and debris of unheated rod 9 and corner rods relocated downwards

Figure 89 QUENCH-18; cross section at bundle elevation 750 mm.
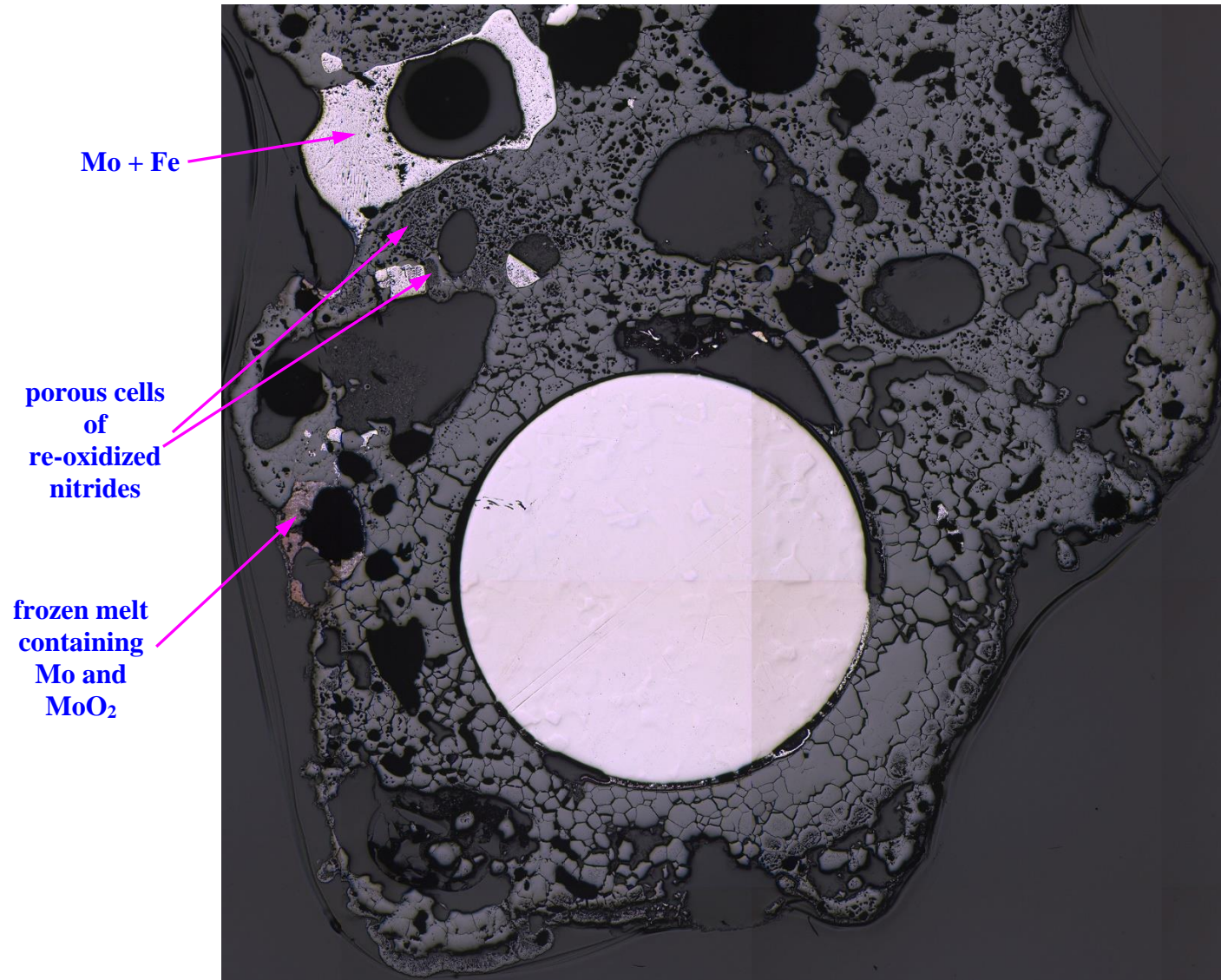
Figure 90   QUENCH-18; heated rod #1 at bundle elevation 750 mm: porous structure of completely oxidized melt, destruction of pellet due to interaction with previously metallic melt.
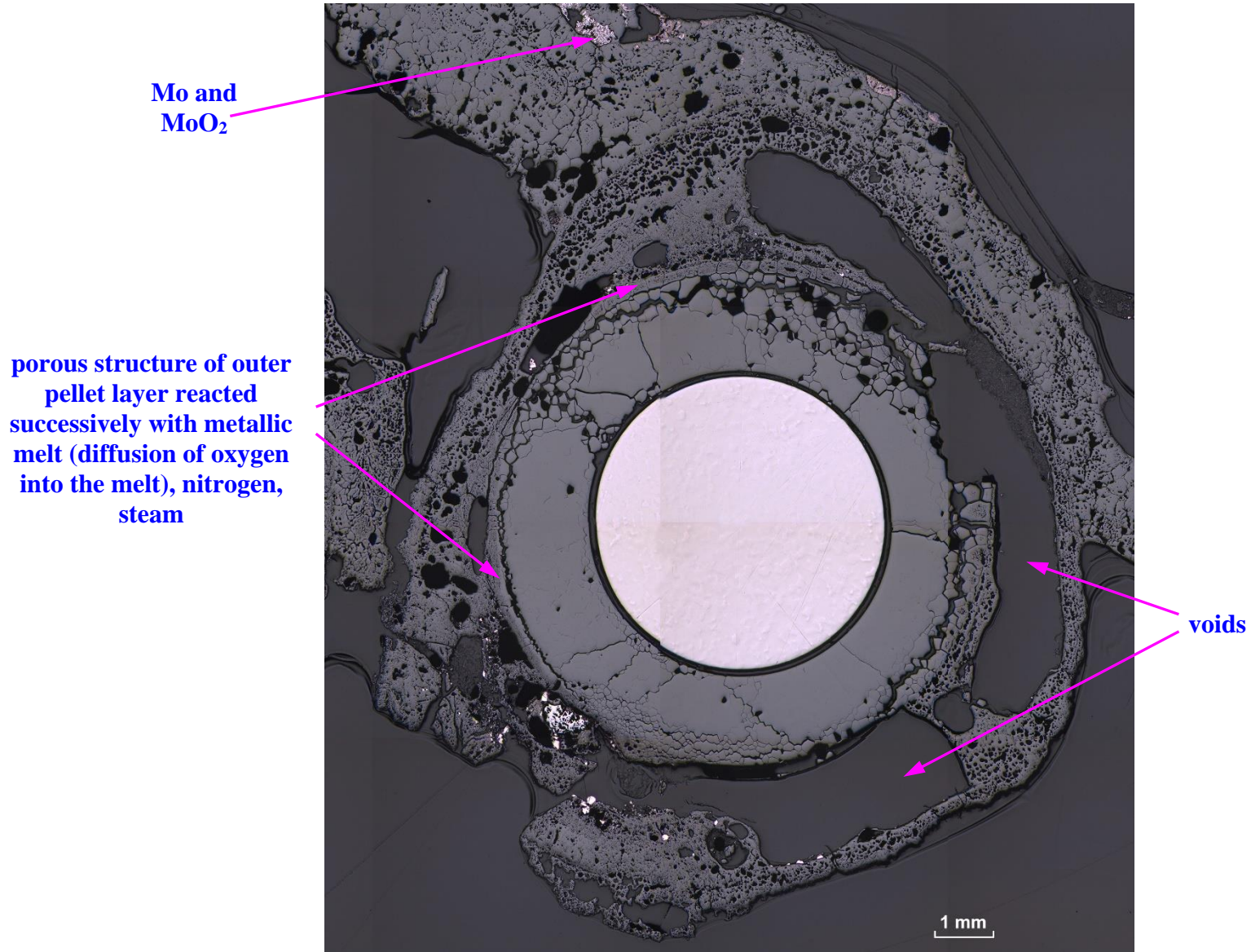
Figure 91   QUENCH-18; heated rod #5 at bundle elevation 750 mm: large voids inside oxidized melt formed during downwards relocation of metallic melt.

completely oxidized part of the cladding not dissolved by metallic melt

oxidized melt

1 mm
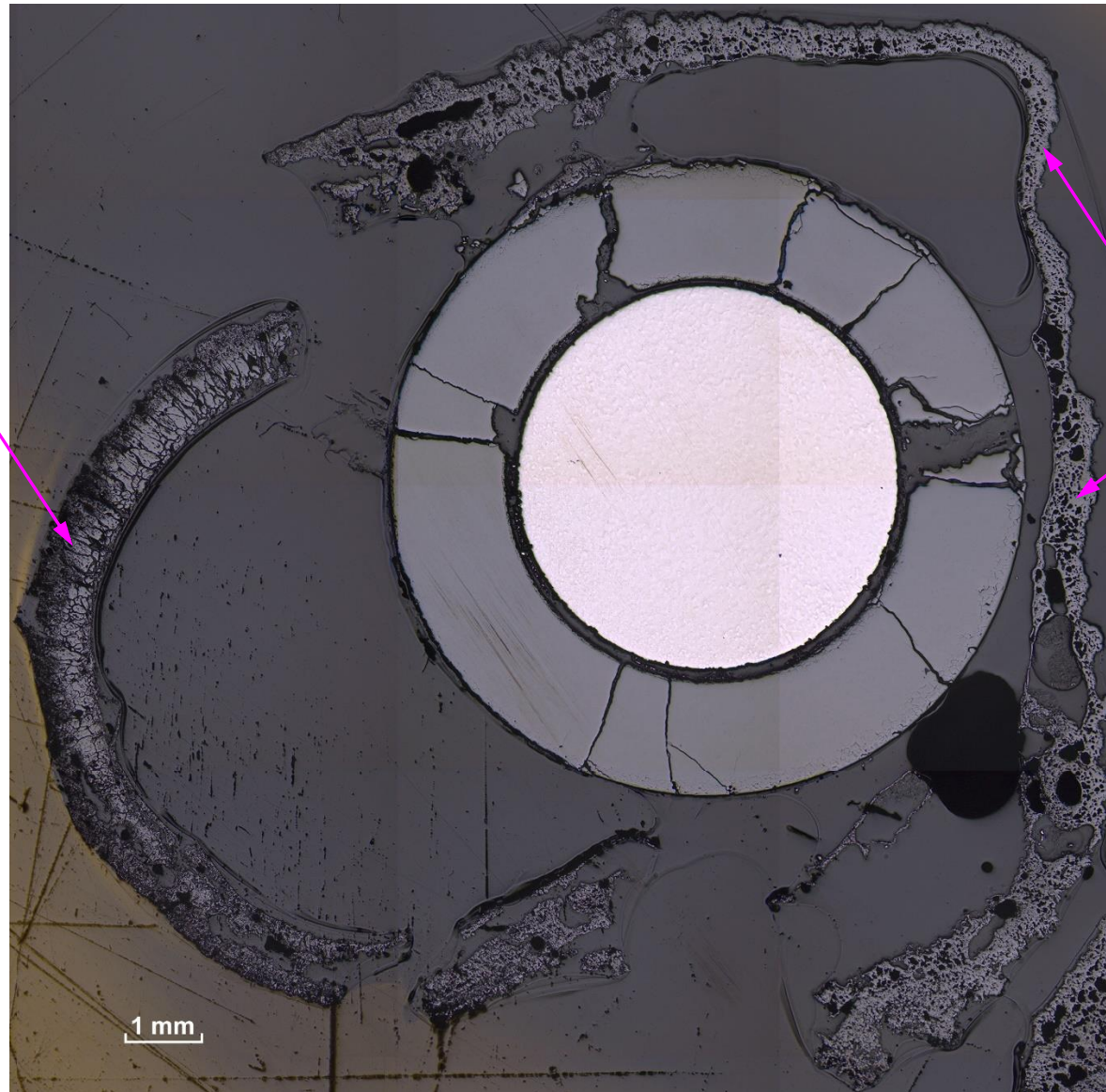
Figure 92   QUENCH-18; heated rod #16 at bundle elevation 750 mm: oxidized structures in surroundings of rod.
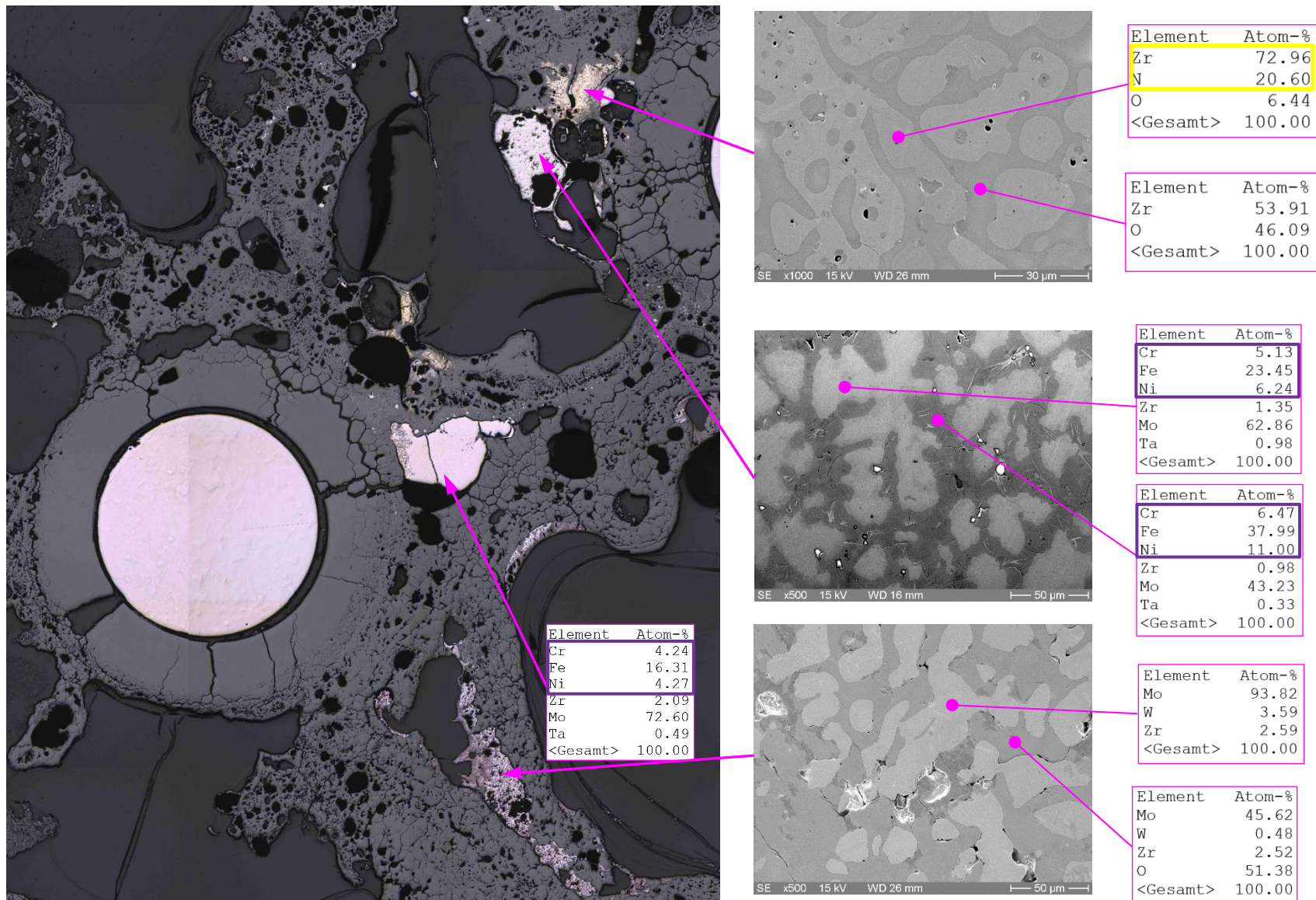
Figure 93 QUENCH-18; heated rod #18 at bundle elevation 750 mm: roughly elemental composition of frozen molten pools, traces of absorber cladding (Fe, Cr, Ni) from neighbour rod #6 and nitrides ZrN; fragments of Mo heater relocated from above.

void at the position of pellet dissolved by Zr melt relocated downwards

completely oxidized Zr melt frozen at the boundary to ZrO$_2$ pellet
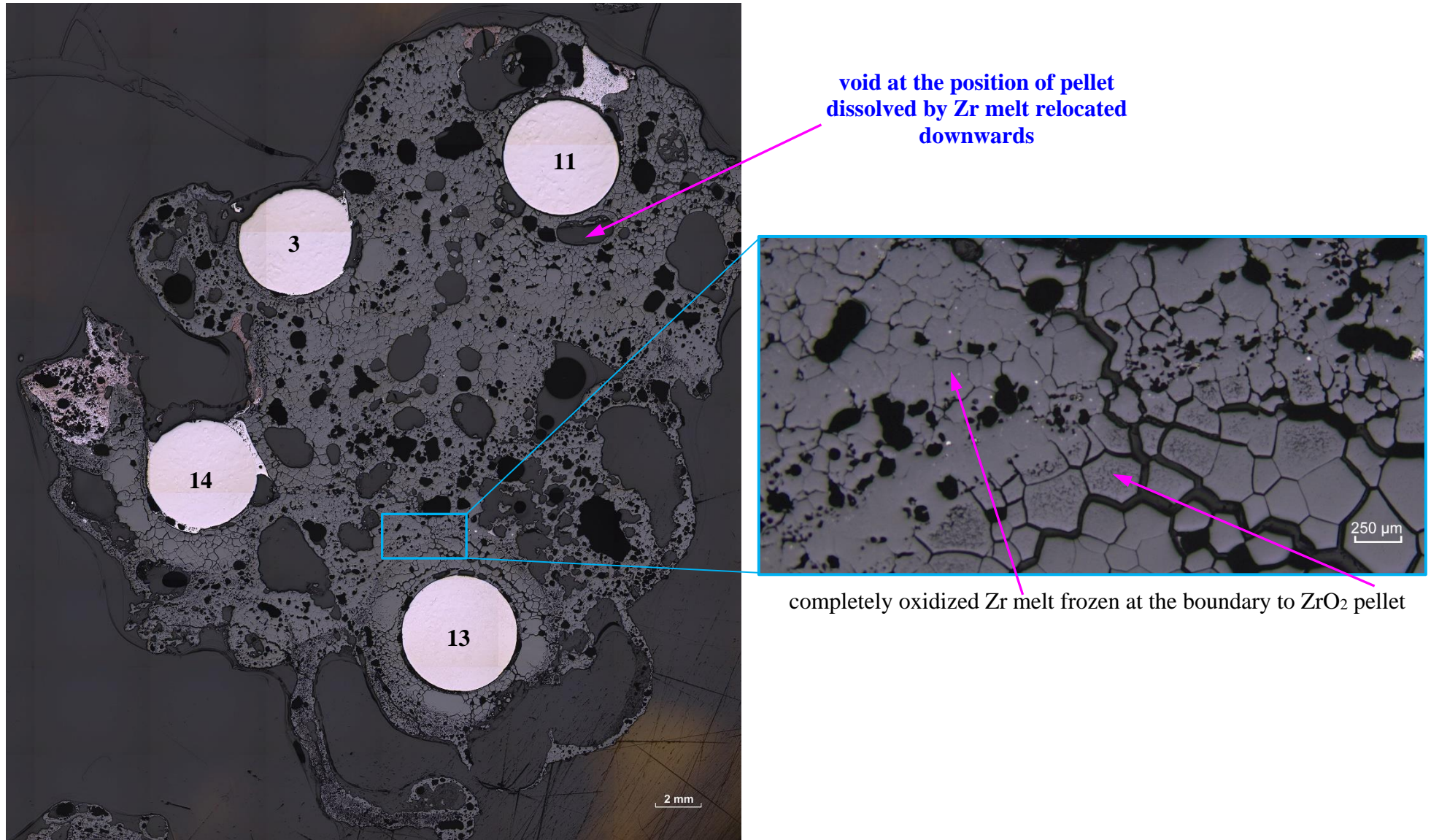
Figure 94   QUENCH-18, elevation 750 mm; completely oxidized porous molten pool relocated from above and formed in the place of vanished absorber rod #12.
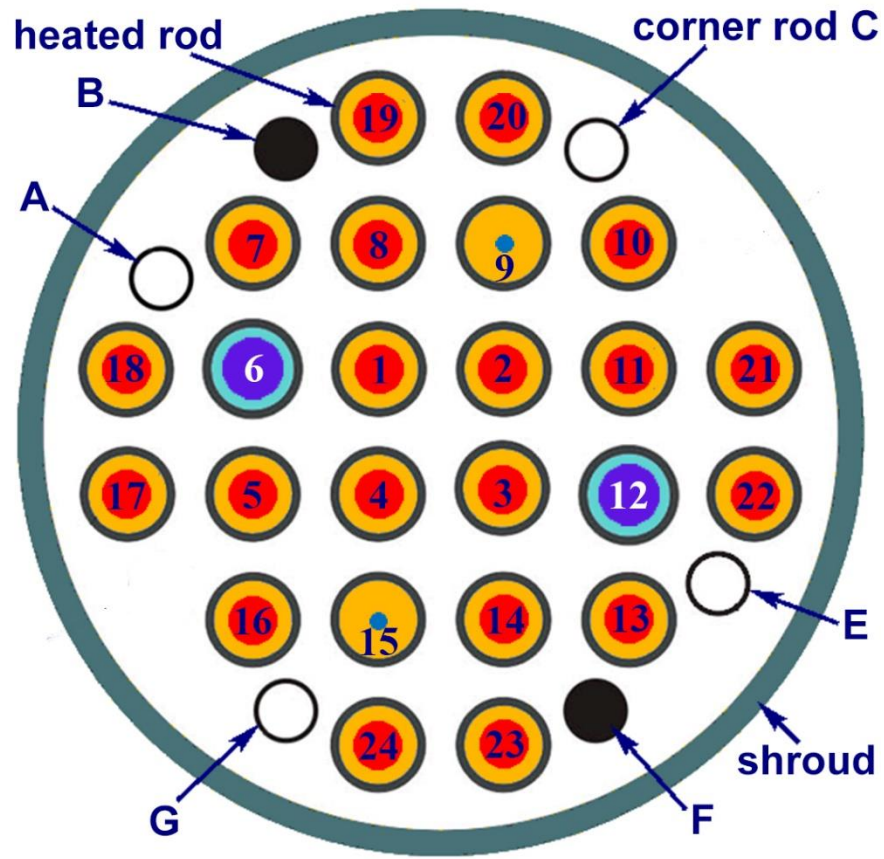
bundle composition, corner rods D and H are withdrawn
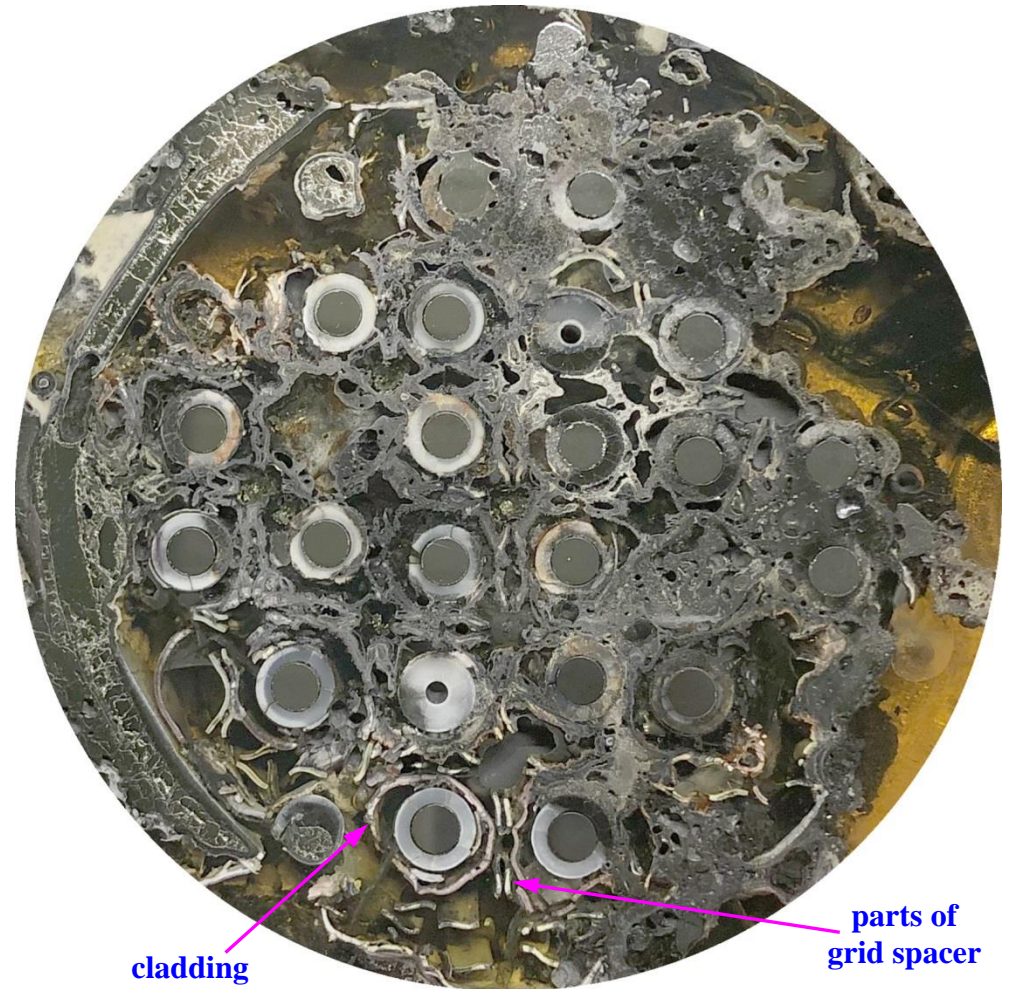
cross section top view(perspective projection),
mirrored bottom of slice 560 - 580 mm

Figure 95 QUENCH-18; cross section at bundle elevation of 560 mm, oxidized melt inside grid spacer, moderate bundle blockage.
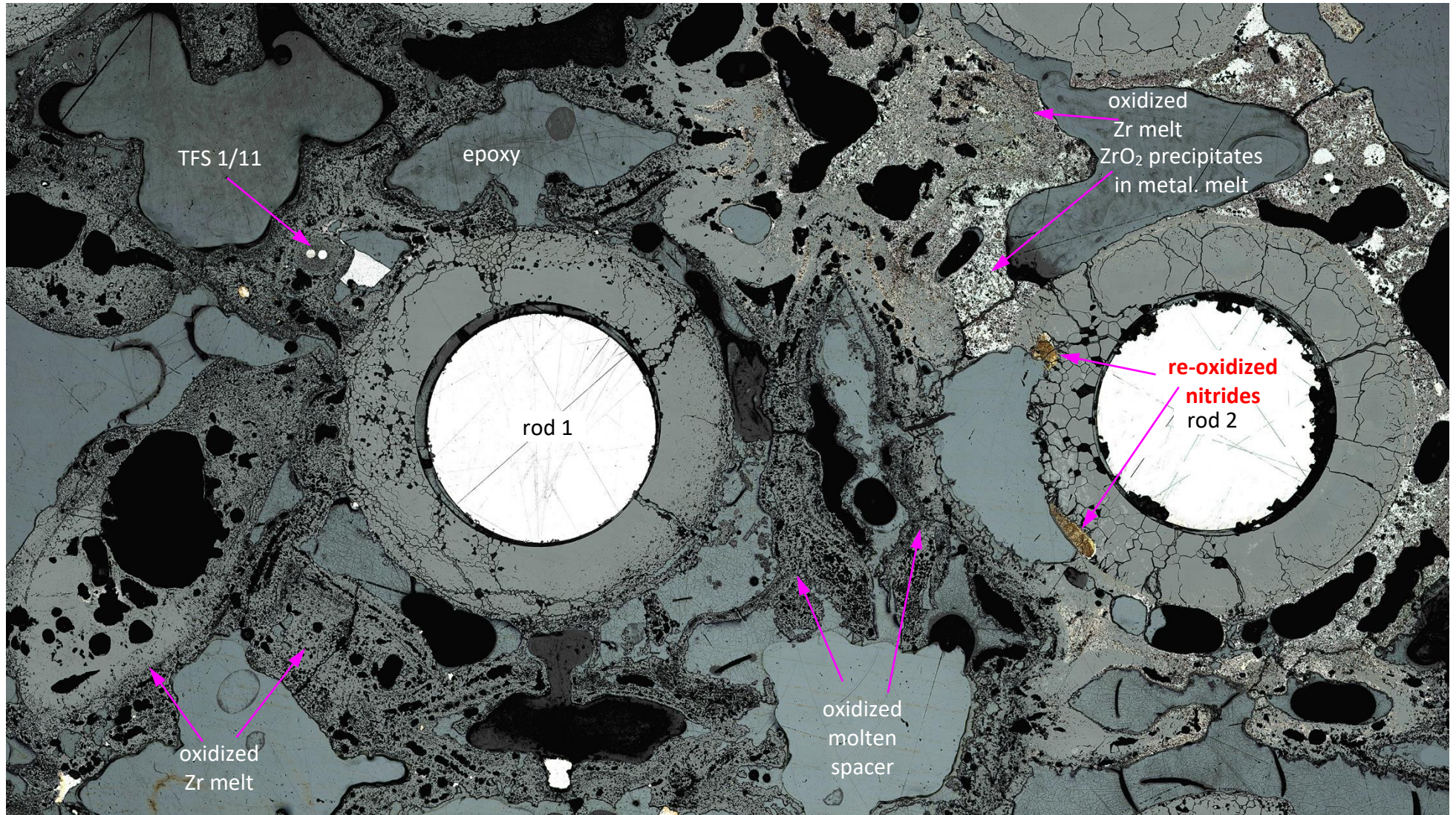
Figure 96 QUENCH-18; surroundings of heated rods 1 and 2 at elevation 560 mm, top view.
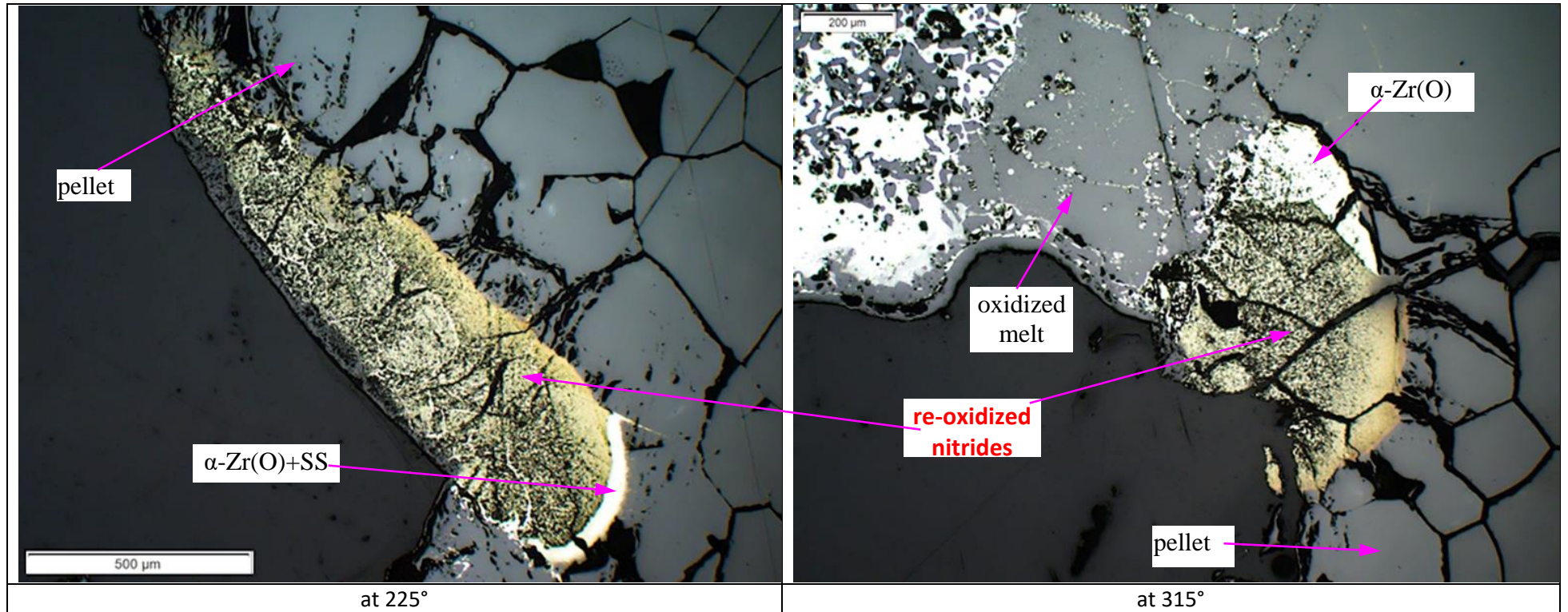
Figure 97 QUENCH-18, re-oxidized nitrides at the outer pellet side of the rod 2 at the elevation 560 mm, top view.
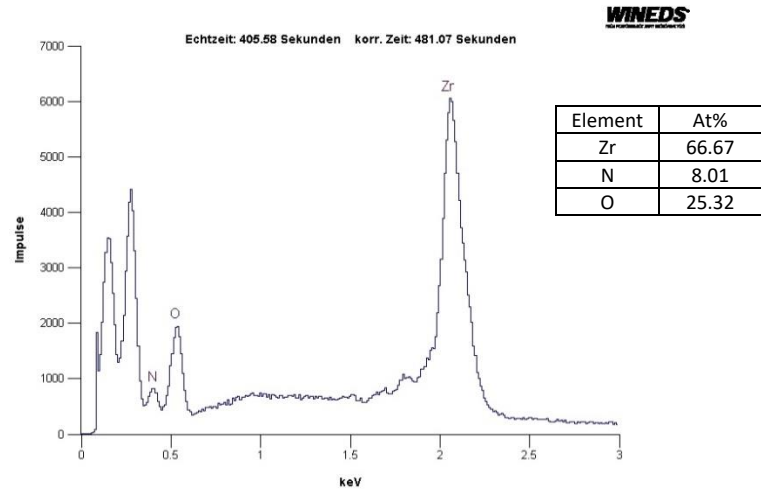
EDX of porous nitride/oxide region at 225°

Element	At%
Zr	66.67
N	8.01
O	25.32

Element	At%
Zr	58.53
N	15.05
O	26.42

EDX of porous nitride/oxide region at 315°

Element	At%
Zr	53.78
O	11.04
Fe	21.65
Cr	6.07
Ni	4.21
Ta	3.25

EDX of "α-Zr(O)+SS" part at 225°

Element	At%
Zr	62.09
O	11.57
Fe	4.40
Cr	5.28
Ni	0.31
N	16.35
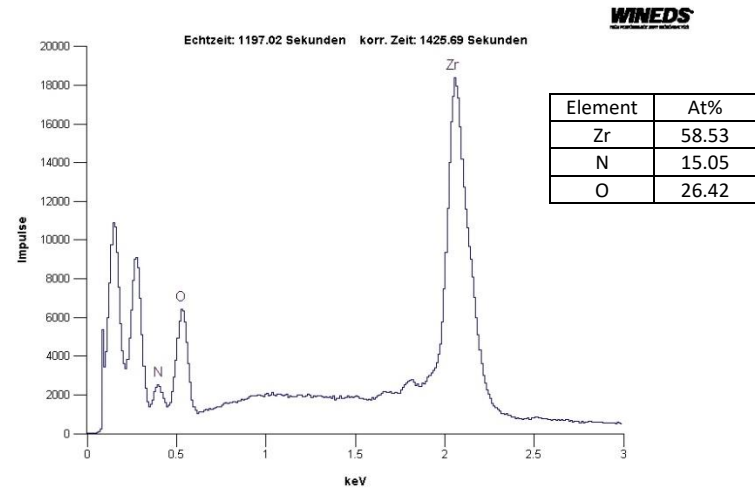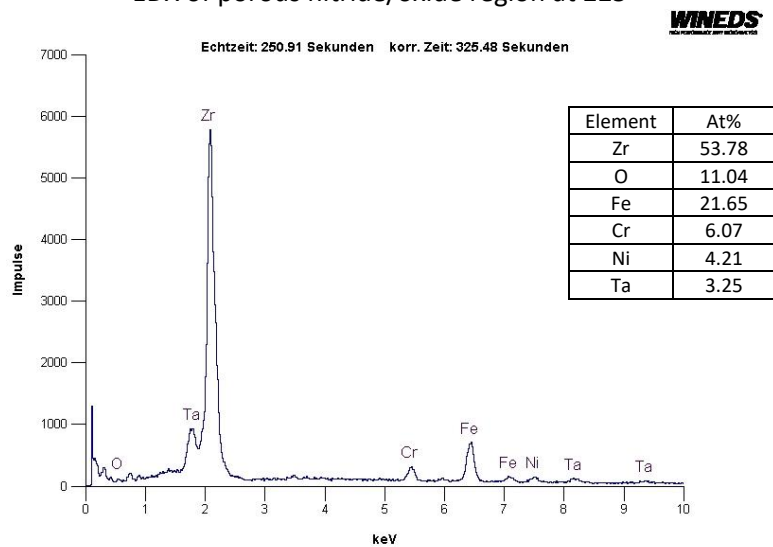
EDX of "α-Zr(O)+SS" part at 315°

Figure 98   QUENCH-18, SEM/EDX analysis of re-oxidized nitride regions showed in previous Figure.
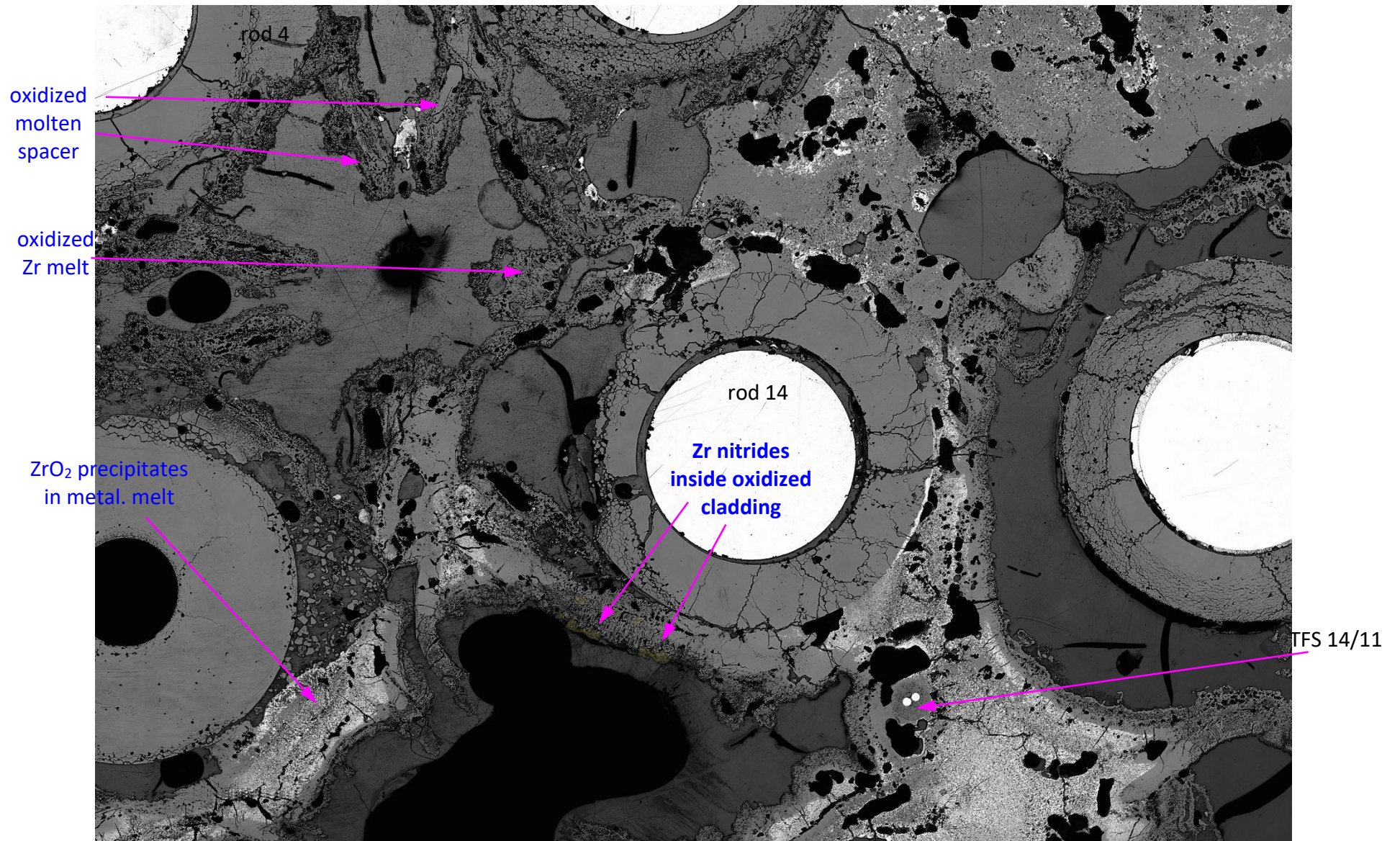
Figure 99 QUENCH-18; surroundings of heated rod 14 at elevation 560 mm, top view: severe destruction of pellet and nitride formation.
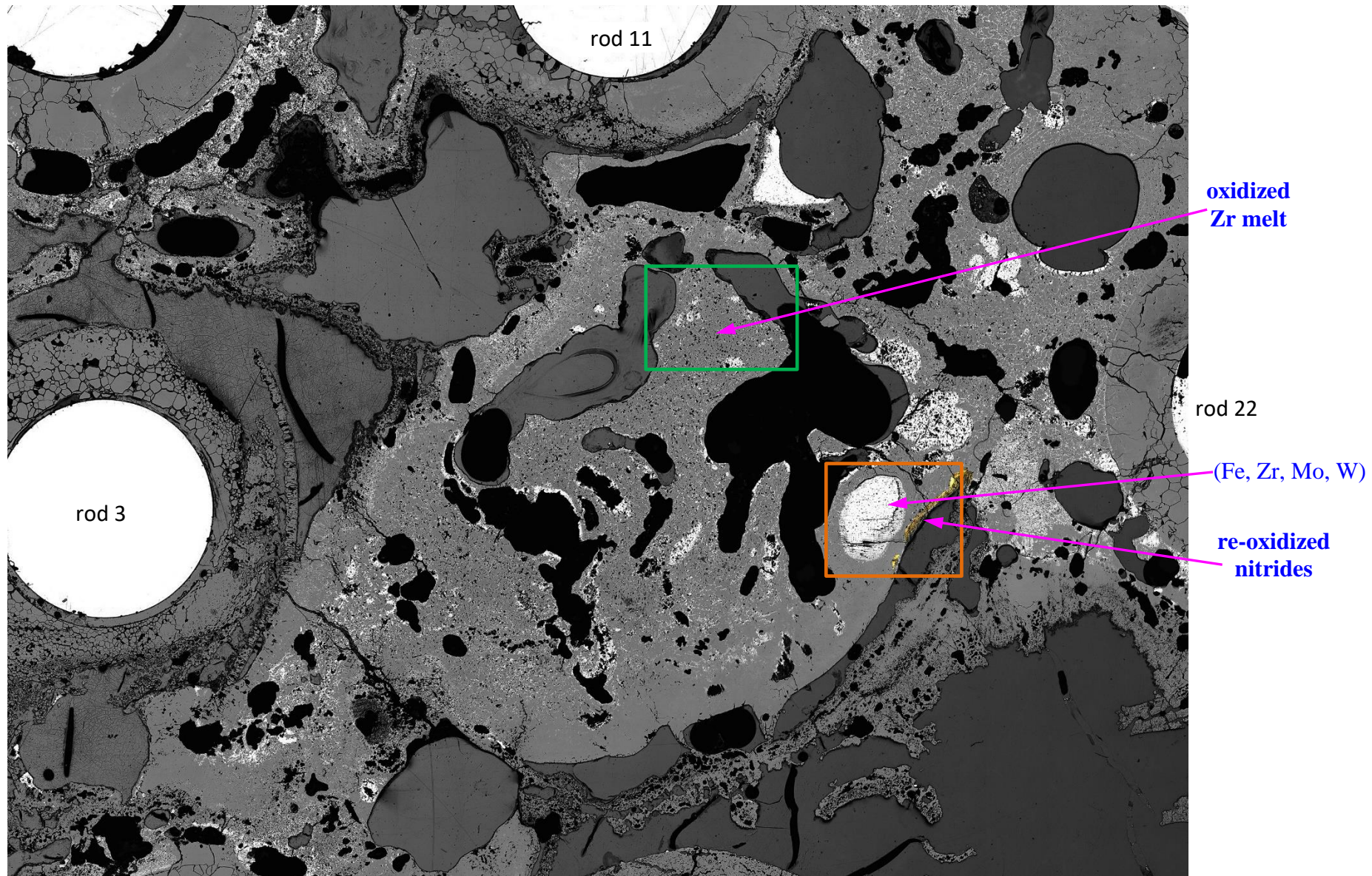
Figure 100 QUENCH-18; surroundings of absorber rod 12 at elevation 560 mm, top view; identification marks for separate spot analysis inside rod 12 position.
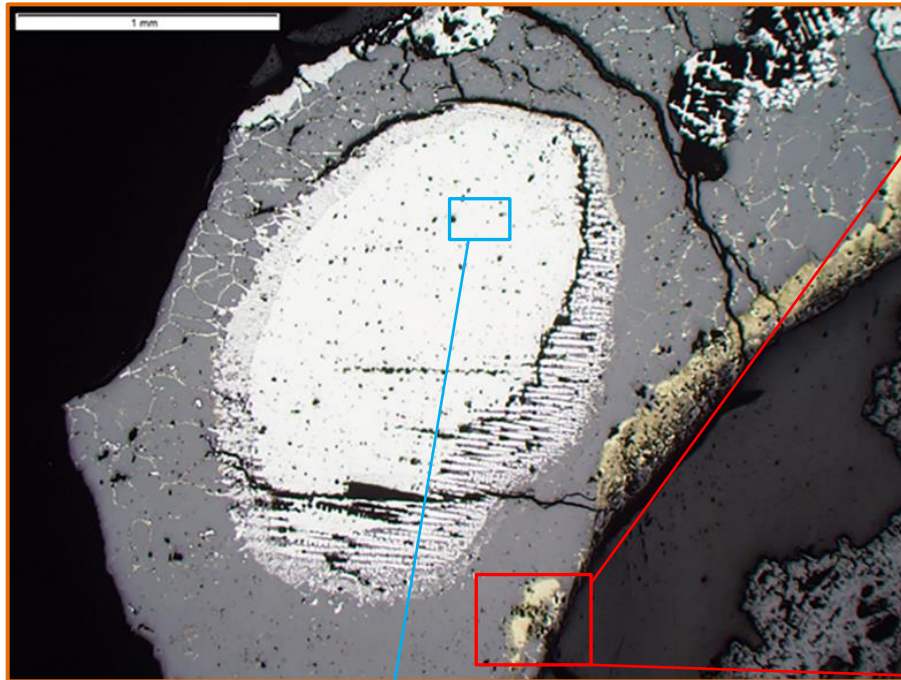
Optical microscope observation of metallic melt spot and nitride oxide edge
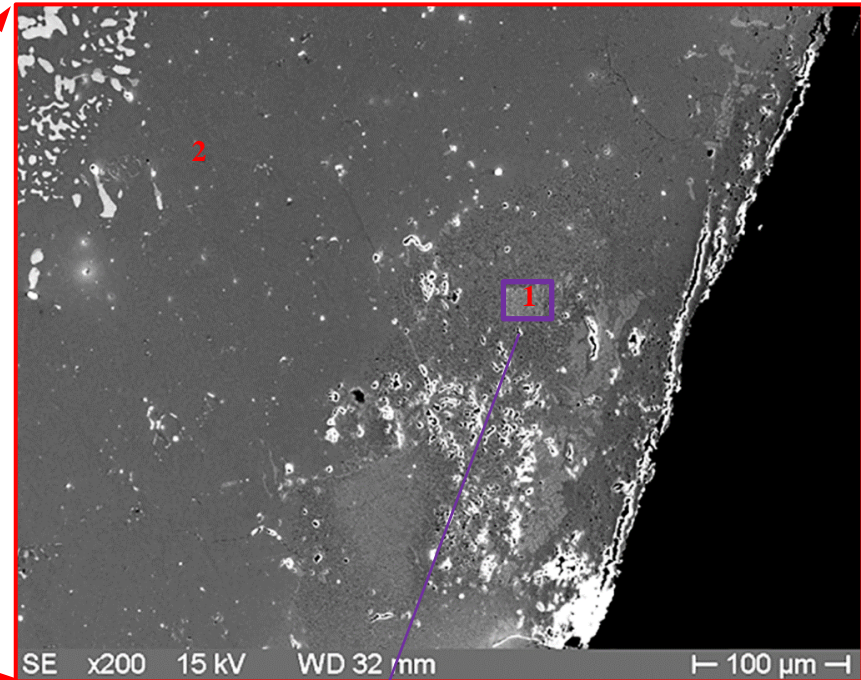
SEM/EDX: 1) zirconium oxides and nitrides ZrN:O, 2) ZrO$_{2-x}$
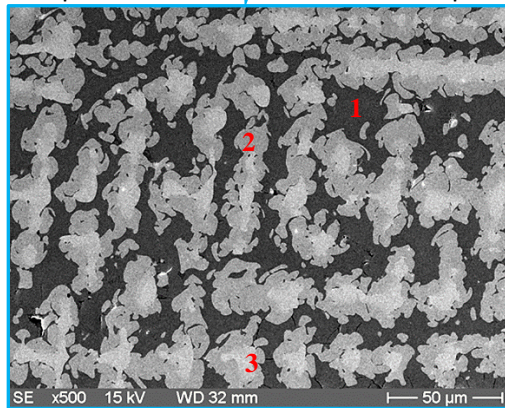
SEM/EDX of metallic melt (wt%): 1) (Fe 35%, Cr 4%, Ni 4%, Zr 35%, Mo 20%), 2) (Mo 80%, W 20%), 3) (Mo 60%, W 35%, Zr 5%)

SEM image and EDX spectrum of zirconium oxides and nitrides porous area

Element	At%
Zr	60.25
N	21.15
O	18.60
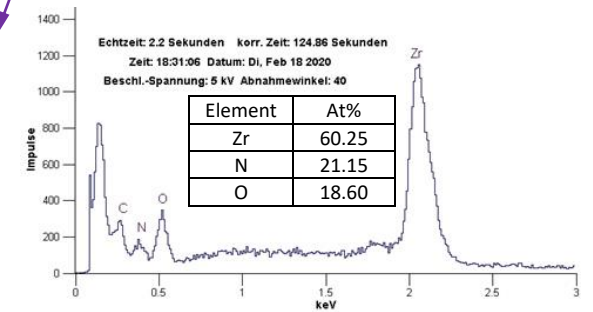
Figure 101   QUENCH-18; metallic molten pool (with well-ordered structure of Mo and W precipitates inside Zr-Fe melt) and zirconium oxides and nitrides at the position of absorber rod 12 at elevation 560 mm.
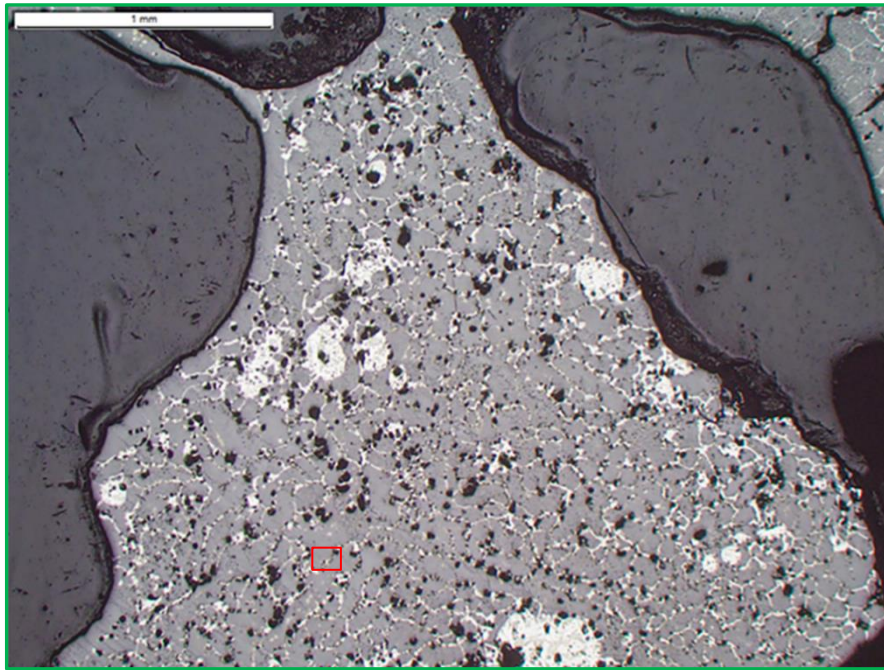
Optical microscope observation of oxidized melt
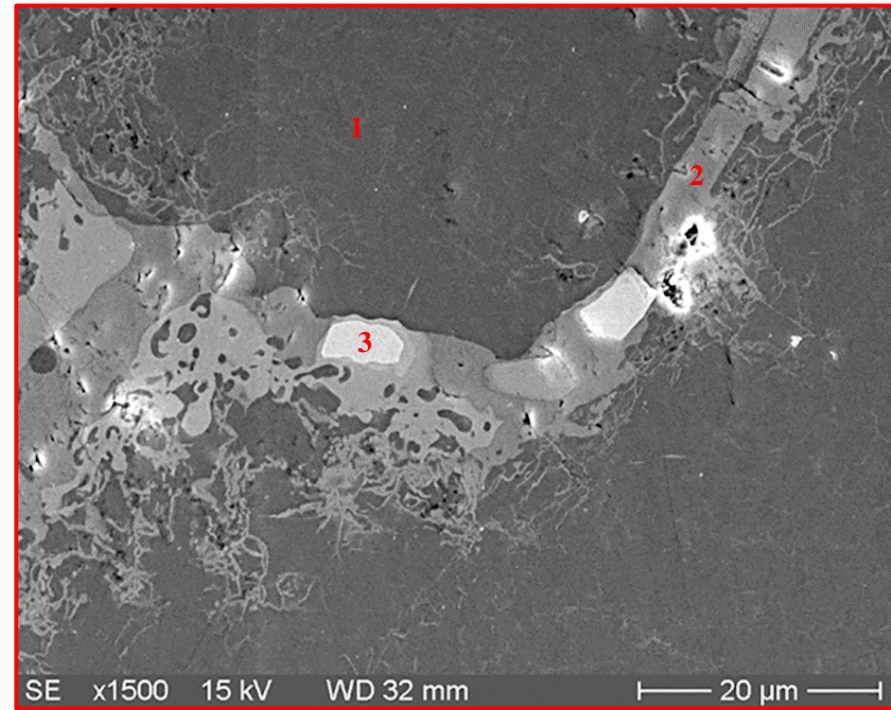
SEM/EDX: 1) ZrO_{2-x}, 2) α-Zr(O), 3) (W, Mo)

Figure 102   QUENCH-18; oxidized melt at the position of rod 12 at elevation 560 mm.
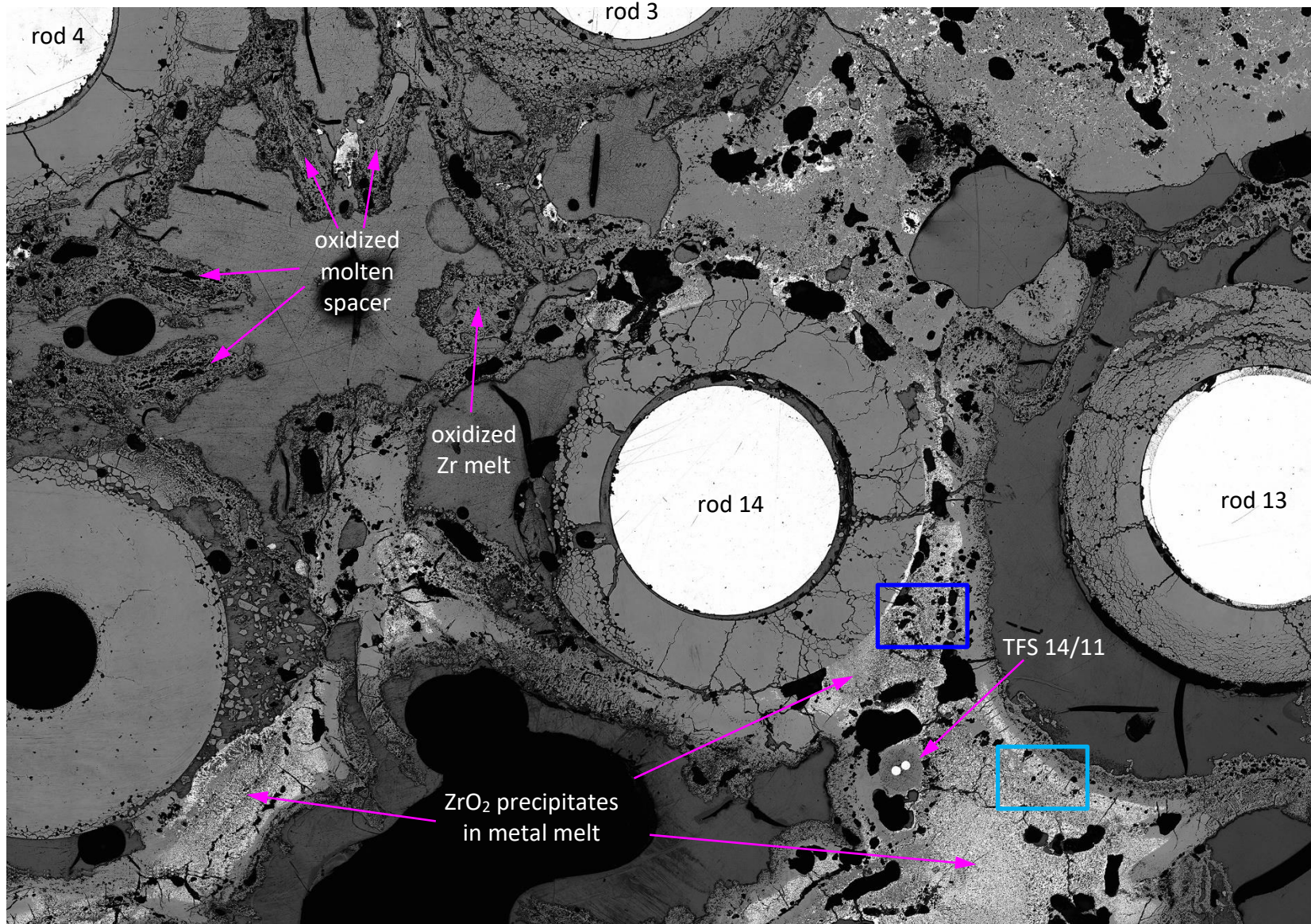
Figure 103   QUENCH-18; surroundings of rods 13 and 14 at elevation 560 mm, top view; marked regions for magnified microscope imaging (next figure).
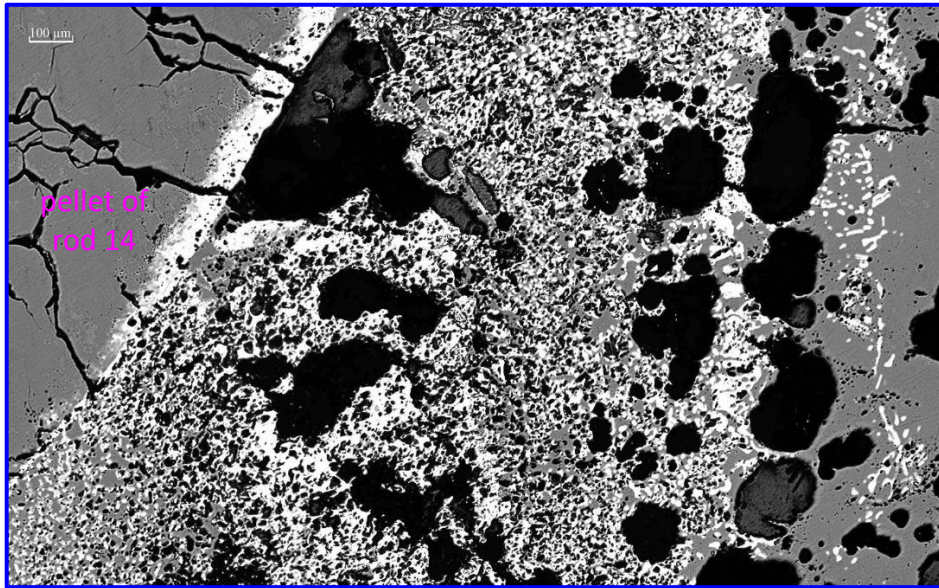
surrounding of rod 14
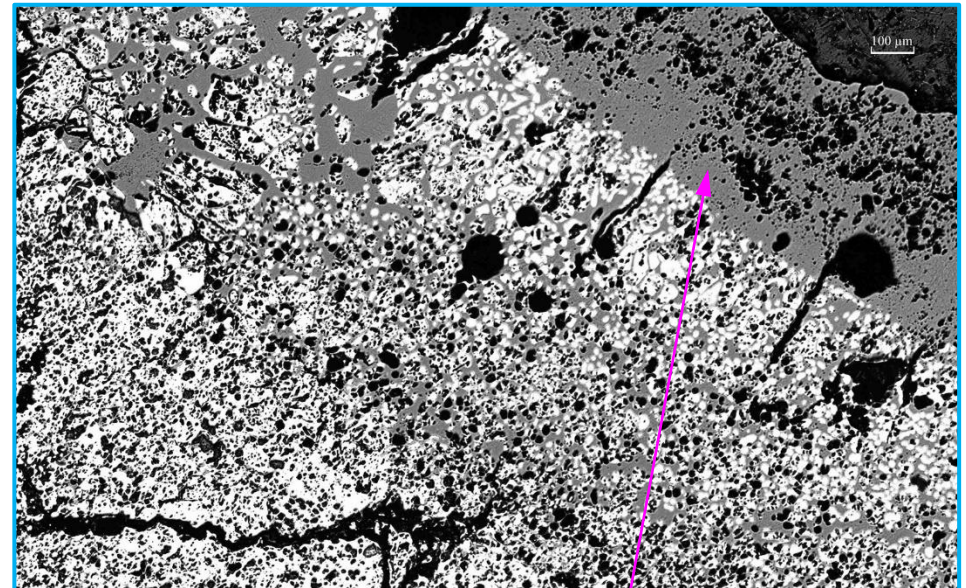
surrounding of rod 13;   cladding oxide of rod 13

Figure 104   QUENCH-18; partially oxidized melt in surroundings of rods 13 and 14 at 560 mm.
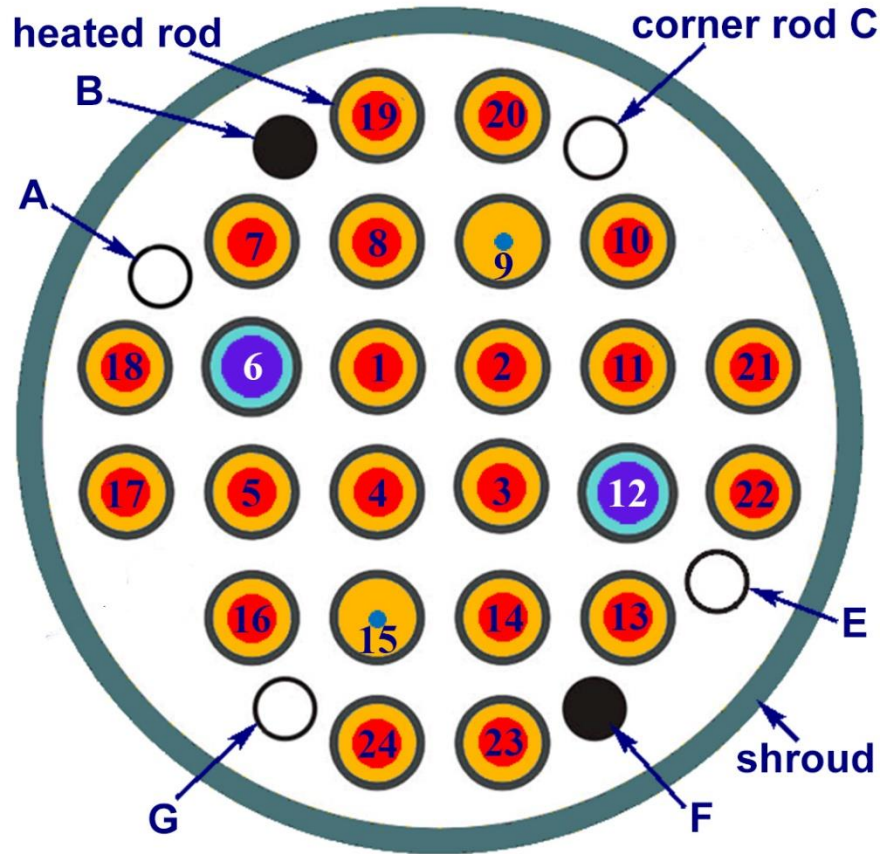
bundle composition, corner rods D and H are withdrawn
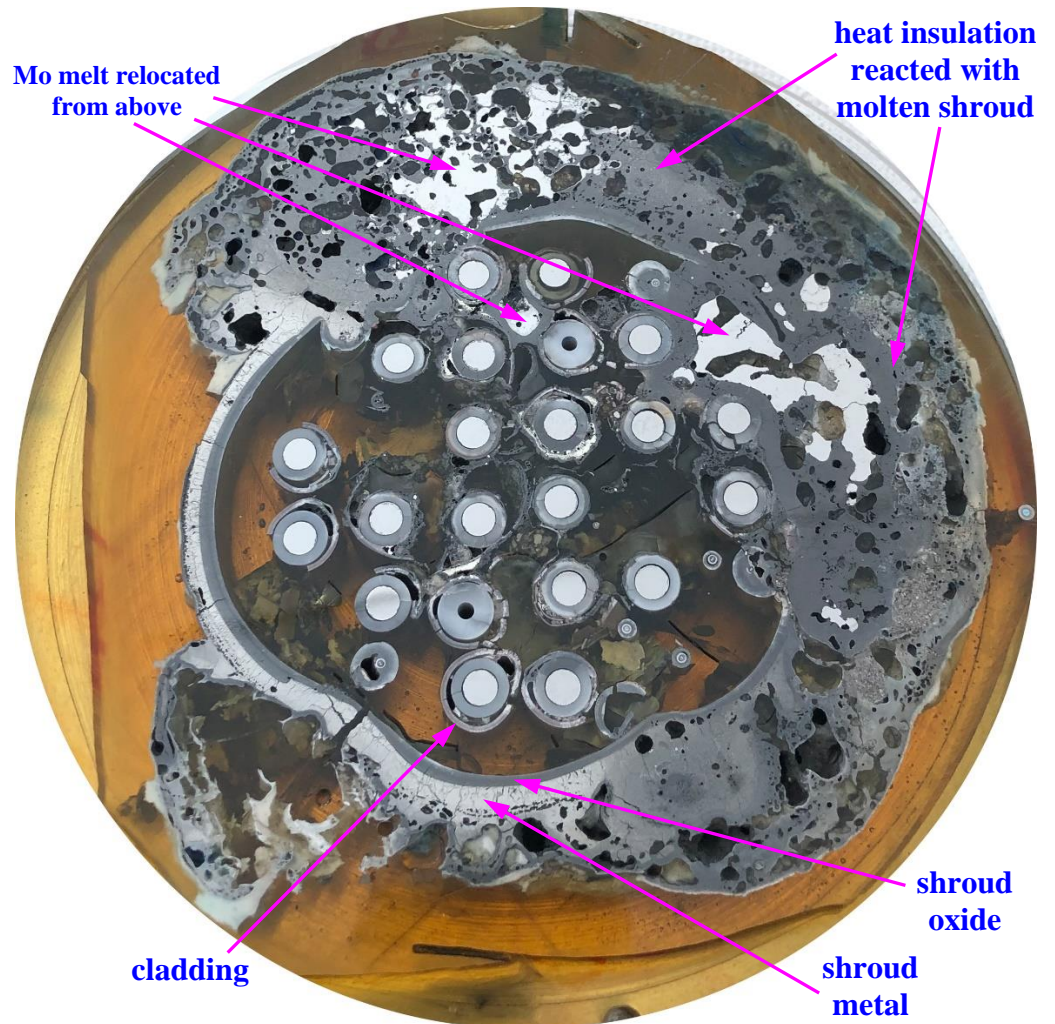
cross section top view (perspective projection)

Figure 105   QUENCH-18; cross section at bundle elevation of 350 mm.
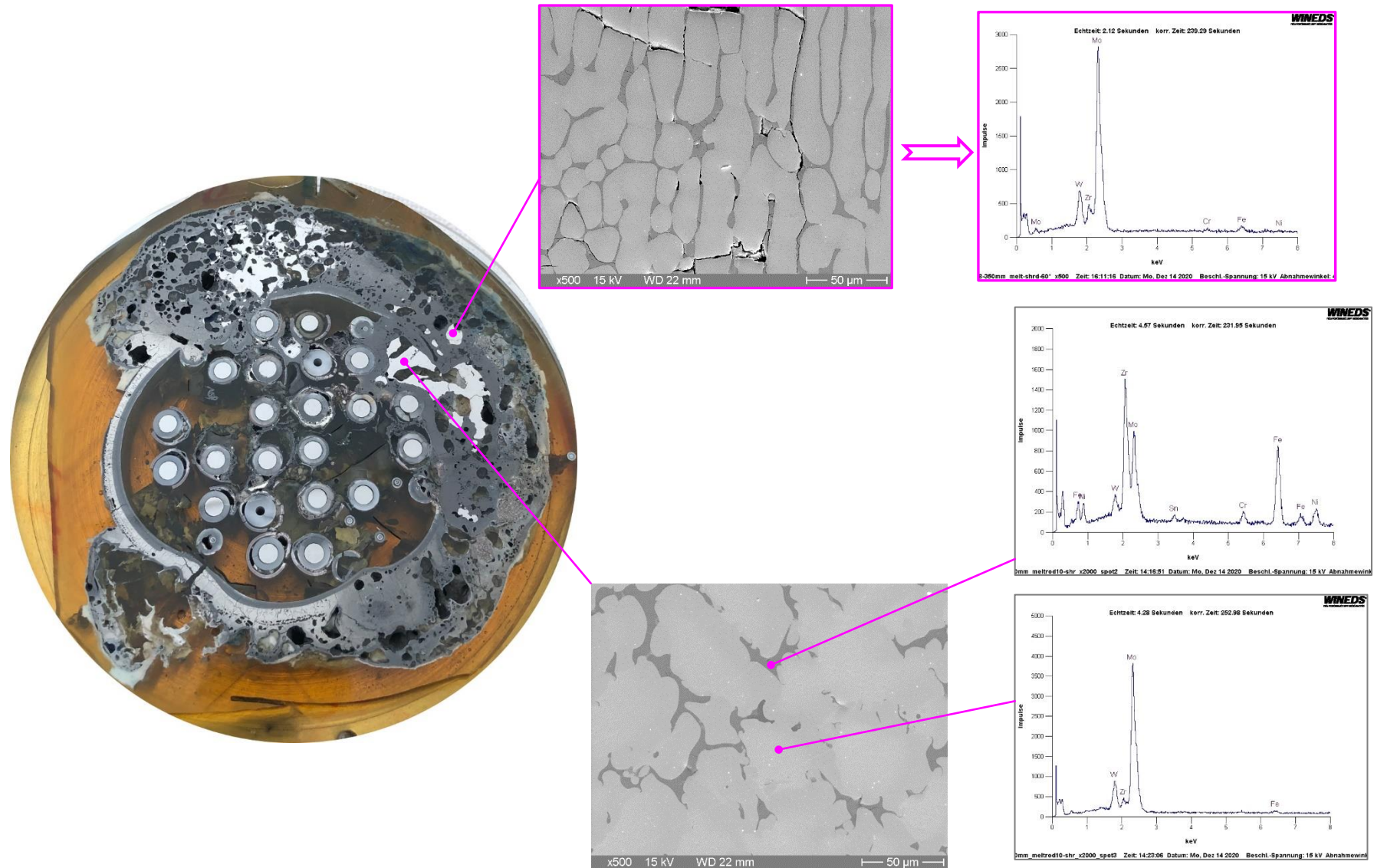
Figure 106 QUENCH-18; Mo bearing melt relocated to 350 mm from elevations above 1050 mm.

320°:
1000

300°:
1750

280°:
2200

α-Zr(O)

260°:
2200

230°:
2300

210°:
2300

205°:
1100

190°:
1700

180°:
1200

130°:
1500

re-oxidized
nitrides

metal melt
with ceramic
precipitates

500 µm

200 µm

y°, xxx - ZrO_2 thickness (µm) at y°
including **re-oxidized ZrN** with
thickness **≈110 µm**

5 mm
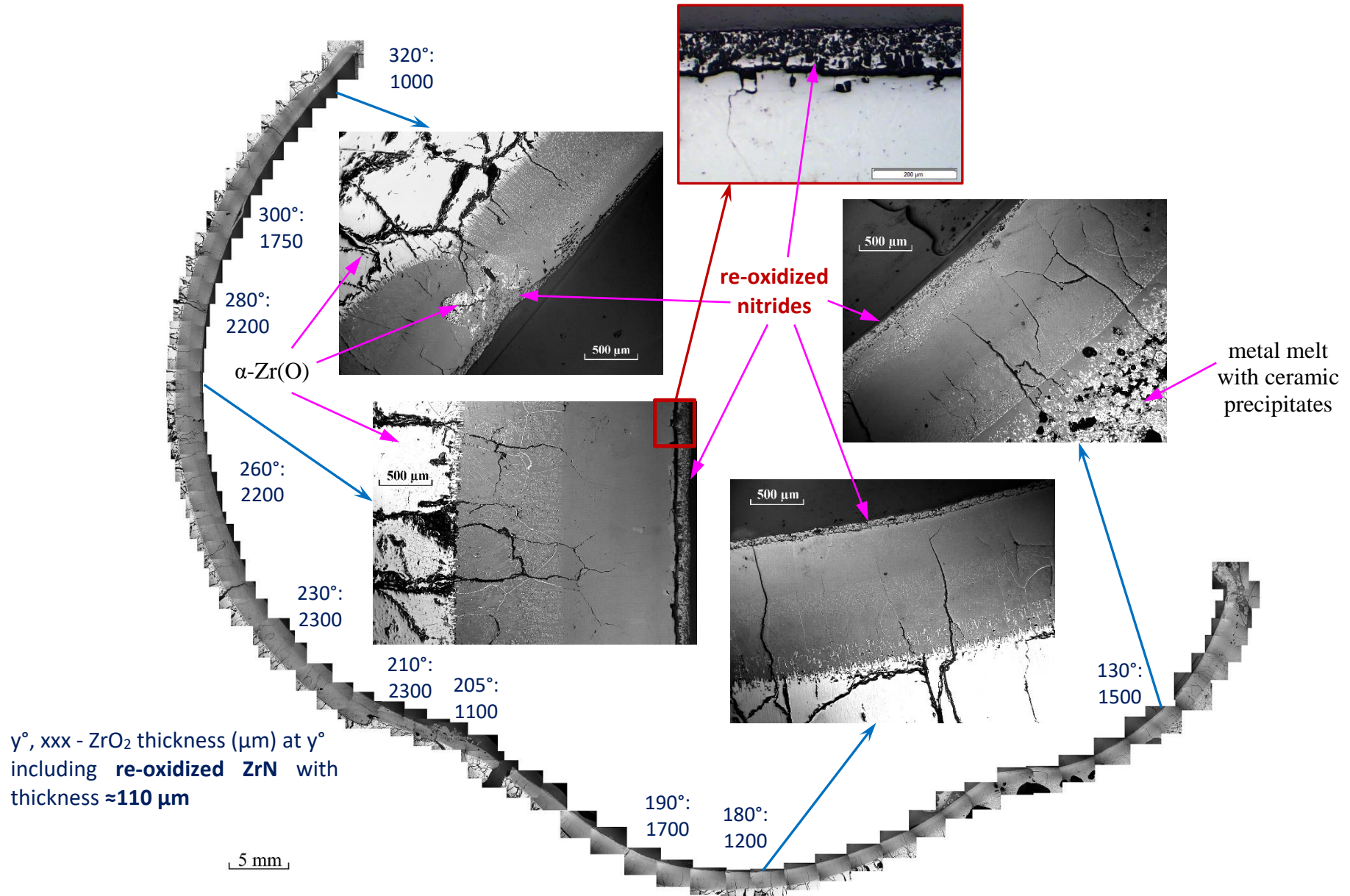
Figure 107 QUENCH-18; Zr shroud at 350 mm: thick oxide layer (between 1 and 1.5 mm) and nitride layer (about 100 µm).
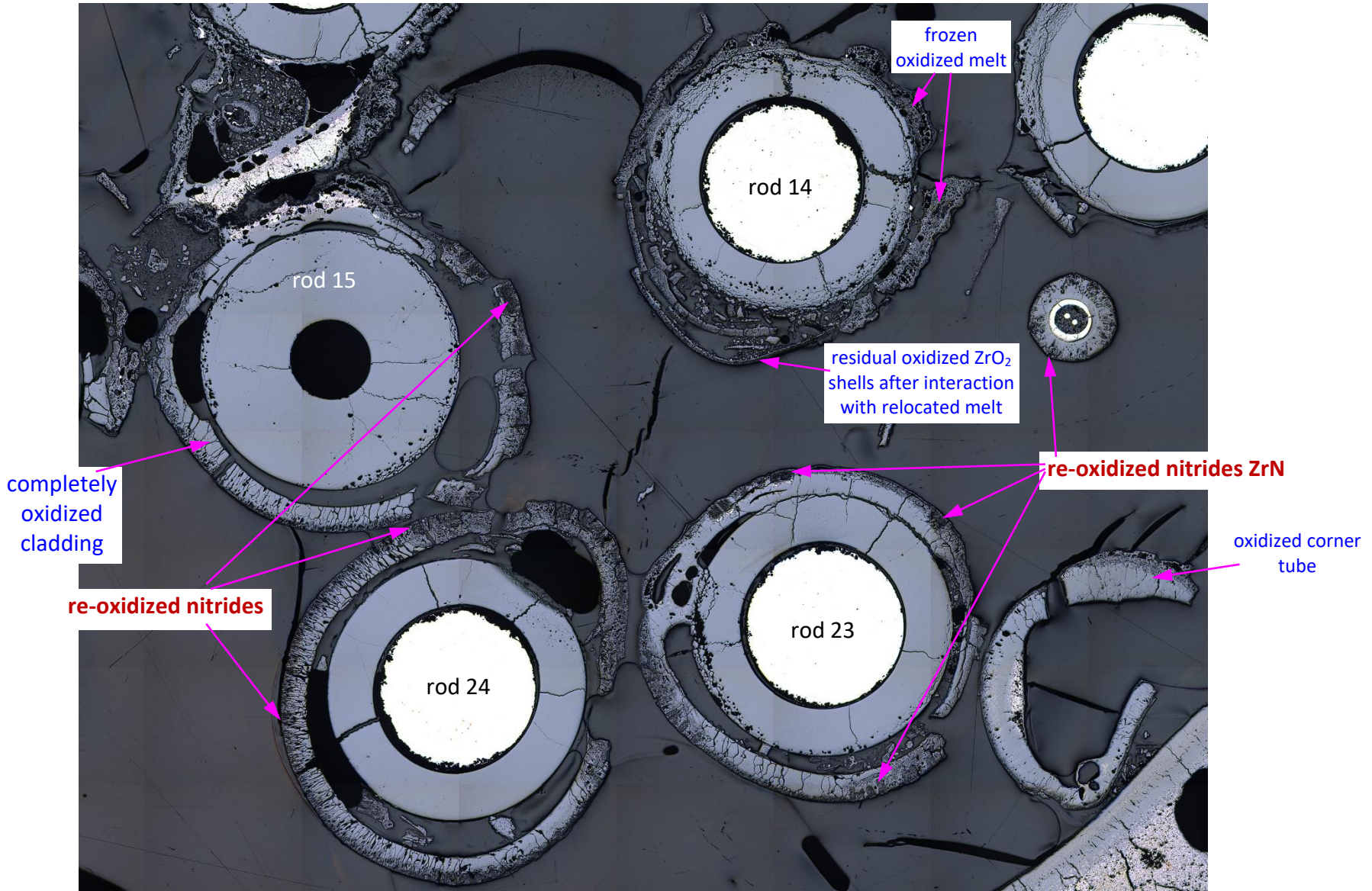
Figure 108   QUENCH-18; 350 mm: melted and completely oxidized cladding #14, locally nitrided relatively cold claddings #15, #23 and #24.
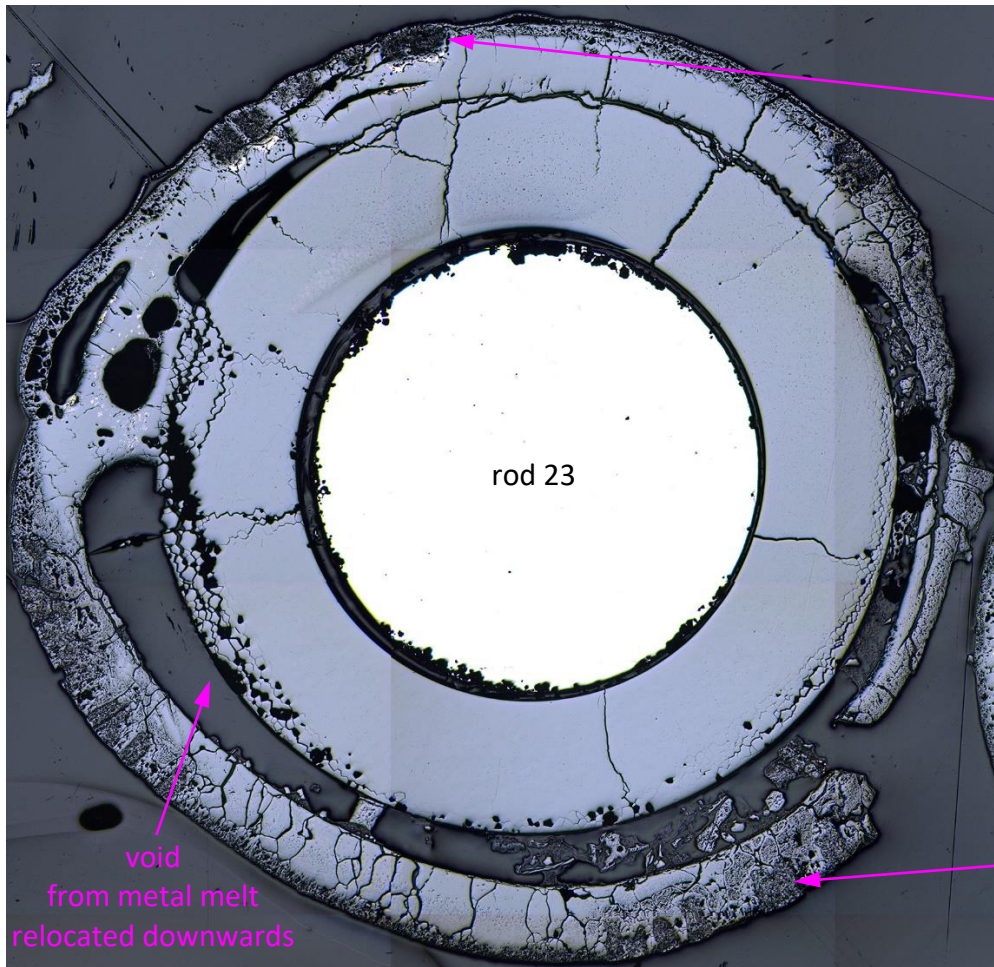
cross section: completely oxidized cladding with re-oxidized nitride cells
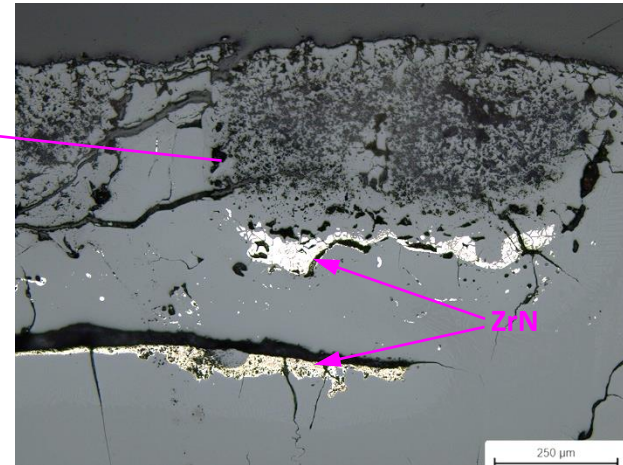
re-oxidized nitride cell at 0° with residues of α-Zr(O) reacted with nitrogen
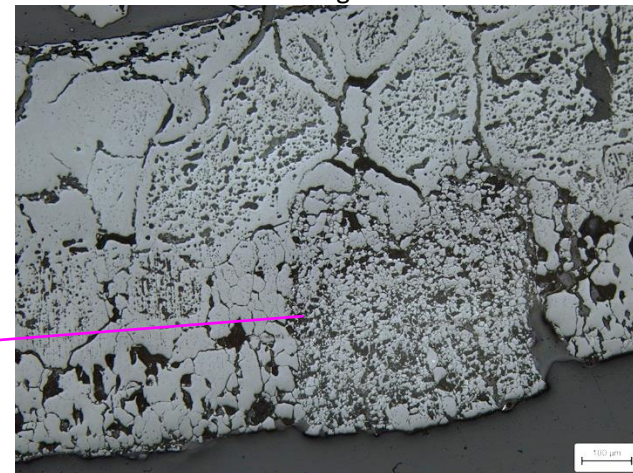
re-oxidized nitride cell at 70°

Figure 109   QUENCH-18; microstructure of rod elements for rod #23 at bundle elevation of 350 mm.
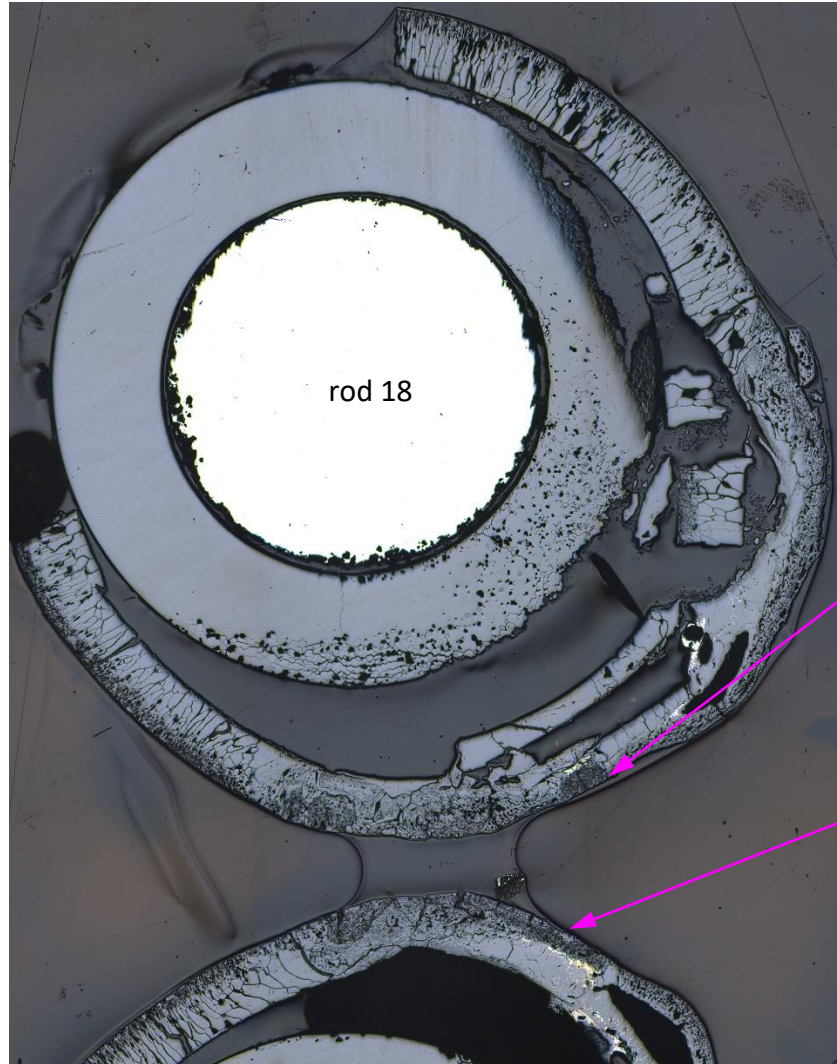
cross section: completely oxidized cladding with re-oxidized nitride cells
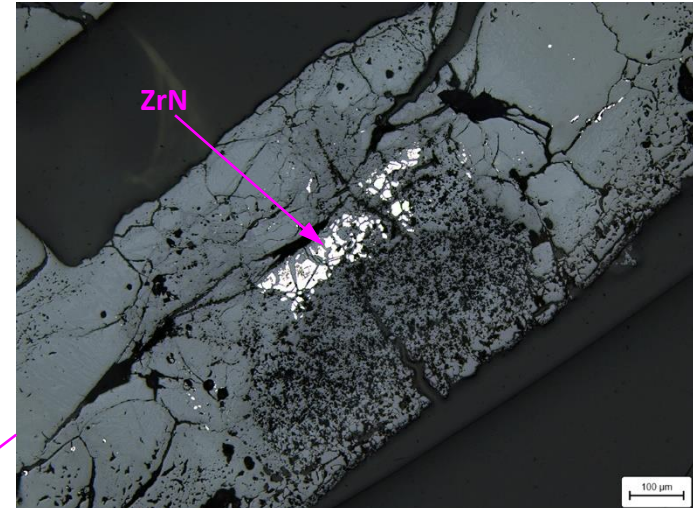
rod #18: re-oxidized nitride cell at 140° with residues of ZrN
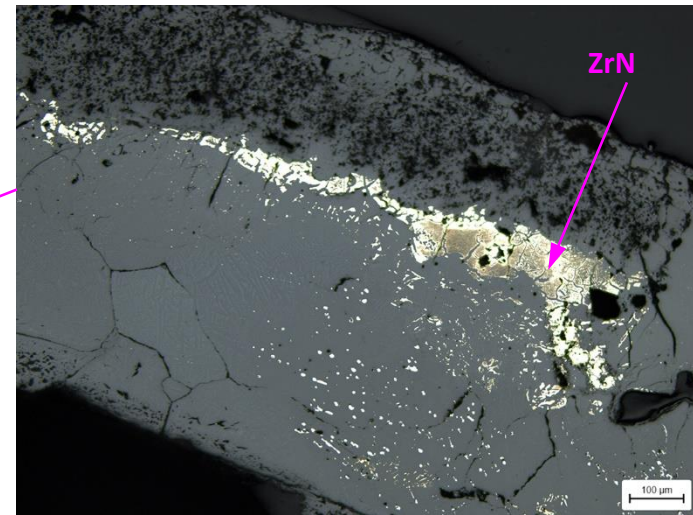
rod #17: re-oxidized nitride cell at 20° with residues of ZrN

Figure 110   QUENCH-18; microstructure of rod elements for rods #17 and #18 at bundle elevation of 350 mm: porous re-oxidized nitrides at the outer cladding surface and residual nitrides at the position of prior α-Zr(O) inside the almost completely oxidized cladding.

137
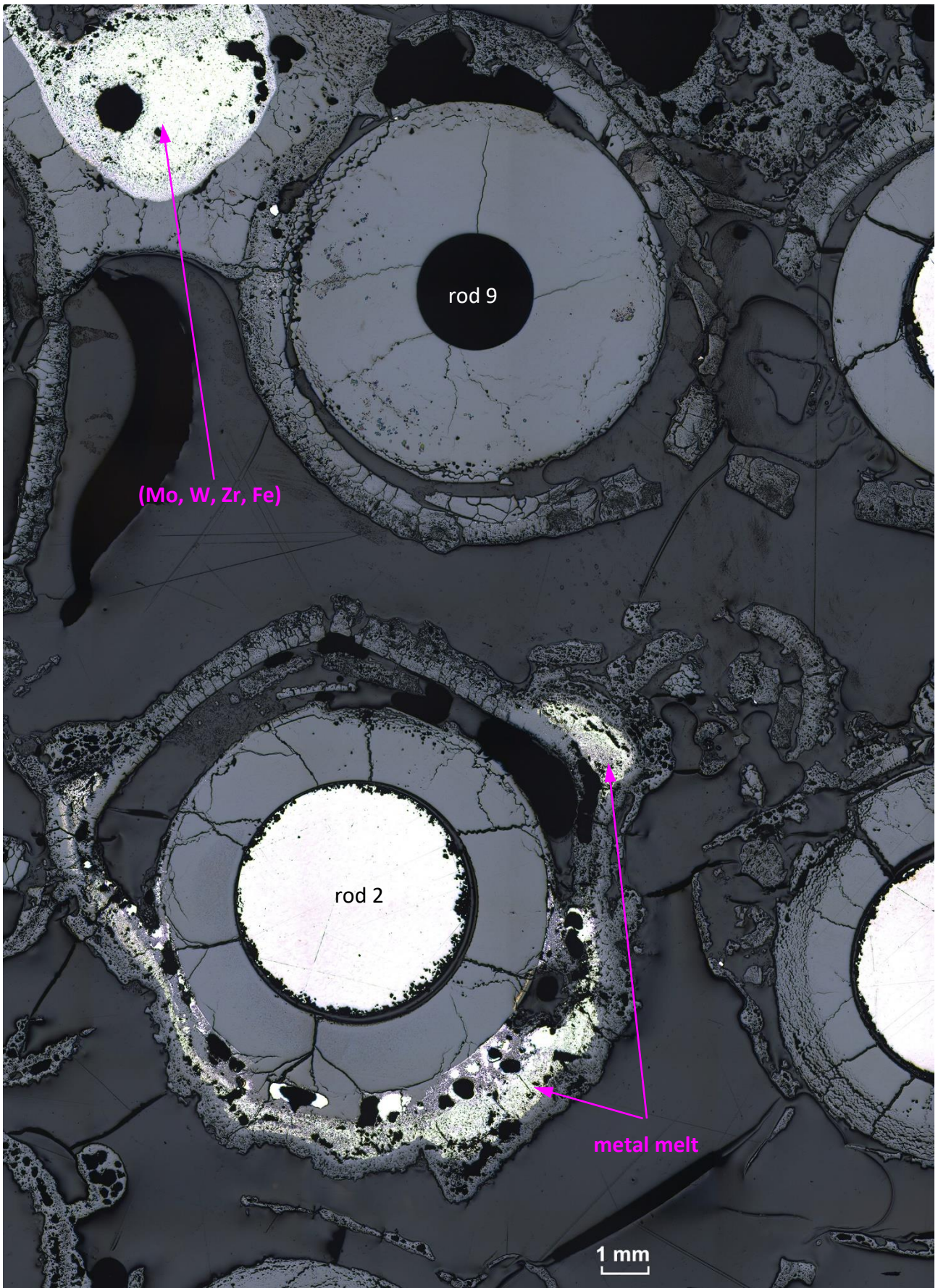
Figure 111 QUENCH-18; 350 mm: completely oxidized clad #9, oxide of clad #2 partially dissolved by melt.
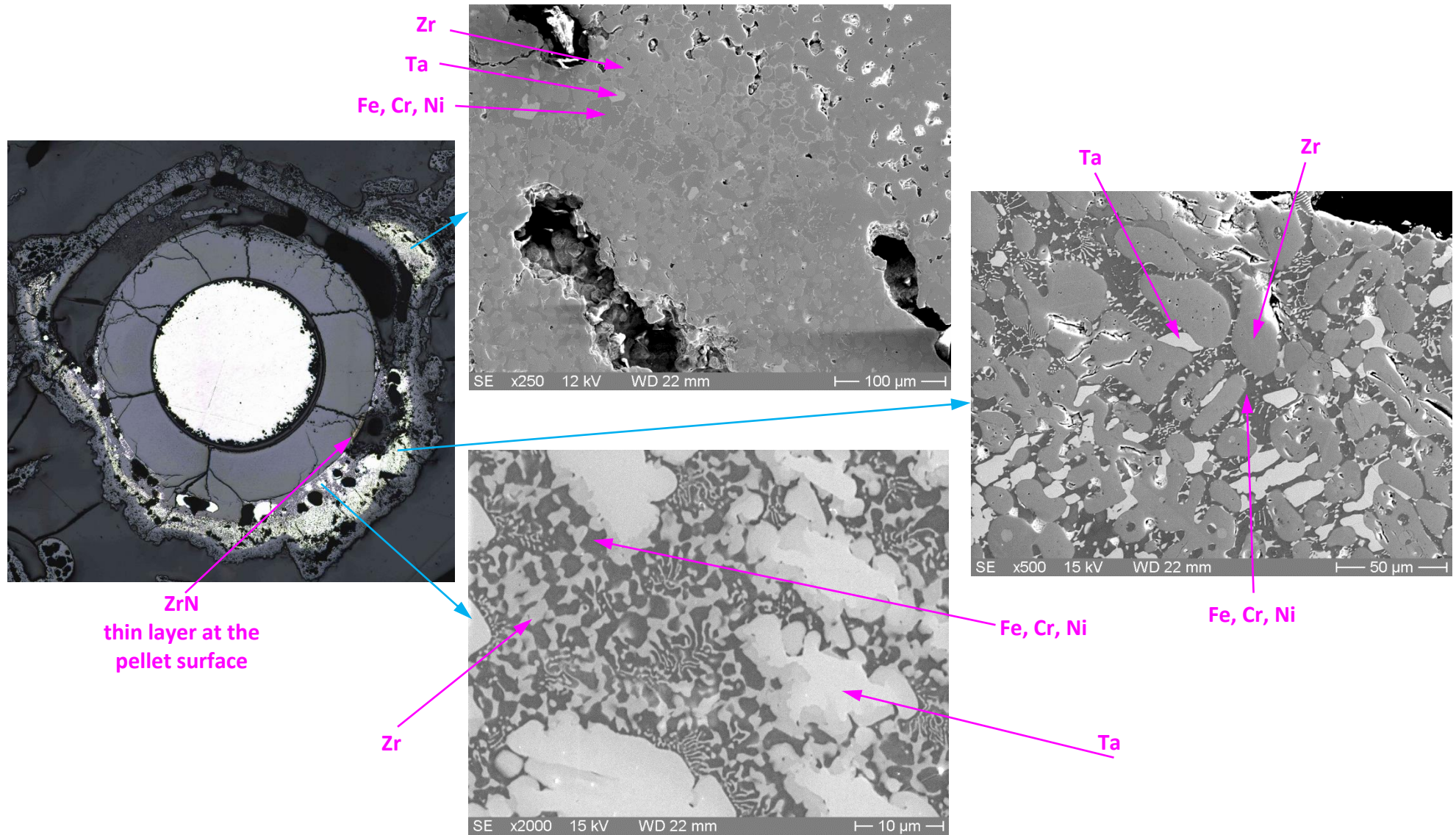
Figure 112   QUENCH-18; 350 mm: frozen metal melt around rod #2 consisting of rod cladding (Zr), absorber cladding (Fe, Cr, Ni) and TC (Ta) elements.
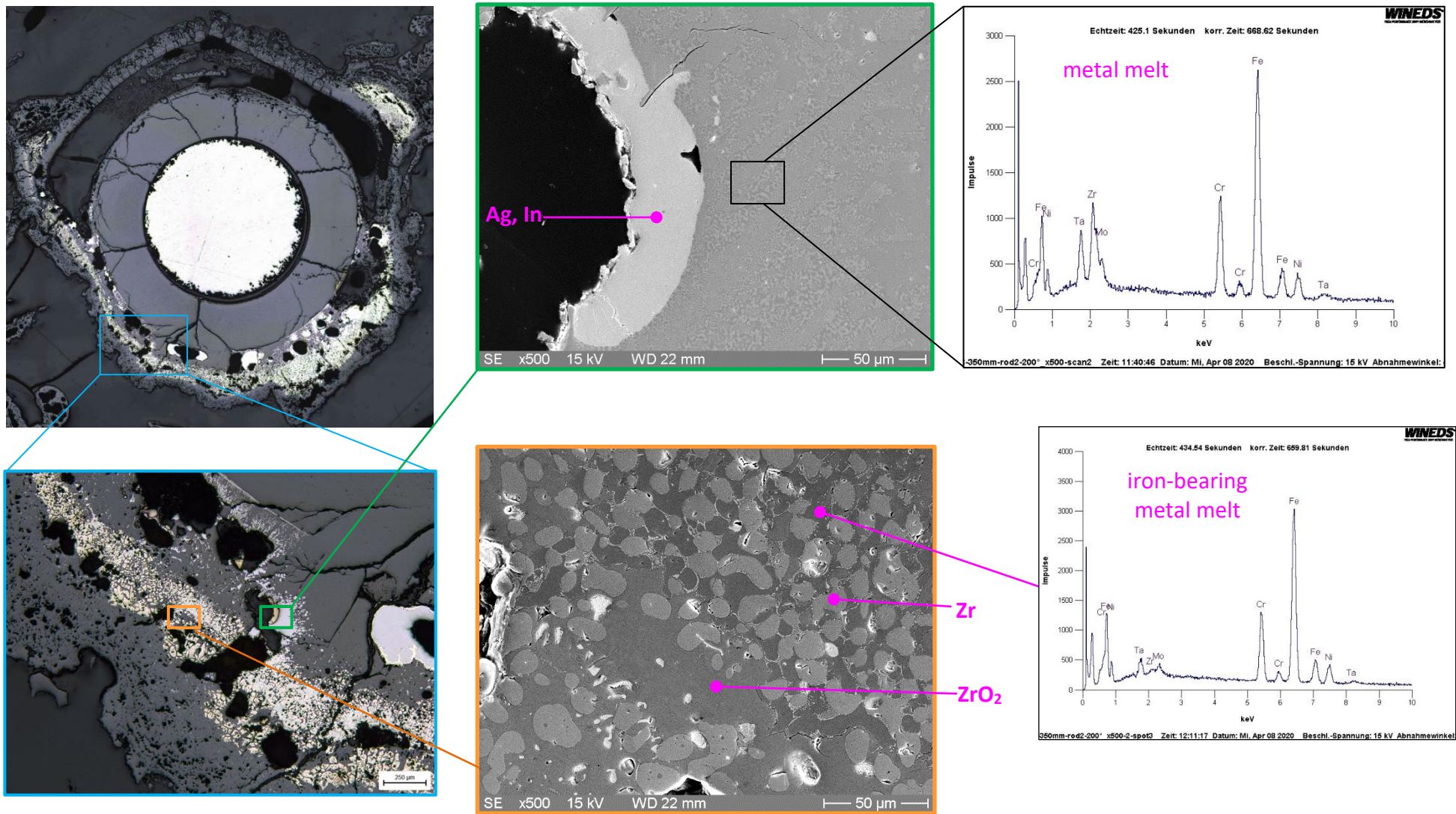
Figure 113   QUENCH-18; 350 mm, rod #2: penetration of molten absorber materials (together with absorber cladding) under oxide of fuel rod cladding.
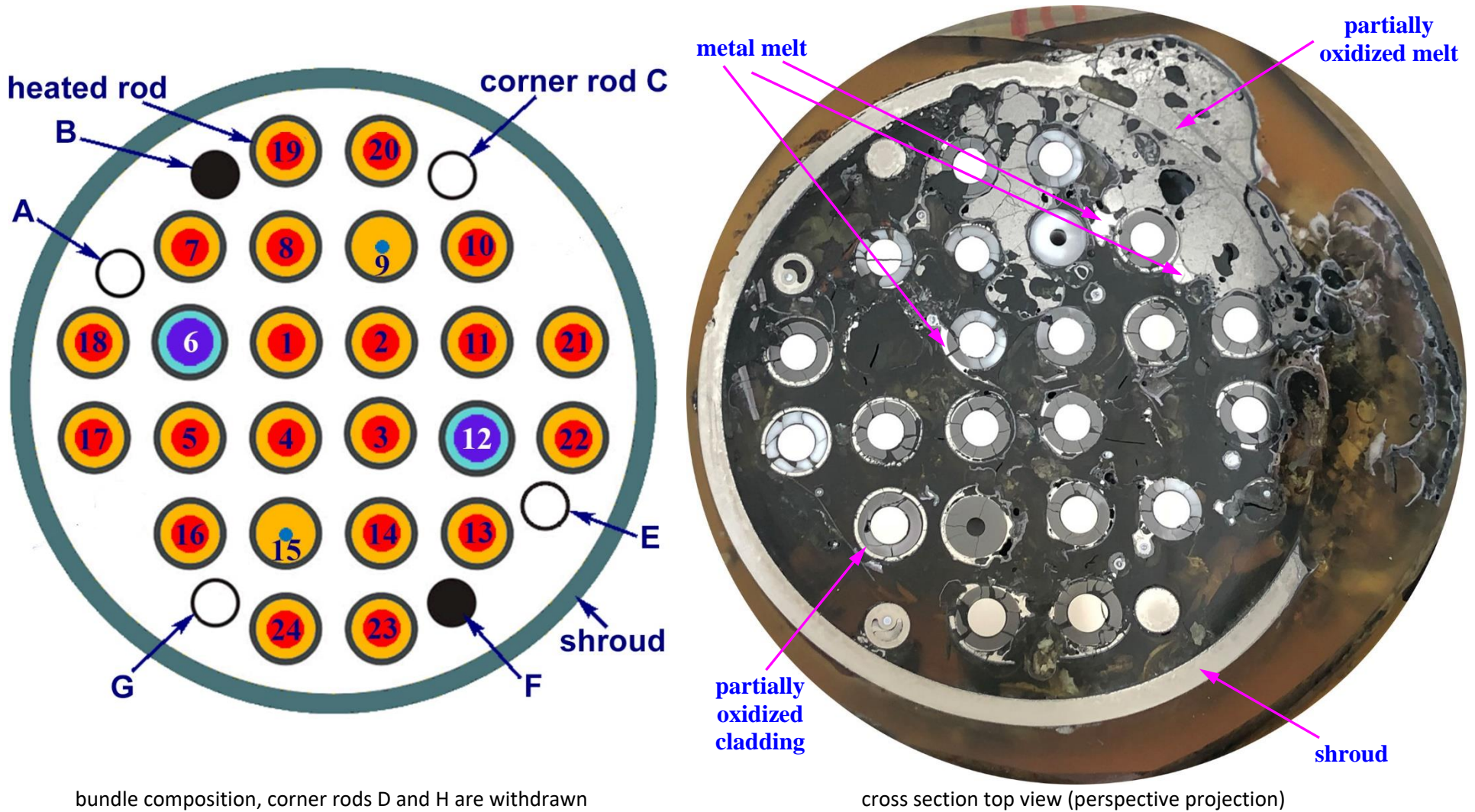
bundle composition, corner rods D and H are withdrawn

cross section top view (perspective projection)

Figure 114   QUENCH-18; cross section at bundle elevation of 160 mm.

Figure 115 QUENCH-18; ZrO_2 and α-Zr(O) layer thicknesses for claddings, corner rods and shroud at bundle elevation of 160 mm.

oxide layer

α-Zr(O) layer

prior β-Zr

Ta

void

1 mm

corner tube A partially filled with metal melt relocated from above

corner rod B

corner tube G partially filled with metal melt relocated from above
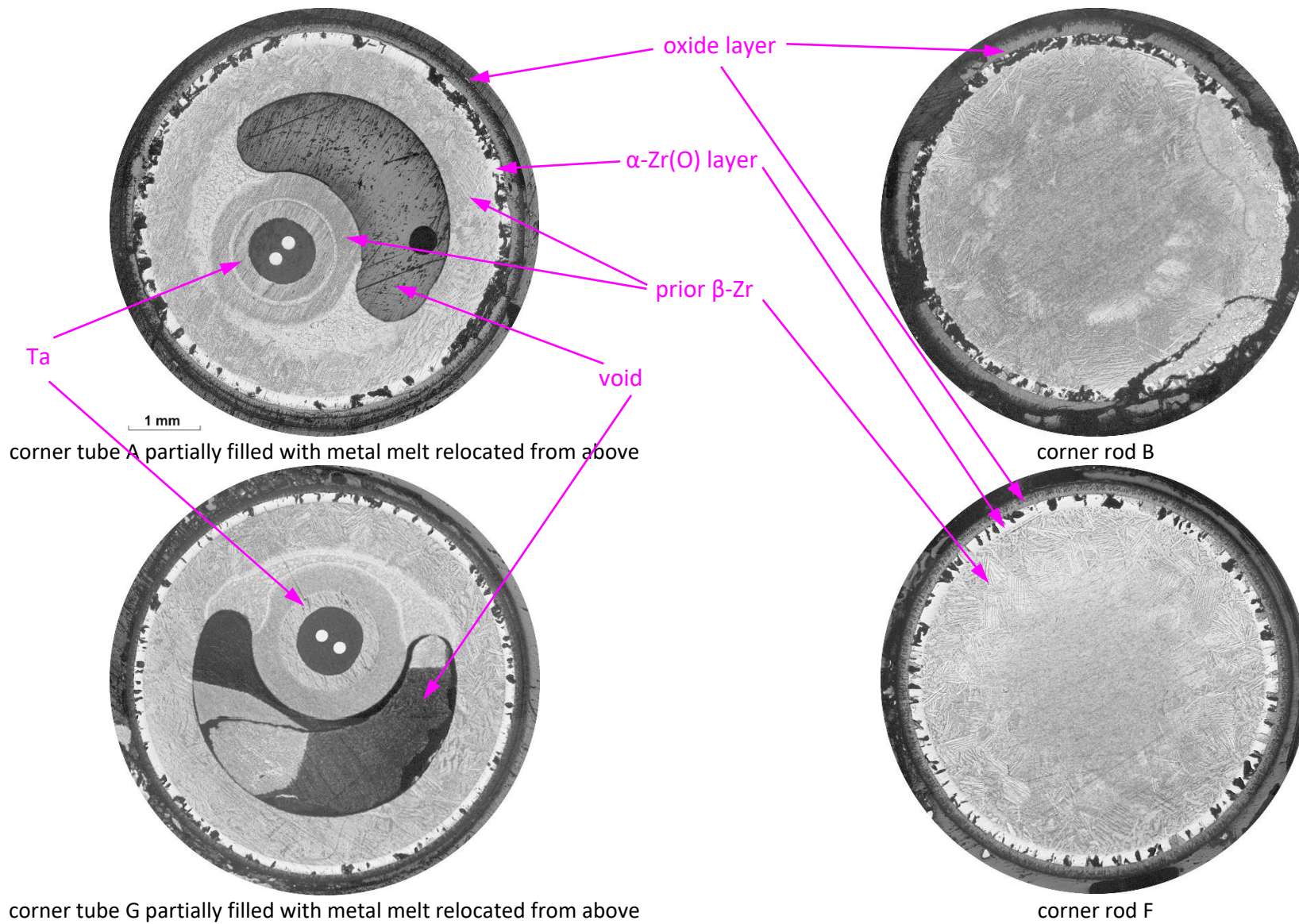
corner rod F

Figure 116   QUENCH-18; structure of corner rods at bundle elevation of 160 mm.
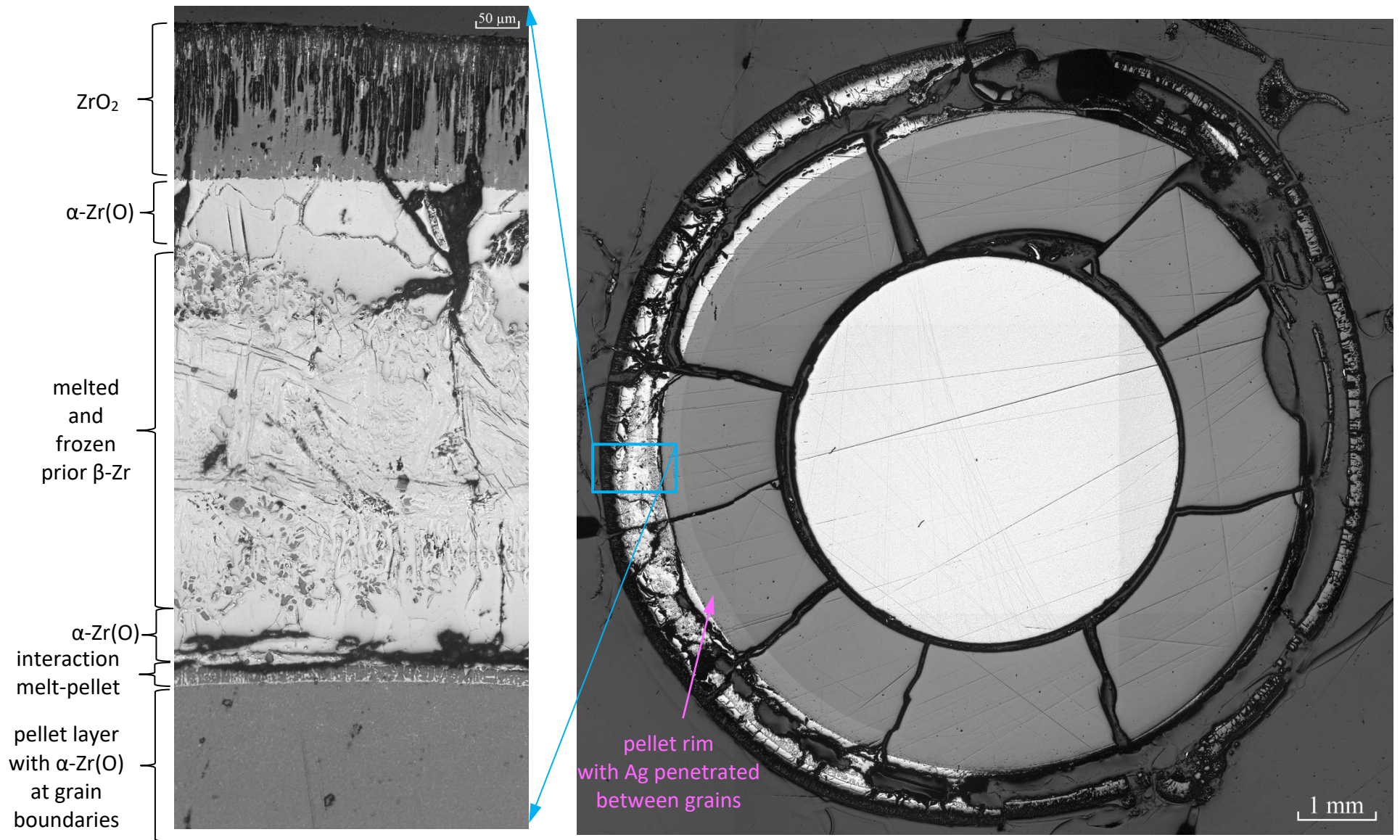
Figure 117   QUENCH-18; microstructure of rod elements for rod #4 at 160 mm.

144
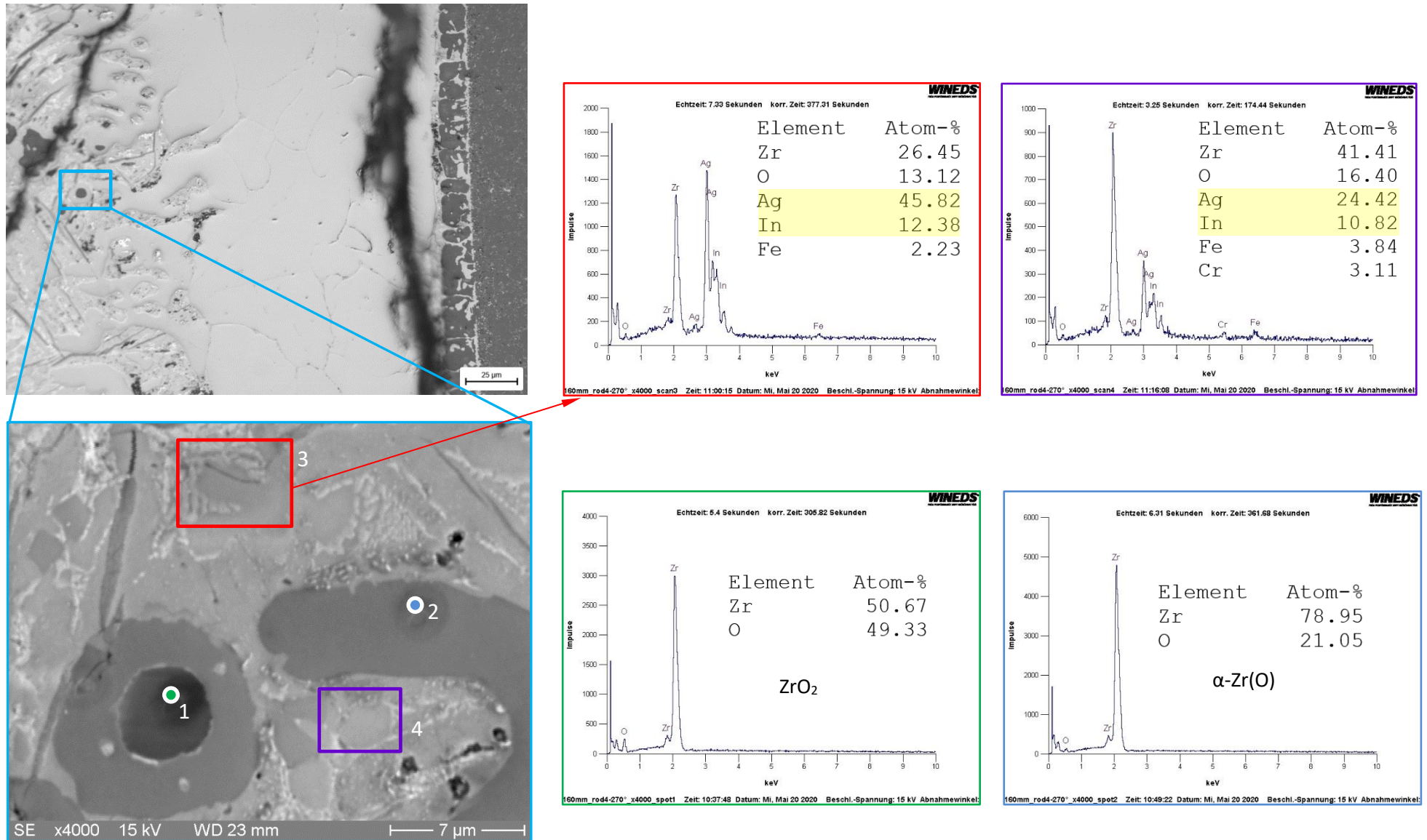
Figure 118 QUENCH-18; microstructure of prior molten cladding layer of rod #4 at 160 mm with results of EDX analysis: penetration of absorber rod and absorber cladding elements from neighbor rod #6 and mixture of these materials with molten prior β-Zr of rod #4.
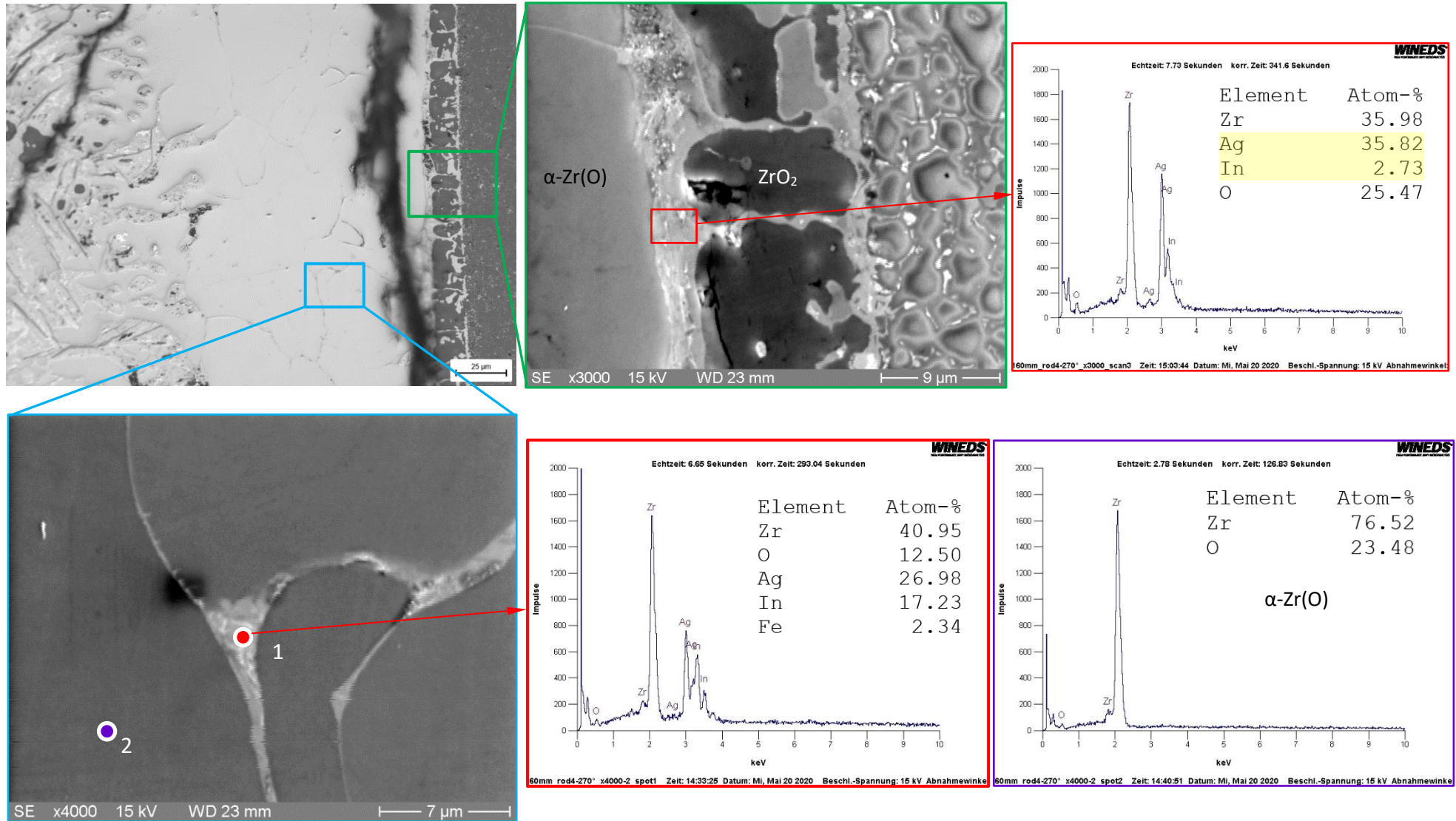
Figure 119 QUENCH-18; microstructure of prior molten cladding layer of rod #4 at 160 mm with results of EDX analysis: precipitation of absorber elements.

Element	atom-%	mass-%
Zr	49.94	80.35
O	45.96	12.97
Ag	**0.39**	**0.75**
In	0.26	0.52
Y	3.45	5.42

structure of outer pellet surface: ZrO$_2$ grain boundaries "decorated" by α-Zr(O) and diffused absorber materials

Element	atom-%	mass-%
Zr	49.17	80.60
O	47.30	13.60
Ag	**0.48**	**0.94**
In	----	----
Y	3.05	4.87

upper picture: optic microscope view of pellet (changed grayscale histogram);
lower text: composition of pellet at 100 μm from outer pellet surface: diffused Ag, no In

Element	atom-%	mass-%
Zr	49.93	81.41
O	46.78	13.38
Ag	----	----
In	----	----
Y	3.28	5.21

unchanged pellet structure at inner pellet surface (yttria stabilized zirconia)

Figure 120 QUENCH-18; interaction of zirconia pellet at 160 mm with molten cladding of rod #4 and absorber materials from rod #6; results of EDX analysis.
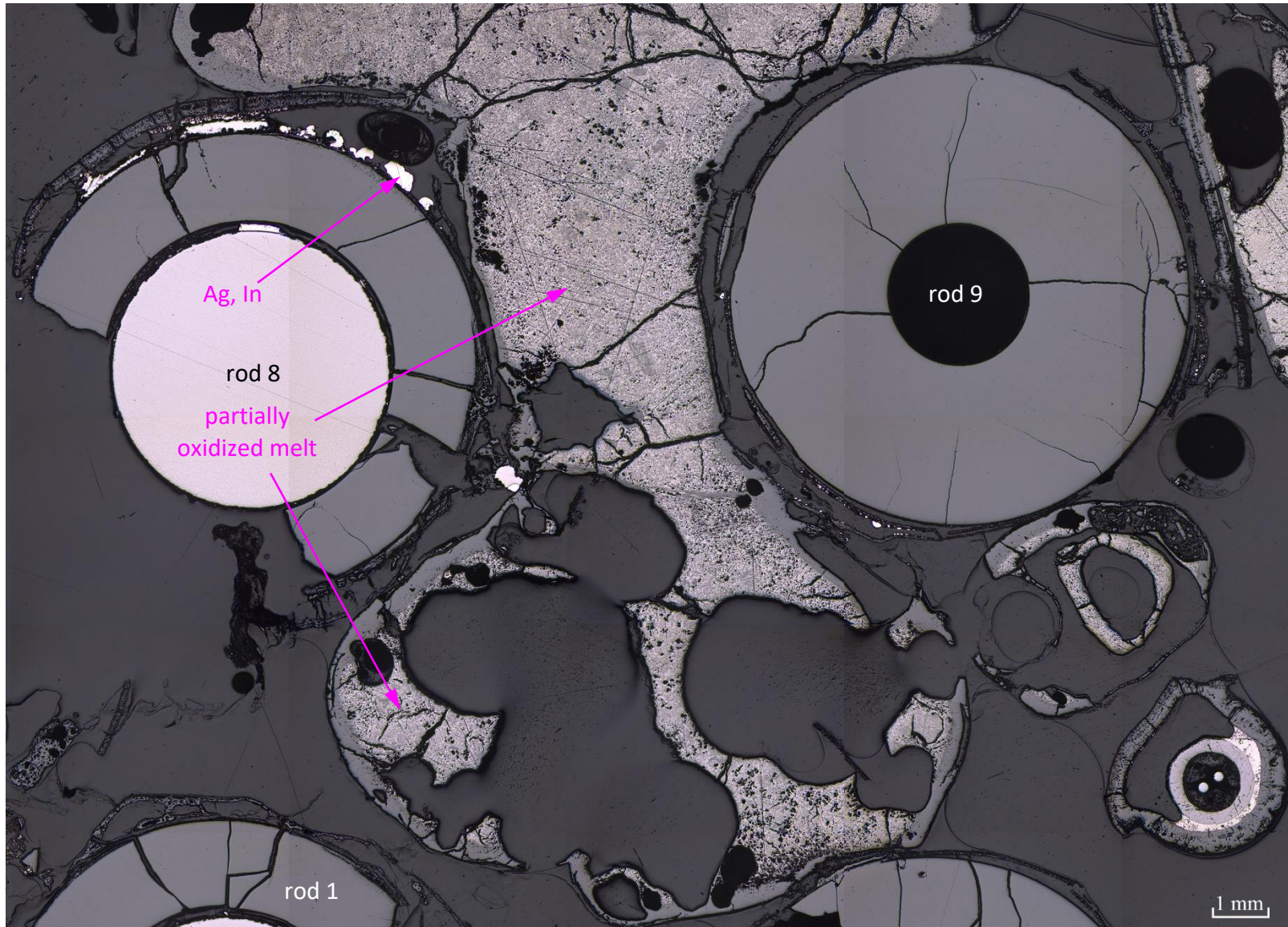
Figure 121 QUENCH-18; melt formation between rods #8 and #9 at elevation 160 mm, penetration of absorber materials in the gap between pellet and cladding.
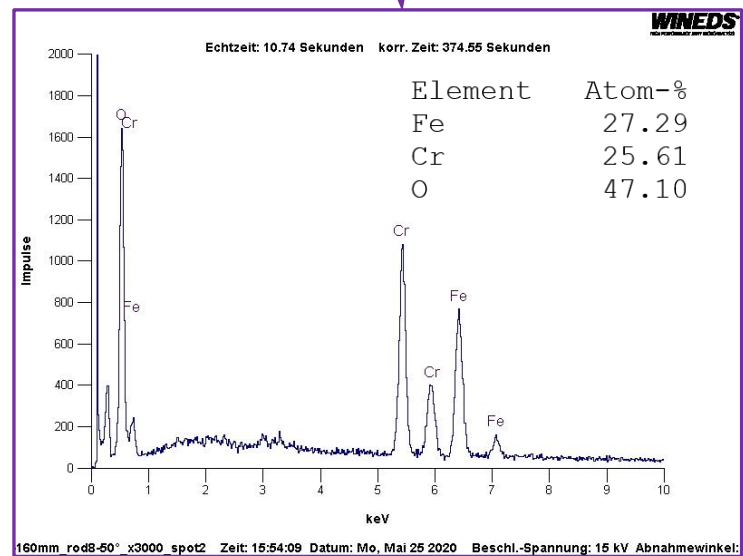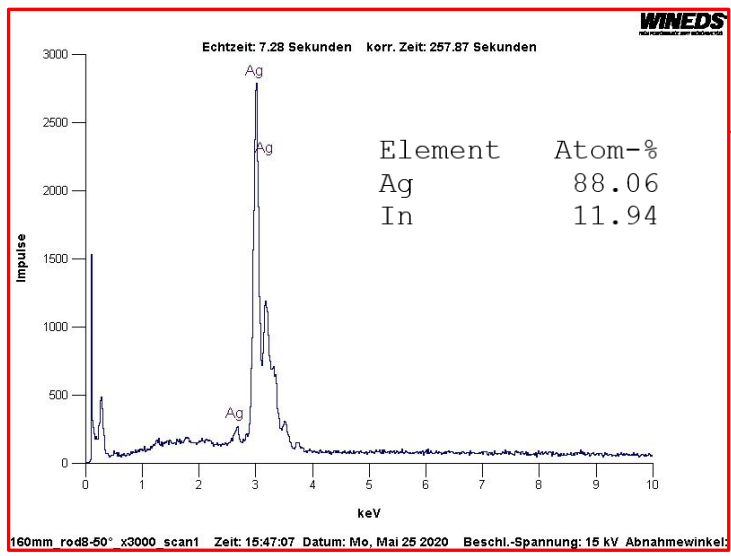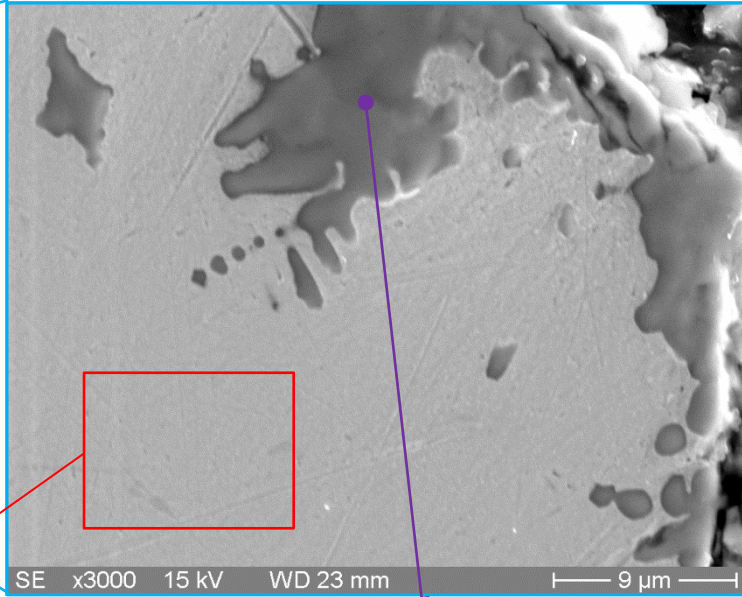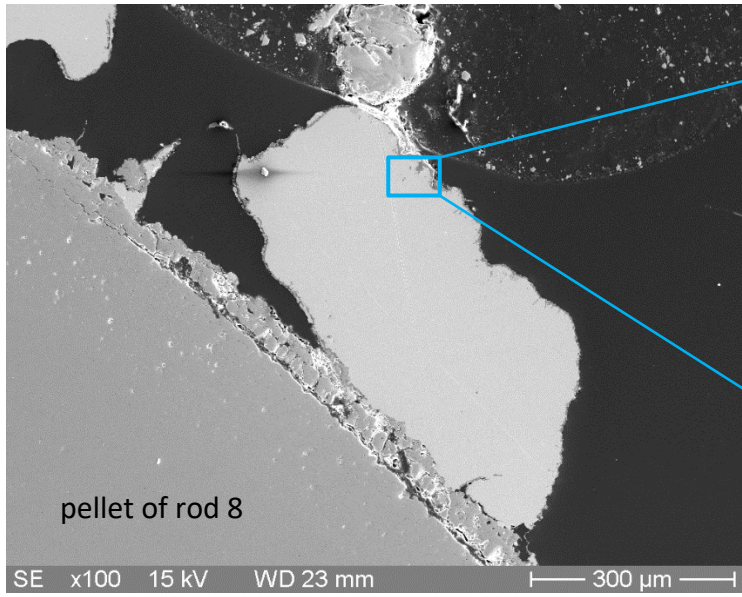
Figure 122   QUENCH-18; absorber molten pools between pellet and cladding oxide of rod #8 at 160 mm, results of EDX analysis.
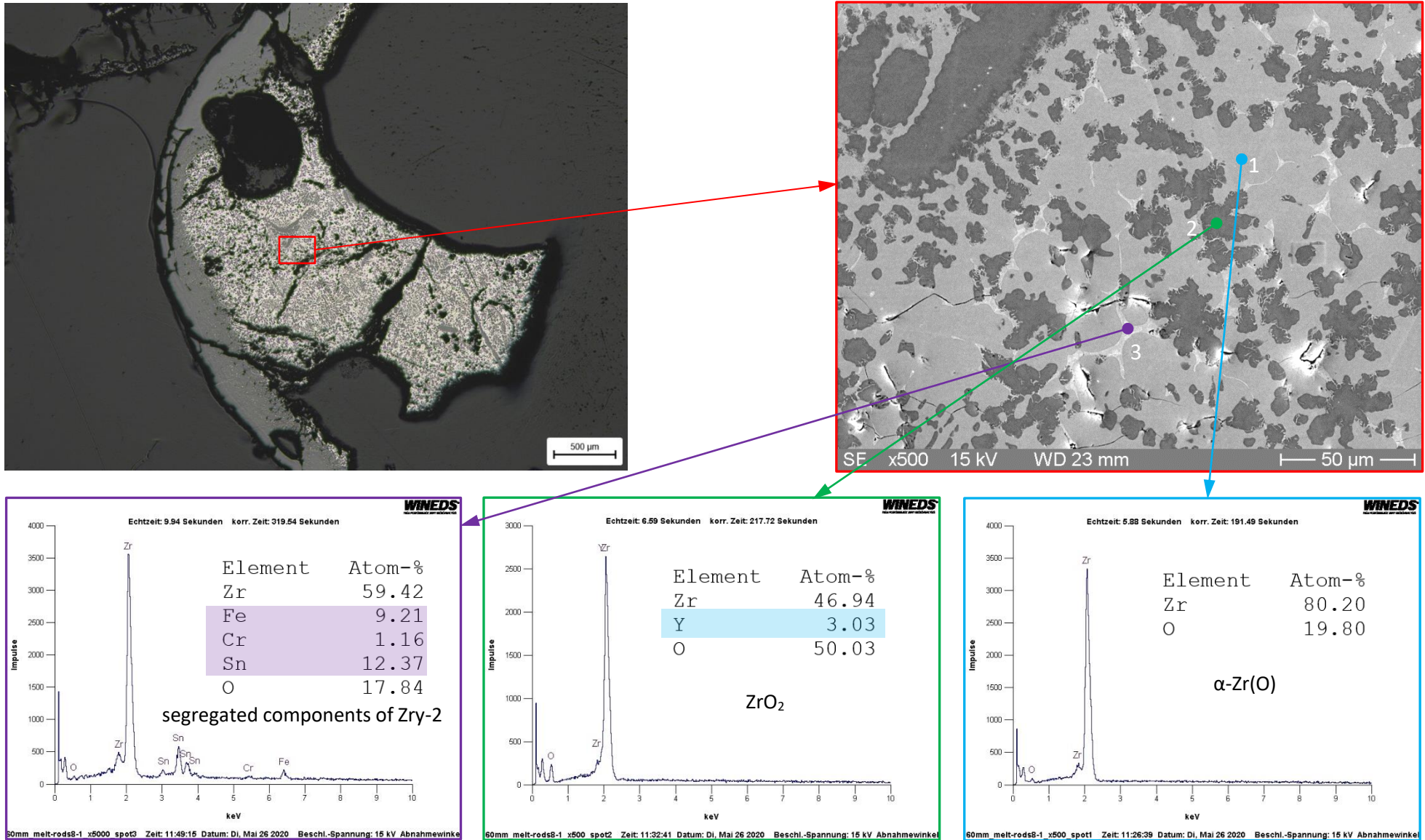
Figure 123 QUENCH-18; microstructure of frozen small molten pool near to rod #8 at 160 mm and results of EDX analysis.
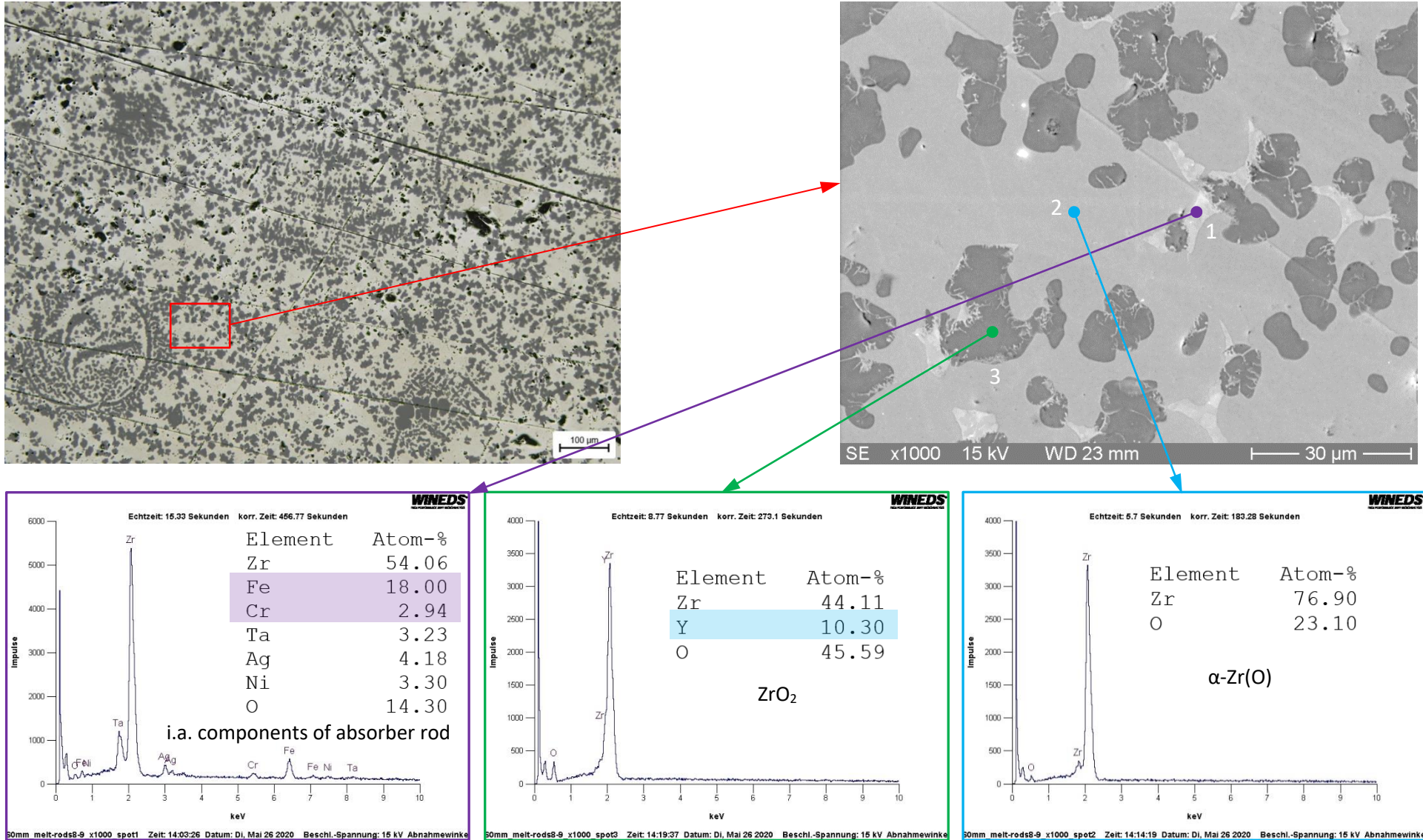
Figure 124   QUENCH-18; microstructure of frozen large molten pool between rod #8 and #9 at 160 mm and results of EDX analysis: part of ceramic precipitates are grains of disintegrated pellets (ZrO_2 stabilized with Y_2O_3).
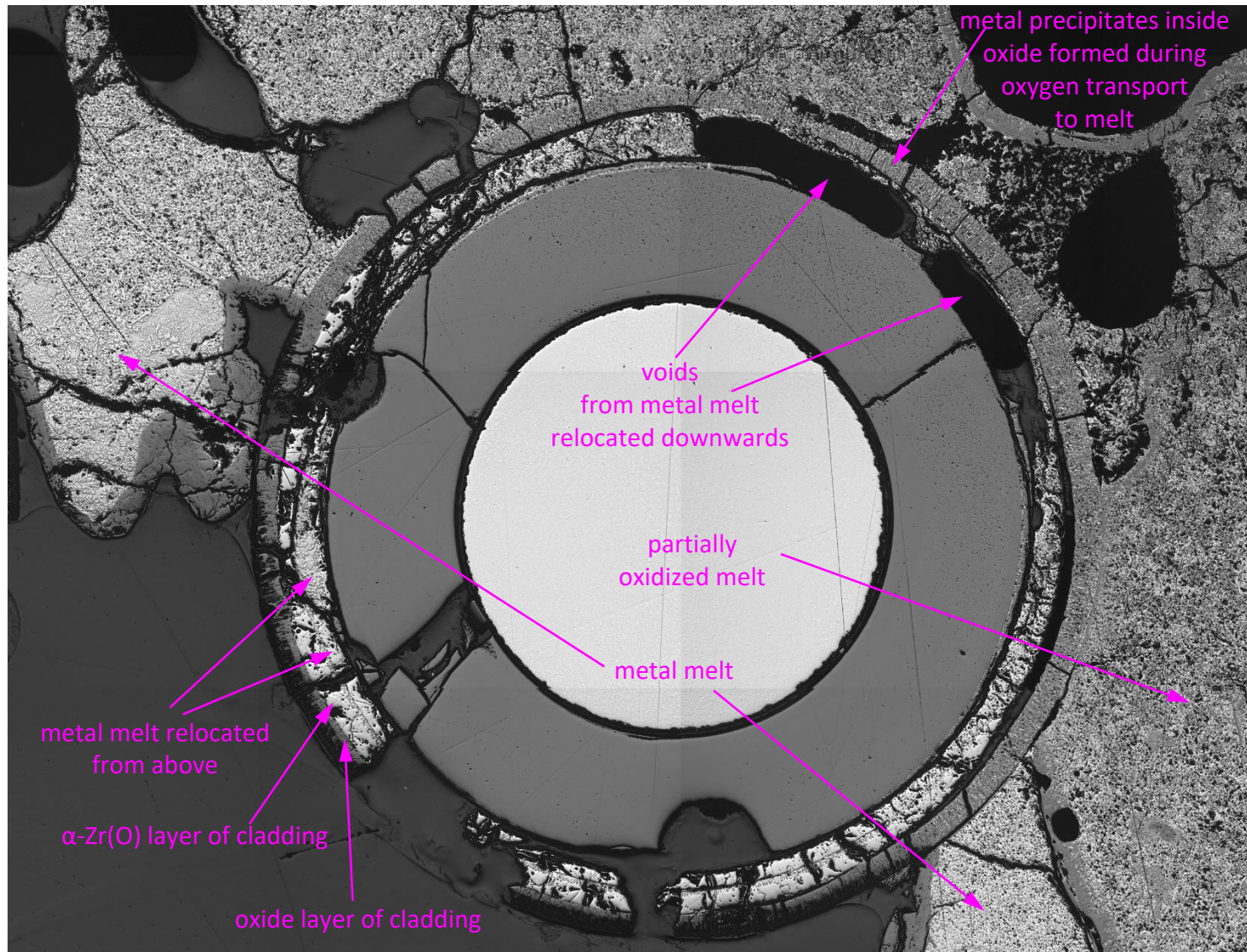
Figure 125   QUENCH-18; microstructure of rod elements for rod #10 and very porous partially oxidized melt at bundle elevation of 160 mm.
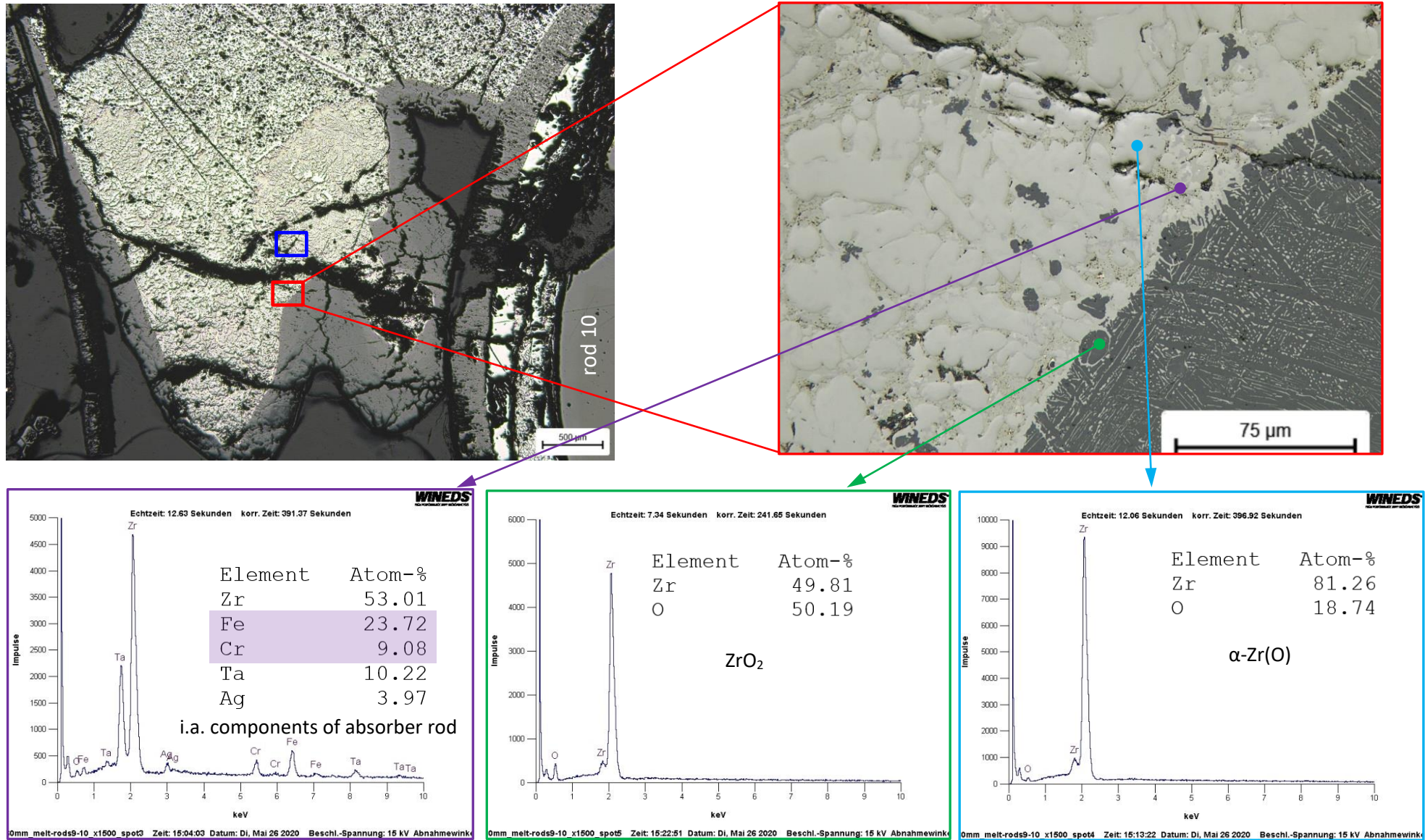
Figure 126 QUENCH-18; microstructure of molten pool near to rod #10 at 160 mm (metallic melt inside the pool and oxidized melt on its border).
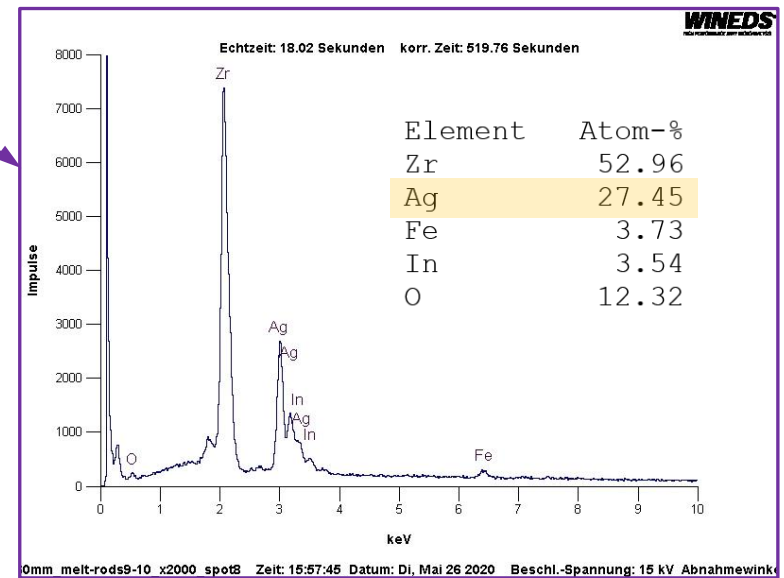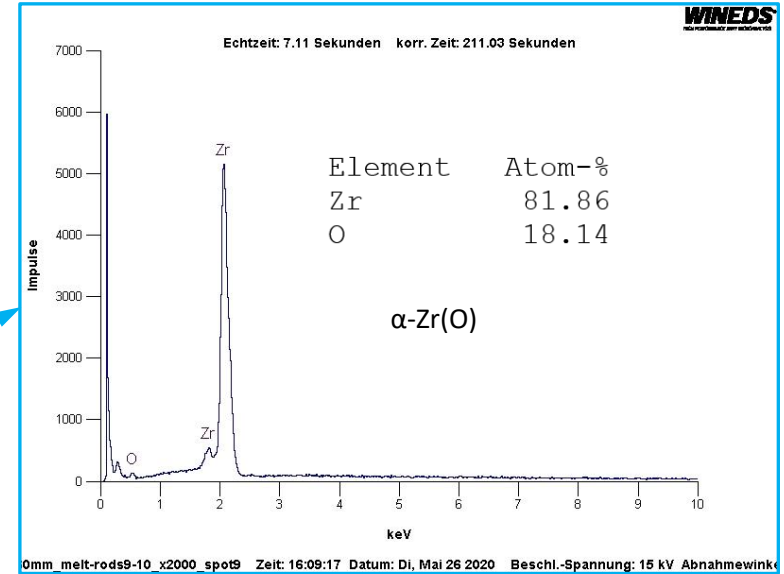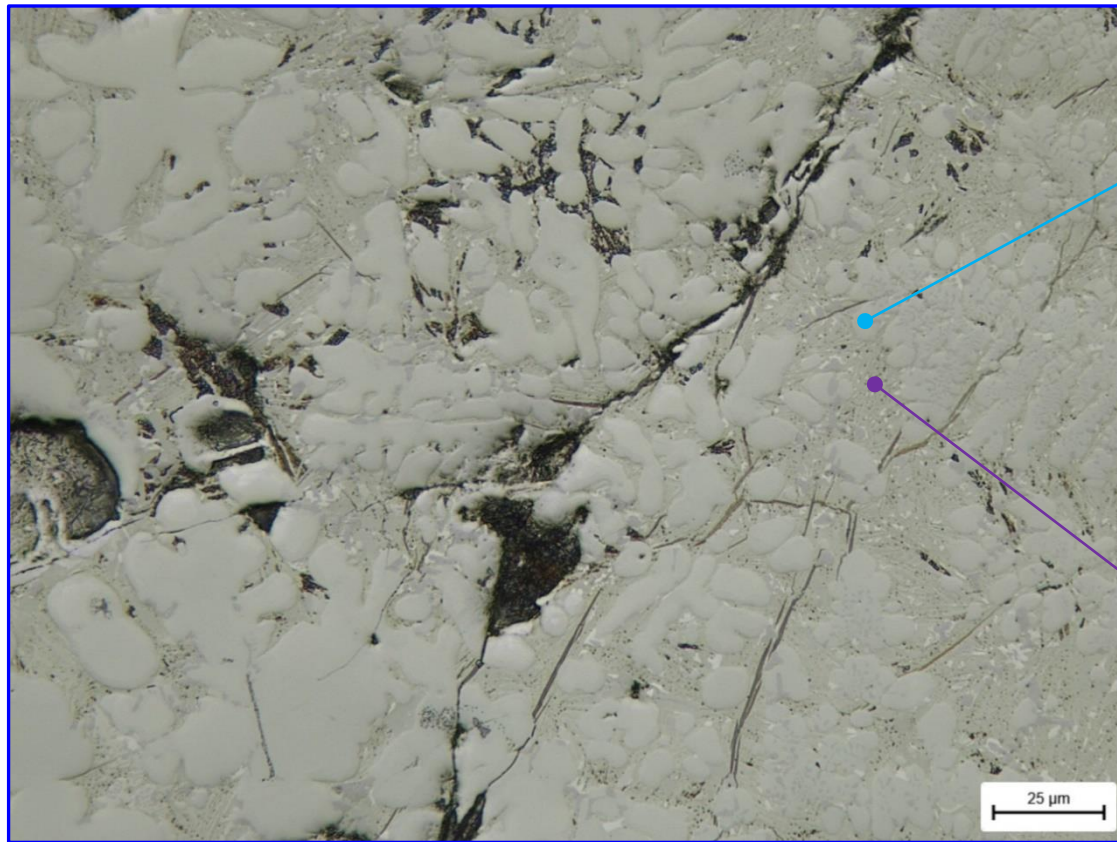
Figure 127 QUENCH-18; microstructure of molten pool between rods #9 and #10 at 160 mm (metallic melt marked with blue in previous Figure).
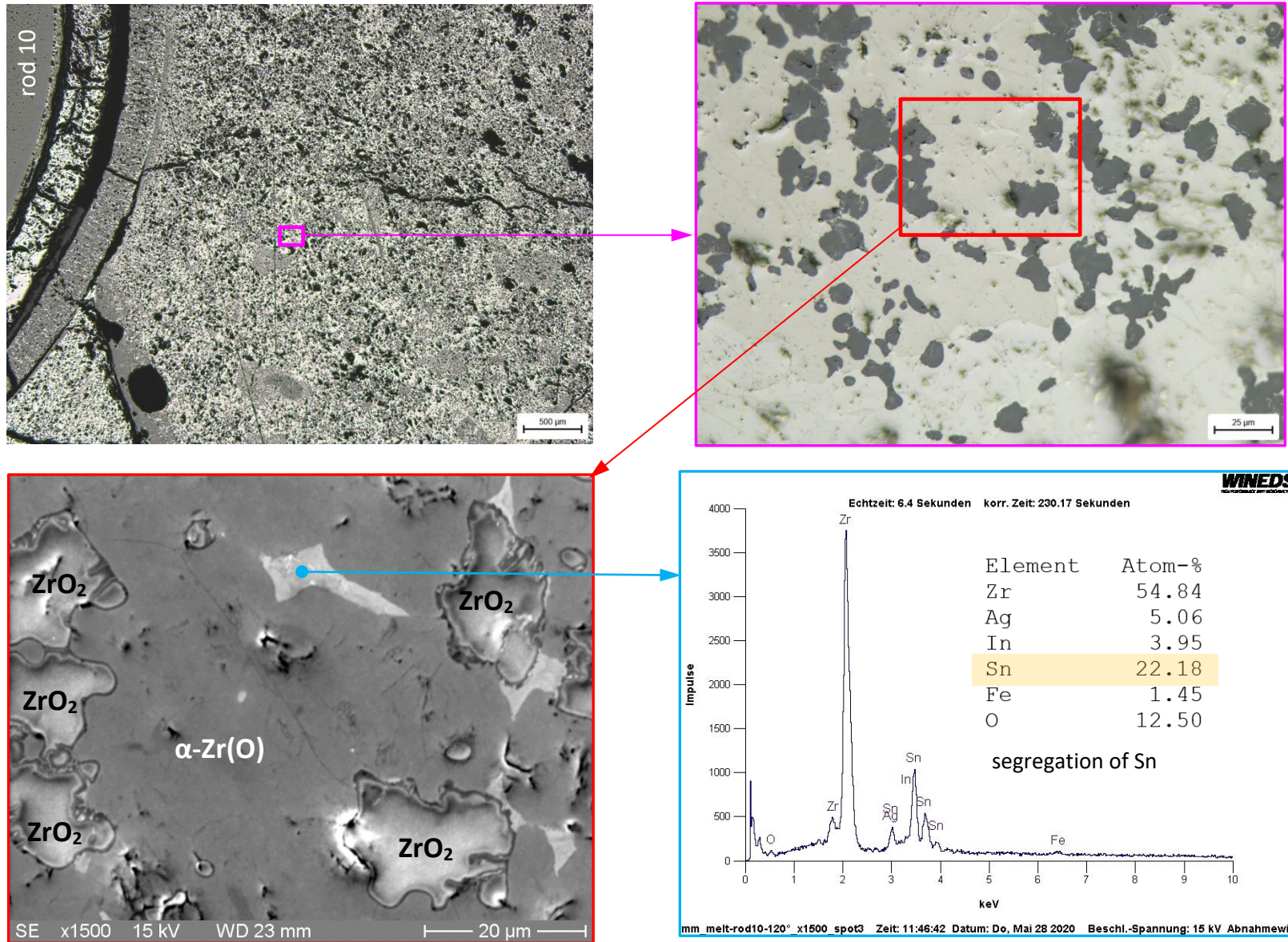
Figure 128   QUENCH-18; microstructure of molten pool between rods #10 and #11 at 160 mm partially oxidized at temperature.
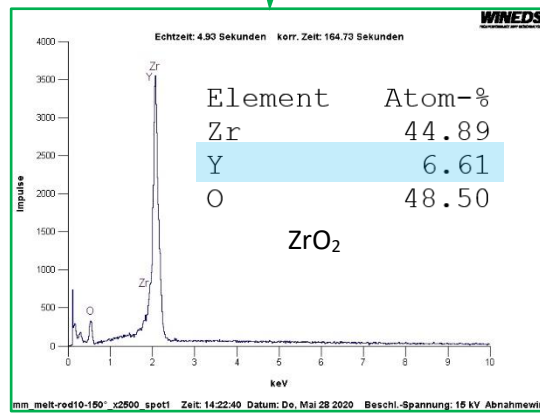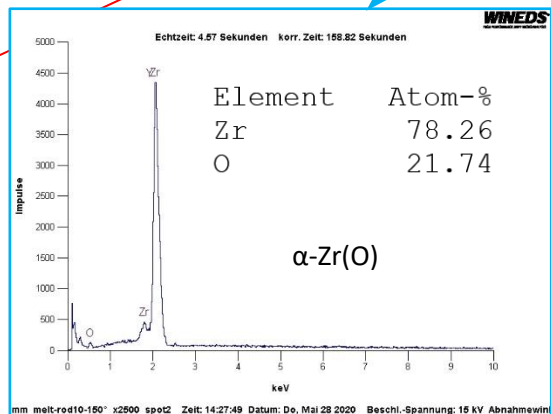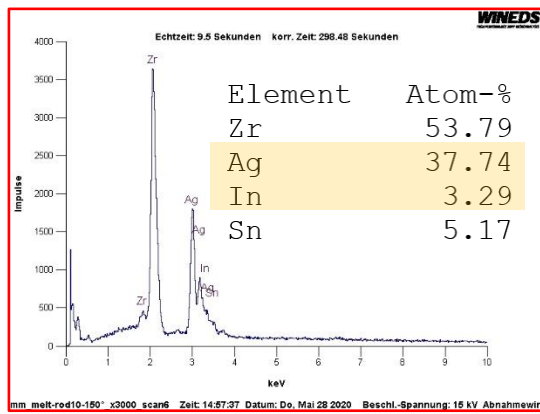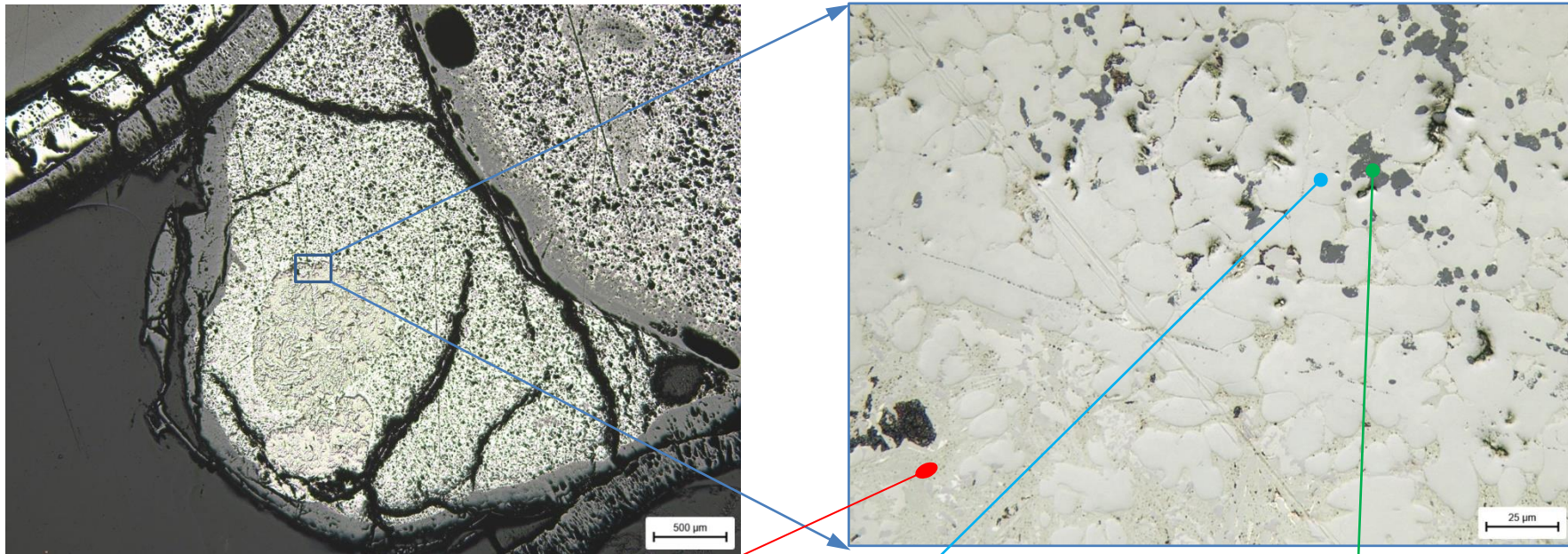
Figure 129 QUENCH-18; microstructure of metal molten pool between rods #10 and #11 at 160 mm.
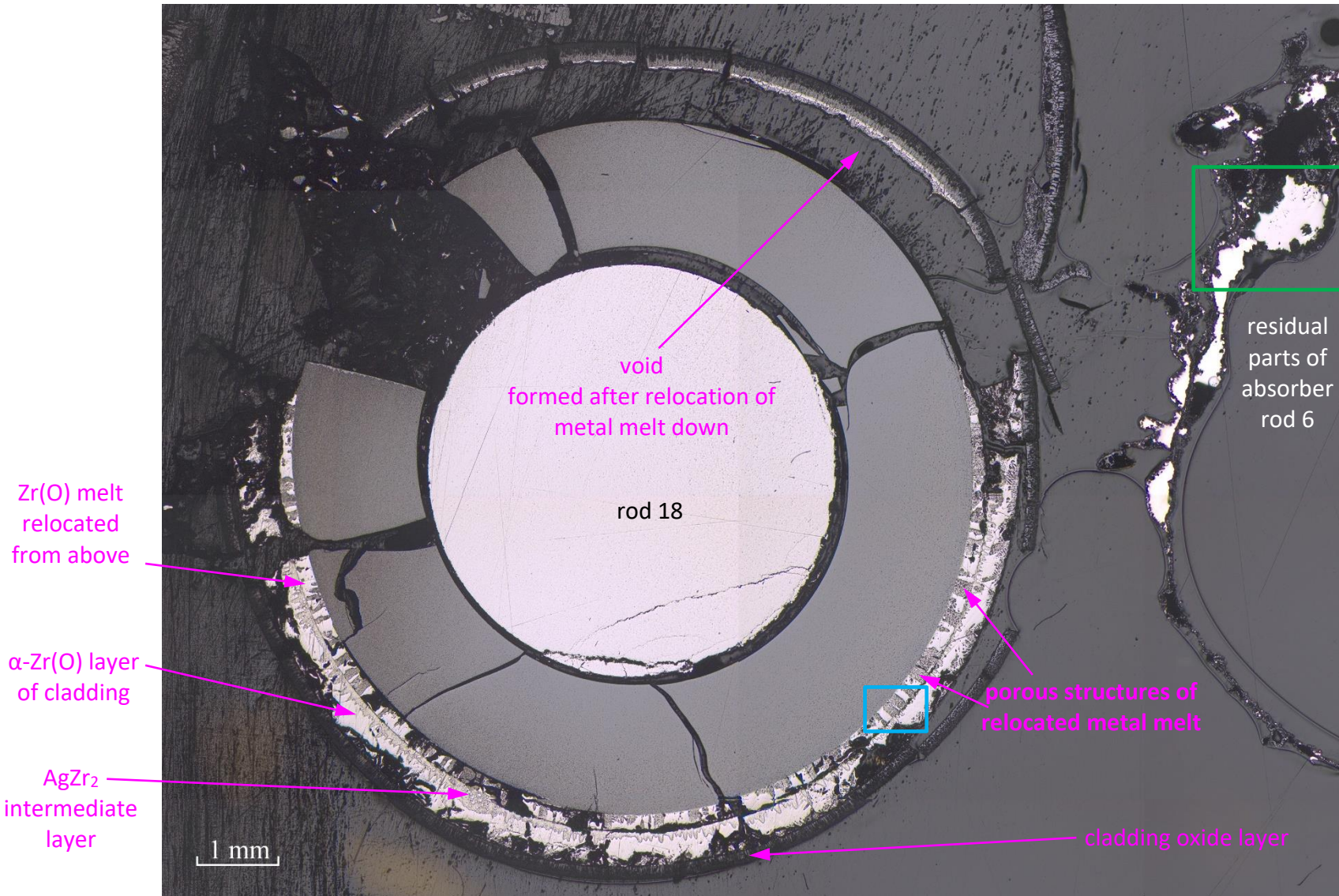
Figure 130   QUENCH-18; microstructure of rod elements for rod #18 and #6 at bundle elevation of 160 mm with regions marked for EDX analysis.
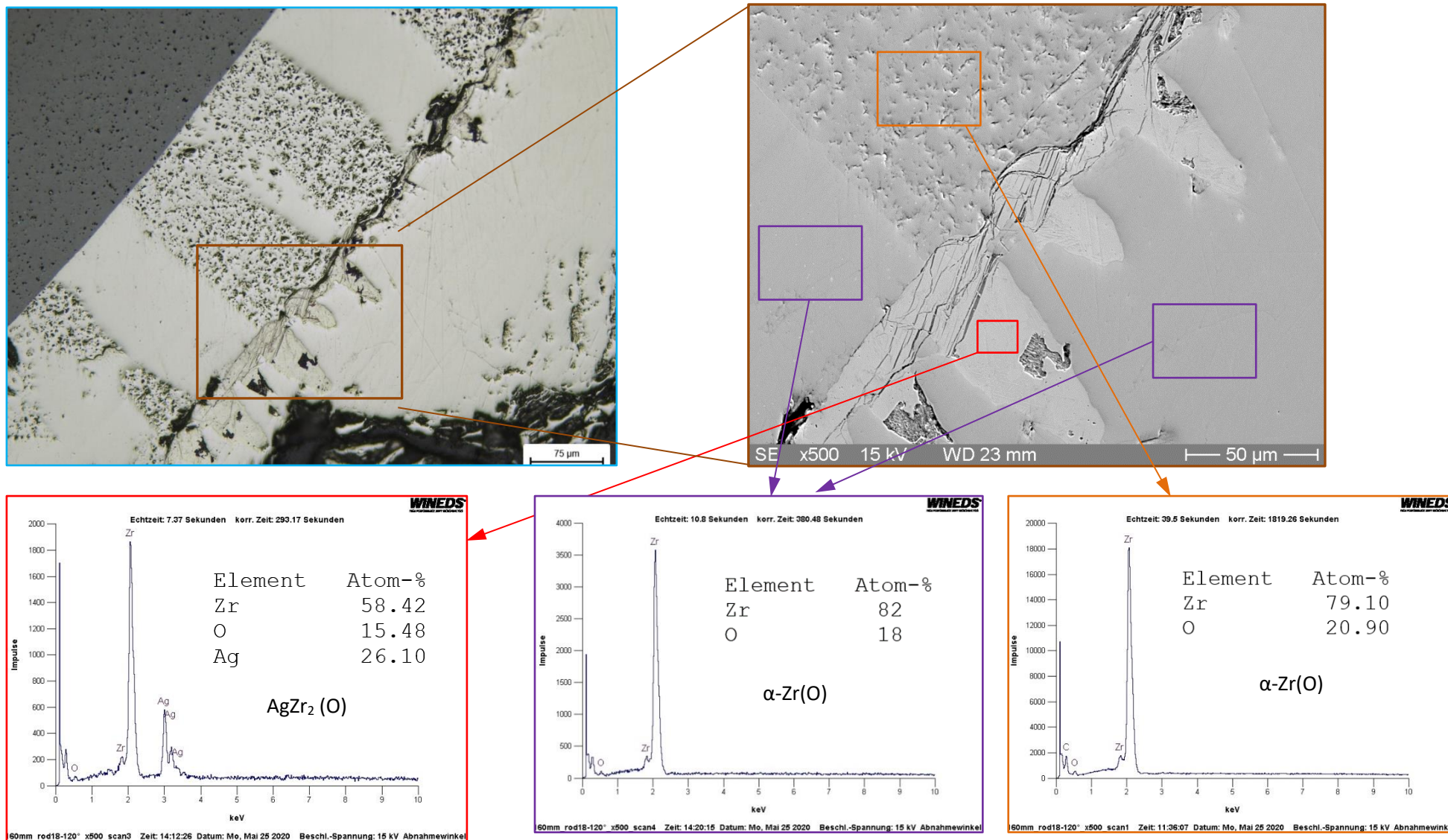
Figure 131   QUENCH-18; microstructure of cladding for rod #18 at bundle elevation of 160 mm: penetration of Ag from absorber rod #6 into the gap between cladding and cladding melt relocated from above.
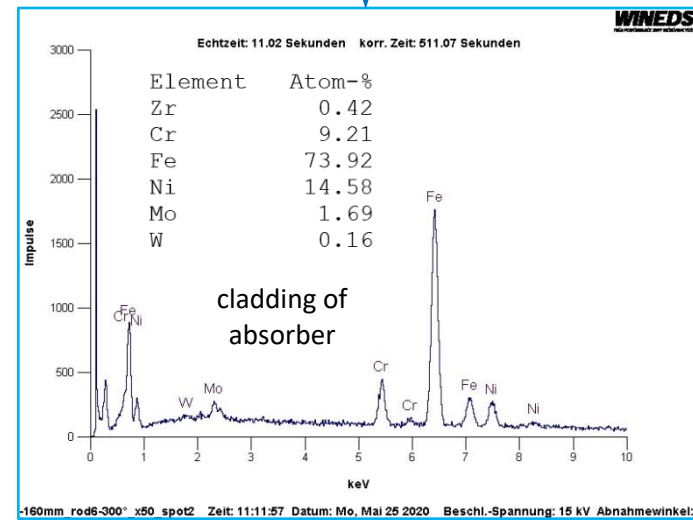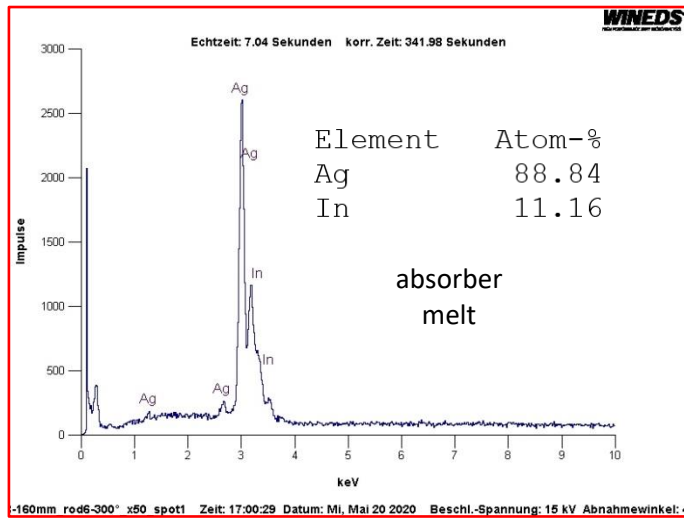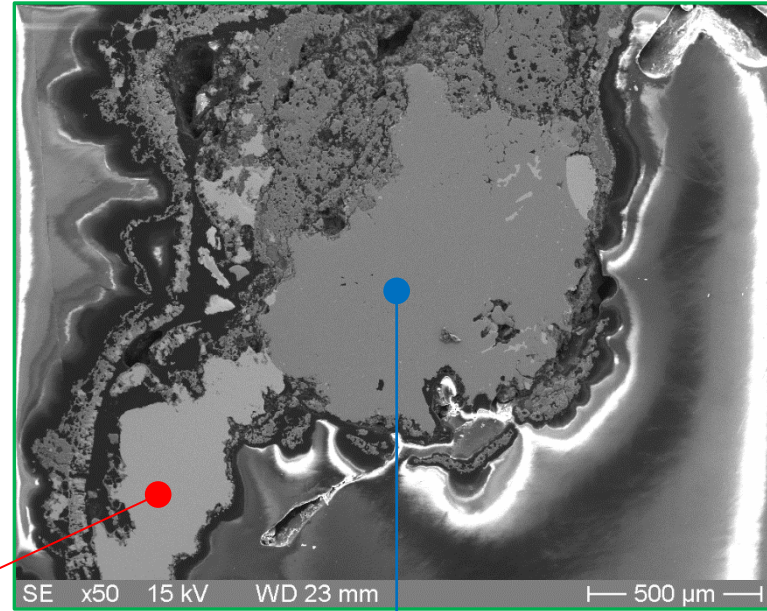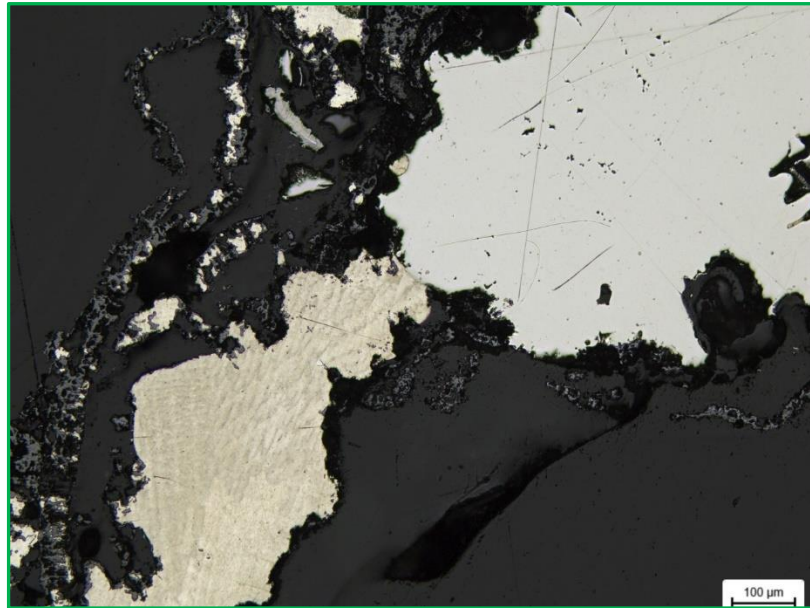
Figure 132 QUENCH-18; frozen absorber melt (AgInCd) and melt of absorber cladding (SS 316L: Fe, Cr, Ni, Mo) of rod #6 at elevation 160 mm.

heated rod

B

A

corner rod C

D

E

shroud

H

G

F

bundle composition

relocated and frozen (Ag,In) melt

relocated and frozen Zr-based metal mixture with Ag, In

relocated and frozen (Ag,In) melt

not oxidized cladding

grid spacer

5 mm

cross section, perspective projection, mirrored bottom view of slice 65-95 mm
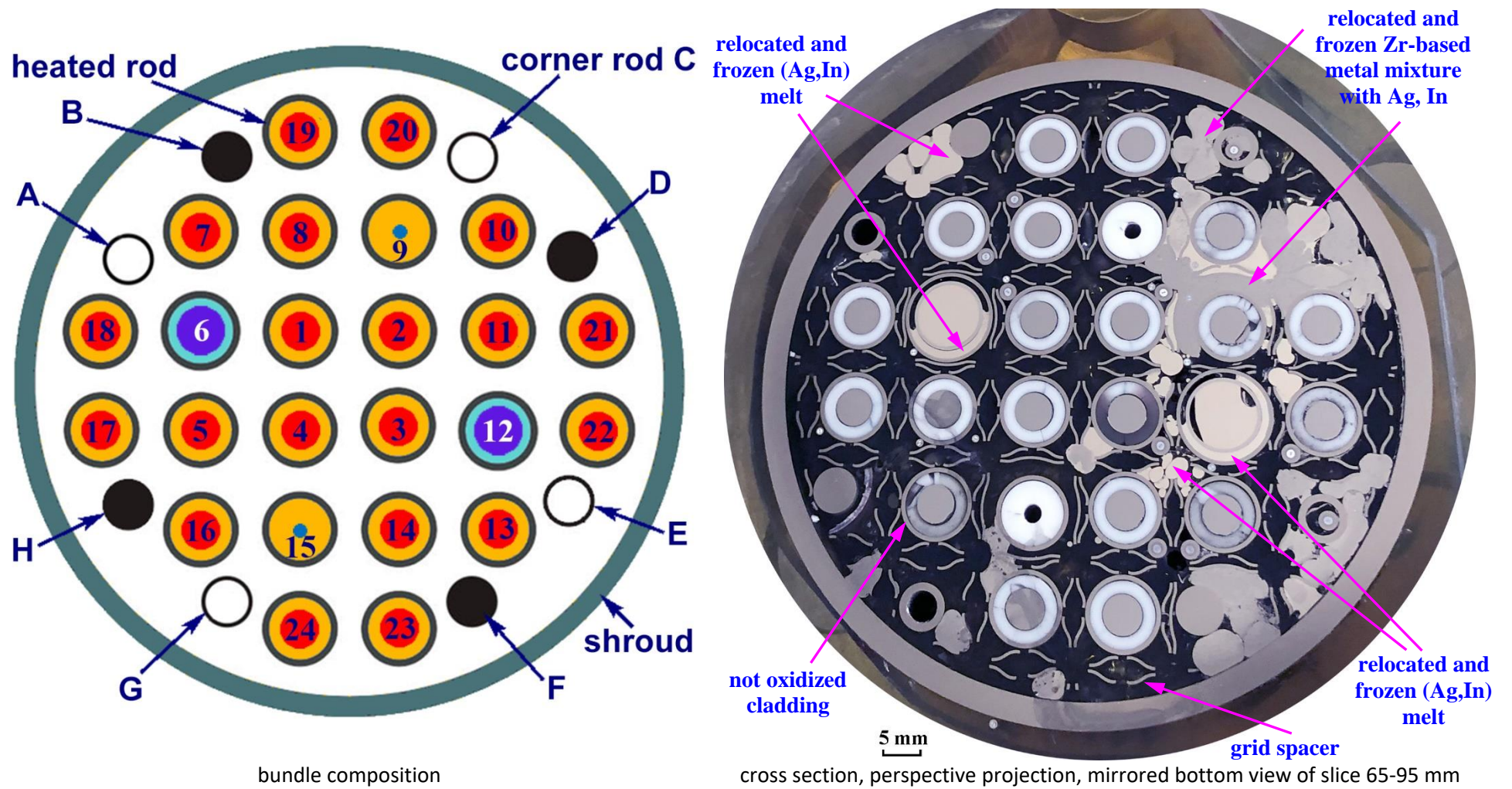
Figure 133 QUENCH-18; cross section at bundle elevation of 65 mm: metallic melts (AgInCd and Zr-bearing) downwards relocated and frozen inside grid spacer.
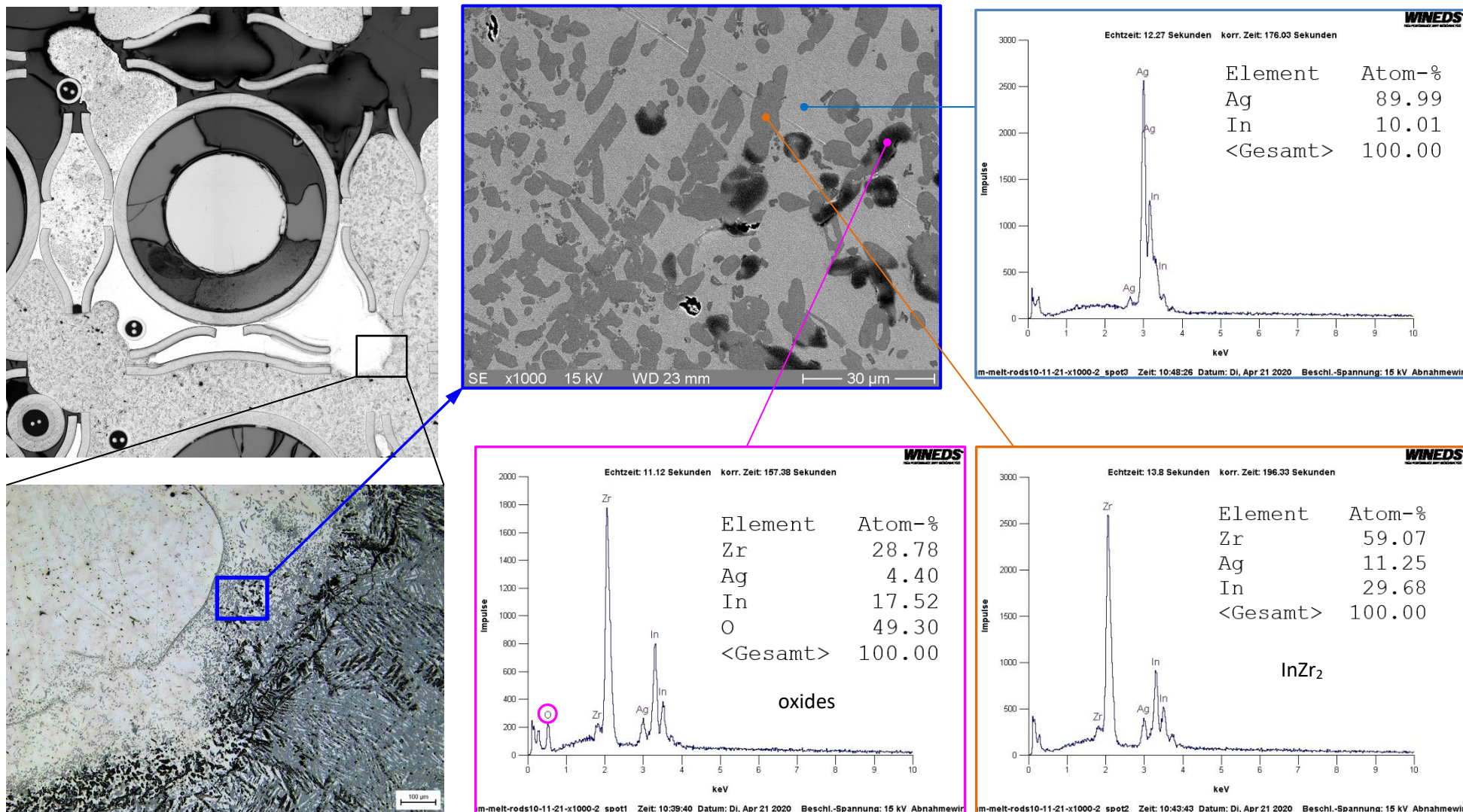
Figure 134   QUENCH-18; relocated absorber melt in the surroundings of rod #10 at bundle elevation of 65 mm, not oxidized cladding and grid spacer, roughly elemental composition: InZr$_2$ precipitates inside Ag melt.
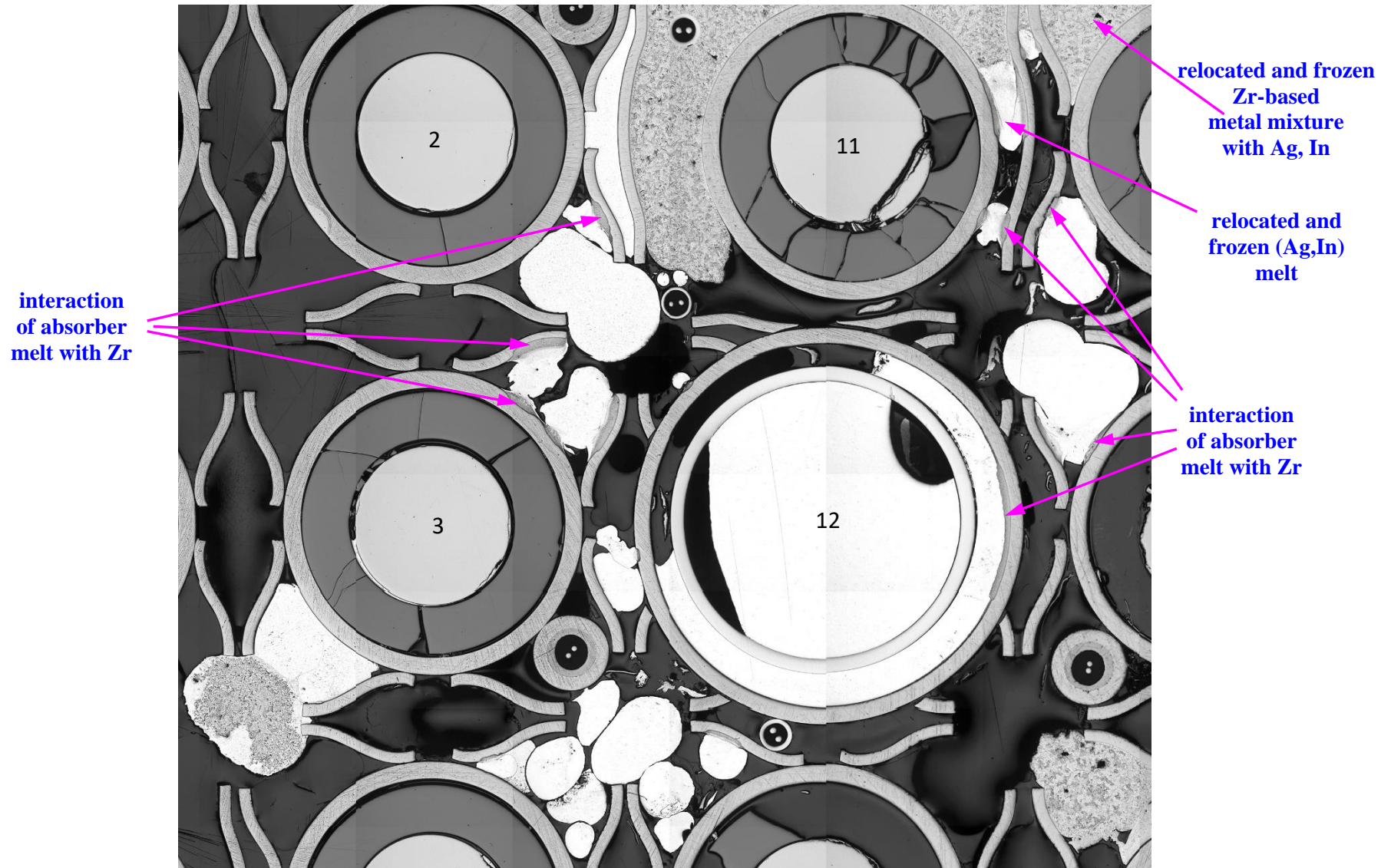
Figure 135 QUENCH-18; molten pools at elevation 65 mm formed around absorber rod #12 from absorber material relocated from upper bundle elevations.
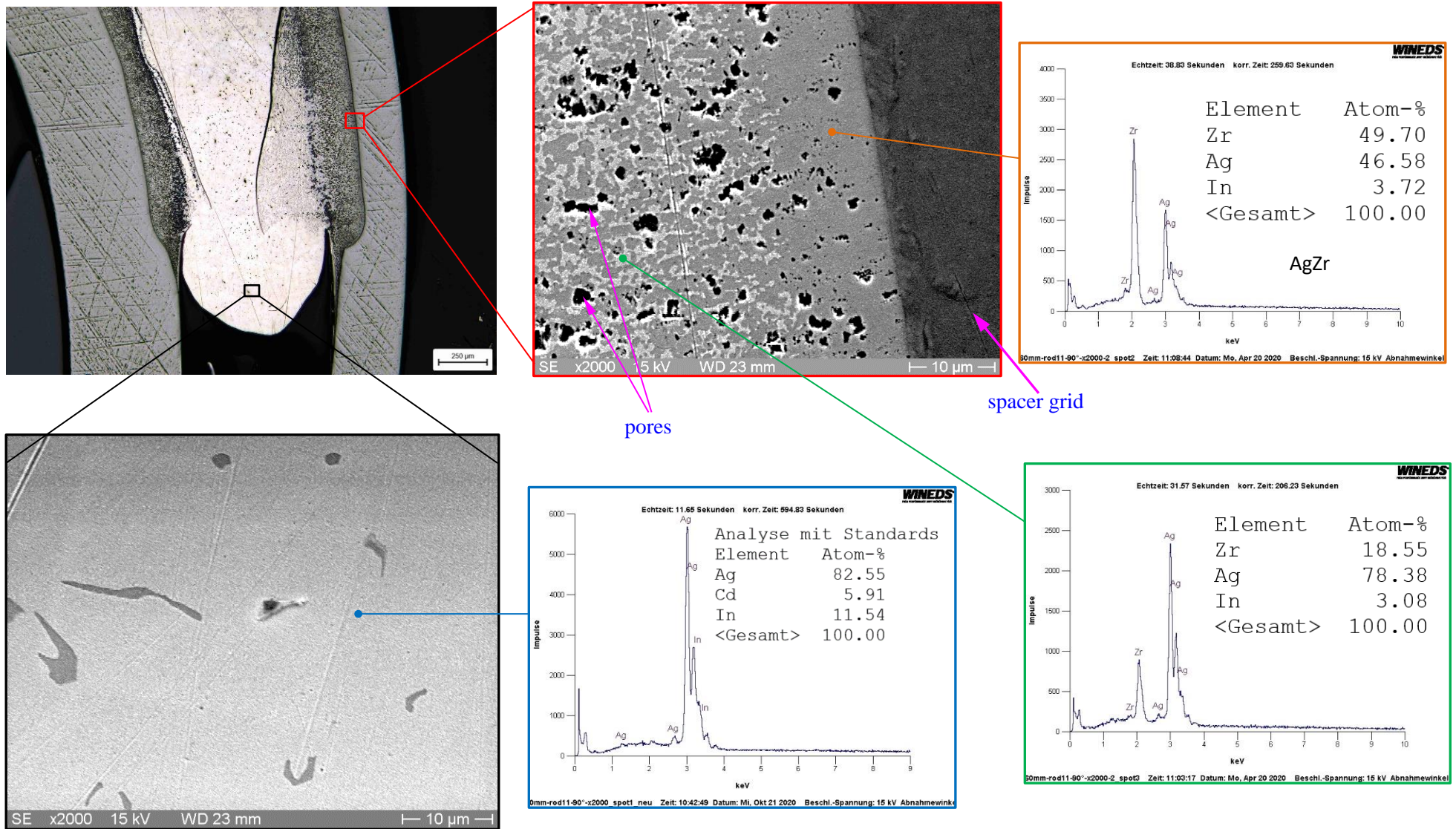
Figure 136 QUENCH-18; absorber melt at elevation 65 mm frozen between cladding of rod #11 and grid spacer, interaction of absorber melt with Zr, roughly elemental composition: AgZr precipitates inside Ag melt.
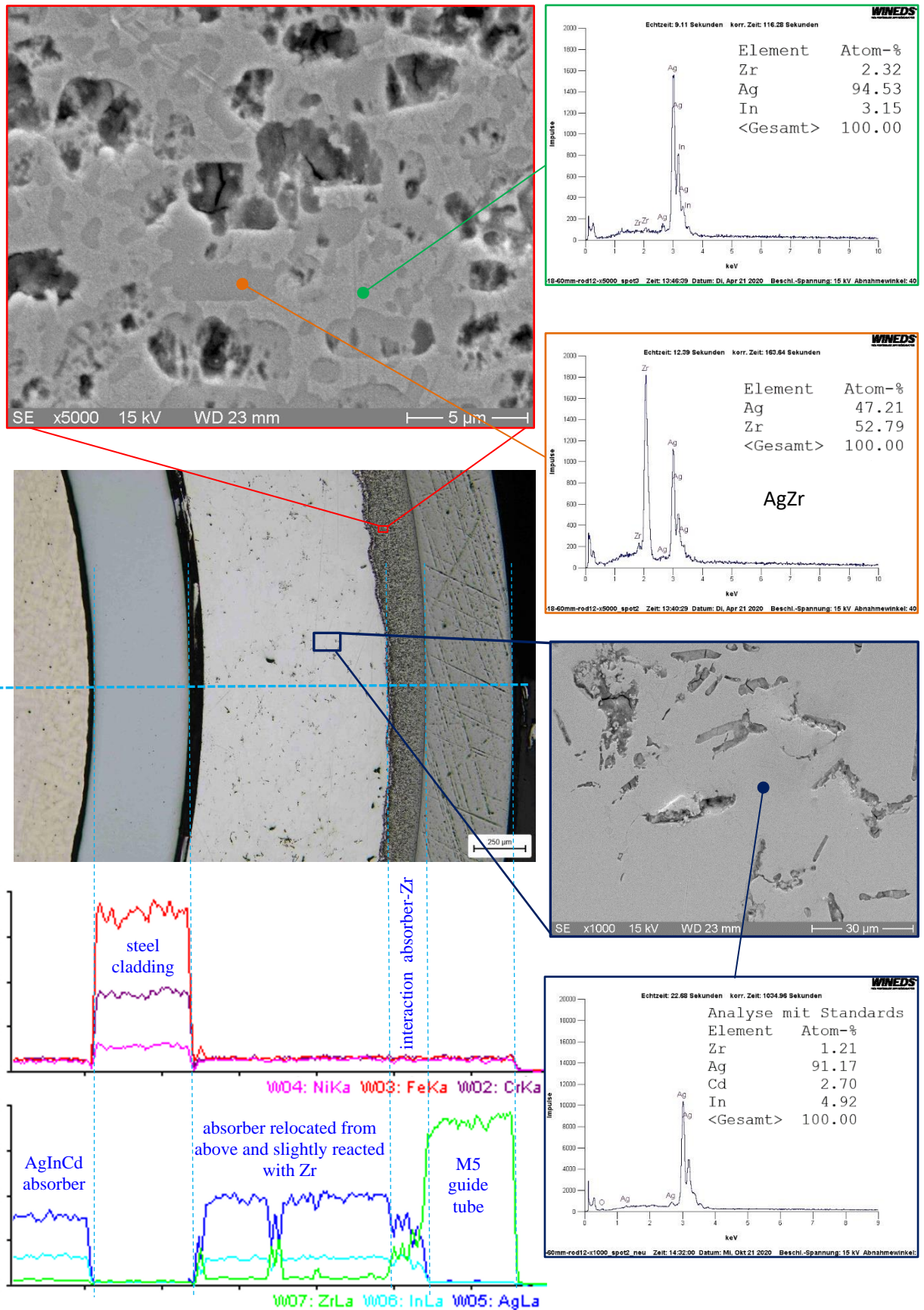
Figure 137 QUENCH-18; structure and approximate elemental composition of absorber rod #12 at elevation 65 mm: line EDX scan: AgZr precipitates in Ag melt inside zone of interaction between released absorber and Zr cladding.
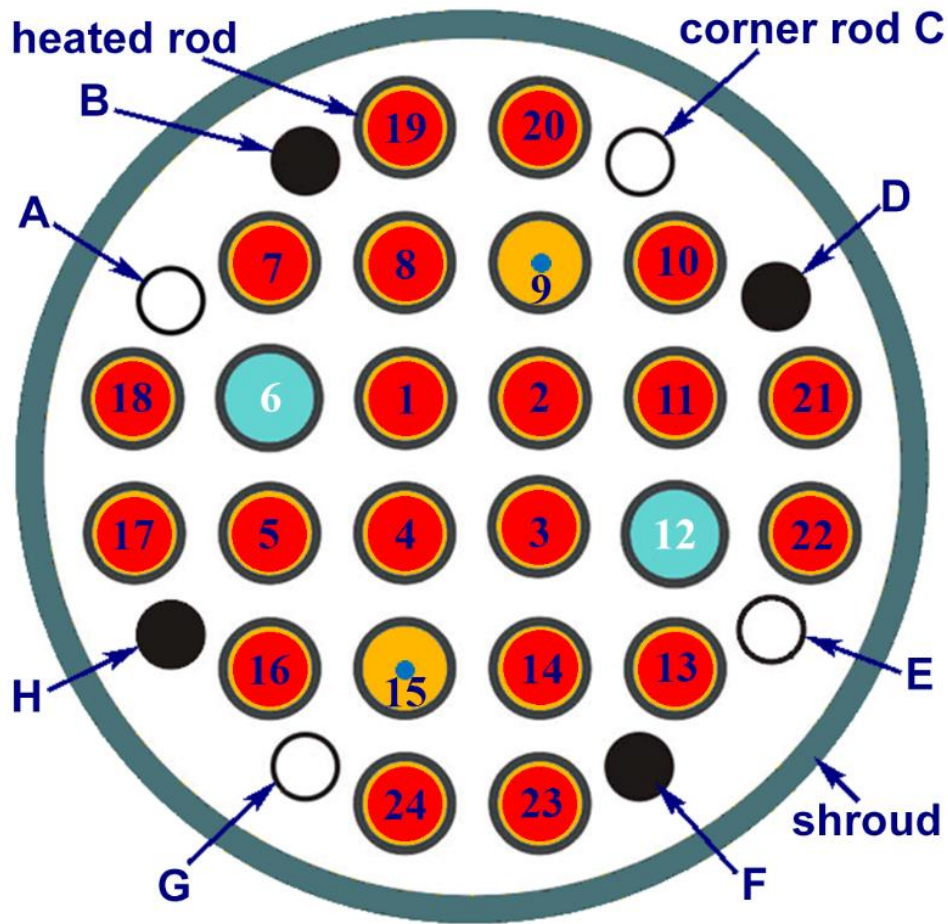
bundle composition: Mo heaters inside heated rods, stainless steel plugs in lower parts of absorber rods
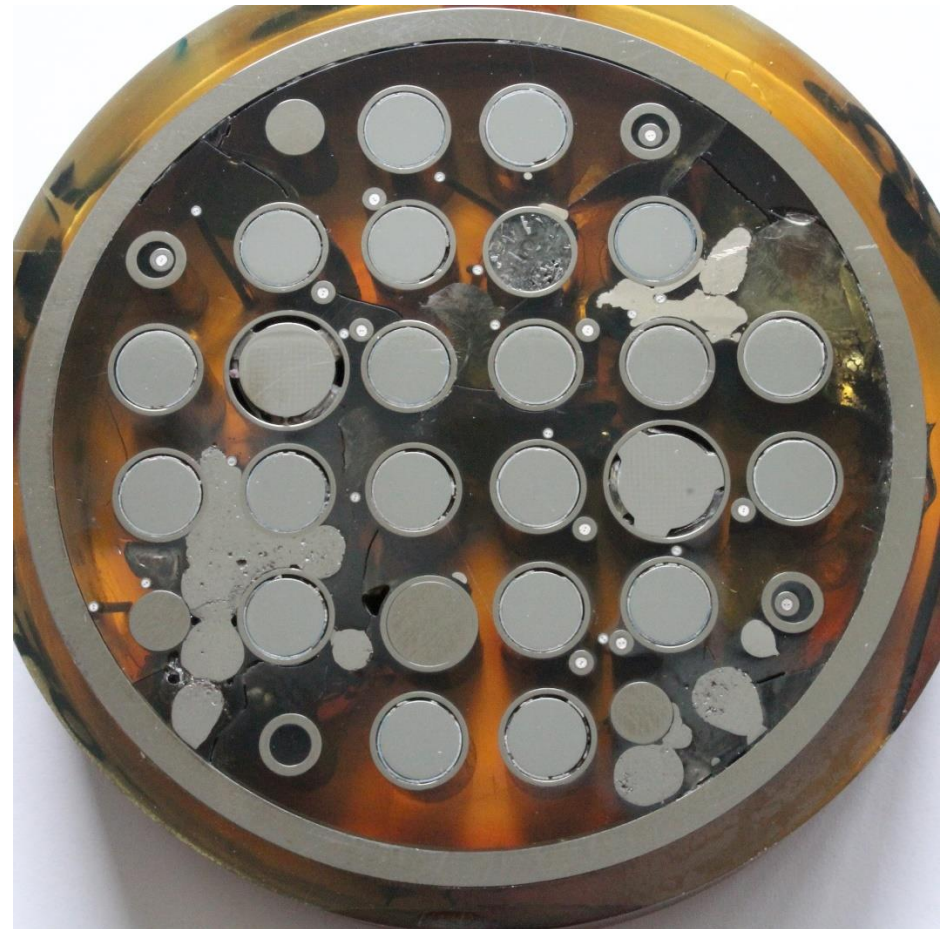
cross section mirrored bottom view of slice -40…-15 mm: frozen molten metal pools relocated from upper elevations

Figure 138   QUENCH-18; cross section at bundle elevation of -40 mm.
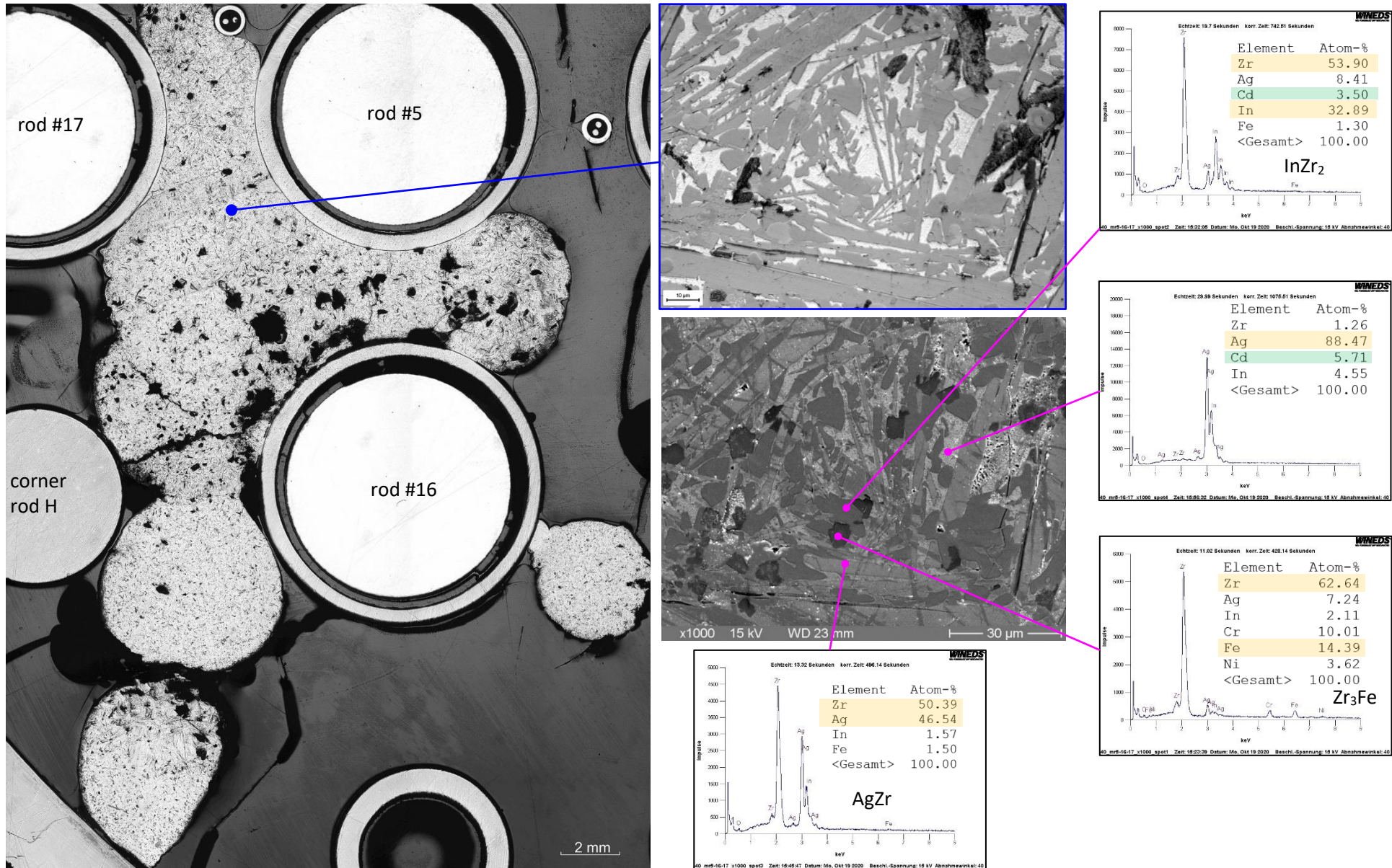
Figure 139 QUENCH-18; microscale "Widmanstätten pattern" of frozen indium-bearing absorber melt (from rod #6) relocated between rods #5 and #17 from upper elevations to -40 mm: AgZr lamellae as well as InZr$_2$ and Zr$_3$Fe precipitates formed in (Ag, In, Cd) melt.
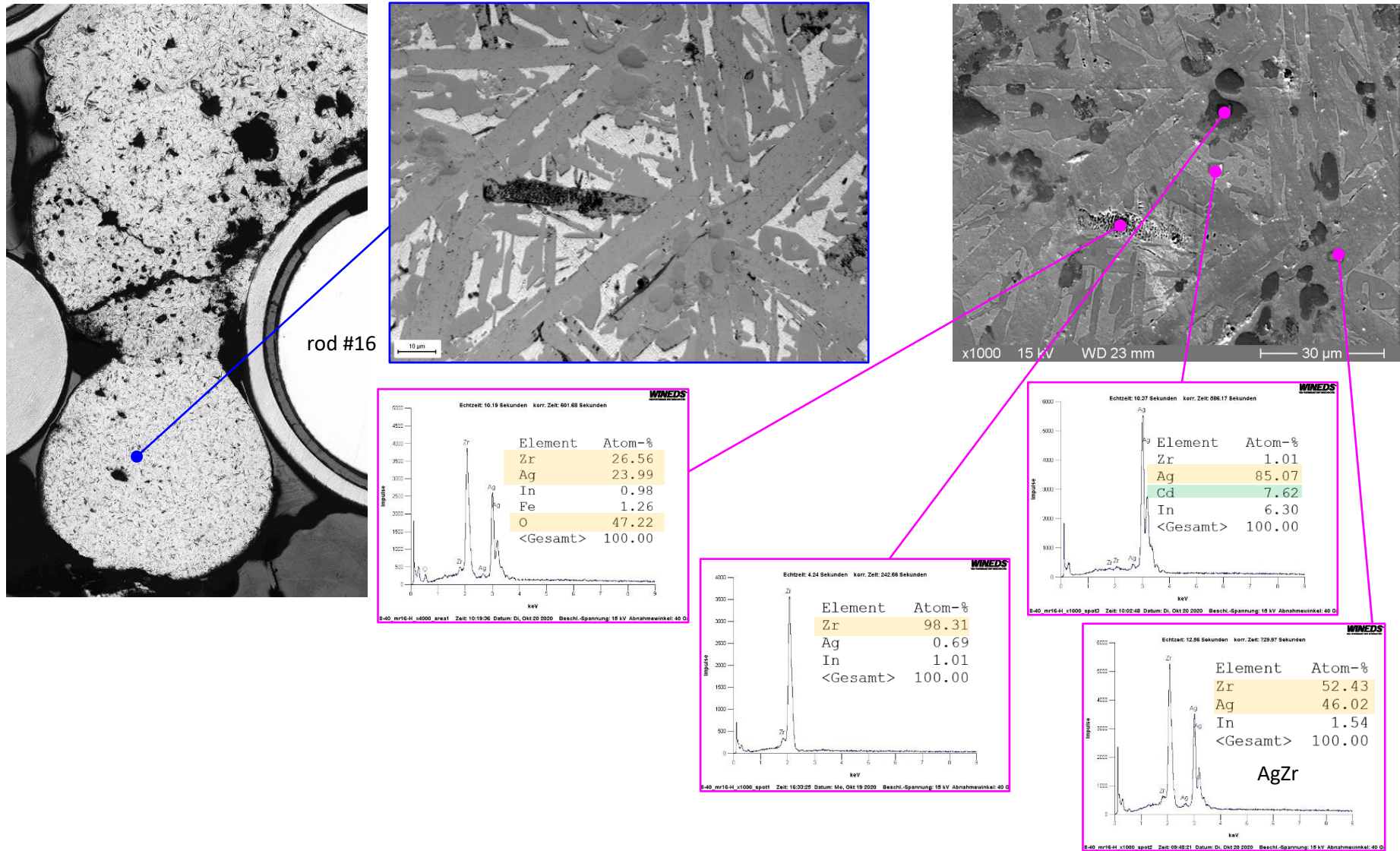
Figure 140 QUENCH-18; microscale "Widmanstätten pattern" of frozen low-iron absorber melt (from rod #6) relocated between rods #16 and #H from upper elevations to -40 mm: AgZr metal and porous oxidized lamellae (with included Zr particles) formed in (Ag, In, Cd) melt.
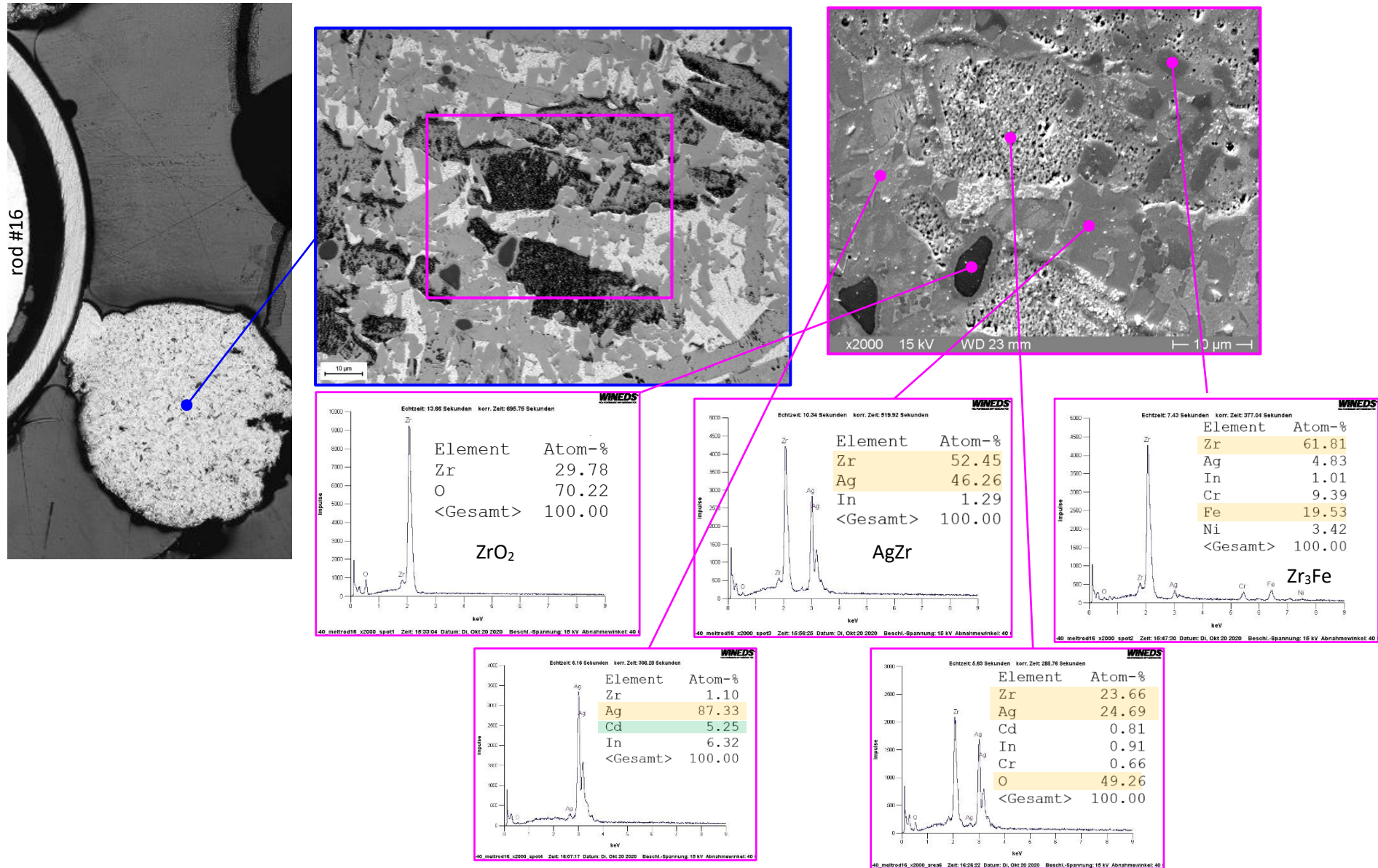
Figure 141 QUENCH-18; structure of frozen iron-bearing absorber melt (from rod #6) relocated between rods #15 and #16 from upper elevations to -40 mm: AgZr metal and porous oxidized precipitates as well as Zr_3Fe and ZrO_2 precipitates formed in (Ag, In, Cd) melt.
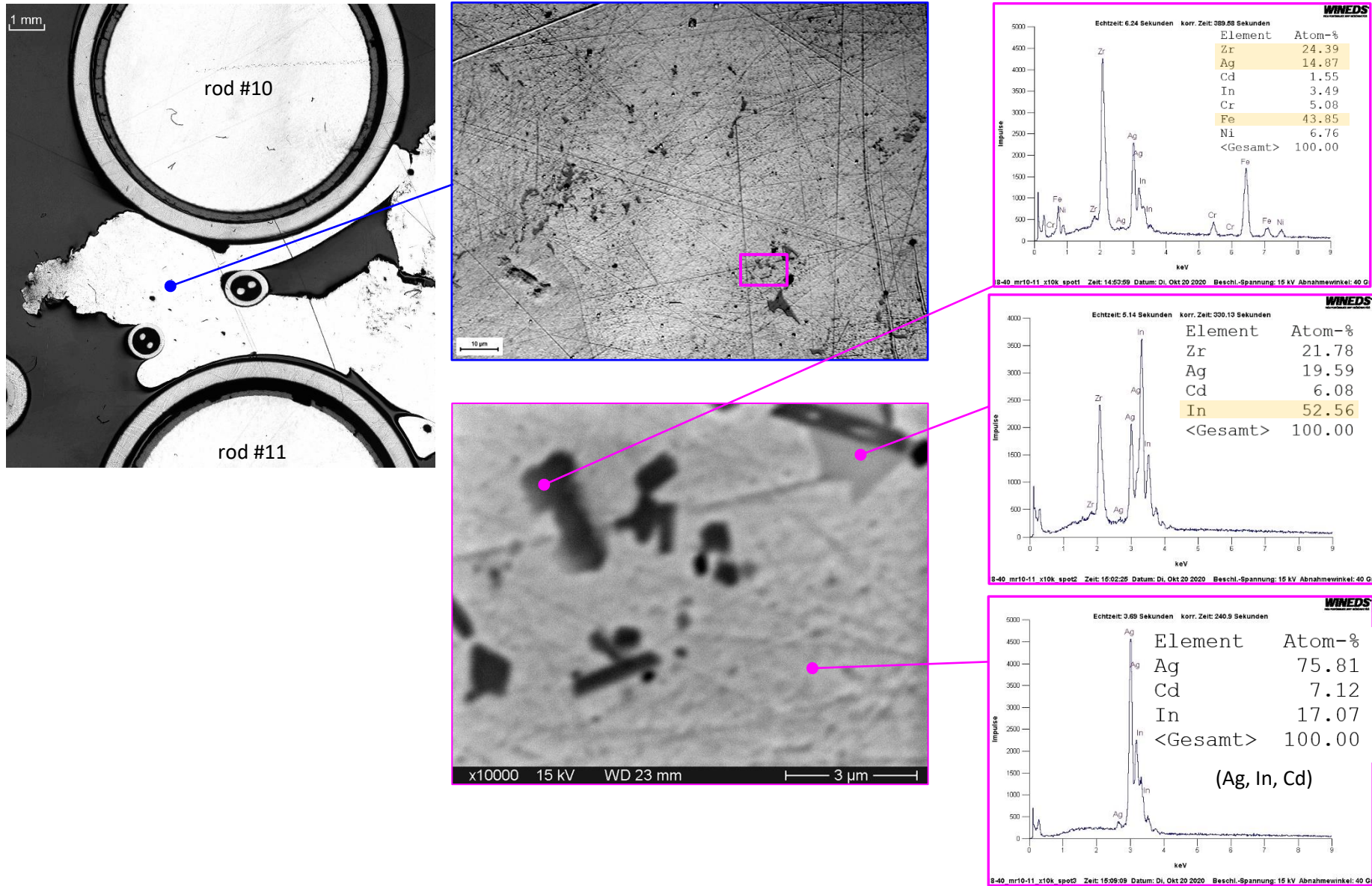
Figure 142 QUENCH-18; structure of frozen absorber melt (from rod #12) relocated from upper elevations to -40 mm: Fe and Zr precipitates inside (Ag, In, Cd) melt.
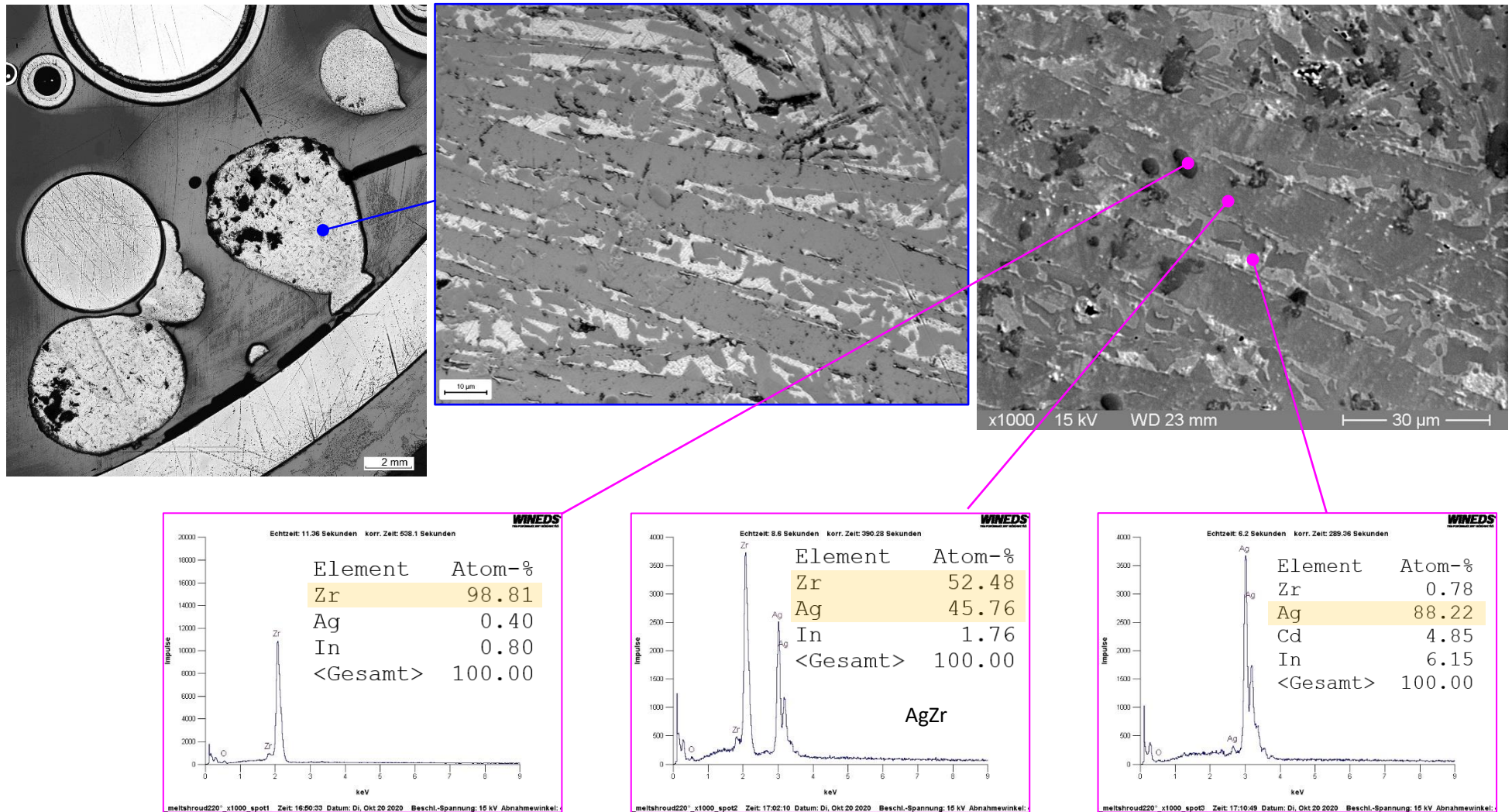
Figure 143   QUENCH-18; microscale "Widmanstätten pattern" of frozen absorber melt (from rod #12) relocated along the shroud from upper elevations to -40 mm: AgZr lamellae formed inside (Ag, In, Cd) melt.
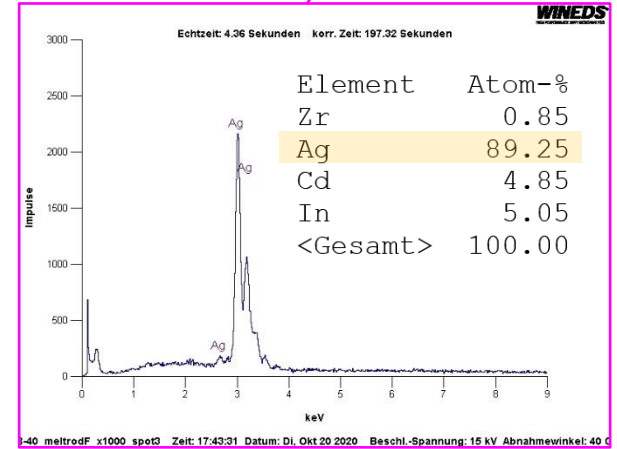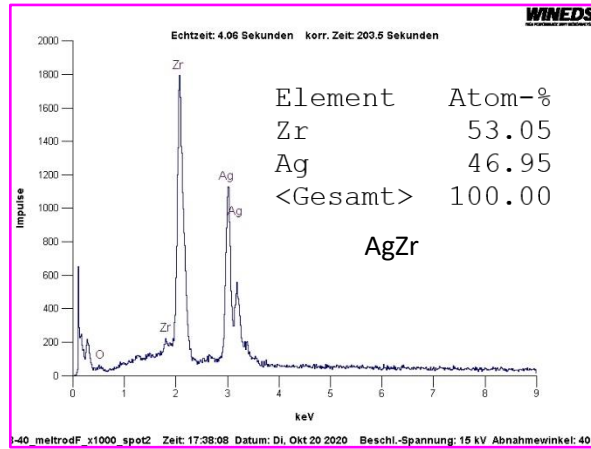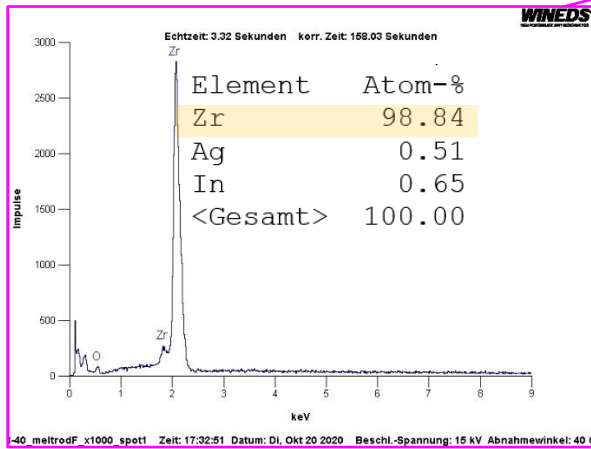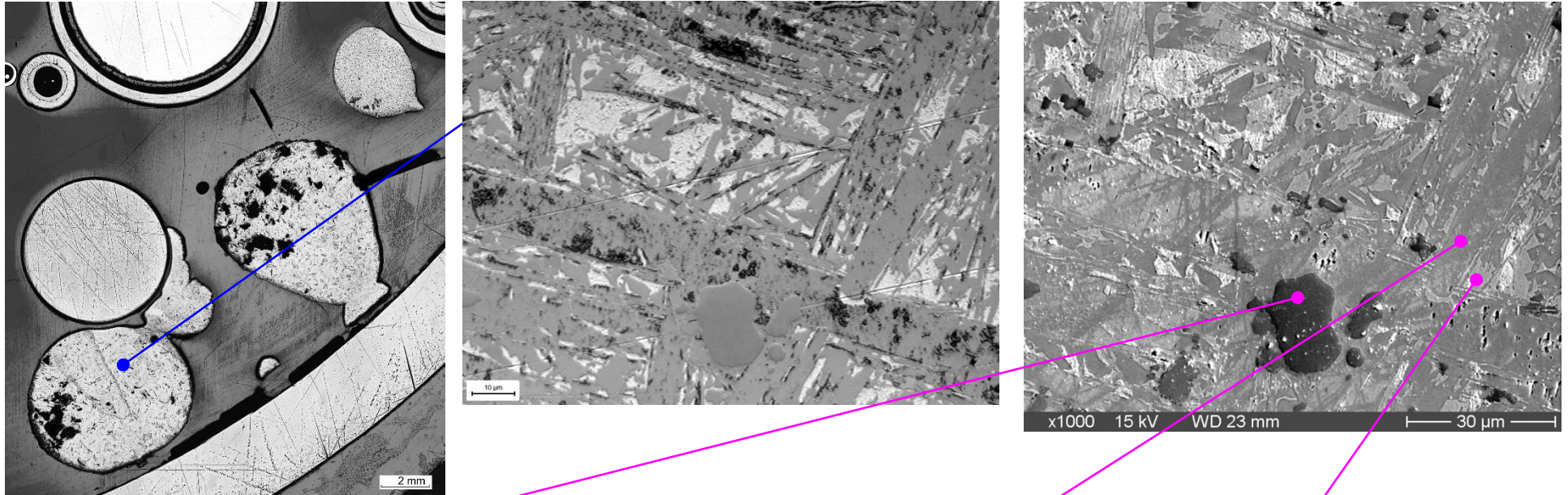
Figure 144 QUENCH-18; AgZr precipitates and Zr particles inside (Ag, In, Cd) melt relocated from upper elevations to -40 mm.

Zr-Fe

Ag-Zr

In-Zr

Ag-In

Ag-Cd

Cd-In
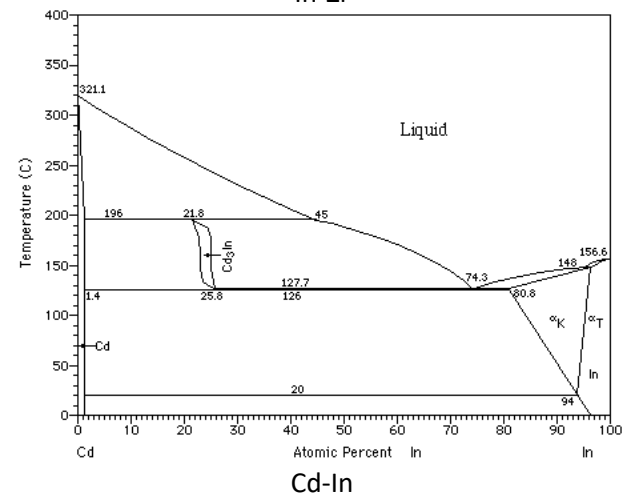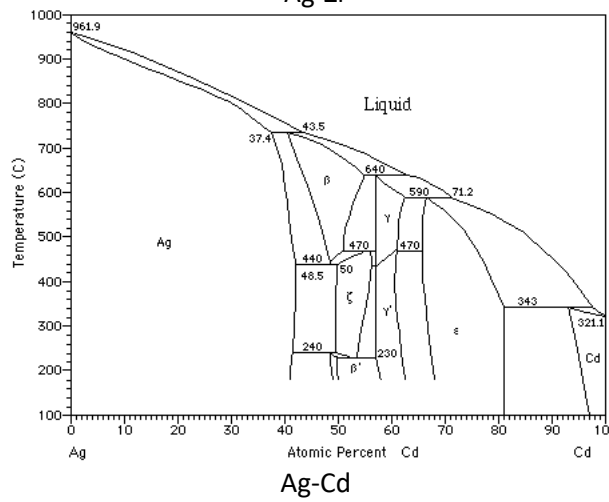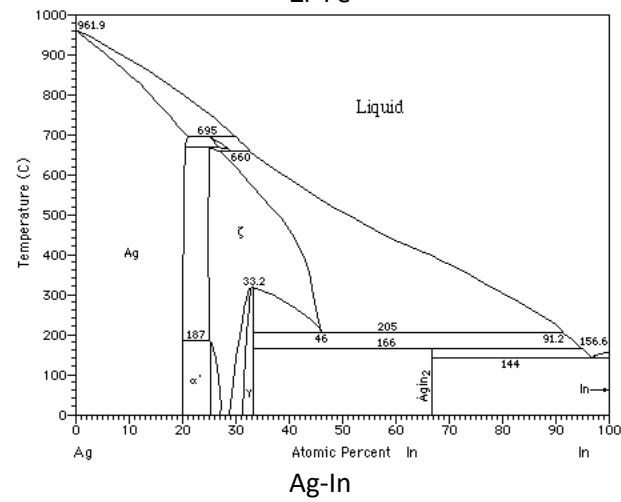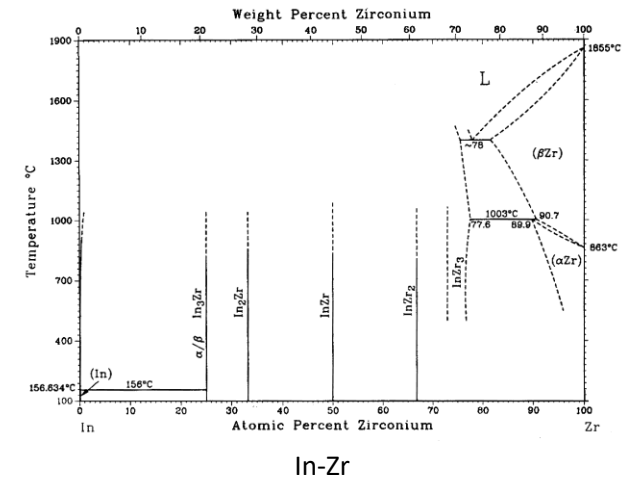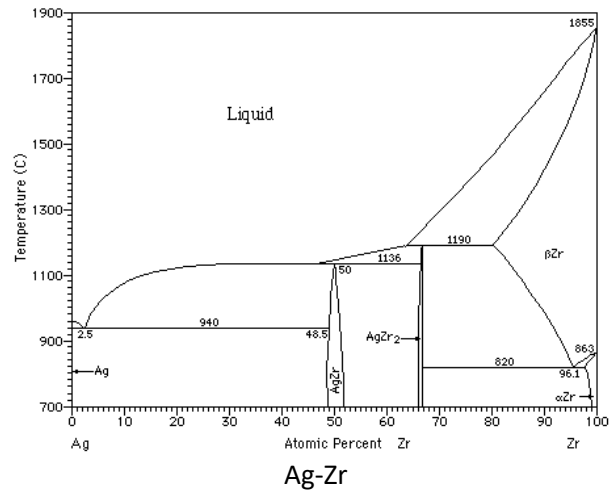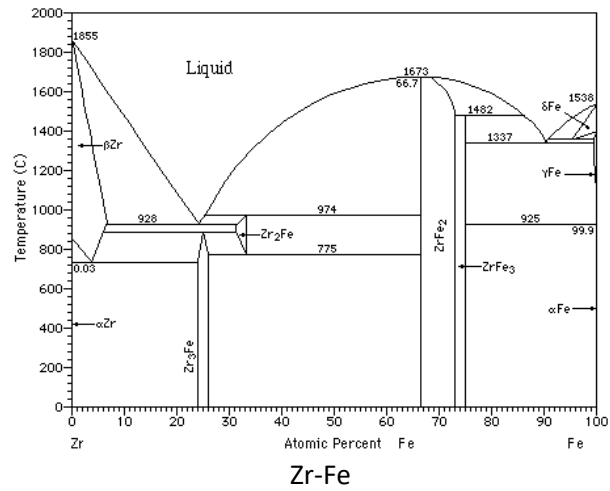
Figure 145   Binary phase diagrams.

172

In the framework of the international ALISA project, the QUENCH test was conducted as the first large-scale bundle test including a prototypical experiment stage in air + steam mixture. The bundle contained 20 heated and 2 unheated rods with M5® cladding as well as 2 Ag-In-Cd absorber rods surrounded by stainless steel cladding and M5® guide tube. Three typical features of QUENCH-18 were: 1) moderate pre-oxidation to ≈80 μm of oxide layer (less than in the reference QUENCH-16 test on air ingress), 2) a long period of oxygen starvation during the air and steam ingress stage (1770 s instead 800 s for the QUENCH-16 test performed without steam injection during air ingress), and 3) reflood initiation at the melting point of the cladding (≈2000 K instead of 1700 K for QUENCH-16). The temperature escalation during the air ingress between elevations 150 and 850 mm was significantly stronger than for QUENCH-16 (performed with the air ingress stage without steam flow) mainly due to higher exothermal cladding oxidation in oxygen, nitrogen and steam (corresponding total chemical power of ≈8 kW that is twice as much as electric power simulating decay energy). Releases of aerosols were registered at the beginning of temperature escalation (failure of absorber rods). Simultaneously, the readings of cladding surface thermocouples below elevation of 550 mm indicated the relocation of absorber melt.

During the starvation period about 100 and 450 g oxygen and steam, respectively, were consumed. During the steam consumption period about 45 g hydrogen were released. In the same time a partial consumption of nitrogen (about 120 g) was registered. Due to the relatively low heat input (≈12 kW as a result of electrical heating and exothermal reactions with steam and air), as well as the high specific heat of fusion of zirconium in comparison with its specific heat at the stage of temperature escalation, the escalation stopped when the melting point was reached. The cladding melt appearing at ≈2000 K remained localized between the outer oxide layer and the pellet.

Initiation of reflood with 50 g/s water caused a very strong temperature escalation to about 2430 K at elevations above 550 mm resulting in about 238 g hydrogen release. It is significantly more, than for QUENCH-16 (128 g performed also under air ingress conditions, but with the formation of a smaller amount of melt, and a total area of metallic zirconium only 8% less than that of QUENCH-18. Due to the re-oxidation of zirconium nitrides more than 54 g nitrogen and 15 g hydrogen were released. The rest and the largest part of the released hydrogen should be associated with the oxidation of the claddings in the upper part of the bundle and the oxidation of the metal melt in the middle part of the bundle.

The metallographic investigations of the bundle show residual re-oxidized nitrides at elevations below 950 mm. The cladding melt formed in the upper elevations and relocated downwards to 350 mm, was completely oxidized and mostly collected inside the grid spacer at 550 mm. For the bundle elevation 65 mm only two kinds of frozen pools were detected: 1) Zr based metal mixed with Ag, In and Cd, and 2) (Ag, In, Cd) melt reacted with Zr bearing spacer grids. Part of this metal melt was relocated downwards as far as elevation -40 mm.